TECHNISCHE UNIVERSITÄT MÜNCHEN

Fakultät Wissenschaftszentrum Weihenstephan für Ernährung, Landnutzung und Umwelt

High fat diet accelerates esophageal dysplasia in a mouse model of Barrett Esophagus through IL-8 (KC) mediated inflammatory niche formation

Natasha Stephens Münch

Vollständiger Abdruck der von der Fakultät Wissenschaftszentrum Weihenstephan für Ernährung, Landnutzung und Umwelt der Technischen Universität München zur Erlangung des akademischen Grades eines

Doktors der Naturwissenschaften

genehmigten Dissertation.

Vorsitzende: Univ. – Prof. Dr. Martin Klingenspor

Prüfer der Dissertation:
1. Univ. – Prof. Dr. Dirk Haller
2. Priv.-Doz. Dr. Michael Quante

Die Dissertation wurde am 23.08.2016 bei der Technische Universität München eingereicht und durch die Fakultät Wissenschaftszentrum Weihenstephan für Ernährung, Landnutzung und Umwelt am 12.10.2016 angenommen.

To my parents, thank you for instilling in me a fascination for science!

Table of Contents

Table of Figures & Tables

9

Zusammenfassung

Barrett-Ösophagus (BE) beschreibt eine gutartige Metaplasie des distalen Ösophagus in der Plattenepithel durch Zilinderepithel des Magens ersetzt wird. Die epidemiologisch beobachtete ansteigende Inzidenz an BE und Adenokarzinom des ösophago-gastralen Übergangs (AEG) erfolgt parallel zur adipösen Entwicklung der westlichen Gesellschaft. So ist ein hoher Body-Mass-Index (BMI) mit ösophegealem Reflux assoziert, welche wiederunm stark mit dem Auftreten von BE und AEG korreliert. Dem ungeachtet ist allerdings der genaue Mechanismus, durch den Adipositas für das vermehrte Erscheinen von BE und AEG verantwortlich sein könnte, bisher unbekannt. Eine Hypothese ist, dass wiederholte Exposition des gastro-ösophagealen Übergangs (EGJ) mit Säure- und Gallensäure-Reflux aufgrund der Fettleibigkeit zustande kommt und zu einer Schädigung und Reihe von entzündlichen Veränderungen der Ösophagusschleimhaut führt. Die Entzündung würde mit der Freisetzung entzündungsvermittelnder Zytokine korrelieren, was zur Infiltration des Gewebes durch Immunzellen führt die dann eine gesteigerte Karzinogenese verantworten. Desweiteren könnte aber auch eine durch die Adipositas direkt gesteigerte Entzündungsreaktion zur Akzeleration der Karzinogenese führen. Diese Thesen gilt es am Mausmodel zu testen:

Das Ziel dieser Arbeit war es also, die Rolle von Entzündung und Fettleibigkeit in einem neuen Mausmodell für BE und AEG zu verstehen. Überexpression von IL-1beta im Ösophagus führt in diesem Mausmodell zur Einwanderung von in der Kardia gelegenen Stammzellen in den Ösophagus, welche als Grundlage für Metaplasie und Dysplasie dienen. Wildtyp-Mäuse (WT) und Il-1beta exprimierende Mäuse wurden einer Hochfettdiät ausgesetzt und das Tumorwachstum im Unterschied zur Normaldiät verglichen. Weiterhin wurden zur Charakterisierung der feinen und komplexen Unterschiede auf den Metabolismus in diesem Modell folgende Merkmale untersucht: Zusammensetzung des Bluts (Serum), Hormonspiegel, Energiebilanz, Fressverhalten und Aktivität, Organmorphologie und –Physiologie sowie –Histologie.

IL-1beta-Mäuse unter Hochfettdiät zeigen einen beschleunigten Tumor-Phänotyp indem sie, im Alter von 9 Monaten, zu 100 Prozent eine Dysplasie entwickeln, wohingegen 12 Monate alte Mäuse unter Normaldiät zu 80% kleinere Tumoren aufweisen. Interessanterweise wurden unter HFD häufig Plattenepithelkarzinome im unteren Ösophagus beobachtet, was in diesem Modell bisher nicht der Fall war. Die metabolische Bewertung der HFD-Mäuse zeigte erstaunlicherweise einen ausgeprägten Phänotyp mit sehr wenig Körperfettanteil und schwacher Gewichtszunahme aber starker Progression zu Dysplasie und Tumorentstehung. Mithilfe von Micro-Array-Analyse und einer weitergehenden Beurteilung des „Tumor-Micro-Milieus" mittels Durchflusszytometrie (FACS) konnte eine mögliche Rolle von bestimmten Zytokinen in der entzündlichen Nische mit Rekrutierung spezifischer myeloider Zellen gezeigt werden. Besonders das Zytokin IL-8 scheint für den verstärkten Phänotyp verantwortlich zu sein. Dies unterstützend zeigen Mäuse einer Kreuzung aus dem IL-1beta Modell mit Mäusen eines Modells mit vermehrter IL-8 Expression einen bemerkenswert ähnlichen Phänotyp wie Il-1beta-HFD-Mäuse. In beiden Modellen akzelerieren bestimmte, aus der Kardia des Magens eingewanderte, Stamm- und Vorläuferzellen die Proliferation und Entartung aufgrund einer gesteigerten inflammatorischen Komponente im Ösophagusgewebe.

Zusammenfassend konnten wir also zeigen, dass im BE-Mausmodell eine HFD zu einer verstärkten lokalen und systemischen Entzündungsreaktion mit Ausbildung einer inflammatorischen Nische durch Rekrutierung von Immunzellen in den Ösophagus führt. Hierbei kommt es zur verstärkten Stammzell Expansion die zu einer gesteigerten Karzinogenese beiträgt. Folglich trägt die HFD mit ihrem Effekt auf Immun-(Stroma-) Zellen zur Entstehung einer karzinogenen Nische mit einem bestimmtem Zytokinprofil entscheidend bei.

Overview

Barrett Esophagus (BE) is a premalignant condition of the distal esophagus where normal squamous epithelium is replaced by columnar epithelium. The increasing incidence of BE and esophageal adenocarcinoma (EAC) is occurring in parallel to the obesity epidemic. A high body mass index (BMI) is associated with gastroesophageal reflux disease and frequent reflux strongly correlates with BE/EAC. Nevertheless, the distinct mechanisms by which obesity may be responsible for an increased progression from BE to EAC is unknown. Repeated exposure of the esophageal gastric junction (EGJ) to acid and bile reflux is thought to be obesity related which sets into motion a series of inflammatory changes in the mucosa. This can trigger inflammatory cytokines resulting in lymphatic tissue infiltration. Additionally obesity itself is discussed to accelerate inflammatory stimuli.

The aim of this thesis was to understand the role of inflammation and obesity in a novel mouse model where IL-1beta overexpression in the esophagus leads to expansion of cardia stem cells into the esophagus, giving rise to metaplasia and dysplasia. Wildtype (WT) and IL-1beta over-expressing mice were fed high fat diet (HFD) and tumor development was compared to normal Chow diet. Characterization by analysis of serum hormone levels, energy balance, feeding and activity, organ morphology, physiology and histology was conducted to elucidate subtle and complex traits unique to the metabolism of this model.

IL-1b mice on HFD show an accelerated esophageal phenotype with 100% of mice developing dysplasia by 9-months of age in contrast to mice on Chow that develop smaller tumors in 80% of mice by 12-months of age when compared on a pathological scale. Surprisingly with HFD squamous carcinoma in the upper esophagus presented frequently, this was previously not observed in this model. Metabolic profiling revealed a distinct phenotype with very low fat mass accumulation and low weight gain, but rapid progression to dysplasia and tumor development. An in depth study, through microarray analysis and detailed assessment of the microenvironment through flow cytometry elucidated a potential role for cytokines in an inflammatory niche with recruitment of myeloid cells and especially IL-8 (KC) as a key player in the acceleration of this

phenotype. Furthermore, crossing the BE mouse model with a mouse model of human IL-8 over-expression showed a remarkably similar phenotype as seen on HFD, with a microenvironment driven by neutrophils recruitment in the esophagus as was observed in the IL-1beta model on HFD. In both models distinct stem and progenitor cells from the cardia are expanding and contribute to increased proliferation malignant transformation.

In the BE mouse model HFD induces an increased systemic and local inflammation with and inflammatory niche through recruited immune cells in the esophagus that attracts stem cell migration and accelerates the progression to dysplasia. Thus the effect of HFD on the immune (stromal) cells contributes to a distinct pro-carcinogenic niche that is elicited by a specific cytokine profile.

Chapter 1: Introduction

1.1 Obesity

Obesity has become a global epidemic in the 21st century. The World Health Organization (WHO) defines obesity as "abnormal or excessive fat accumulation that presents a health risk", and is crudely assessed using the measure of body mass index (BMI)[1]. BMI is calculated by dividing a person's weight (kilograms) by their height (meters) squared. According to the Center for Disease Control (CDC, USA) and WHO, an adult with a BMI between 25.0 and 29.9 is classified as overweight and a BMI equal to or more than 30 is classified as obese. BMI, however, is a crude measure of obesity, as it does not account for the distribution of body fat or overall composition of body mass in the body. Other measures of obesity may be more specific in determining relative risk for associated diseases, such as waist circumference (WC), waist to hip ratio, assessment of visceral fat using computed tomography (CT) or magnetic resonance imaging (MRI). However, BMI remains the most widely used measure because of its simplicity and ease of comparison[2, 3].

Being overweight and obese are risk factors for the development of numerous chronic and comorbid diseases, including diabetes, cardiovascular diseases, several cancers and mortality[4, 5]

Like most metabolic diseases, the etiology of obesity is complex; involving interactions among an individual's genetic background, hormones and direct and indirect environmental factors[6, 7].

1.1.1 Prevalence

Obesity rates in Europe and North America are generally high, and appear to be on the rise in developing counties over the last few decades with no sign of slowing down[8, 9]. The WHO states that worldwide obesity has more than doubled since 1980, with estimates for 2014 showing that more than 1.9 billion adults (18years and older) were overweight and of these over 600 million were obese[1]. If recent secular trends continue unhindered, absolute values for 2030 are projected as high as 2.16 billion overweight and 1.12 billion obese

adults[10]. This nearly doubling effect of obese adults within the next fifteen years will most certainly be accompanied in parallel with increased risk for disease and mortality; posing a huge burden on health-care industries globally.

As a result, large efforts have been underway since the 1980s to understand every facet of this disease. While a wealth of knowledge has already been amassed regarding the social and environmental factors, the current understandings of mechanisms and relationships between obesity, inflammation and metabolic syndrome, cardiovascular disease, cancer and other disorders has only scratched the surface.

1.1.2 Development

The human body metabolizes proteins, carbohydrates and fats in order to meet daily energy requirements. As an organism, the body has adapted to store energy in the form of fat, to be mobilized in times of energy deprivation. However, a modern lifestyle and Westernized diet are associated with increased prevalence of overweight and obese individuals, resulting from palatable energy-dense foods in combination with reduced requirement of physical activity[11].

The body stores and releases lipids in the form of triglycerides in adipose tissue in cells called adipocytes. Adipose tissue expansion occurs through adipocyte engorgement, which can lead to insulin resistance, a condition of decreased glucose utilization by insulin-sensitive tissues resulting from impaired insulin action[12, 13]. Furthermore, this accumulation of adipose tissue overtime has been linked to increased morbidity, disability and premature mortality from cardiovascular disease (CVD), diabetes, cancers and musculo-skeletal disorders[8, 14, 15].

Excess accumulation occurs when energy intake exceeds energy expenditure, resulting in an imbalance and storage of triglycerides in white adipose tissue (WAT). WAT serves as an energy reservoir, while also functioning as an endocrine organ that secretes adipocytokines[16]. In addition to muscle tissue and the liver, WAT is crucially involved in systematic processes including glucose tolerance and inflammatory response via secretion of adipokines[17, 18]. Thus adipose tissue is no longer considered an inert tissue devoted to energy storage. It is now clear that this endocrine organ actively participates in regulating

physiologic and pathologic processes, including immunity and inflammation[19]. Besides adipocytes, adipose tissue contains connective tissue matrix, nerve tissue, stromovascular cells, and immune cells that all play important roles in tissue housekeeping, removal of detritus, and apoptotic cells and tissue homeostasis maintenance in a non-obese setting[20]. However, excess fat accumulation can cause alterations in the secretory function of adipose tissue and immune cells. This can lead to an increase in the number and activity of macrophages, mast cells, neutrophils, and T- and B- lymphocytes, ultimately leading to the imbalance associated in the development of obesity-related local and systemic inflammation[16, 20].

1.1.3 Obesity and Inflammation

A key initiator of the obesity-inflammatory response is adipose tissue. Overweight and obese individuals are characterized by an increase in number of adipose cells (hyperplasia) and increase in the size of these adipocytes (hypertrophy)[21-23]. These enlarged adipocytes are deficient in perilipids; phosphoproteins that prevent the hydrolization of triacylgycerides to release free fatty acids (FFAs) by lipases[24, 25]. As a result obese individuals have an increased rate of basal lipolysis and subsequently increased levels of circulating FFAs and an increased likelihood for the development of insulin resistance[26].

Epidemiological and clinical studies have laid the groundwork showing that overweight and obese individuals have higher levels of circulating proinflammatory cytokines and lower levels of anti-inflammatory cytokines, in comparison to healthy-lean individuals[23]. Adipose tissue includes of bone marrow derived macrophages, which appear to be present in higher numbers in obese individuals due to their role of scavenging dying adipocytes, which increases with obesity[27]. Activation of these adipose tissue macrophages (ATMs) releases a an array of chemokines, which in turn recruit additional macrophages, resulting in a feed-forward loop of increased ATMs, propagating a state of chronic low-grade inflammation[28].

Several different pathways are involved in the adipocyte mediated inflammatory response, which are regulated by the release of free fatty acids and

adipocytokines such as tumor necrosis factor-alpha (TNF-a), IL-1beta (IL-1b), IL-6, and monocyte chemotactic protein-1 (MCP-1) secreted by WAT[23, 29].

While the relationship between inflammatory reactions and lipid metabolism and insulin resistance is known, the mechanisms underlying the onset of low-grade inflammation is not fully understood[29]. The discovery that obese murine and human adipose tissue is infiltrated with highly increased populations of macrophages was a critical advance in understanding the mechanisms by which obesity propagates inflammation[28, 30, 31]. These obese-individual ATMs have been shown to be highly proinflammatory, with increased expression of genes important for macrophage adhesion, migration and inflammation in comparison to lean-individual ATMs, which have a more anti-inflammatory profile [28, 31-33].

This low-grade state of inflammation switches from M2 to M1 state in the obese state[34]. M2 macrophages or alternatively activated macrophages release anti-inflammatory cytokines (IL-10, IL-1Ra). M1 macrophages on the other hand are classically activated macrophages that produce pro-inflammatory cytokines (TNF-a, IL-6)

Briefly, macrophages get recruited into adipose tissue via the MCP-1/CC chemokine receptor 2 (CCR2) cascade. The phenotypic switch from M2 to M1 results in reduced IL-10 and arginase production, and an increase in TNF-a production. Obesity induced inflammation also activates other proinflammatory pathways including the group of c-Jun N-terminal protein kinases (JNK), while ablation of JNK results in protection from diet–induced obesity and inflammation[20, 35, 36].

Production of adiponectin, a potent inhibitor of TNF-a induced monocyte adhesion and adhesion molecule expression is significantly reduced with obesity. TNF-a increases adipocyte lipolysis, mediate by the decrease in perilips as described above, this can lead to an increase in systemic insulin resistance[37].

IL-6 levels have been shown to have a 10-fold increase in expression in obese individuals, when normalized to total number of adipocytes[38]. Circulating plasma levels of IL-6 also increase by obesity[39], which has been associated with increased lipolysis and fat oxidation[40], insulin resistance and an

increased risk for development of type-2 diabetes and myocardial infarction[26, 41, 42]. A brief overview is illustrated in Figure 1.1.3, below.
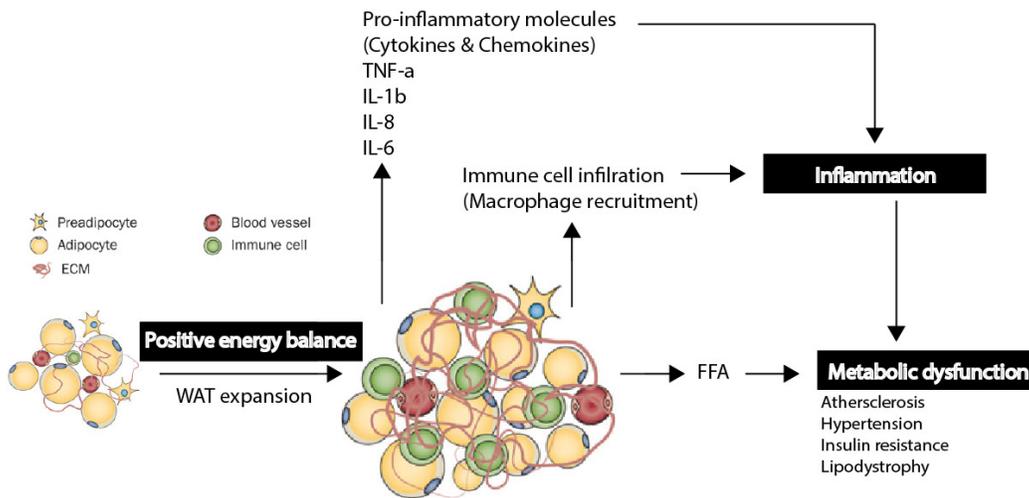
Figure 1.1.3: Adipose tissue inflammation.
The onset of a positive energy balance and low energy expenditure can cause adipocytes to store energy in the form of triglycerides as they expand in size. Adipocyte growth can occur faster than vascularization and can result in low oxygen supply. Adipocytes secrete pro-inflammatory molecules that attract immune cells, e.g. macrophages and neutrophils. An increase in pro-inflammatory molecules can lead to a state of chronic inflammation in adipose tissue, which can lead to metabolic dysfunction. Figure adapted from Shen 2014 and Berryman 2013 [43, 44].

1.1.4 Diet and Inflammation

Obesity is a modifiable risk factor for a number of diseases and diet is one of the key environmental risk factors associated with obesity and is also the most easily modifiable. Obesity-associated chronic low-grade inflammation is influenced by energy balance. Over consumption of energy dense foods results in increased markers of inflammation[33, 45, 46]. These increases can be observed with or without weight gain (post-prandial), suggesting that obesity-associated chronic inflammation may be strongly influenced by caloric load[47]. It has also been shown that caloric restriction can increase inflammation[45, 48]. Both findings highlight the importance of energy balance in preventing diet-induced inflammation. Dietary macronutrients play a pivotal role in obesity-associated inflammation and include proteins, fats, carbohydrates and fiber; of these, dietary fats are of particular interest.

1.1.5 Dietary Fat

The inflammatory potential of a dietary fat or lipid is related to its composition. These dietary fats are made up of triglycerides, phospholipids and sterols, and can be classified as saturated or unsaturated fatty acids. Saturated fatty acids (SFA) are present in processed meat, refined grain and fried foods[45]. The inflammatory effects of SFA have been implicated in numerous *in vitro* and *in vivo* studies, via the Toll-like receptor (TLR) 1 pathway with increases in inflammatory markers such as C-reactive Protein (CRP) and IL-6 [49-51]. Studies have shown a causal relationship between saturated fatty acids (SFA) and polyunsaturated fatty acids (PUFA) and a strong pro-inflammatory phenotype[23]. While no direct and clear associations have been reported, the relationship between SFA and pro-inflammatory markers and/ -or adipokines can be supported by biological mechanisms[52]. Two pathways have been suggested for SFA-mediated inflammatory mechanisms; a TLR-4-dependent and a TLR-4-independent pathway[28]. SFAs such as Lauric, Palmitic and Stearic acid stimulate macrophages via the TLR-4-dependent pathway, through lipid domains known as "lipid rafts", resulting in increased IL-6 gene expression [53]. A study by Mu and colleagues examined a healthy adult population with a wide range of inflammation levels to assess the effect of SFA on inflammation, showing a proinflammatory role of Palmitic acid through increased levels in IL-6 levels in serum [54]. SFAs also initiate the TLR-dependent pathway via the production of reactive oxygen species (ROS), which combine to form apoptotic speck protein complexes (ASC) with pyrin domain inflammasomes 3(NLRP3) known as NLRP3-ASC inflammasome complexes, which regulate the release of IL-1beta. The increase in IL-1beta reduced insulin signaling, suggesting a possible a role for SFA-mediated inflammation in insulin resistance[55].

1.1.6 Obesity and Cancer

In recent years the link between obesity and cancer risk has been of keen interest. Estimates correlate approximately 20% of all cancers to be caused by excess weight[56]. Epidemiological studies show that obesity leads to an increased risk of several cancers including colon, breast, endometrium, liver, kidney, esophagus, gastric, pancreatic, gallbladder, and leukemia as briefly

illustrated in Figure 1.1.6. Obesity can also lead to poor treatment response, worsened prognosis and increased cancer-related mortality[57]. Increased body weight has been associated with increased death rates for all cancers combined and for cancers at multiple specific sites[57, 58]. The influence of obesity on carcinogenesis has been elegantly highlighted by the rise in esophageal adenocarcinomas cases following the worldwide rise in obesity, which will be discussed in great detail further on[56]. Another example associating weight gain with an increase in postmenopausal breast cancer risk in women who are not on menopausal hormone therapy[59]. Furthermore, the Swedish Obese Subjects (SOS) study clearly illustrated that weight loss of an average of 20kg, through bariatric surgery, in patients with an initial BMI above 40kg/m^2 reported a significant reduction in cancer incidence in follow ups longer than 10 years[60, 61].

Males	
Esophageal	1.52
Colon	1.24
Liver	1.24
Pancreas	1.07
Prostate	1.03

Females	
Endometrial	1.59
Gall bladder	1.59
Breast (postmenopausal)	1.12
Pancreas	1.12
Colon	1.09

Figure 1.1.6: The association between obesity and cancers.
Relative risks of GI cancers in obese men and women, risks per 5 kg/m^{2}increase in body mass index (data extracted from Aleman, 2014 and Long, 2014 [3, 62]).

While the biological mechanisms underlying the association between obesity and cancer are complex and not fully understood, there is extensive research being conducted on obesity-related hormones, growth factor, modulation of energy balance and calorie restriction, multiple signaling pathways, and inflammatory processes[57, 63-65]. Postulated mechanisms by which obesity might be promoting cancer include (1) increased production and bioavailability of growth factors such as insulin and insulin-like growth factor (IGF-1), (2) increased production of sex steroid hormones such as estrogen and its down stream targets, (3) alterations in adipocytokines profiles of leptin and adiponectin which are key regulators of energy balance but know to have growth, immune and tumor-regulatory function, (4) low-grade or chronic inflammation, oxidative stress influencing cytokine production and immune modulation, and (5) an altered intestinal microbiome[57, 66-72].

1.2 The Esophagus, Obesity and Cancer

1.2.1 The Esophagus

Food is processed in the body starting in the oral cavity; it then passes through the esophagus and into the stomach. Food is propelled through the esophagus via active peristalsis into the stomach where digestion and absorption can begin.

1.2.2 Anatomy and Physiology
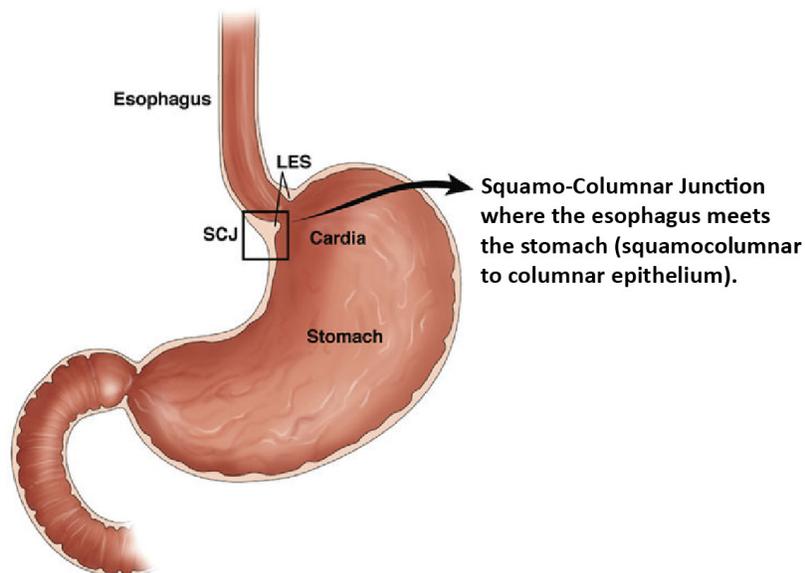
Figure 1.2.2: Anatomy of the human esophagus and stomach.
The esophagus is a muscular tube that connects the pharynx with the stomach. The intersection where the esophagus and the stomach meet is known as the squamo-columnar junction (SCJ). Figure adapted and used with permission from M. Quante [73].

During week 10 of development, the esophagus forms from the foregut and is lined by ciliated epithelial cells. During the fourth month of development, the ciliated epithelium begins to be replaced by a stratified squamous epithelium, this process continues until birth[74]. The adult esophagus as seen in Figure 1.2.2 is fashioned as a long, hollow muscular tube of around 18 to 26cm that spans from the upper esophageal sphincter (UES; not visible in Figure 1.2.2) to the lower esophageal sphincter (LES)[75]. Structurally, the wall of the esophagus comprises four layers: the innermost mucosa, submucosa, muscularis propria, and adventitia. The esophagus, unlike the stomach and the rest of the GI

tract lacks a serosal layer but is connected by a thin layer of connective tissue[74, 76].

The mucosa of a normal esophagus is made up of stratified squamous epithelium until the LES where the squamous epithelium joins with the gastric columnar epithelium[76]. There are few glands and limited secretory functions in the esophagus compared to the rest of the gut. The high-pressure area of the LES has an intrinsic and extrinsic functional component. Intrinsically, the LES consists of esophageal muscle fibers under neurohormonal influence and extrinsically, it consists of the diaphragm muscle that that assists with the movements of respiration[74]. Defects or dysfunction in these components can result in symptoms such as dysphagia, chest, pain, or heartburn. Esophageal motility disorders fall into 3 groups; achalasia, distal esophageal spasm (DES) and gastroesophageal reflux disease (GERD)[77]. GERD is the most prevalent of the three; its associated symptoms can impact quality of life, as well as changes in mucosal structure[78].

1.2.3 GERD

The term GERD encompasses all manifestations of exposure of the esophagus to gastric content and presents with symptoms of mucosal damage produced by abnormal reflux of gastric contents into the esophagus or beyond, into the oral cavity or lung[79-82]. Manifestations of GERD can be divided into typical, atypical and extra-esophageal symptoms[81]. GERD symptoms usually present following a meal, and are aggravated by supine position. GERD is currently one of the most dominant clinical problems addressed by primary care physicians and gastroenterologists, with a prevalence of 10%-20% in the western world and less than 5% in Asia[81].

The prevalence of GERD has been on the rise in Western countries over the last 30 years, and this increase has been strongly correlated with the parallel increase of obesity[83]. Several mechanisms have been proposed explaining the relationship between obesity and GERD. It is hypothesized that the volume and distribution of visceral fat causes increased reflux symptoms. Increased visceral fat imparts direct mechanical pressure onto the stomach, increasing intragastric pressure leading to increased frequency of transient lower esophageal sphincter

relaxation and subsequent reflux. Another postulation relates to the amount of visceral abdominal fat compared to subcutaneous fat and the increased circulation of inflammatory cytokines resulting from the low-grade inflammation associated with obesity[84]. Visceral fat has been shown to release a number of proinflammatory cytokines such as IL-6 and TNFa which are known to be up regulated in BE[85]. Evidence is limited linking other environmental factors to the rising prevalence of GERD[86].

Obesity appears to also be related with further complications associated with long-term GERD such as erosive esophagitis, Barrett Esophagus and esophageal adenocarcinoma[77]. However, the exact mechanism by which obesity drives the progression from normal esophageal mucosa to metaplasia, to Barrett low-grade dysplasia, high-grade dysplasia, carcinoma and the later stages of metastasis remains to be understood in detail.

1.2.4 Barrett Esophagus

Barrett esophagus is a medical conditioned named after a pioneer in the field of thoracic surgery, a scholar and teacher, Norman Rupert Barrett[87]. In a 1950 publication entitled "Chronic peptic ulcer of the oesophagus and "oesophagitis"" Dr. Barrett identified the columnar lining of the esophagus in several patients as being of "histologically gastric in type" and hypothesized that BE resulted from proximal migration of stomach epithelium below the gastroesophageal junction[87, 88]. In the 1980's the prevailing hypothesis suggested that reflux-induced damage to the esophageal squamous epithelium led to a reprogramming of sorts of multi-potent stem cells within the basal layer.

BE results as a consequence of chronic GERD, which causes damage to the normally occurring stratified esophageal squamous epithelium and causes it to heal and be replaced through a metaplastic process where columnar cells replace the damaged squamous cells [85, 86]. The metaplastic epithelial regions include different cell types such parietal and chief cells, mucous producing cells and goblet cells as described in Table 1.2.4. BE has been primarily linked to chronic GERD, resulting in chronic inflammation of the esophagus and is diagnosed 10 times more often in patients who complain of constant reflux, as a result, conversion rate of BE to EAC is between 0.4% -0.5% annually[85, 89, 90].

Table 1.2.4: Different cell types associated with Barrett esophagus.

Location	Cell type
Gastric-fundic-type epithelium	Parietal and Chief cells
Transitional-type epithelium	Mucous producing cells
Columnar epithelium	Intestinal-like goblet cells

It is hypothesized that in the gastric corpus and cardia, cells migrate in both directions from the isthmus to differentiate into gastric surface mucus cells that coat the gastric pits, and gastric parietal and zymogenic cells at the base of the gland[91]. Severe damage of the distal esophagus results in the initiation of a wound repair response leads to a migration progenitor columnar cells from the cardia into the esophagus to replace damaged squamous epithelium[73].

Barrett esophagus might involve a switch in the fate of resident stem or progenitor cells that might either reprogram or transdifferentiate squamous esophageal basal cells or cause migration of gastric cardia cells[92].

This abnormal columnar epithelium, characteristic of BE, is an incomplete form of intestinal metaplasia that can be a predisposition to adenocarcinoma [90].

Of the patients suffering from symptoms of reflux, only 10% of individuals develop BE indicating that additional factors might be involved with this progression[93]. Long-standing acid and bile reflux can cause damages to the squamous esophageal mucosa that in turn heals through a metaplastic process in which squamous cells are replaced by columnar-like epithelium[90].

1.2.5 Prevalence and Risk Factors for Barrett Esophagus

The importance of BE arises from its potential to transform into adenocarcinoma, regardless of a low conversion rate of an estimated 0.4% - 0.5% person-year progressing from BE to EAC [94].

BE is usually discovered during endoscopic examinations for evaluation of GERD symptoms in white, male patients 50 years and older[95]. BE is up to three times more common in men as in women, less common in African and Asian races and rare in children[96, 97]. Typically several risk factors for BE overlap with those common to EAC. GERD is considered to be the most common and important

factor. A recent study showed that GERD associated reflux increases the odds of long segmented BE by up to five fold [84]. Other important risk factors include obesity (visceral), cigarette smoking, alcohol consumption, and familial history of BE (between 7 to 11% of all cases)[98-100].

1.2.6 BE and Obesity

It has been well documented that BE is associated with obesity [84, 99, 101-104]. As with GERD, obesity has been shown to increase the risk for BE by similar mechanisms. This includes volume of abdominal fat resulting in increased intragastric pressure and increased inflammatory cytokine production. Visceral fat has been shown to release proinflammatory cytokines including IL-6 and TNFa, which are over expressed in BE[101]. Currently, several studies show confounding associations between BE and BMI. Studies that support the association of a high BMI and increased BE risk were all adjusted for up to four variables such as sex, age, and race. However, they were not adjusted for GERD symptoms, which is the most important risk factor for BE and most likely a potential confounder[105].

1.2.7 Esophageal Cancer

Esophageal cancer is categorized as a leading cause of cancer-associated mortality despite significant advances in the field of clinical oncology.

Worldwide, esophageal cancer currently ranks as the eight most common type of cancer, and the sixth most common cause of cancer death [3, 62].

Esophageal cancer can be classified into two main subtypes: esophageal squamous-cell carcinoma and EAC. EAC incidence increases with age, and rarely occurs in young people. It peaks predominantly in the seventh and eight decades of life, and is three to four times as common in men as it is in women[92]. Squamous-cell carcinoma has a more equal sex distribution. However in the past few decades, rates of esophageal squamous-cell carcinoma have declined. EAC has become the predominant type of esophageal cancer in North America and Europe, accounting for 50% of esophageal cancer[106]. Risk factors for esophageal adenocarcinoma include GERD, obesity, and smoking. Many studies have identified obesity as a key risk factor for EAC for both genders; which is likely due in part to increasing BMIs[107].

1.2.8 Prevalence and Risk factors for EAC

EAC is rising at an alarming rate in many parts of the Western world, as well as developing Asian countries. Currently the increase in the incidence of EAC is greater than that for any other cancer, with esophageal and gastroesophageal junction cancers increasing at a rate of 4-10% annually in Western countries[108]. While there appears to be an increase in all race and gender groups, the most dramatic increase appears to be in white males. Data from the National Cancer's Institute's Surveillance Epidemiology and End Results (SEER) program indicated that EAC in white males rose from 0.8 per 100,000 in 1973 to 5.4 per 100,000 in 2002, a yearly increase of ~8%[94]. Most studies suggest that BE is most common in men, especially in white Americans and Europeans, less common in Africans and mostly uncommon in Asians. As observed in Figure 1.2.8, the increase in the incidence of obesity dramatically parallels with the rise of EAC in the western world. An association between high BMI (>25) and an increased risk of EAC has been reported in men and women, and higher BMIs have been associated with higher cancer risk [94].
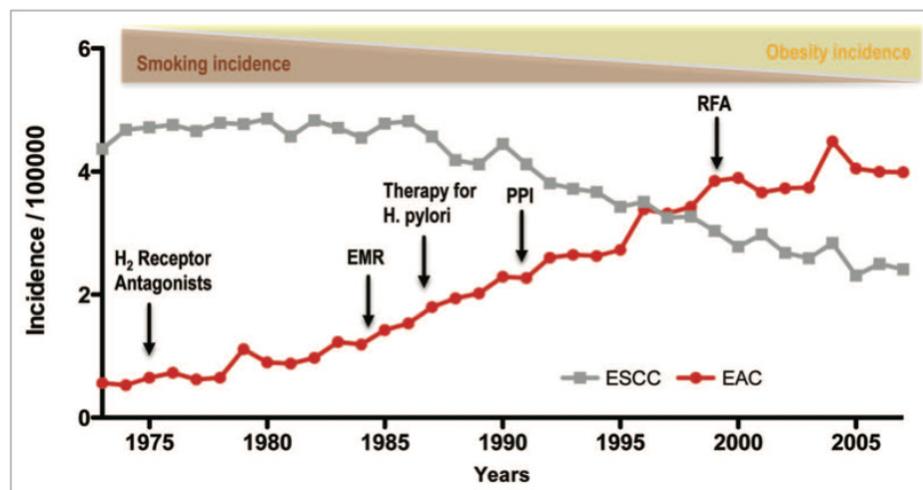
Figure 1.2.8:   The increasing incidence of esophageal adenocarcinoma (EAC) between 1975 and 2005 and its relationship to associated factors.
In the past 30 years, esophageal squamous cell carcinoma (ESCC) has seen a decline in incidence, in relation to its major risk factor, tobacco use. EAC appears to be on the rise concomitantly with obesity, a known risk factor for the disease. Despite medical therapies such as acid inhibition through H2 receptor antagonists and proton pump inhibitors (PPIs), and the treatment of H. pylori, EAC continues to rise in incidence. Data obtained from the Surveillance Epidemiology and End results (SEER) database of the National Cancer institute. Figure used with permission from M.Quante[109].

The epidemiological risk factors of esophageal adenocarcinoma are similar to BE, with GERD and BE being the most prevalent. While GERD is undoubtedly one of the strongest and most well understood risk factors for EAC, a majority of patients with GERD never develop EAC, however, patients with EAC can present without symptoms of GERD[110]. Therefore, it is possible that chronic reflux can promote the development of EAC with out presenting symptoms prior to diagnosis. GERD symptoms including heartburn and acid regurgitation affecting up to 20-30% of people weekly and about 60% of people at some time during the course of a year[111].

The other main risk factor for EAC is BE, which is strongly associated with GERD Barrett esophagus is the initial step in the histopathological progression that can lead to low-grade dysplasia, high-grade dysplasia and ultimately esophageal adenocarcinoma.

Additional risk factors for the development of EAC include alcohol consumption, smoking and tobacco use, and obesity[112, 113]. Alcohol consumption and smoking and tobacco use are strong risk factors primarily for SCC, but EAC as well. It was found that tobacco use increased the risk of EAC by 2.18 fold (95%CI, 1.84-2.58)[110]. The role of obesity in relation to carcinogenesis has been best highlighted by the shift in esophageal cancer morphology from squamous to adenocarcinoma over the last 40 years which appears to be occurring in parallel to the worldwide obesity epidemic, as highlighted in Figure 1.2.8[56]. Obesity, particularly central obesity predisposes to BE and EAC. A BMI of 30 to 39 (kg/m2) is associated with a 2.39 fold increase in risk of EAC. Abdominal or visceral obesity, in particular, is associated with BE and EAC. Current findings suggest that excess body weight and energy consumption are important risk factors for the development of cancer. The high prevalence of the combination of obesity and GERD could contribute to the dramatic increase of EAC in the Western World[3, 107].

1.2.9 EAC & Obesity

A systematic review of prospective studies from regions around Europe, Australia and Asia-Pacific investigating obesity and the risk of EAC was summarized by Alexandre et.al demonstrating an increase in BMI by 5kg/m^2

resulted in an association that was similar between men (RR = 1.52, 95%CI: 1.33-1.74) and women (RR = 1.51, 95%CI: 1.31-1.74)[2].

Although the pathogenesis of EAC is not fully defined, multiple mechanisms postulating the link between obesity and BE and EAC have been proposed, including increased rate of GERD as a result of mechanical force, elevated serum pro-inflammatory adipocytokines, insulin and insulin-like growth factors, and increased leptin levels as a result of increased adipose tissue[114].

Obesity, specifically visceral adiposity, has been shown to increase intra-gastric pressure resulting in a pressure gradient that can promote the formation of hiatal hernia and thereby increase the risk for the development of GERD[114]. However, the robustness of this theory comes into question with data that show that obesity has a weak positive association with lower esophageal sphincter pressure during inspiration and inversely associated during expiration[114].

Another postulation suggests that visceral adiposity is associated with alterations in circulating levels of inflammatory markers know to be associated with BE and EAC.

1.2.10 Disease progression

In combination with the risks detailed in the previous section, BE can progress to EAC as detailed in Figure 1.2.10. Patients with BE, presenting frequent symptomatic heartburn often seek medical attention at early stages of the disease and BE can visualized and biopsied during esophagogastroduodenoscopy (EGD). Endoscopic surveillance methods such as these are insufficient in identifying at risk patients or treating BE lesions and may not be able to detect early cancers in a large percentage of patients[89, 115]. Prior to neoplastic BE cells becoming malignant, some genetic alteration that progress to malignancy cause morphologic changes in the tissue that can be recognized by a trained pathologist as dysplasia[116]. Dysplasia is classified as the histologic expression of genetic alterations associated with unregulated cell growth[117]. Structural abnormalities observed include nuclear changes such as enlargement, pleomorphism, hyperchromatism, stratification, atypical mitoses, loss of cytoplasmic maturation and crowing of tubules and villiform surfaces.
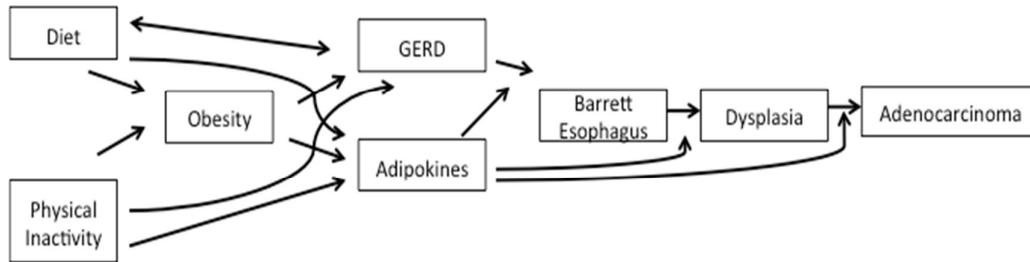
Figure 1.2.10: Associated risk factors in the development and progression of BE and EAC.
BE is thought to progress to EAC in a step-wise manner resulting as a consequence of chronic gastroesophageal reflux, potentially associated with obesity. Figure adapted from Falk, 2011[118].

Due to its aggressive nature, esophageal cancer can spread through a variety of pathways including direct extension, lymphatic spread and via hematogenous metastasis[119].

While the exact stem cells responsible for the development of EAC require further confirmation, it is hypothesized that cardia stem cells differentiate into columnar like epithelium first, and later on into intestinal metaplasia[73]. Based on published observations of the L2-IL-1beta mouse model of BE and EAC, bile acid induced inflammation activated the formation of gastric cardia stem cells migrating into the distal esophagus where they gave rise to columnar like metaplasia and eventually dysplasia. What can be learned from this model is that BE and EAC can arise from gastric progenitor cells[73]. Additionally, this hypothesis of metaplasia spreading proximally was confirmed in the human ProGERD study, where 20% of patients with GERD and IM in the cardia region were found to have BE diagnosed 2 to 5years prior[120].

1.3. Inflammation and Carcinogenesis

There is a growing body of evidence suggesting that on a molecular level, some pathways associated with inflammation and injury are very similar to those involved with carcinogenesis. Inflammation associated with obesity is characterized by abnormal cytokine production, activated immune response and increased inflammatory signaling, resulting in increased circulation of IL-17, IL-22, TNF-a, IL-6 and MCP-1; factors known to play a role in cancer development and progression[62]. The role of inflammation in carcinogenesis is well established and accepted, however, the mechanisms remain to be fully elucidated.

This relationship between an inflammatory state and cancer is complex and two-sided. From a cell-intrinsic perspective, it can be viewed as the result of genetic modifications that initiate protective inflammatory signaling and result in an "inflamed microenvironment", and from an extrinsic perspective, a mechanism in which infection and subsequent chronic inflammation progress towards oncogenesis[121].

In recent years, inflammation has been widely identified and accepted as one of the hallmarks of cancer[122]. While the cell of origin of cancer is a result of genetic alterations, other environmental factors can control the malignant process, creating a unique niche, or microenvironment. Cells that are part of the tumor microenvironment can respond to various stimuli and communicate via contact and secretory mediators. In addition to cancer initiating cells, a tumor microenvironment is home to fibroblasts, macrophages, endothelial cells, lymphocytes, neutrophils, and mast cells[121].

Inflammation within the tumor microenvironment contributes to cellular proliferation and survival of malignant cells, deoxyribonucleic acid (DNA) damage, angiogenesis, metastasis, inhibition of apoptosis and reduced response to hormones and chemotherapeutic agents[123, 124]. Inflammation can promote carcinogenesis by inactivating mutations in tumor-suppressor genes or in posttranslational modifications in DNA repair proteins via reactive oxygen species (ROS)[124].

The inflammatory environment is comprised of cells from the innate immune system as well as the adaptive immune system, Figure 1.3. This diverse and

complex network of immune cells can promote tumorigenesis. Cells of adaptive immunity, such as T-helper (Th) 17 and Th2 cells can contribute to inflammation through the production of cytokines, growth factors, enzymes, and angiogenic mediators. Cells of innate immunity, such as tumor-associated macrophages (TAMs), mast cells (MCs), neutrophils and myeloid derived suppressor cells (MDSCs), can contribute to tumor development. This network also promotes immune cell recruitment to the tumor site, where proliferation and invasion occur. Neutrophils are the first leukocytes that are recruited to sites of inflammation. This occurs through concerted signaling of several chemoattractants such as chemokines.
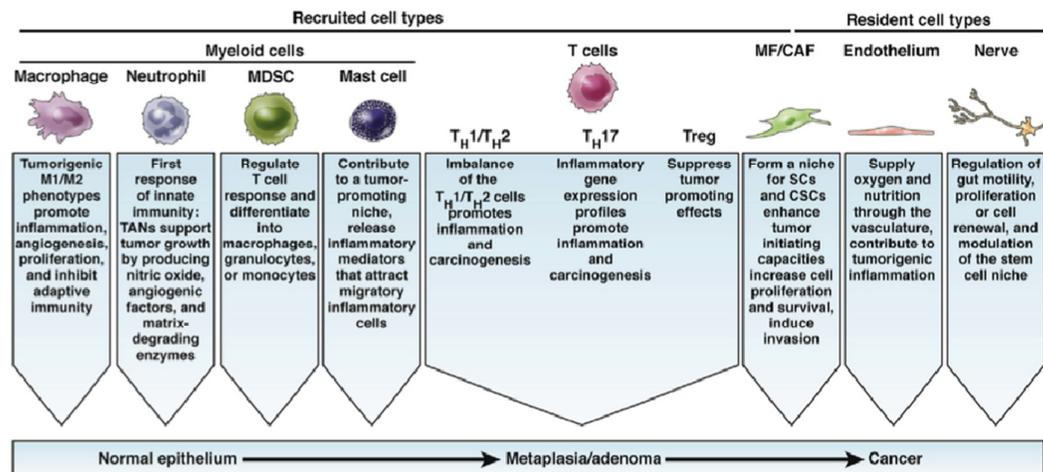
Figure 1.3: Different cell types reside or are recruited to the tumor microenvironment and are involved in the progression to carcinogenesis. Resident cells including CAFs, endothelial cells and nerves, and recruited cells including myeloid cells, T-cells and cancer associated fibroblasts (CAFs) comprise a complex signaling network that influences the progression of normal to metaplastic and dysplastic epithelium in the gastrointestinal tract. Figure used with permission from M.Quante[125].

1.3.1 Cytokines

Cytokines are small, nonstructural proteins that range in weight from 8 to 40,000 Daltons. Some cytokines promote inflammatory processes, while others serve to suppress genes for pro-inflammatory cytokines and have an anti-inflammatory role. They play a key role in immunity and inflammation, including innate immunity, antigen presentation, bone marrow differentiation, cellular recruitment and activation and adhesion molecule expression[126]. Some cytokines are primarily derived from mononuclear phagocytic cells and antigen

presenting cells (APCs); these promote cellular infiltrate and damage to resident tissue characteristic of inflammation. Monocytes can also be triggered to produce cytokines via the innate immune system. Receptors such as the lipopolysaccharide (LPS) receptor are able to recognize stereotypic components of pathogens not occurring in mammalian cells. Cytokines predominantly produced by monocytes include TNF and several interleukin molecules[126]. And are capable of controlling immune and inflammatory settings through the activation of numerous downstream effectors, such as NFkB, AP1, STAT, and SMAD transcription factors, and caspases, in favor of antitumor immunity (through IL-12, TRAIL, IFNg) or enhanced tumor progression (through IL-6, IL-17, IL-23). Additionally; they can have direct effects on cancer cell proliferation and survival (through TRAIL, TNFa, EGFR ligands, TGFb and IL-6)[127].

1.3.2 Chemokines

Chemokines are a family of "chemotactic" cytokines that regulate leukocyte migration. Similarly to an infection-associated inflammatory process, chemokines are responsible for immune cell infiltration into tumor tissues[127]. This leads to the conundrum of whether the increased production of chemokines at tumor sites is an indication of progression to malignancy or a defense mechanism to a state of inflammation by malignant cells[121]. Chemokines not only act as chemoattractants, but are involved in other cellular processes including angiogenesis, hematopoiesis, embryogenesis, maturation of dendritic cells, tumor growth and metastasis and autoimmune and inflammatory processes[128]. Inflammatory chemokines are family of structurally related 8-10 kilo Dalton (kDa) protein molecules that are secreted in diverse tissues in regulation of hematopoietic cells and inflammatory processes[121]. The primary role of chemokines is to regulate recruitment of leukocytes to the tumor site. Chemokines can also influence the recruitment and migration of adaptive immunity cells towards the tumor site and secondary lymphoid organs[69].

The expression profiles of chemokines and cytokines within the tumor microenvironment might be more relevant than the specific immune cell content, since cytokines can either promote or inhibit tumor development and progression regardless of their source[129].

1.3.3 Cytokines and Chemokines of Interest

The link between obesity and BE and EAC is associated with changes in adipose related cytokines such as leptin and adiponectin. Injury as a result of repeated exposure to gastric contents causes an influx of inflammatory cytokines (IL-1b, IL-6, IL-8) that are thought to contribute to the progression of BE and EAC.

1.3.3a IL-1beta

IL-1beta is an important proinflammatory cytokine that is released in response to infection, cellular injury, or antigen challenge. The IL-1 family includes two bioactive ligands (IL-1alpha and IL-1beta) and the IL-1 receptor antagonist (IL-1Ra). All three molecules bind to the same IL-1receptors. Binding of the receptors initiates a potent proinflammatory immune response through the recruitment and activation of macrophages and neutrophils, vascular dilation and fever[130]. The IL-1 family is a pleiotropic group of cytokines capable of inducing several genes that promote cancer growth and metastasis. These include vascular endothelial growth factor (VEGF) and TGFb.

Working directly or in combination with other inflammatory cytokines, IL-1beta acts on a number of different cell types to induce this inflammatory state. IL-1beta is released upon activation of a multi-protein innate immune pathogen-sensing complex – the inflammasome. Active and mature forms of IL-1beta are secreted as a result of proteolytically processing by Caspase-1 upon inflammasome activation[131]. While macrophages are the most abundant IL-1beta producers, other cell types from different tissues are also capable of IL-1beta production.

IL-1beta can induce the expression of adhesion molecules, increase prostaglandin production and stimulate chemokine release; contributing to cell chemotaxis, angiogenesis and increased cell adhesiveness –known hallmarks of cancer.

1.3.3b IL-8

One mechanism of interest linking the similarities between inflammatory and carcinogenic pathways involves NFkB and its downstream product IL-8. NFkB is a key transcription factor regulator of inflammatory responses and has been shown to activate genes involved in the progression of cancer[132].

Interleukine-8, also known as chemokine (CXCL)-8, plays an important role as an initiator of inflammation, and has been noted for its functions within the tumor microenvironment. Upon transcription, the IL-8 gene encodes for a protein of 99 amino acids that will be subsequently processed to yield a signaling protein of either 77 amino acids in non-immune cells or 72 amino acids in monocytes and macrophages[133].

Expression of IL-8 receptors has been shown in cancer cells, endothelial cells, neutrophils, and tumor-associated macrophages, suggesting that IL-8 secretion from cancer cells might profoundly impact the tumor microenvironment[133, 134]. IL-8 can be produced by virtually all nucleated human cells, but is primarily expressed by nonepithelial cell types[135]. The 4 subfamilies of chemokines (C, CC, CXC, and CX3C) are classified based on structure and function and are released in response to infections. IL-8 is a CXC-type chemokine that signals through CXCR1 and CXCR2 G-protein-coupled receptors. Since these receptors are expressed in normal as well as cancerous cells, including endothelial cells, neutrophils and tumor-associated macrophages, they are utilized by other chemokines as well, as targets for autocrine and paracrine signaling[136]. CXCR1 binds IL-8 and the chemokine NAP-2, and CXCR2 binds to several CXC chemokines, including CXCL1 and IL-8 and is proposed to mediate angiogenic activity and direct tumor proliferative effects of IL-8[135].

At sites of inflammation, the primary secretor of IL-8 appears to be myeloid cells, where the gene is transcriptionally activated by AP1 and NFKb[135]. Activation of this proinflammatory molecule and its receptors promotes invasion and metastasis. Within the tumor microenvironment, IL-8 takes effect by initiating leucocyte infiltration and neovascularization, which precede invasion and metastasis. Indicating that IL-8 contributes to the inflammatory microenviroment by aggravating the inflammatory state and enabling cancer cells to not only survive but to migrate from the primary site[121].

A comprehensive understanding of the role of IL-8 in the development and progression of carcinogenesis has been limited due to the lack of a homologous genetic mode, further complicated by the redundancy of the other chemokines that share CXCR1 and CXCR2[121]. In addition to the limitations of animal models, the homologue of human IL-8 is absent from the genome of rodents and

it was assumed that IL-8 in mice was compensated for by the ligands CXCL1/KC and CXCL2[135].

1.4 Animal Models

Rodents, primarily mice and rats are the most commonly used animal models of BE and EAC, mainly because of lower cost of maintenance and the possibility of genetic modification for mechanistic studies. Rodents are susceptible to BE and EAC through induction of reflux or stimulation by carcinogens, however, it is important to keep in mind that the rodent esophagus differs from the human esophagus in terms of keratinization and the absence of submucosal glands[137].

1.4.1 L2-IL-1beta Model

The transgenic interleukin (IL)-1beta mouse or L2-IL-1beta is a model of chronic esophagitis that progresses to BE and eventually EAC as it ages. This model was developed and established at Columbia University, USA, in the lab of Dr. Timothy Wang by Dr. Michael Quante and described in detail in the publication "Bile Acid and Inflammation Activate Gastric Cardia Stem Cells in a Mouse Model of Barrett-Like Metaplasia" [89]. In short, modified human IL-1beta cDNA[138] was inserted downstream of an Epstein-Barr virus (ED-L2)[140] promoter, targeting the oral cavity, esophagus and squamous forestomach, as illustrated in Figure 1.4.
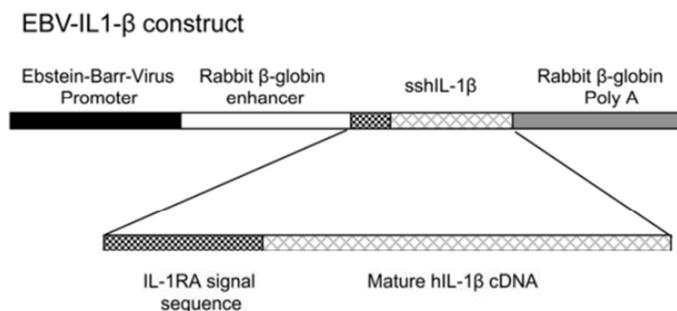
Figure 1.4: Generation of human IL-1beta transgenic mice.
Human IL-1beta transgenic mice were generated by targeting expression of h-IL-1beta in the esophagus via the Epstein Bar virus promoter. A constitutively secreted form (i.e. not requiring caspase-1 cleavage) of mature human IL-1beta cDNA was fused with the signal sequence derived from the structurally related human IL1-RA as previously described[138, 139]. These sequences were subcloned along with the hGH/polyadenylation sequence, downstream of the EBV promoter, into the pB-KS+ vector, linearized and injected into C57BL/6 x SJL F2 hybrid zygotes. Figure and text used with permission by M. Quante, supplementary figure[89].

The "L2" in the mouse model name, sometimes denoted as "pL2" refers to "promoter location-2". The origins of BE-like lesions were verified through lineage tracing to be Lgr5+ progenitor cells in the cardia region. This model nicely illustrates the expansion of the gastric cardia that results from IL-1beta induced inflammation in the squamous esophagus with the proximal migration of columnar like epithelium migration[89].

1.4.2 IL-8 Transgenic Model

The IL-8 Transgenic (IL-8Tg) model was designed to recapitulate human physiologic IL-8 expression through a physiologically regulated transgene using a bacterial artificial chromosome (BAC; 166 kDa) encompassing the entire human IL-8 gene. This model was developed and established in the lab of Dr. Timothy Wang by Dr. Samuel Asfaha and described in detail in the publication "Mice that express human Interleukin-8 have increased mobilization of immature myeloid cells, which exacerbates inflammation and accelerated colon carcinogenesis" [135]. In short, a human bacterial artificial chromosome encompassing the entire IL-8 gene (hBAC, RPL11-997L11, CHORI, USA) was transfected into murine dendritic DC2.4 cells and treated with mouse IL-1beta to ascertain proper splicing. Upon confirmation by PCR, transgenic mice (CBA/C57BL/6) bearing IL-8hBAC were generated at Columbia University, USA. IL-8Tg mice do not exhibit detectable circulating IL-8 at baseline, however following inflammatory stimulation they show significant increased levels of IL-8 in diseased tissue and circulation[135].

1.4.3 Mc4r^{X16} Genetic Obesity Model

MC4R, a G-coupled protein receptor, is expressed in hypothalamic nuclei and involved in energy balance[141]. Mc4r^{X16}knock-in mice were generated using gene targeting and develop hyperphagia, impaired glucose tolerance, severe obesity and an increased body length, that is characteristic of *Mc4r* deficiency[142]. Given this distinct and reproducible genetically driven obesity phenotype, it was expected to nicely demonstrate the hypothesis of obesity accelerating the L2-phenotype.

1.5 Aims of This Work

This work is presented in three parts.

Aim 1: Characterization of the L2-IL1beta model, a mouse model of BE and EAC resulting from IL-1beta overexpression.

The aim of the first part was to metabolically characterize this transgenic mouse model. The main focus was to observe the development of a unique phenotype over the course of aging and the development of BE and progression of the disease, presented in Chapter 3.

Aim 2: Effect of high-fat diet on the progression of the BE disease state in the L2-IL-1beta model.

As obesity and diet are regarded as strong risk factors for the development and progression of BE and EAC, the aim of the second part was to subject these mice to a lifetime of high fat feeding in order to observe the effect of obesity and high-fat diet in combination with the overexpression of IL-1beta already present in the model, presented in Chapter 4.

Aim 3: Role of IL-8 in the progression of BE to EAC in the L2-IL-1beta model.

The aim of the third part was to understand the role of the cytokine IL-8 in relationship to IL-1beta overexpression, obesity and BE development in this model, presented in Chapter 5.

Chapter 2: Methods and Materials

All animal procedures were conducted under the approval of the district government of Upper Bavaria, (Regierung von Oberbayern).

All animal experiments were conducted in accordance with German Federal Animal Protection Laws and approved by the Institutional Animal Care and Use Committee at the Technical University of Munich.

Az. 55.2.1.54-2532-125-12

2.1 Mouse Lines & Housing

All mouse strains including C57BL/6J, L2-IL-1beta and IL-8Tg were bred in specific-pathogen-free facilities (SPF). The founder mice for colonies established in Freising, Germany were obtained from the Klinikum rechts der Isar mouse facility, Munich, Germany. Original founder mice were transferred to the Klinikum rechts der Isar from Columbia University, USA. Mice were introduced into the specific pathogen free (SPF) facility via embryo-transfer.

SPF mice (Freising and Munich): A primary cohort of L2-IL-1beta and IL-8Tg mice established from the SPF embryo-transfer remained at the SPF facility. Male and female mice were used for experimental and/ or phenotyping purposes. All mice were kept at room temperature (23°C ± 1°C) with a 12-hour light/dark cycle.

2.1.1 IL-1beta Line

To understand the pathogenesis of BE and EAC, a mouse model of chronic esophageal inflammation was studied. This model was generated and previously described in detail by Quante et al.[89]. In short, modified human IL-1B cDNA[138] was inserted downstream of an Epstein-Barr virus (ED-L2) promoter[140], targeting the oral cavity, esophagus and squamous forestomach. These mice exhibit esophagitis, develop BE by 6-months of age and progress to EAC as they age[89]. L2-IL-1beta mice used for experimental studies were backcrossed with C57BL/6J mice, for at least 8 generations. Littermates without IL-1beta expression as observed by genotyping served as Wild Type (WT) controls.

Mice were maintained at a constant temperature (22°C) and humidity (55%) with a 12-hour light/ dark cycle with ad libitum access to food and water. Mice were housed in type II long, individually ventilated cages (IVC) with wood chips as cage bedding material (TECHNIPLAST® Green Line IVC Sealsafe PLUS, surface area: 540 cm^2).

2.1.2 IL-8 Line

Previously, the lack of a homologous genetic model and the complications arising from the redundancy of the chemokines that share CXCR1 and CXCR2 limited the understanding of the function of CXCL8 in cancer progression. Asfaha and colleagues recently generated a physiologically regulated transgenetic IL-8 mouse model using a bacterial artificial chromosome (BAC; 166 kDa) that encompassed the entire human IL-8 gene[135]. Experimental data from these IL-8Tg mice shows human-like IL-8 expression in appropriate murine tissues. L2-IL-1beta mice were crossed with IL-8Tg mice to generate a model that overexpresses human IL-1beta as well as human IL-8. IL-1beta$^{-/-}$ and IL-8$^{-/-}$ mice served as controls.

The following genotypes and abbreviations were used:

L2: *L2-IL-1beta*

WT: *L2-IL-1beta$^{-/-}$*

IL-8Tg: *IL-8-Transgetic*

For genotyping, mouse ears were punch tagged, or when necessary a tail clip was taken, this was done between three and four weeks of age and DNA isolation and PCR was performed as described in Section 2.2.1-2.2.2.

2.2 DNA/RNA Isolation

2.2.1 DNA Isolation for Genotyping

Genotyping was carried out using Polymerase Chain Reaction (PCR) technology. DNA was isolated from mouse ear clips or tail tips using the tail and tissue lysis buffer DirectPCR® Lysis Reagent Tail (Peqlab, Germany) with the addition of 5% Proteinase K (Roche, Germany). A ratio of 1uL Proteinase K to 100 μL lysis buffer was used. Ear clips or tail tips were incubated over night at 55°C, with lysis buffer and Proteinase K. Samples were inactivated for 45 minutes at 85°C. Following a quick spin-down, 0.5μL of lysate was used as template for PCR.

2.2.2 Genotyping PCR

- L2-IL-1beta mice genotyping PCR was performed using RedTaq Ready Mix (Sigma, Germany) with 1 μL DNA template (Section 2.2.1) and primers (Sigma, Germany) at a final concentration of 10 pM.

The following conditions were applied for amplification on a Thermal Cycler (T100, BioRad, California).
For L2-IL-1beta mice: 94°C 30 sec, 57°C 30 sec, 72°C 30sec for 35 cycles.
For IL-8 mice: 94°C 30 sec, 55°C 30 sec, 72°C 30sec for 35 cycles.

Genotyping results were visualized on 1.5 % agarose gels.
The following genotyping primers were used with the appropriate band sizes:
L2-IL-1beta: GT Forward: 5'-CTT CCT GTT CCA TTC AGA GAC GAT-3'
L2-IL-1beta: GT Reverse: 5'-CTC CAG CTG TAG AGT GGG CTT ATC-3'
L2-IL-1beta: 277bp (single band)
L2-IL-1beta wt: 0bp – no band

IL-8: GT Forward: 5'-TGA GGT CAA GGG CTA GGA GA-3'
IL-8: GT Reverse: 5'AAA TTT GGG GTG GAA AGG TT-3'
IL-8: GT 300bp (single band)
IL-8 wt: 0bp – no band

Mc4r^{X16}: GT Forward: 5'-CCT ATG CCA AAT GAT ACC CCA CC-3'

Mc4r^{X16}: GT Reverse: 5'-CTC TAA GAT GAA ATG AAC GCT GGA CC-3'

Mc4r^{X16} ki: 277bp (single band)

Mc4r^{X16} het: 277bp and 132bp (double band)

Mc4r^{X16} wt 132bp (single band)

2.2.3 RNA Isolation

From each experimental mouse, tissues of interest were resected, washed in sterile PBS (Gibco, by Life Technologies, USA), blotted on paper towel and immediately snap frozen in liquid nitrogen, followed by storage at -80°C until ready to use.

Two methods of ribonucleic acid (RNA) isolation were performed. RNA isolation from abundant tissue samples such as liver, kidney, spleen, fat, and brain was performed using the AllPrep DNA/RNA/Protein Mini Kit (Qiagen, Germany), while less abundant samples such as neutrophils isolated from spleen was carried out using the RNeasy Micro Kit (Qiagen, Germany).

Briefly, tissues samples were retrieved from -80°C storage and immediately homogenized in RLT-buffer with 1% B-Mercaptoethanol. RNA extraction was performed according to manufacturer's protocol. RNA concentrations were measured on a Nano-Drop 2000 spectrophotometer (Thermo Scientific), quality of samples was checked on a 1% agarose gel.

Additionally, for esophagus and stomach tissue the Trizol® method of RNA isolation was performed. Briefly, snap frozen tissue was homogenized with Trizol® (Life Technologies, USA) and extraction was performed according to manufacturer's protocol.

RNA isolations were always carried out using diethylpyrocarbonate (DEPC, Sigma, Germany) treated water. DEPC inactivates RNase enzymes by covalent modification of histidine, lysine, cysteine and tyrosine.

Furthermore, sodium acetate (Ambion, USA) precipitation was carried out to "clean-up" isolated RNA when poor 260/280 or 260/230 ratios were measured. Briefly, 1:10 volume of 3M sodium acetate was added to the RNA, along with 4 volumes of 100% ethanol, mixed and incubated overnight at -20°C (16 hours). Following centrifugation at 16,000 x g for 30 minutes at 4°C, supernatant was

discarded and the RNA pellet was washed with ice-cold 80% ethanol (up to two times if necessary). All traces of ethanol were aspirated or left to dry out for 5-10 minutes before resuspending in RNase-free water. Finally, RNA concentrations were measured as detailed above.

2.2.4 cDNA Synthesis

A total of 1ug RNA was used for cDNA synthesis using the QuantiTect Reverse Transcription Kit (Qiagen, Germany). Genomic DNA (gDNA) elimination was performed prior to reverse transcription (RT) using gDNA Wipeout Buffer at 42°C for 2 minutes. For RT the entire genomic DNA elimination reaction RNA was incubated with Quantiscript Reverse Transcriptase, Quantiscript RT Buffer and RT Primer Mix and incubated at 42°C for between 15-30 minutes and stopped by an inactivation incubation at 95°C for 3 minutes.

2.3 Dietary Information

2.3.1 Dietary Treatment

Following genotyping, mice were caged in groups (up to 6 mice per cage) based on genotype. Dietary treatment lasted up till the ages of 3-, 6-, 9- and 12-months.
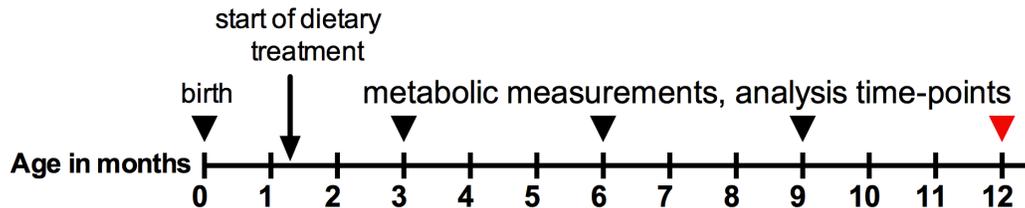
Figure 2.3.1: Timeline of dietary treatment and end-points for analysis.
Mice were started on dietary treatment between 6-8weeks of age. Following genotyping, mice were separated by genotype and assigned an experimental diet. L2-IL-1beta and their WT littermates were fed either a standard lab Chow diet or a high-fat diet (HFD) (20% palm oil). Mice were sacrificed at 3-, 6-, 9- and 12-months of age for dissection and organ sampling for gene and protein expression, as well as for histological analysis. Each cohort was comprised of 12mice per diet.

2.3.2 Diet Composition

Mice were allowed a standard lab Chow diet (pellet form) from birth until weaning and water *ad libitum*. Following weaning between 6 and 8 weeks of age, mice were assigned an experimental diet or remained on the standard Chow diet (Figure 2.3.1). Breeding pairs were also allowed the lab Chow diet and water *ad libitum*. Animals were maintained in groups of 5-6 per cage. Only when food intake was monitored mice were separated and singly housed for the duration of the experiment. All diets were manufactured by Ssniff Spezialdiäten GmbH (cat. no. V1124-300 [standard Chow], S5745-E712 [20% Palm Oil]) and served in pellet form. The standard Chow diet was autoclaved prior to introduction into the SPF housing facility, while the HFD was received as sterilized γ-irradiated pellets. Diet composition (Table 2.3.2) was not constant between the two diets, furthermore HFD was stored at 4°C to prevent rancidity.

On going experiments detailed in this thesis include a study utilizing an experimental high fat diet with identical composition to the HFD Palm oil diet, where the Palm oil was substituted for Pork lard. This diet was also purchased

from Ssniff Spezialdiäten GmbH (cat. No S5745-E730) and was stored and utilized in the same manner as the Palm oil diet; details of diet composition outlined in Table 2.3.2.

Table 2.3.2: Composition of diets.

Shown is the percentage of energy (en%) of macro- and micronutrients in the standard Chow and high-fat diets.

Dietary components	V1124-000 Standard Chow	S5745-E712 HFD Palm oil	S5745-E730 HFD Pork lard
Gross Energy (GE)	16.7 MJ/kg	21.9 MJ/kg	21.9 MJ/kg
Metabolizable Energy (ME)	14.0 MJ/kg	19.7 MJ/kg	19.7 MJ/kg
Protein [kJ%]	27	18	18
Fat [kJ%]	12	48	48
Carbohydrates [kJ%]	61	34	34
Crude Nutrients [%]			
Protein	22.0	21.2	21.2
Fat	4.5	25.1	25.1
Fiber	3.9	5.0	5.0
Ash	6.2	5.3	5.3
Starch	34.2	26.7	26.7
Sugar	5.1	6.1	6.1
N free extracts	51.2	37.7	37.7
Amino Acids [%]			
Lysine	1.5	1.8	1.8
Methionine	0.5	0.8	0.8
Met + Cys	0.4	1.1	1.1
Threonine	0.9	0.9	0.9
Tryptophan	0.3	0.3	0.3
Minerals [%]			
Calcium	1.0	0.9	0.9
Phosphorus	0.7	0.7	0.7
Sodium	0.2	0.2	0.2
Magnesium	0.2	0.2	0.2
Vitamins [IU/kg]			
Vitamin A	25,000.00	18,000.00	18,000.00
Vitamin D_3	1,500.00	1,800.00	1,800.00
Vitamin E	135	180	180
Fatty acids [%]			
C 12:0	-	0.01	0.05
C 14:0	0.01	0.21	0.29
C 16:0	0.54	9.18	5.37
C 18:0	0.14	1.11	2.88
C 20:0	0.02	0.1	0.08
C 16:1	0.02	0.05	0.60
C 18:1	1.03	9.19	9.64
C 18:2	2.42	4.67	4.55
C 18:3	0.28	0.35	0.49

2.4 End-Point Sample Collections

At the end of all experimental trials, mice in a non-fasting state were killed by CO_2 inhalation, Isofluran CP® (CP-Pharma, Germany) inhalation or cervical dislocation when CO_2 or Isofluran were unavailable.

The animal was placed in the euthanasia chamber and 100% carbon dioxide was introduced at a rate of 60%/minutes. With the use of CO_2 and Isofluran the expected time to unconsciousness was usually within 2 minutes. Each animal was closely observed for lack of respiration, then the animal was removed from the cage; otherwise the exposure to CO_2 or Isofluran was continued. Death was verified after euthanasia and prior to organ retrieval.

Next, blood was immediately drawn from the heart and placed into a microvette (500 Z-Gel, Sarstedt, Germany) and stored on ice. Once all samples were collected, blood was centrifuged at 10,000 x g for 5 minutes at 20°C. Serum was separated from the plasma, which stayed in the gel phase. Serum was collected and snap frozen in liquid nitrogen (N_2) until later use.

The hypothalamus was collected by punch biopsy after removing the brain from the skull, and immediately snap frozen in liquid N_2.

Liver, kidney, spleen, epididymal adipose tissue (EAT), colon, esophagus and stomach were collected and snap frozen in liquid N_2. Whole spleen weight was recorded prior to snap freeing.

In addition, at the end of the feeding trial, body weight and body composition of mice was measured 24 hours prior to sacrifice. Finally, a fecal sample was extracted from the rectum when available and snap-frozen in liquid N2.

Moreover, during the last week of the feeding trial, feces produced were collected, dried at 60°C to constant weight and pulverized. Fecal gross energy content was determined using an isoperibol bomb calorimeter as detailed in Section 2.5.5.

2.5 Metabolic Phenotyping

Understanding the complex genetic and physiological modulation of metabolic diseases and the impact of the external environment through dietary habits and physical activity are critical to detect new candidate genes and metabolic pathways that predispose and contribute towards disease state[143].

Impaired energy balance regulation can be linked as a contributing factor to several metabolic disorders, thus metabolic phenotyping of a genetically modified mouse model can assist with a greater understanding of the disease.

2.5.1 Study Design

This work was based on an intervention study design comparing the effect of a high-fat diet. Male and female L2-IL-1beta mice and WT littermates were kept in an SPF facility. They were housed with up to 6 mice per cage and were introduced to the experimental diet between 6-8weeks of age. The animals (n = 6 per genotype and gender) were assigned to either a standard lab Chow diet or a HFD. To analyze the effects of long-term high fat feeding, mice were assed at several time points before termination of the experiment.

The study included the following measurements and physiological tests on live animals:

1. Body mass monitored bi-weekly
2. Body composition measured at 3-month increments
3. Food and activity monitored at 3-, 6- and 12-month time-points
4. Feces collected for a week at 9- and 12-month time-points

Experiments were concluded at 12-months of age with tissue dissection and sampling for gene and protein expression and histological analysis as detailed in Figure 2.5.1.
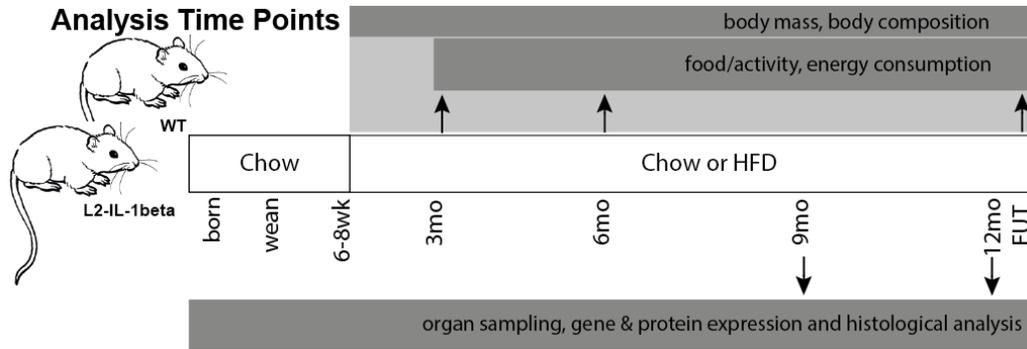
Figure 2.5.1: Phenotype study design.
48 mice per time point (n = 24 L2-IL-1beta and n = 24 WT littermates) aged to 3-, 6-, 9- and 12-months as part of a long-term dietary study. Mice of both genotypes were assigned a standard lab Chow diet and a high-fat diet (HFD). Body mass was measured bi-weekly, body composition, food intake and activity, direct and indirect calorimetry were conducted at indicated analysis time points. Mice were sacrificed (euthanized with CO_2 (EUT)) at the end of each time point and organs were sampled for future gene and protein expression and histological analysis.

2.5.2 Body Mass and Composition Analysis

Body mass is regulated by energy balance; overweight and obesity are the result of a sustained positive energy balance. While body mass and body composition are simple measurements, they can provide insight into mid- and long-term derangements in energy allocation[143].

2.5.2a Body Mass refers to the basic measurement of total body weight. Body mass of experimental mice was measured starting at 6 weeks of age, following weaning and at the onset of dietary treatment. Further body mass development was measured in bi-weekly intervals until the end of the dietary treatment at 52 weeks of age. Weighing was conducted in the morning hours between 10:00-12:00 a.m., mice were placed in a plastic beaker that was previously tarred, and total body weight was recorded to two significant figures in units of grams.

2.5.2b Body Composition includes fat mass and lean mass. Lean mass (fat-free mass) includes organic matter, water and inorganic ash from bone minerals[143]. Body composition of experimental mice was determined using a whole animal body composition NMR analyzer with Bruker Minispec plus and OPUS v5.5 software (Minispec Bruker, Germany). Measurements were conducted

at the onset of dietary treatment, 3-, 6-, 9- and 12-months of age. Prior to data acquisition, the NMR analyzer was calibrated with a standardized control provided by the manufacture. Single mice were placed in a polycarbonate restrainer, colored red to allow for observation of the mouse. Animals were not anesthetized; the animal in the restrainer was placed horizontally into the magnet of the scanner at room temperature for the 2-5 minutes measurement period. Following measurement the mice were returned to their original housing cages.

2.5.3 Food Intake and Feces Collection

Food intake was measured during locomotor activity assessment. Food baskets were weighed, filled and added to single caged mice at the start of the measurements. Food baskets were weighed at the end of the measurement prior to returning the mouse to its original cage. Food intake in g was determined by subtracting leftover food from the initial mass of fresh food. Energy intake was determined by multiplication of food intake in g with gross energy determined by bomb calorimetry.

Feces was collected at the end of the measurement from the single cages, and dried for several days at 60°C and used further for bomb calorimetry. Urine mass was not taken into account as it might have evaporated in the ventilated single cage system over the measurement period.

2.5.4 Indirect Calorimetry Setup

At all four analysis time-points three mice from each group were analyzed for energy consumption for a total of 24 hours. Mice were acclimatized for two days prior in single cages and on the day of measurement, mice were transferred to specific individual cages (same design as housing cages) in a climate simulation station (22°C, Feutron, Germany). Cages were specially sealed in order to measure oxygen consumption and carbon dioxide exhalation using a TSE Systems Calorimetry module "CaloSys" (Germany). During all measurements, animals had *ad libitum* access to food and drinking water, as well as visual contact with other mice. In brief, volumes of oxygen consumed ($\Delta vol\%O2$) and volumes of carbon dioxide ($\Delta Vol\%CO2$) produced by each mouse were measured during 60 sec every 2 to 4 minutes.

2.5.5 Bomb calorimetry [Energy Intake]

For the determination of assimilation efficiency all excreted feces were collected over a period of 1-week prior to sacrifice at the 9- and 12-months of age time points. Food and feces samples were dried to constant weight in a drying oven (Memmert, Germany) at 60°C and energy content of food and feces was measured by bomb calorimetry with a Parr® 6300 Calorimeter (Parr Instrument Co., USA). In short, dried food and feces were prepared for measurement by homogenizing with a TissueLyser II (Qiagen, Germany) to a powder consistency. The powder was then weighed and pressed into pill form, weighing approximately 1 g. A standardized ignition thread (Parr 845DD2, USA) was secured with a knot between the two terminals of the removable headpiece and the pre-weighed pellet was place over the remaining end of the ignition thread. The removable headpiece was then returned to the calorimeter and energy content of each pellet was measured. Energy in MJ/kg was determined by manufacturer software based on the exact pill mass that was provided. Assimilated energy was calculated as total amount of energy consumed minus energy loss via feces excretion. Energy loss through urine could not be measured directly and was assumed to be small and equal between groups.

2.5.6 Locomotor Activity

In order to assess the impact of diet and genotype on locomotor activity, animals were single cages in specific open-style cages (Ehret, type II, surface area 825cm^2, Germany) for five consecutive days, following a 2-day acclimatization period. The floor of the cage was covered with identical bedding to the original home cage and Food and water was available *ad libitum*. Mice had olfactory and acoustic contact with littermates at time of measurement. The cage consisted of a frame that measured locomotor activity whenever the animals broke a light beam path (TSE Systems Drinking and Feeding Monitor module, using the TSE Labmaster v2.1.5 software (TSE Systems, Germany)). Central and peripheral movements were also counted. The data collected was plotted for every dietary group over a 72 hour period. The first two data collection days were disregarded despite the initial acclimatization period due to the different nature of the measurement cages.

2.6 Macroscopic Scoring

2.6.1 Photography

Upon sacrifice and organ sampling, the stomach (including the esophagus and part of the duodenum) was opened along the greater curvature, rinsed in sterile PBS and then spread out on a piece of Whattman paper (Schleicher & Schuell, Germany). The esophagus was opened down the center from the inner curvature as shown in Figure 2.6.1. Macroscopic pictures were taken using a point and shoot camera (Ricoh CX6, China) in macro mode.
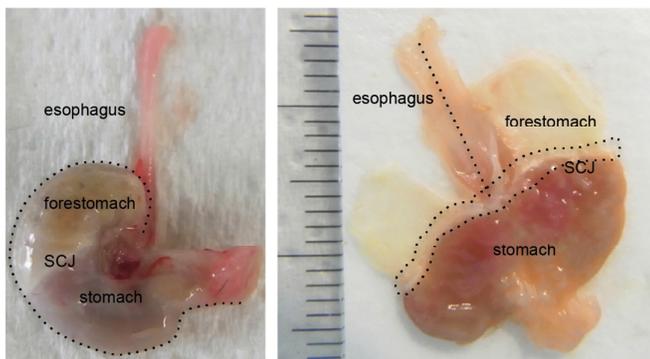
Figure 2.6.1: Macroscopic view of a murine esophagus and stomach.
An unopened stomach (left) and an opened stomach (right) highlighting the esophagus, forestomach, squamocolumnar junction (cardia region) and the stomach as observed in a WT mouse. For the purpose of this study the stomach was cut open along the greater curvature and opened to reveal the squamocolumnar junction (SCJ). Lesions/ tumors in the esophagus and SCJ were macroscopically scored.

2.6.2 Scoring

In order to evaluate the macroscopic phenotype in the mouse models a scoring system was established. Using the scale bar (mm) accompanying each macroscopic stomach image a range of values was assigned as follows.

Esophagus: First, the percentage of the esophagus covered in tumors was graded and assigned a score. Second, tumors were measured and tallied based on size as detailed in Table 2.6.2A.

Table 2.6.2A: Criteria used for scoring percentage of tumor coverage.

Tumor score extent at esophagus and cardia regions	Description
0	No abnormalities
1	Focal tumors (<20%)
2	Partial tumors (20-50%)
3	Increased tumors (>50-80%)
4	Continuous tumors (>80%)

Squamocolmnar junction (SCJ) or Cardia: First, the percentage of the cardia region covered in tumors was graded and assigned a score. Second, size of tumors were averaged and assigned a score as detailed in Table 2.6.2B.

Table 2.6.2B: Criteria used for scoring size of tumors.

Tumor size score	Description
0	No abnormalities
1	>0.5mm
2	>1.0mm
3	>2.0mm
4	>3.0mm

Finally, for the cardia region a combined score was calculated by taking the average of the percentage score and the size score, this was done to give a more representative value to the extent of tumor development as detailed in Table 2.6.2C.

Table 2.6.2C: Example of macroscopic scoring.
The esophagus and squamocolumnar junction of each mouse was individually scored for % lesion/tumor coverage in the esophagus and cardia regions. In addition, individual tumor size was measured in the esophagus and cardia. These values were taken together to compile an overall cardia and esophagus score.

Cohort: WT 12months on Palm Oil HFD														
ET	% Esophagus		Esophagus tumor size and number						Cardia				Overall Score	Overall cardia + esophagus	Comments
	%	Score	0.5	1	1.5	2	3	4	%	Score	Tumor size	Score			
137	0	0							0	0			0	0	Esophagus tumor score NA
144	0	0							0	0			0	0	Esophagus tumor score NA
145	0	0							0	0			0	0	Esophagus tumor score NA
146	0	0							0	0			0	0	Esophagus tumor score NA
763	0	0							0	0			0	0	Esophagus tumor score NA
766	0	0							0	0			0	0	Esophagus tumor score NA
AVG	0.00	0.00							0.00	0.00			0.00	0.00	
STD	0.00	0.00							0.00	0.00			0.00	0.00	
Cohort: PL2 12months on Palm Oil HFD															
ET	% Esophagus		Esophagus tumor size and number						Cardia				Overall Score	Overall cardia + esophagus	Comments
	%	Score	0.5	1	1.5	2	3	4	%	Score	Tumor size	Score			
123	65	2		3	3	3	2		85	4	>3.0mm	4	4	3.33	
136	85	4	3	2	2	2		1	85	4	>2.0mm	3	3.5	3.67	
147	75	3		3	8	4			85	4	>3.0mm	4	4	3.67	Larger esophagus lesions
198	45	2			3				85	4	>2.0mm	3	3.5	3.00	One very long lesion
188	35	2		2	2	4			85	4	>2.0mm	3	3.5	3.00	
285	90	4	3	3	4	2	3	3	100	4	>3.0mm	4	4	4.00	SJC covered in lesions + upper cardia
AVG	65.83	2.83	3.00	2.60	3.67	3.00	2.50	2.00	87.50	4.00		3.50	3.75		
STD	22.00	0.98	0.00	0.55	2.25	1.00	0.71	1.41	6.12	0.00		0.55	0.27		

2.7 RNA Analysis

Immediately following organ resection, tissue samples were flash frozen in liquid nitrogen and stored at -80°C until later use.

2.7.1 Real-Time PCR

Expression of specific target genes was evaluated using real-time PCR (RT-PCR). For each sample, 10 ng of extracted RNA were used per reaction using the as previously described in Section 2.2.3.

Primer design was executed for primer specificity, or, commercially available primers were used from Sigma. RT-PCR was performed using SYBR Green I dye (Qiagen, Germany). The following thermal cycling conditions were used: 30 minutes at 50°C (cDNA synthesis), 15 minutes at 95 °C (RT enzyme inactivation). The PCR conditions were as follows with 40 cycles at 95°C for 15 s, 55 °C for 30 sec and 72°C for 30 sec. Glyceraldehydephosphate dehydrogenase (GAPDH) and cyclophilin A served as the internal controls to normalize the data. The sequences of primers are listed in Appendix Table 2.15.1. All primers pairs were checked for self-complementation and "blasted" with NCBI Primer-BLAST software to exclude annealing to non-specific target sequences (www.ncbi.nlm.nih.gov/tools/primer-blast). Furthermore, primer efficiency was tested utilizing the standard curve method and line of regression method prior to use.

2.7.2 Microarray

Flash-frozen cardia tissue stored at -80°C was processed for RNA isolation using the Trizol method according to the manufacturer's protocol. Sodium acetate precipitation was carried out as an additional "clean-up" step as detailed in Section 2.2.3. RNA was stored at -80°C, and 4 µL of each sample were shipped on dry ice to the Kompetenzzentrum Floureszente Bioanalytik der Universität Regensburg, Germany (KFB). 3 mice per genotype and diet, for a total of 12 samples at a concentration of 50 ng/uL (WT-Chow and –HFD and L2-Chow and – HFD) were run on a Mouse Gene 2.1 Affymetrix GeneChip® (USA). Comparison analysis data was received from KFB (Regensburg, Germany) and further processed by bioinformatician Dr. Richard Friedman in collaboration with Dr.

Timothy Wang (Columbia University, USA). As previously published, genes were defined as being up-regulated or down-regulated if they exhibited >1.5 fold increase in gene expression or if they showed <0.67 fold decrease in gene expression in Affymetrix arrays[144]. Further gene filtering was conducted based on genes that may have potentially important roles in accelerating the phenotype observed in the L2-model on HFD and in the L2/IL-8Tg model resulting from IL-8 over-expression.

Microarray results were further analyzed using gene set enrichment analysis (GSEA) using the online platform provided by the BROAD Institute. Differentiated gene sets were further compared with the BIOCARTA data set.

2.8 Histological Analysis

2.8.1 Production of FFPE-Tissue Samples

Upon indicated time points (3-, 6-, 9-, 12-months) or tumor progression with noticeable symptoms of disease such as cachexia and/ or pain (erected fur and hunched posture) the mouse was weighed and euthanized in a CO_2 chamber. The esophagus and stomach were resected and dissected open, so that the inner part of the stomach and esophagus were exposed. Additionally, parts of the liver, kidney, and spleen were resected. All organs were fixed in Formalin fixative overnight, up to one week. Tissue samples were then dehydrated with increasing concentrations of ethanol, xylol and paraffin in a Leica S300 tissue-processing unit. Finally, the formalin fixed organs were embedded in liquid paraffin and allowed to cool and harden. The formalin-fixed, paraffin-embedded (FFPE) blocks were stored at room temperature.

2.8.2 Paraffin Sections

FFPE-blocks were cut to 2-3 μm on a microtome (Thermo Scientific, Microm HM 355S, USA) and transferred to a 50°C water bath for stretching and collected on microscopic glass slides (Thermo Scientific, USA). Sections were allowed to dry overnight. Following drying, slides were heated at 58°C for 60 minutes in a Heraeus Instruments Function line Incubator (Thermo Scientific, USA).

2.8.3 Hematoxylin and Eosin

For hematoxylin and eosin (H&E) staining paraffin sections were rehydrated in Xylol (Herdinger, Germany) for 20 minutes, followed by alcohols at decreasing concentrations (Isopropanol 96% ethanol and 70% ethanol, for ~4 minutes each) as described in Table 2.8.3. After washing, slides were stained with Meyers haemalaun (MRI Pharmacy, Germany) for 2 minutes to visualize acidic structures (nuclei) in violet, followed by a counterstain with eosin (Merck, Germany) for 2 minutes to label basophilic structures (cytoplasm, connective tissue and other extracellular structures) in pink. Slides were washed and dehydrated in (70% ethanol, 96% ethanol, Isopropanol and Xylol (2 minutes each) and covered with mounting medium (VectaMount, Vector Labs, USA) and glass coverslips (Menzel-Gläser, Germany). Slides were scanned on an Aperio CS2 image capture device (Leica Biosystems, Switzerland) at a magnification of 20X.

Table 2.8.3: Pre- and post-staining treatments of paraffin slides.
Hand stained and auto-stained slides were subject to the same de-paraffinization and re-hydration steps.

Pre-staining		Post-staining	
Solution	Incubation Time (minutes)	**Solution**	Incubation Time (minutes)
Xylol I	10	70% EtOH I	1
Xylol II	10	70% EtOH II	1
Isopropanol I	2	96% EtOH I	1
Isopropanol II	2	96% EtOH II	1
96% EtOH I	2	Isopropanol I	1
96% EtOH II	2	Isopropanol II	1
70% EtOH I	2	Xylol I	5
70% EtOH II	2	Xylol II	5

2.8.4 Alcian blue-PAS

Alcian blue is a staining method used to identify acid mucopolysaccharides and acetic mucins, and Periodic Acid-Schiffs (PAS) stains structures containing a high proportion polysaccharides such as glycogen, glycoproteins, proteoglycans typically found in connective tissues, and mucus. For Alcian blue-PAS staining paraffin sections were deparaffinized and rehydrated as described in Table 2.8.3. Slides were then washed in tap water and subsequently with Alcian blue (Merck,

Germany) for 1 minute to visualize acidic mucins in blue, Barrett goblet cells specifically. Tissue on slide was then oxidized by exposure to Periodic Acid (Roth, Germany) for 10 minute. This oxidative process results in the formation of aldehyde groups-treatment with Schiff's reagent (Roth, Germany) for 15 minute allowed for the detection of these aldehyde groups. Slides were stained with hematoxylin for 1 minute to visualize acidic structures (nuclei) in violet. Slides were washed and dehydrated according to Table 2.8.3 and covered with mounting medium (VectaMount, Vector Labs, USA) and glass coverslip (Menzel-Gläser, Germany).

2.8.5 IHC protocol

A general IHC staining protocol was used for stainings, with antibodies and exceptions detailed in Table 2.8.4 below.

First, slides were deparaffinized and rehydrated according to Table 2.8.3. Antigen retrieval was carried out by boiling slides for 20 minutes in Citrate Buffer pH 6.0 (2L dH20 + 5.88g Citrate (Sigma, Germany) in a pressure cooker, followed by a 20 minute cool down or with unmasking solution (Vector Labs, Cat # H-3300) at 450W, followed by a 15minute cool down or by boiling slides for 20 minutes in 0.3%Triton/ PBS for permeabilization, followed by a 20 minute cool down. The area around the tissue of interest was dried and outlined using PAP pen (Daido Sangyo, Japan) and immediately endogenous background was blocked, for 10minutes at room temperature (RT). The slides were then rinsed 3x with TBS-T or PBS for 5 minutes each time. Next, blocking was carried out for 30 minutes at RT. Blocking solution was removed and primary antibody in TBS-T or PBS was added to the tissue and incubated in a wet chamber for 60 minutes at RT or over night. The slides were then rinsed 2-3x with TBS-T or PBS for 5 minutes each time. The tissue was then incubated with the secondary antibody solution, in TBS-T or PBS containing biotinylated goat anti-rabbit antibody for 30 minutes at RT. The slides were then rinsed 3x with TBS-T or PBS for 5 minutes each, with a final wash for 5 minutes in PBS. During the incubation with the secondary antibody, ABC solution (Vectastain ABC kit, Vector Labs, USA) was prepared by adding 40uL of solution A and 40uL of solution B to 1mL of PBS. The freshly prepared ABC solution was incubated at 10 minutes at RT. Then the

tissue was incubated with 200uL/ slide of freshly prepared ABC solution for 30 minutes at RT. Following incubation with the ABC solution the slides were rinse 3x with PBS for 5 minutes each time. This was followed by 200uL/slide of freshly prepared DAB solution (2.5mL dH2O + 1drop buffer +1drop H2O2 +2 drops DAB) from the DAB Peroxidase Substrate Kit (Vector Labs, USA), for approximately 1 minute at RT. The first slide was used to set the incubation time of the DAB solution by checking under the staining under the microscope. Slides were immersed in fresh PBS to stop the staining, and were washed several times in fresh dH20 thereafter. Lastly, slides were counterstained with Haematoxylin for 1 minute, then rinsed with PBS and dehydrated according to Table 2.8.3. Tissue was mounted using (Vector Labs, USA) and glass coverslip (Menzel-Gläser, Germany).

Table 2.8.4: Primary antibodies and conditions for IHC

Antigen	Host	Dilution	Unmasking	Blocking	Company
Ki67	Rabbit	1:500	Citrate buffer, pH 6.0	3% H2O2 & 5% GS/TBS-T	Abcam (ab15580)
Dclk1	Rabbit	1:500	Citrate buffer, pH 6.0	3% H2O2 & 5% GS/PBS	Abgent (AP7219b)
aSMA	Rabbit	1:400	Unmasking solution (Vector Labs)	3% H2O2 & 5% GS/3%BSA/TBS-T	Abcam (ab5694)
F480	Rat	1:75	0.3%Triton/ PBS	3%H2O2 & 3%BSA/PBS	eBioscience (17-4801-82)
Ly6C	Rat	1:100	0.3%Triton/ PBS	3%H2O2 & 3%BSA/PBS	eBioscience (56-5931-82)
Ly6G	Rat	1:100	0.3%Triton/ PBS	3%H2O2 & 3%BSA/PBS	eBioscience (12-5932-82)

2.8.6 Lgr5

In order to detect the abundance of Lgr5 within murine tissue that Advanced Cell Diagnostics RNAscope 2.5HD Assay- BROWN kit with the Mm-Lgr5 probe (ACD, USA) was followed as specified in the manufacturers protocol.

2.8.7 Counting and Quantifying of IHC Stainings

Histopathological evaluation of HE stainings was carried out by a pathologist and medical doctor separately, and in a blinded fashion according to the scoring system listed below. The entire esophagus, cardia and stomach regions were evaluated.

Inflammation Score
0 no inflammation
1 mild inflammation
2 moderate inflammation
3 severe inflammation

Metaplasia Score
0 no metaplasia
1 rare mucus cells
2 single metaplastic glands
3 multiple metaplastic glands

Dysplasia Score
0 no dysplasia
1 superficial epithelial atypia
2 atypia in glanular complexity
3 low-grade dysplasia
4 high-grade dysplasia

For PAS, Ki67, Dclk1 and aSMA, the percentage (%) of positive cells in the cardia region of 9-and 12-month old L2-IL-1beta mice on Chow diet or HFD quantified from assessment of 3-4 regions of esophagus/ stomach tissue per mouse; 5-8 mice were assessed per genotype and diet time-point.

F480, Ly6C and Ly6G staining quantification was carried out by assessing one high-magnification field (40X) per 3-4 regions of esophagus and cardia tissue per mouse; 3 mice were assessed per L2-Chow and L2-HFD groups.

Lgr5 staining was quantified by assessing five high-magnification fields (40X) per 3-4 regions of cardia tissue per mouse; 3 mice were assessed per L2-Chow and L2-HFD groups.

Statistical analysis was carried out using Graph Prism 6; based on the number of groups compared either Student's t-tests or one-way or two-way ANOVA's were utilized with p-values noted in each corresponding figure.

2.9 Flow Cytometry Analysis

Flow cytometry was used to analyze different immune cell populations from the esophageal and cardia regions of L2-IL-beta mice.

2.9.1 Preparation of Tissue

Mice were euthanized by Isofluran inhalation. Blood was retrieved immediately from the beating heart and added to 5mL red cell lysis buffer (Sigma, Germany). This was left at room temperature until further processing. Stomach and esophagus, liver, spleen and colon were resected and placed in PBS on ice.

Resected organs were place in individual 6cm dishes with 1.0mL of 0.5M EDTA (Invitrogen, Germany). The tissue from the esophagus, forestomach and cardia, stomach, and colon were chopped into minute fragments using fine tipped scissors.

Tissue samples were transferred into 5mL of digestion buffer and incubated on a shaker (150rpm) at 37°C for 30minutes (Table 2.9.1A).

Table 2.9.1A: Individualized digestion buffers base on organ of interest. Individual buffers were prepared freshly on the day of FACs for esophagus, cardia, colon and liver samples.

Organ	Digestion buffer formulation
Esophagus	5mL Krebs Ringer buffer + 4%(w/v) BSA (0.2g) + 2mg/mL collagenase
Cardia/Stomach	5mL RPMI or DMEM + 2mg/mL collagenase P + 2mg/mL Pronase
Colon	5mL RPMI or DMEM + 2mg/mL collagenase P
Liver (~ 0.1g)	15mL RPMI or DMEM + 2mg/mL collagenase

*Collagenase and pronase were added to RPMI/DMEM prior to use with tissue. Krebs Ringer solution detailed below (Table 2.9.1B)

Following digestion, samples were passed through a cell strained (Thermo, 40um) and pushed through the strainer using the back of a syringe. Samples were spun down at 400 x g for 5-10minutes at 4°C. Supernatant was discarded and cell pellet was re-suspended in FACs buffer (PBS + 2% FBS + 2mMEDTA).

Blood was centrifuged at 350-400 x g for 10 minutes. Supernatant was discarded and 1mL of red cell lysis (Sigma) buffer was added to lysis cells a second time, followed by a spin down for 5-10 minutes at 4°C. Esophagus, forestomach and cardia, and colon did not require red cell lysis. However, spleen and liver were treated in a similar fashion as blood samples.

Staining of cell surface markers was done in a dimly lit area on ice, due to light sensitivity of the markers. When samples were not more than 10^8 cells, 5 0uL of FACs buffer with 0.5 µL antibody (eBioscience, Germany) was substituted. Cells were washed twice with FACs buffer, spun down at 400 x g for 5-10 minutes at 4°C. Lastly, cells were re-suspended in 120 µL FACs buffer, with an addition of 5 of 7-AAD live-dead cell marker. The live-dead cell marker was usually added prior to starting at the flow cytometry machine. Samples were stored on ice until flow cytometry was performed.

Table 2.9.1B: Formulation of Krebs Ringer solution. Krebs Ringer solution was freshly prepared for each experiment and used in the preparation of FACs digestion buffers.

Krebs Ringer solution (Made in ddH$_2$O, adjusted to pH 7.4)		
118 mM	NaCl	6.9 g/L
24.8 mM	NaHCO$_3$	2.08 g/L
1.2 mM	KH$_2$PO$_4$	0.16 g/L
4.8 mM	KCl	0.358 g/L
1.25 mM	CaCl$_2$	0.139 g/L
1.2 mM	MgSO$_4$	0.14 g/L
10 mM	HEPES	2.3831 g/L

2.10 Immune Cell Isolation: Neutrophils

Neutrophils were isolated from tissues of interest using the EasySep™Magnet and corresponding Mouse APC Selection Kit (10e9 cell, Stemcell technologies, Canada). Mice were euthanized by Isofluran inhalation. Organs of interest were resected and rinsed in sterile PBS on ice. Tissue samples were processed as described in the flow cytometry protocol in Section 2.9.1. Following the digestion step, samples were passed through a 40 um strainer several times. The cell suspension was collected and centrifuged at 400 x g for 10minutes at 4°C. A cell suspension with a concentration of 1×10^8 was re-suspended in pre-prepared FACs buffer (Table 2.91A) and transferred to a 5mL polystyrene round bottom tube. Species-specific FcR blocking antibody at a concentration of 10uL/mL murine cells was added and mixed in by pipetting up and down several times. Next, APC-conjugated antibody at a final concentration of 0.3-3.0ug/ mL was added and mixed in by pipetting up and down several times, followed by 15 minute incubation at room temperature. Following the incubation, the magnetic nanoparticles were added in at a concentration of 50/ mL and vigorously mixed by pipetting up and down more than 5 times, followed by a 10 minute incubation at room temperature. The cell suspension was brought to a total volume of 2.5 mL with the addition of FACs buffer and mixed gently, followed by 5 minute incubation. Following the incubation, the tube with the cell suspension was placed into the magnet, and in one swift motion the magnet was inverted (2-3 s) and the supernatant fraction was collected in a 50 mL Falcon tube. The tube was removed from the magnet, an additional 2.5 mL of FACS buffer was added and incubated for 5 minute, then the tube was returned to the magnet, inverted and the supernatant fraction was collected. This was repeated one more time. Following the third inversion, the positively selected cells were collected from the 5 mL polystyrene tube and RNA was isolated from the cells of interest using the Qiagen RNeasy Micro RNA Isolation kit (Qiagen, Germany) according to manufacturers instructions.

2.11 Cytokine Profiling

Murine serum and tissue lysate were analyzed for detection of numerous cytokines. The Proteome Profiler™ Array (Mouse XL Cytokine Array Kit, USA) was used to detect the relative levels of cytokines and chemokines secreted in mouse serum and in tissues of interest. Briefly, blood was drawn from the beating heart, and allowed to clot for 2 hours at room temperature prior to being centrifuged at 2,000 x g for 15 minute to separate the serum and plasma. 200 of pooled serum from L2-Chow (n = 4) and L2-HFD (n= 6) were used for the array. For tissue lysates, fresh tissue was resected and rinsed in cold, sterile PBS. Esophageal, forestomach and cardia tissue was pooled and protein extracted using a plastic, manual tissue disrupter (Bel Art Products, USA). Protein concentrations were measured from each mouse using the Pierce BCA Protein Assay Kit (Thermo Fisher Scientific) following the manufacturers protocol. 200 μg of pooled tissue lysate from L2-Chow (n = 4) and L2-HFD (n = 6) was used for the array. The cytokine array was carried out as described in the manufacturers protocol with no exceptions made. Following the final washing, membranes were exposed to X-ray film for 1 to 5 minute. Presence of cytokines and chemokines were observed on the membranes by overlapping with the template provided by the manufacturer show in Figure 2.11.
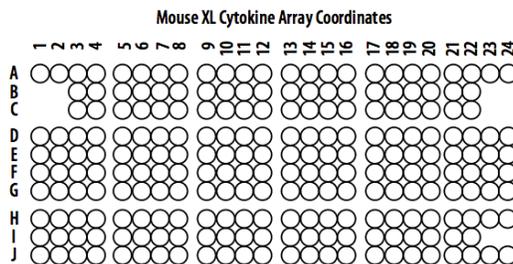
Figure 2.11: Template overlay for the RD Systems Proteome Profiler Array. Positive signals seen on developed film were identified by placing the transparency overlay template on the array image and aligning it with the pairs of reference spots in three corners of each array.

2.12 Cell Culture

In-vitro studies were carried out on organoids isolated from the cardia regions of mice. These organoids were cultured and passaged utilizing the techniques detailed below. It is important to note that these techniques were established in the Quante lab, based on protocols received from the Wang lab, Columbia University, USA.

2.12.1 Media Preparation

Several different media were used during the process of isolating cardia organoids, growth and expansion.

2.12.1a Complete Medium without Growth Factors (CM w/o GF)

500 mL Advanced DMEM/F12 (Life Technologies, Germany) was complemented with 5 mL Glutamax 100 x, 5 mL HEPES 1M and 5 mL Penicillin/Streptomycin (Pen/Strep) (10,000 Units/mL Penicillin Stock; 10,000 µg/mL Streptomycin Stock (Life Technologies, Germany)). Complete medium was stored at 4°C for up to 4 weeks.

2.12.1b Wnt-Conditioned Complete Medium (CCM)

L Wnt-3A fibroblasts were thawed in Dulbeco's Modified Eagle Medim (DMEM) and complemented with 10% fetal calf serum (FCS) (Life Technologies, Germany) and 1% Pen/Strep and incubated overnight at 37°C. Cells were split at a 1:15 ratio using Tripsin-EDTA (Ethylenediaminetetraacetic acid) (Life Technologies, Germany) and re-suspended in fresh DMEM (10% FCS, 1% Pen/Strep) prior to seeding in new Petri dishes. Wnt producing cells were selected for 7 to 10 days with the marker G418, also known as Geneticin, at a concentration 4 µL/mL. Following the expansion, medium was collected and filtered with a 0.22 µm strainer (Sarstedt, Germany).

2.12.1c Wnt-Conditioned Complete Medium with Growth Factors and ENR (Wnt-CCM with GF and ENR)

A 40 mL pre-made aliquot of Wnt-conditioned CM was thawed and complemented with 800 µL B27 (50X Stock) (Thermo Scientific, Germany), 400 µL N-2 (100X Stock) (Thermo Scientific, Germany) and 100 µL n-acetylcysteine

(500mM Stock). Additionally, 4 μL EGF (Epidermal growth factor), 40 μL Noggin and 350 μL R-Spondin were added. The obtained CCM with GF and ENR was aliquoted and frozen at -20°C for future usage.

2.12.2 Culturing Cardia Organoids

2.12.2.a Cardia Organoid Isolation.

The cardia tissue from resected murine stomachs was disrupted into minute fragments in a petri dish containing PBS (Life Technologies, Germany)–FBS (Heat Inactivated Fetal Bovine Serum) (Life Technologies, Germany) using a scalpel and fine tipped scissors. This suspension was transferred to a falcon tube with 25 mL PBS-EDTA- (Life Technologies, Germany)-EGTA (Roth, Germany) and incubated on a shaker at 4°C for 45 minutes. Following the incubation period, 10 mL PBS-FBS was added to the suspension and transferred through a 70-μM strainer into a new falcon tube. The remaining tissue was transferred back from the strainer to the original tube and washed again with 10 mL PBS-FBS, followed by another round of filtering. This procedure was repeated 6 to 7 times to obtain approximately 80 mL of cardia crypt organoid suspension. The fractions were then centrifuged at 800 x g for 8 minutes at 4°C. After removing the supernatant, pellets were re-suspended in 100 to 200 μL of Matrigel™ Matrix (BD Biosciences, UK), depending on the number of wells to be seeded (50μL per well). 50 μL of the crypts in Matrigel™ were pipetted into each well of a pre-warmed 24-well-plate and then transferred to the incubator for 5 to 10 minutes to allow the Matrigel™ drop to solidify. 500 μL Wnt-CCM with GF and ENR was warmed to room temperature then added to each well before returning the plate back to the incubator.

2.12.2.b Passage and Maintenance of Cardia Organoids.

Passaging of cardia organoids was carried out every 7 to 10 days, spitting at a ratio of approximately 1:2. First, media from each well was aspirated, and then 1 mL of cold CM without GF was added to each well to dissolve the Matrigel™. The medium was transferred to a 15 mL falcon tube. 1 mL of medium was added to the well to wash it and then transferred to the tube. The cell suspension was pipetted up and down on ice to separate and dissolve the crypts organoids. 2 mL

cold medium were added to the tube prior to centrifuging at 800 x g for 8 minutes at 4°C. The supernatant was discarded and the pellet was re-suspended in Matrigel™ and pipetted into new wells. The plate was then transferred to the incubator (37°C) for approximately 10 minutes for the Matrigel™ drop to solidify. Then 500 μL Wnt-CCM with GF and ENR was added and the plate was returned to the incubator.

2.12.2.c Treatment of Cardia Organoids with h-IL-8

Cardia crypts *in vitro* cultures were treated with 100 ng/mL recombinant human IL-8 or CXCL8 (PeproTech, USA) to investigate the influence IL-8 on cardia organoid growth and development. IL-8 was diluted in PBS + 0.1% BSA and stored in aliquots at -20°C according to manufacturer's instructions. This was added directly into the wells containing 500 mL Wnt-CCM with GF and ENR every 24 hours for 48 to 72 hours total. PBS + 0.1% BSA was used in the same manner as a control.

2.12.2.d Treatment of Cardia Organoids with L2-HFD Serum

Cardia organoids isolated from L2-Chow mice were treated with serum from L2-HFD mice in order to assess the role of the HFD in combination of IL-1beta over-expression. Blood was collected from three 12-month-old L2-HFD mice and centrifuged at 10,000 x g for 5 minutes. Serum was pooled together and 55 μL of pooled serum was added to each well containing 500 mL Wnt-CCM with GF and ENR every 24 hours for 48 to 72 hours total, resulting in a final treatment concentration of 10% serum. Serum from 12-month-old L2-Chow mice was used as a control.

2.12.2.e Treatment of Cardia Organoids with Human Lean and Obese Serum

Cardia crypt organoids isolated from L2/IL8Tg mice were treated with human lean and obsess sera to assess the effects on cardia organoid growth and development. These organoids were treated with 10% serum from obese and lean individuals obtained from collaboration partners at Columbia University, USA. The organoids were treated immediately after splitting. Cardia organoid medium containing either 10% obese or lean serum was exchanged every 24 hours for a total of 48 hours.

2.13 Microbiome Analysis

2.13.1 Sample Collection and Processing

Fresh stool samples from the L2-Chow and L2-HFD cohorts, along with WT-dietary and age-matched control mice were collected by massaging the lower abdominal area and retrieved with forceps, that were disinfected between use, directly from the rectum at 3-, 6-, 9- and 12-months. Samples were flash frozen in liquid N_2 and stored at -80°C. DNA was isolated and the V4 region of the 16s region was sequenced in a collaborative effort with Dr. Thomas Clavel, Technische Universität München, Germany.

2.13.2 Data Analysis

Sequenced data was analyzed using the Quantitative Insights Into Microbial Ecology software (QIIME), and operational taxonomic units (OTUs) were identified based on sequence similarity. Additionally, linear discriminant analysis Effect Size (LEfSe) analysis was performed to distinguish potential carcinogenic biomarker OTUs[145]. Data analysis was carried out by Jonas Ingermann.

2.14 Disclosures

While the majority of the data collected, analyzed and reported in this thesis was the work of Natasha Stephens Münch, several colleagues and collaborators have contributed to the data presented here.

The L2/IL-8Tg study was initiated by Dr. Carlo Maurer in 2014, additional breeding, sample collection, data analysis and completion of project was carried by Natasha Stephens Münch (January 2015-present).

The data presented on cardia organoids were part of Victoria Kellner's Masters Thesis project that was planned, supervised and corrected by Natasha Stephens Münch under the guidance of Dr. med Michael Quante.

Flow cytometry and analysis was carried out together with Dr. Hsin-Yu Fang with the assistance of Jonas Ingermann.

As a result of being pregnant towards the end of this project, several experiments including running cytokine arrays, additional Lgr5 *in-situ* and some RT-PCR runs were assisted by Dr. Fang, Jonas Ingermann and Vincenz Sahm, further data analysis was done by Natasha Stephens Münch.

Collaborations partners:

Prof. Dr. Timothy Wang Columbia University, NY, NY, USA

Prof. Dr. Martin Klingenspor, Technische Universität München, Germany

Prof. Dr. Dirk Haller, Technische Universität München, Germany

Dr. Thomas Clavel, Technische Universität München, Germany

Dr. James Fox, Massachusetts Institute of Technology, Cambridge, USA

Dr. Joanne Lysaght, Trinity Collage, Dublin, Ireland

Dr. Jacintha O'Sullivan, Trinity Collage, Dublin, Ireland

Prof. Dr. Hana Algül, Technische Universität München, Germany

2.15 Appendix Figures & Tables

Table 2.15 : RT-PCR Primer Sequences.

Name	Sequence	Length	Tm	GC%	Products on target templates
m-Cyclo. A	ATGGTCAACCCCACCGTGT	19	61.46	57.89	NM_008907.1 *Mus musculus* peptidylprolyl isomerase A (Ppia), mRNA
	TTCTGCTGTCTTTGGAACTTTGT	23	58.98	39.13	
m-Gapdh	GACATCAAGAAGGTGGTGAAGCA	23	61.06	47.83	NM_001289726.1 *Mus musculus* glyceraldehyde-3-phosphate dehydrogenase (Gapdh), transcript variant 1, mRNA
	ATACCAGGAAATGAGCTTGACAA	23	58.08	39.13	
m-KC	TGGGATTCACCTCAAGAACA	20	56.36	45	NM_008176.3 *Mus musculus* chemokine (C-X-C motif) ligand 1 (Cxcl1), mRNA
	TTTCTGAACCAAGGGAGCTT	20	56.95	45	
m-Cxcr2	AGCAAACACCTCTACTACCCTCT	23	60.5	47.83	NM_009909.3 *Mus musculus* chemokine (C-X-C motif) receptor 2 (Cxcr2), mRNA
	GGGCTGCATCAATTCAAATACCA	23	59.87	43.48	
h-IL-1Beta	CTCCACCTCCAGGGACAGGATA	22	62.38	59.09	NM_000576.2 *Homo sapiens* interleukin 1, beta (IL1B), mRNA
	TCTTTCAACACGCAGGACAGGT	22	62.38	50	
m-Cxcr1	CCGTCATGGATGTCTACGTG	20	58.16	55	XM_011238503.1 PREDICTED: *Mus musculus* chemokine (C-X-C motif) receptor 1 (Cxcr1), transcript variant X3, mRNA
	CAGCAGCAGGATACCACTGA	20	59.46	55	
Dclk1	AGCACTGCAGCAGGAGTTTCTG	22	63.33	54.55	XM_006500981.2 PREDICTED: *Mus musculus* doublecortin-like kinase 1 (Dclk1), transcript variant X4, mRNA
	AGTCCTCCGATTCCCGAGTTCAA	23	63.28	52.17	
h-IL8	CGTGGCTCTCTTGGCAGCCTTC	22	65.9	63.64	NM_000584.3 *Homo sapiens* chemokine (C-X-C motif) ligand 8 (CXCL8), mRNA
	TCCACAACCCTCTGCACCCAGTT	23	66.13	56.52	
m-Lgr5	GACGCTGGGTTATTTCAAGTTCA	23	59.5	43.48	NM_010195.2 *Mus musculus* leucine rich repeat containing G protein coupled receptor 5 (Lgr5), mRNA
	CAGCCAGCTACCAAATAGGTGCT	23	62.82	52.17	
m-Wnt7a	CGACTGTGGCTGCGACAAG	19	61.66	63.16	NM_009527.3 *Mus musculus* wingless-type MMTV integration site family, member 7A (Wnt7a), mRNA
	CTTCATGTTCTCCTCCAGGATCTTC	25	60.68	48	

m-Wnt5a	GACGCTTCGCTTGAATTCCT	20	58.92	50	NM_009524.3 *Mus musculus* wingless-type MMTV integration site family, member 5A (Wnt5a), transcript variant 1, mRNA
	AGAGGCTGTGCACCTATGAT	20	58.5	50	
m-Wnt5b	ATGCCCGAGAGCGTGAGAAG	20	62.29	60	NM_001271758.1 *Mus musculus* wingless-type MMTV integration site family, member 5B (Wnt5b), transcript variant 3, mRNA
	ACATTTGCAGGCGACATCAGC	21	62.14	52.38	
m-Wnt7b	TCTCTGCTTTGGCGTCCTCTAC	22	62.04	54.55	NM_009528.3 *Mus musculus* wingless-type MMTV integration site family, member 7B (Wnt7b), transcript variant 1, mRNA
	GCCAGGCCAGGAATCTTGTTG	21	61.83	57.14	
m-IL1beta	CAATTCCAGAAACCGCTATGA	27	58.56	32.14	NM_031168.1 *Mus musculus* interleukin 6 (Il6), mRNA
	TCTGGCTTTGTCTTTCTTGTTATC	30	59.68	26.78	
m-Wnt3a	CACCACCGTCAGCAACAGCC	20	64.21	65	NM_009522.2 *Mus musculus* wingless-type MMTV integration site family, member 3A (Wnt3a), mRNA
	AGGAGCGTGTCACTGCGAAAG	21	63.19	57.14	

Chapter 3

3.1 Metabolic Phenotyping of L2-IL-1beta Model

As previously described by Quante et al. (2012) a novel mouse model of Barrett Esophagus and subsequent EAC was developed and showed a remarkable disease progression similar to that observed in humans[89]. The correlation between obesity and BE and EAC has been widely speculated and is currently being studied by numerous research groups. Having access to a novel model of the disease of BE and EAC, and given the established risk association between obesity and BE and EAC it was of interest to understand the effects of diet induced obesity (DIO) by having a high fat diet (HFD) available *ad libitum* throughout the duration of a long-term aging study. A HFD with 48% energy from fat composed of 20% Palm oil and 5% Soybean oil was utilized.

Mice on a HFD were observed in parallel to mice on a standard lab Chow diet (henceforth referred to as Chow) as detailed in Figure 2.5.1 in the Materials and Methods section. To understand the mechanisms propelling the disease in this genetic mouse model, metabolic phenotyping was carried out in parallel to disease progression.

3.2 Morphology of the L2-IL-1beta Model

L2-IL-1beta mice (henceforth referred to as L2-mice, L2-model, or L2-Chow and L2-HFD depending on dietary treatment) were bred specifically for this study; offspring were born at a normal Mendelian ratio. At the time of weaning, L2-pups appeared smaller in appearance and were often visually discernable from their WT littermates prior to genotyping. Controls for the study included littermates genotyped as L2-IL-1beta$^{-/-}$ i.e. mice negative for the IL-1beta transgene were used as Wildtype controls. Morphologically. L2-mice remained smaller in size than their WT littermate controls (henceforth referred to as WT-Chow or WT-HFD) as they aged. Figure 3.2 and Appendix Figure 3.6.1 displays an overview of the observation of a remarkably smaller sized phenotype in the L2-model over the 12-month dietary and aging period. L2-mice presented with a much leaner

over-all appearance and at 9- and 12-months of age had a more pronounced skeletal appearance.

With the addition of HFD, the L2-model exhibited a more severe lean morphological appearance compared to L2-mice on Chow. While WT-HFD mice increased significantly in size and had visibly increased fat depots over time. L2-HFD mice present with miniscule to no fat depots. Additionally, the fur of WT-HFD mice appeared smooth and well-groomed, only slightly oily in texture appeared. Contrary to the appearance of L2-HFD mice, which revealed a more "hunch-backed" posture starting around 6 months of age, which was exacerbated as the animals aged; this caused the mice to appear even smaller in stature. L2-
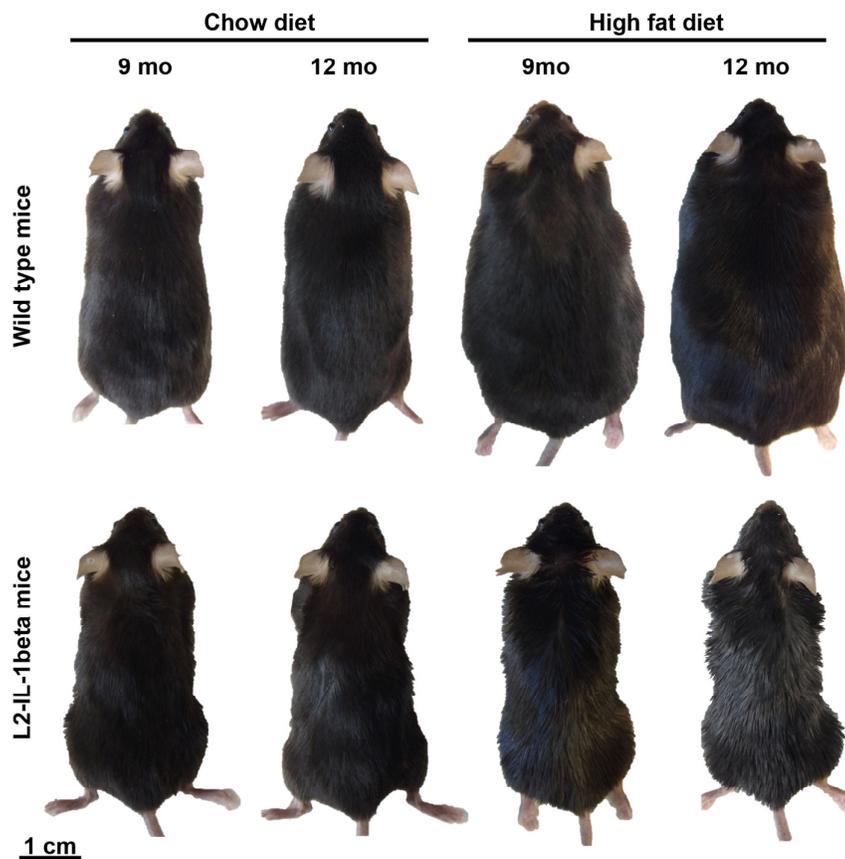
Figure 3.2: HFD results in an obese phenotype in WT-mice but L2-mice do not follow the same trend.
Groups of WT- and L2-mice were assigned either Chow or High Fat diet (HFD) 2-3 weeks after weaning, and aged to 12-months. At 9- and 12-months of age WT-mice on Chow progressed to expected body mass ranges and WT-mice on HFD gained body mass as expected. L2-IL-1beta mice revealed a lean, almost cachexia phenotype throughout their lifetime (morphological pictures of 3- and 6-month old mice in Appendix Figure 3.6.1).

HFD mice displayed a drastically leaner than the L2-mice on Chow. The fur of L2-mice appeared matted with oil from the diet, in addition to being slightly raised and not well groomed.

3.3 Body Mass and Composition of the L2-IL-1beta

Diet induced obesity provokes an increase in adipose tissue that subsequently affects overall body mass. Additionally, an increase in circulatory cytokines and adipokines released by engorged adipose sites can lead to a state of low-grade inflammation.

3.3.1 Body Mass

Body mass was measured every other week to record weight gain or loss in compliance with the study. These findings are reflected in the body mass development curve, illustrating changes in body mass at each analysis time point (Figure 3.3.1). Initial body mass was recorded for both genotypes at the start of the dietary study. The average body mass for the L2-IL-1beta group was 20.38g ±1.64g and for the WT littermates was 22.95g ±1.11g (Appendix Table 3.6.1 details body mass for all subsequent time-points) at the start of the study.

Body mass was assessed by factoring genotype, diet and time. Utilizing a Three-way ANOVA (generated using SigmaPlot software), there appeared to be significant differences over all three factors as noted in Figure 3.3.1, details of statistical outcomes are outlined in Appendix Table 3.6.2. A significant difference of $p < 0.001$ was noted across the afore mentioned factors, highlighting the impact of HFD over time on L2-mice in particular. While the L2-Chow mice showed a tendency towards slight weight gain, this appeared slower and lower in comparison to that of the WT-Chow mice.

The L2-model did not appear to be prone to DIO; L2-mice fed HFD until 12-months of age did not show significant increases in body mass compared to L2-IL-1beta mice on a Chow diet, rather L2-HFD mice had lower body mass throughout the study when compared to L2-Chow and WT-Chow and –HFD mice. Between 9- and 12-months of age, L2-HFD showed a sudden and sharp decrease in body mass than L2-Chow mice. WT-mice showed an expected body mass increase on Chow diet, and showed and increase body mass on HFD starting at 6-months of age.

In summary, the addition of HFD appeared to have a significant impact on the L2-mice over time, observed with lower weight gain over the study period, and a

decrease in body mass between 9- and 12-months of age. It is important to note that as body mass increased in the WT groups so did the error bars, revealing a higher variation of body mass within the same group.
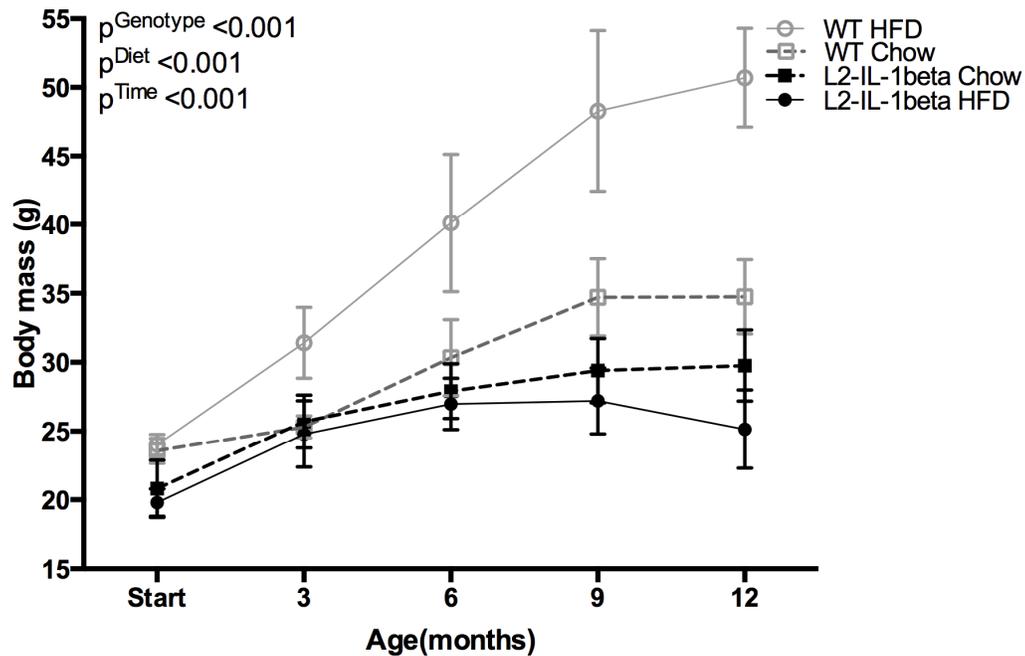
Figure 3.3.1: Body mass development in WT- and L2-mice on HFD.
WT-controls and L2-mice (n=6) per group and per time point) were fed either Chow or HFD and aged up to 12 months. Body mass was recorded every other week and summarized at each analysis time point. All data are means ± standard deviation. Statistical analysis was performed using Three-way ANOVA and Holm-Sidak's multiple comparisons test. Refer to Appendix Table 3.6.2 for detailed statistical analysis.

3.3.2 Fat and Lean Mass

Changes in body mass were also reflected in fat mass (FM) and lean mass (LM) compositions as determined by NMR spectroscopy.

Utilizing a Three-way ANOVA (generated using SigmaPlot software) analysis of fat mass across the 4-groups revealed significant difference between the factors of time, genotype and diet, Appendix Table 3.6.3. As the mice aged on the designated diets, a clear distinction of the effect of HFD was noted; with WT-HFD displaying the highest FM values and L2-HFD mice displayed the lowest FM value as both groups aged. Additionally. L2-Chow mice revealed low FM values, however these values did not appear to be drastically different from WT-Chow FM values until the 12-month time point where a divergence was noted (Figure 3.3.2 A, B) (Appendix Table 3.6.1 details body mass for all subsequent time-points).

Additionally, analysis of lean mass by Three-way ANOVA showed no significant differences across the 4-groups, Appendix Table 3.6.3. As the mice aged on the designated diets the observed trend showed lower LM values for L2-mice on Chow and HFD compared to WT-mice on both diets. However there appeared to be larger standard deviations for this measure.

By 3-months of age, WT-HFD mice began to show an increasing trend in FM compared to the WT-Chow mice but not in the L2-dietary groups. LM appeared to increase significantly in all groups except for the L2-HFD group from the start of the intervention to the 3-month time point. At 6-months onwards WT-HFD showed a steady increase in FM and LM that was statistically significant compared to the other groups. Between 3- and 6-months of age the L2-groups showed very similar FM and LM development patterns.

By 9- and 12-months the WT-mice more clearly distinguished themselves in terms of FM (Figure 3.2.2 A, B) and LM (Figure 3.2.2 C, D) patterns with significantly higher FM or LM mass (g) values than the L2-mice on each of the respective diets.

In summary, the effect of HFD on FM was noticeable in the WT-group, with WT-HFD showing proof of principle of DIO. WT-mice maintained statistically higher FM values compared to WT-Chow and L2-Chow and –HFD mice from 6-months

onwards. L2-mice on HFD presented in the lowest measured values out of the four groups for both FM and LM.
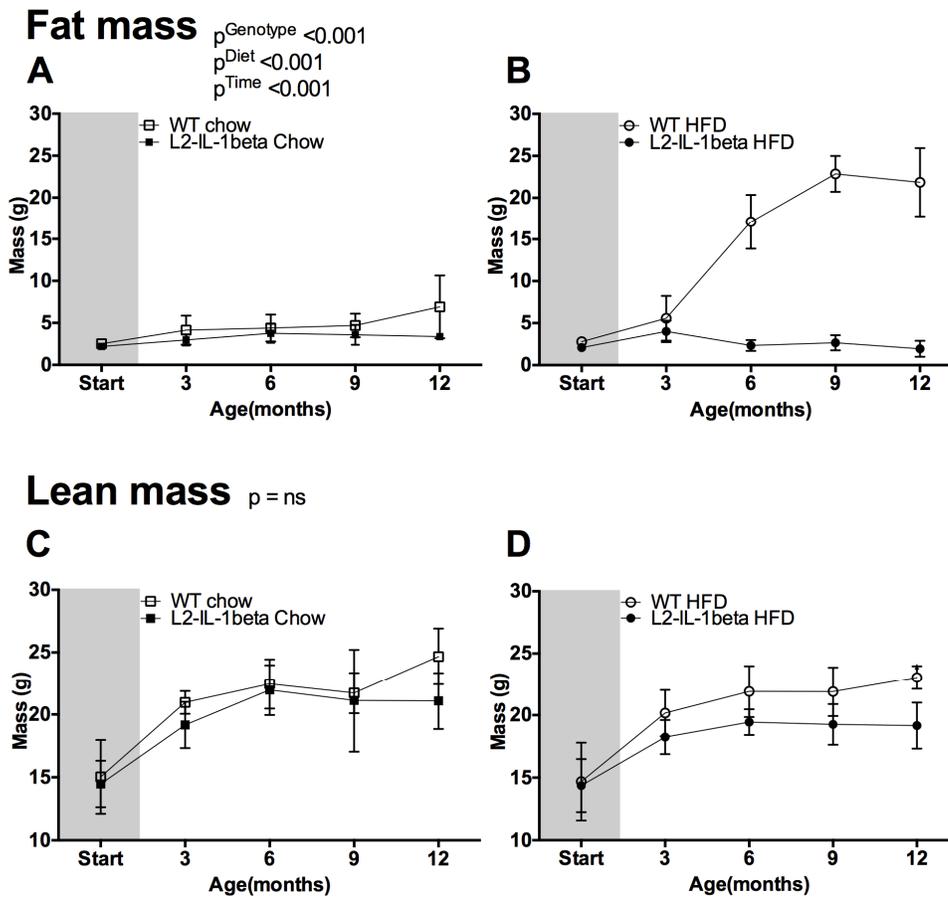
Figure 3.3.2: Fat and lean mass development in WT- and L2-mice on HFD.
WT- and L2-mice n=6 per group and per time point) were fed either a standard lab Chow diet or a high fat diet and aged up to 12months. (A, B) Fat (FM) and (C, D) lean mass (LM) on Chow and HFD respectively, were determined by NMR spectroscopy at all analysis time points, on Chow and HFD respectively. All data are means ± standard deviation. Statistical analysis was performed using Three-way ANOVA and Holm-Sidak's multiple comparisons test. Refer to Appendix Table 3.6.3 for detailed statistical analysis. Data is separated by diet for better visualization; grey shaded area represents time prior to dietary intervention where all mice were on Chow diet.

3.4 Food and Energy Balance in the L2-IL-1beta Model

Gross energy values for the standard Chow (16.7 MJ/kg) and HFD (21.9 MJ/kg) were obtained from the dietary composition references provided by the Company Ssniff. It is to be noted that bomb calorimetry was used to confirm these values for standard Chow (16.424 ± 0.79MJ/kg) and HFD (21.85 ± 0.63MJ/kg). The values measured by bomb calorimetry were comparable to those from the diet manufacturer and were used for calculation purposes.

Around 10 % energy (en%) in the Chow diet and 48 en% in the high fat diet was from Fat. Fat was the macronutrient contributing to close to half and thereby most of the energy in the HFD.

In order to assess whether the unique phenotype was the result of differences in food intake, weekly food consumption was assessed for each time-point when mice were single caged. Food intake, energy intake, energy excreted, and assimilated energy were assessed by factoring genotype, diet and time by utilizing a Three-way ANOVA (generated using SigmaPlot software).

Comparison of the 4-groups of mice, in terms of food intake revealed no significant differences across three factors as noted in Figure 3.4.1 A, B, however, a potential trend was observed for the factor of time ($p = 0.051$), details of statistical outcomes are outlined in Appendix Table 3.6.4. This trend could be observed in the decrease in food intake seen in WT- and L2-mice that were on HFD following the 6-month time point and the fairly stable consumption noted in WT- and L2-mice on Chow throughout the dietary intervention. Factoring for genotype and diet showed no significant differences in weekly food intake.

Energy intake was calculated using the gross energy values based on diet, as mentioned at the beginning of this section. Multiplying these established values by the weight of weekly food intake resulted in the energy intake values noted over the dietary intervention period. Comparison of the 4-groups of mice, in terms of energy intake showed a significant difference in terms of diet and a potential trend for differences was observed for the factor of time ($p = 0.063$) Figure 3.4.1C, D, details of statistical outcomes are outlined in Appendix Table 3.6.4.

Food intake

Energy intake

$p^{Diet} < 0.001$

Assimilated energy

$p^{Genotype} < 0.001$
$p^{Diet} < 0.001$
$p^{Time} < 0.001$
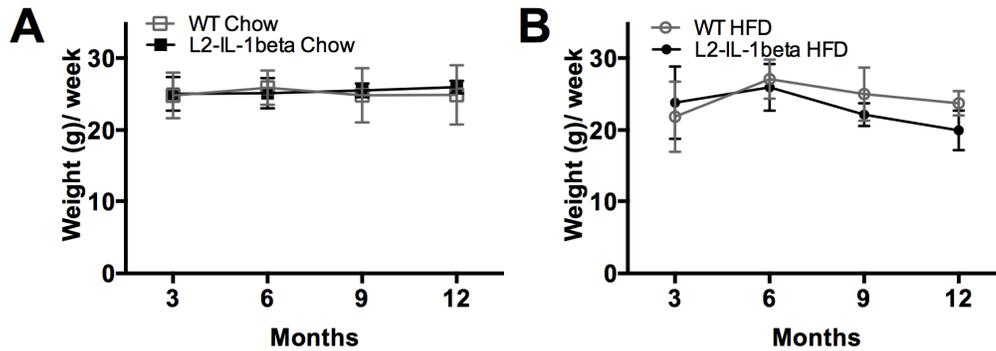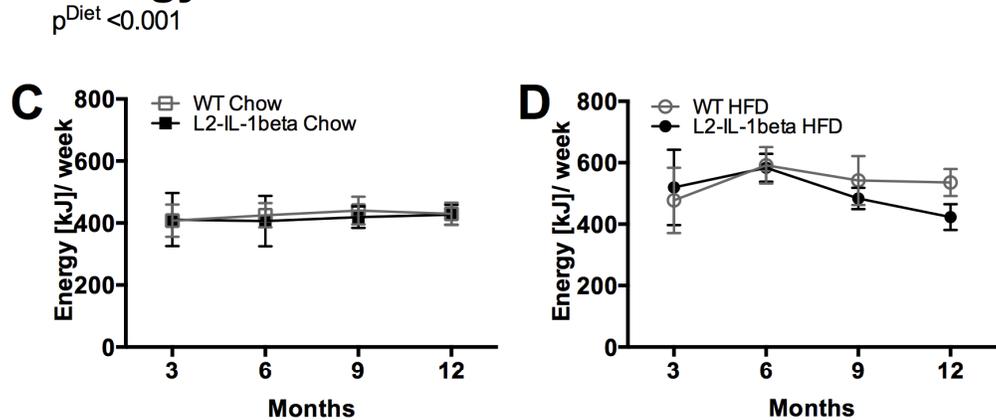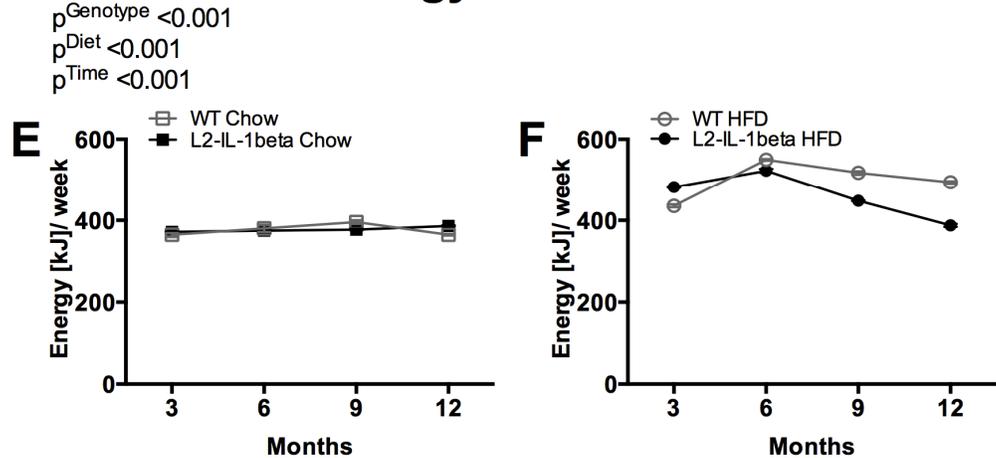
Figure 3.4.1: Energy balance in WT- and L2-mice on HFD.
Shown are the average values for weekly (A, B) food intake and (C, D) energy intake, and (E, F) assimilated energy over the dietary intervention period (3-12 months of age). Group size (n=5). All data are means ± standard deviation. Statistical analysis was performed using Three-way ANOVA and Holm-Sidak's multiple comparisons test. Refer to Appendix Table 3.6.4 for detailed statistical analysis. Data is separated by diet for better visualization.

In terms of diet, significance resulted from the higher energy content of the HFD in comparison to Chow. Furthermore, the trend observed over the factor of time (p=0.063) followed the trend observed over time for food intake; showing a similar decrease in energy intake in WT- and L2-mice following the 6-month time point.

In addition, energy excreted was also calculated based on the energy measured in excreted feces only, measured through bomb calorimetry. Comparison of the 4-groups of mice in terms of energy excreted showed a significant difference over genotype, diet and time as noted in Appendix Figure 3.6.2, details of statistical outcomes are outlined in Appendix Table 3.6.4.

Lastly, assimilated energy was determined by calculating the difference between energy intake and energy excreted ($E_{ass} = E_{intake}-E_{excreted}$). It is important to state that in these instances energy excreted did not include energy excreted by urine, rather only by feces. Urine excreted was not measured.

Assimilated energy values were similarly plotted over the dietary intervention period, Figure 3.4.2 C, D. Comparison of the 4-groups of mice, in terms of assimilated energy showed a significant difference over genotype, diet and time, details of statistical outcomes are outlined in Appendix Table 3.6.4. Taking into account the energy content of both diets a clear difference was noted between the Chow- and HFD-mice, which can further be noted in terms of the WT and L2 genotypes, and as well as in the factor of diet as seen in Figure 3.4.2 C, D.

In summary, while L2- and WT- mice did not consume statistically different amounts of food, significant differences were noted in terms of the factor of diet for energy intake and energy excreted, which subsequently led to significant differences observed in assimilated energy based on the metabolism of the mouse genotype across the factors of genotype, diet and over time.

3.5 Indirect Calorimetry and Locomotor Activity

Since HFDs are associated with the development of obesity resulting from altered energy metabolism and reduced physical activity the effect of HFD on L2-IL-1beta mice was investigated in terms of indirect calorimetry and locomotor activity. This was carried out in comparison to L2-Chow and WT-Chow and –HFD mice. Indirect calorimetric measurements were carried out at all four analysis time points, however locomotor activity was only measured at 3-, 6- and 12-month time points.

3.5.1 Indirect Calorimetry

For indirect calorimetry mice were housed in single cages for an acclimation period of 3 days prior to measurement. Indirect calorimetric measurements were carried out over 24 hours and graphs of the respiratory exchange ratio (RER) and volume oxygen ($V(O_2)$) values are illustrated in Figure 3.5.1.1 for 12-month old mice, and in Appendix Figure 3.6.3 for 3-, 6- and 12-month old mice.
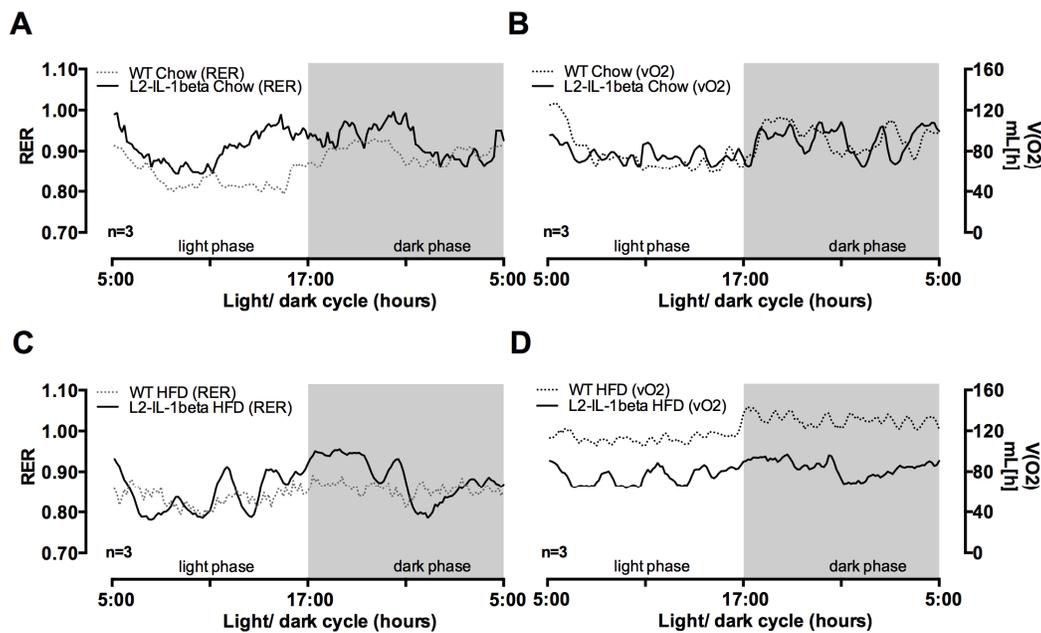
Figure 3.5.1.1: Energy consumption (indirect calorimetry) of WT and L2-mice at 12-months of age.
Mice on Chow (A, B) and HFD (C, D) were analyzed for energy consumption including measures of respiratory exchange ratio (RER) and volume oxygen consumed ($V(O_2)$) over 24hours (n=3).

In order to assess the unique phenotype RER and heat production (HP) over the dietary intervention was assessed at each time-point by factoring genotype, diet and time by utilizing a Three-way ANOVA (generated using SigmaPlot software). RER over time appeared significantly different over the factors genotype ($p=0.001$) and diet ($p<0.001$) as both groups aged on both diets, Figure 3.5.1.2, details of statistical outcomes are outlined in Appendix Table 3.6.5.

Respiratory exchange ratio $p^{Genotype} = 0.001$
$p^{Diet} <0.001$

Heat production $p^{Genotype} <0.001$
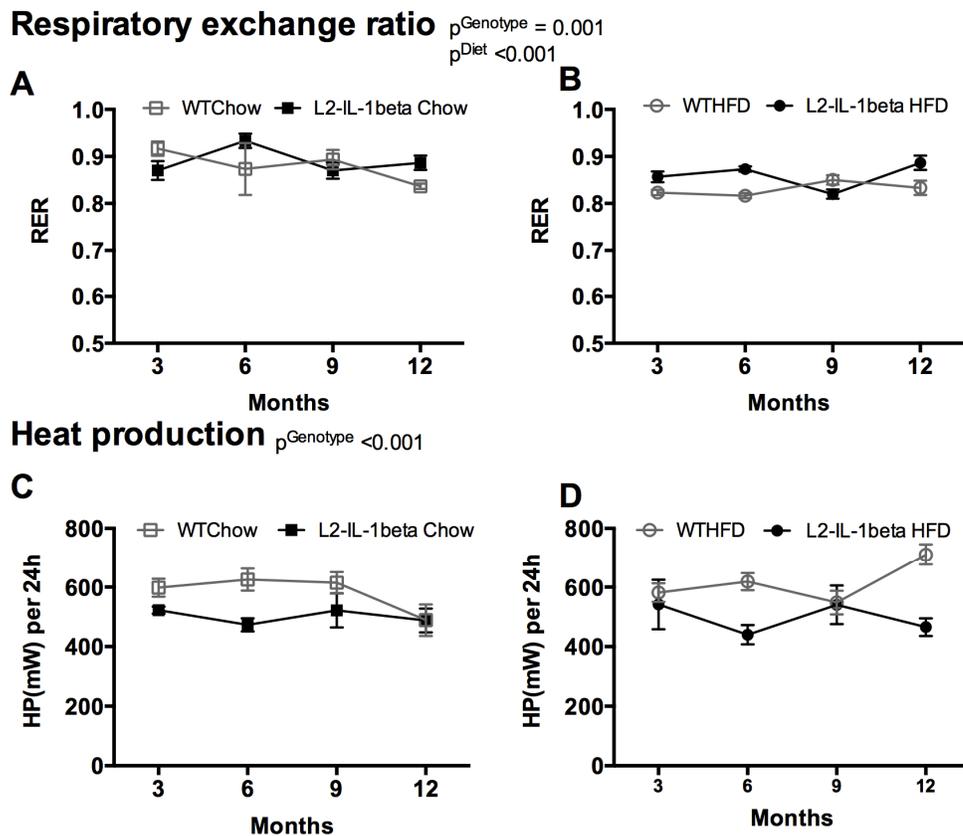
Figure 3.5.1.2: Energy consumption (indirect calorimetry) over the dietary intervention period (3- to 12-months).
WT- and L2-mice on Chow and HFD were analyzed for energy consumption over 24hours (n=3). (A, B) Respiratory exchange ratio and (C, D) heat production (HP). Statistical analysis was performed using Three-way ANOVA and Holm-Sidak's multiple comparisons test. Refer to Appendix Table 3.6.5 for detailed statistical analysis. Data is separated by diet for better visualization.

HP in WT- and L2-Chow mice appeared to stay fairly constant until the 12-month time-point, Figure 3.5.1.2. HFD WT- and L2-mice showed less of a trend over time, rather WT-HFD mice showed a decrease in HP at 9-months, but then a steep increase at 12-months, while HP of L2-mice on HFD appeared to decrease at 6-month, rose at 9-months and decreased again at 12-months. Despite these

interesting changes, there appeared to be a significant difference in the factor of genotype over the dietary treatment period as analyzed by Three-way ANOVA, details of statistical outcomes are outlined in Appendix Table 3.6.5.

Furthermore, resting metabolic rate (RMR) and maximal metabolic rate (MMR) was also assessed, as illustrated in Appendix Figure 3.6.4. There appeared to be significant differences over the factors genotype and diet for RMR, while MMR only showed significant differences for the factor genotype, details of statistical outcomes are outlined in Appendix Table 3.6.5.

3.5.2 Locomotor Activity

For locomotor activity WT- and L2-mice were observed for 5 consecutive days while being fed a Chow or HFD following a single housing acclimation period 3days prior to measurement. It is important to note that since the housing chamber for the activity monitoring differed from the acclimation cages, the first two days of activity measurements were disregarded.

As expected, all mice were most active during the dark phase. As the mice aged, there appeared to be a drop in over all activity, as notable in Appendix Figure 3.6.5 in 3- and 6-month old mice and in Figure 3.5.2.1 in 12-month old mice.

When cumulative activity was graphed over time, a clear separation was noted between WT- and L2-mice on both diets. WT-mice on Chow appeared to be more active than L2-Chow mice. On a HFD, L2-mice appeared to be more active than WT-mice. WT-mice showed very low activity over time, while L2-HFD mice appeared to be very active at 3- and 6-months of age, with a steep decline in activity at 12-months of age. Analysis of cumulative activity by Three-way ANOVA showed significant differences for the factor of time (p=0.007) across the 4-groups, Appendix Table 3.6.5.

When cumulative distance was analyzed using Three-way ANOVA there appeared to be significant differences for the factors of time (p=0.029) and genotype (0.001) across the 4-groups, Appendix Table 3.6.6. These trends can be observed in Figure 3.5.2.2.

Daily activity over 72 hours
12 months
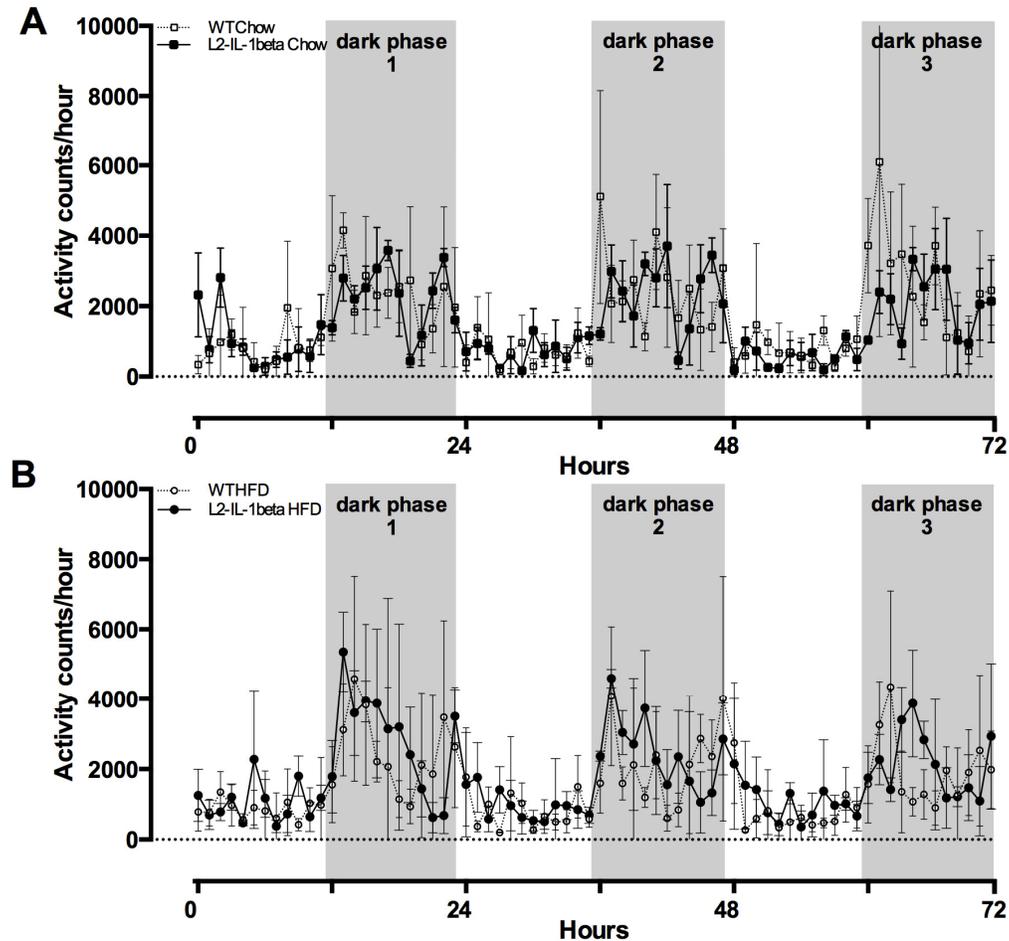
Figure 3.5.2.1: Activity monitoring of WT- and L2-mice on Chow and HFD over a period of 72 hours.
At 12-months of age the (A, B) activity counts of WT- and L2-mic were assessed for changes in behavior. Graphs are separated based on diet for easier viewing. Grey regions represent the dark phase hours (17-5h).

In summary WT-HFD mice showed reduced activity at 6- and 12-months compared to the level observed at 3-months, as their body mass increased. The L2-mice began to show a reduction in activity counts at 6-months, which was further reduced at 12-months. While this was not statistically significant, the trend in decreased activity is noticeable in the L2-group.

Activity $p^{Time} = 0.007$
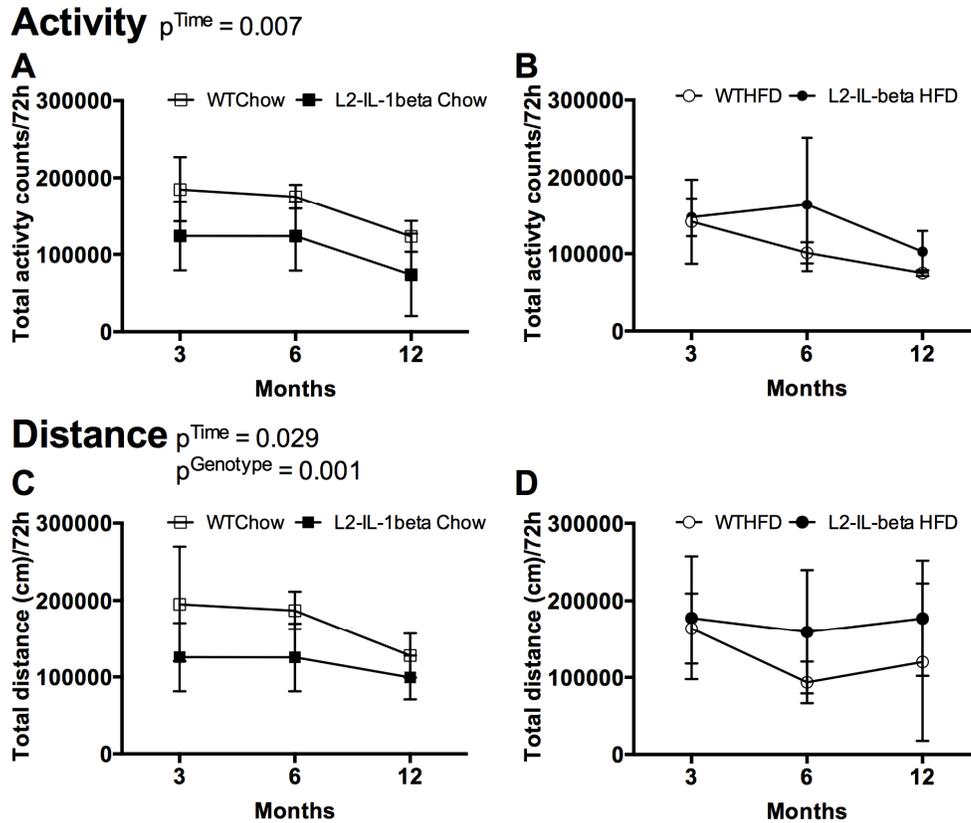
Figure 3.5.2.2: Locomotor activity and distance covered over a period of 72 hours.
At 12-months of age the (A, B) cumulated activity and C, D) over the dietary intervention period (3-to 12-months of age) were graphed based on diet. All data are means ± standard deviation. Statistical analysis was performed using Three-way ANOVA and Holm-Sidak's multiple comparisons test. Refer to Appendix Table 3.6.6 for detailed statistical analysis. Data is separated by diet for better visualization.

In summary, the few methods used for metabolic phenotyping revealed the effects of diet and genotype in some instances, on the lean phenotype observed in the L2-HFD model. While a clear metabolic profile was not distinguishable, further experiments and larger cohorts sizes might reveal a deeper understanding of the metabolism of this model. The next steps were to assess pathological and molecular changes in the L2-model on HFD.

This study has several limitations. First, the diet used as a control was not a strictly defined diet that only differed in fat content. This shortcoming has been rectified in ongoing studies involving the L2-model. Additionally, the western

style diet that is associated with adult obesity is more complex and high in protein, cholesterol, fructose, and salt, which may also have detrimental effects on EAC progression in the L2-model as well as patients. Furthermore, several metabolic measurements were carried out with small sample sizes, which might have contributed to non-significant results, this has been taken into consideration for future studies involving the L2-model.

3.6 Appendix Figures & Tables
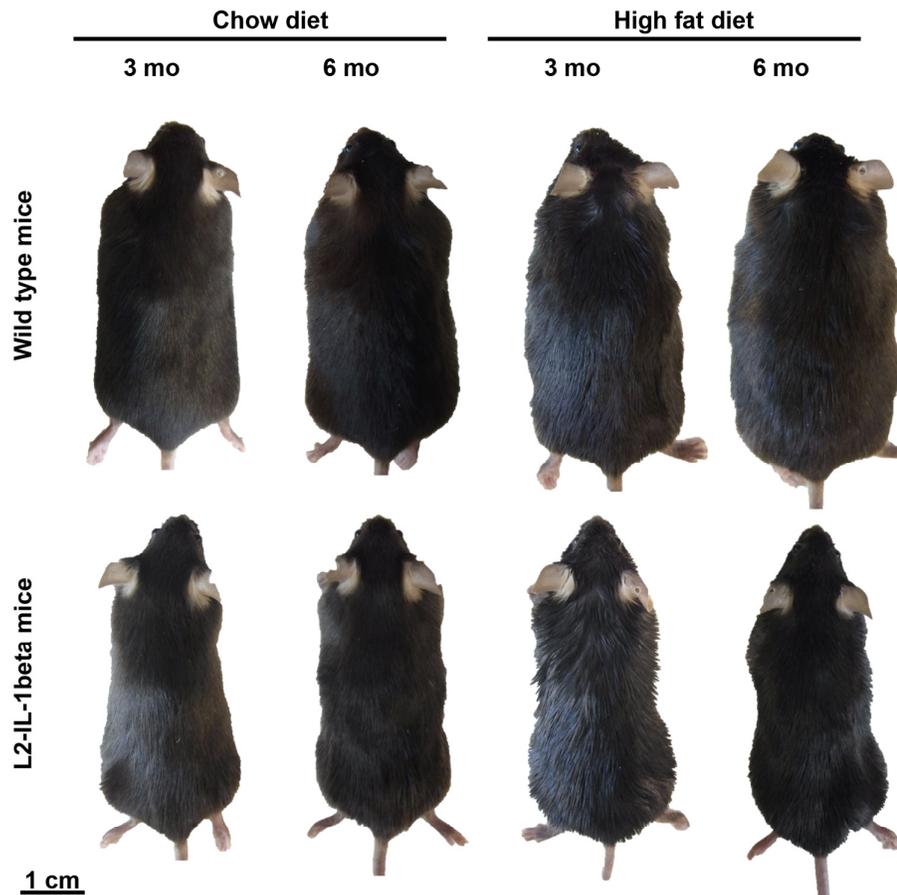
Figure 3.6.1: HFD results in an obese phenotype in WT-mice but L2-mice do not follow the same trend.
Groups of WT- and L2-IL-1beta littermates were assigned either a chow or a High Fat diet 2-3weeks after weaning and aged to 12-months. At 3- and 6-months of age WT-mice on chow diet progressed to expected body mass ranges and WT-mice on HFD gained body mass as expected. L2-IL-1beta mice revealed a lean, low body mass phenotype at 3- and 6-months of age.

Appendix Table 3.6.1: Effects of HFD on L2-mice on body mass and spleen weight.

(Values were calculated as means ± standard deviation (n=6) per genotype and dietary group at 3-. 6-. 9- and 12-months of age.)

	WT	L2-IL-1beta	Start			3months			6months	
			WT-Chow	WT-HFD	L2-Chow	L2-HFD	WT-Chow	WT-HFD	L2-Chow	L2-HFD
Initial (g)	22.95 ± 1.11	20.38 ± 1.64								
Final (g)			25.31 ± 0.79	31.41 ± 2.57	25.71 ± 1.92	24.80 ± 2.40	30.34 ± 2.75	40.13 ± 4.99	27.92 ± 1.98	26.99 ± 1.87
Fat mass (g)	2.52 ± 0.34	2.20± 0.19	4.147 ± 1.726	5.58 ± 2.67	2.971 ± 0.65	4.02 ± 1.27	4.39 ± 1.59	17.10 ± 3.23	3.77 ± 1.14	2.35 ± 0.66
Lean mass (g)	15.04 ± 2.93	14.47 ± 1.84	20.96 ± 0.91	20.17 ± 1.85	19.17 ± 1.84	18.24 ±1.36	22.44 ± 1.97	21.91 ± 2.06	21.11 ± 4.09	19.44 ± 1.97
Spleen (mg)			78.61 ± 1.19	90.59 ± 4.20	91.60 ± 3.14	93.02 ± 1.73	101.28 ± 1.43	110.06 ± 2.76	96.00 ± 1.49	105.45 ± 2.22
Spleen (%BM)			0.26 ± 0.03	0.29± 0.13	0.33 ± 0.11	0.380 ± 0.091	0.36 ± 0.05	0.27 ± 0.09	0.34 ± 0.07	0.40 ± 0.06

	9months				12months			
	WT-Chow	WT-HFD	L2-Chow	L2-HFD	WT-Chow	WT-HFD	L2-Chow	L2-HFD
Initial (g)								
Final (g)	34.71 ± 2.80	48.29 ± 5.84	29.40 ± 2.32	27.20 ± 2.40	33.84 ± 2.91	50.71 ± 3.59	29.77 ± 2.58	25.15 ± 2.84
Fat mass (g)	4.70 ± 1.41	22.86 ± 2.14	3.58 ± 1.19	2.67 ± 0.90	6.90 ± 3.74	21.85 ± 4.08	3.36 ± 0.35	1.95 ± 0.95
Lean mass (g)	21.72 ± 1.61	21.89 ± 1.96	21.11± 4.09	19.26 ± 1.63	24.66 ± 2.24	23.05 ± 0.92	21.08 ± 2.23	19.17 ± 1.84
Spleen (mg)	83.01 ± 1.31	85.05 ± 1.20	92.42 ± 1.34	103.7 ± 3.33	82.05 ± 0.59	92.52 ± 1.22	96.98 ± 0.99	100.94 ± 3.60
Spleen (%BM)	0.24 ± 0.03	0.17 ± 0.02	0.32 ± 0.09	0.45 ± 0.20	0.24 ± 0.02	0.18 ± 0.02	0.29 ± 0.11	0.37 ± 0.17

Appendix Table 3.6.2: Body mass

Three Way Analysis of Variance: Body mass
Balanced Design
Dependent Variable: Body mass
Normality Test (Shapiro-Wilk)   Passed (P = 0.215)
Equal Variance Test: Failed   (P < 0.050)

Source of Variation	DF	SS	MS	F	P
Time	4	5694.078	1423.520	74.242	<0.001
Genotype	1	3553.148	3553.148	185.311	<0.001
Diet	1	644.054	644.054	33.590	<0.001
Time x Genotype	4	1635.600	408.900	21.326	<0.001
Time x Diet	4	344.760	86.190	4.495	0.002
Genotype x Diet	1	1121.344	1121.344	58.482	<0.001
Time x Genotype x Diet	4	671.276	167.819	8.752	<0.001
Residual	220	4218.283	19.174		
Total	239	17882.543	74.822		

There is a statistically significant interaction between Time, Genotype and Diet (P = <0.001). This indicates that the effect of one factor is not consistent at all combinations of the two other factors; and, therefore, an unambiguous interpretation of the main effects is not possible, SigmaStat will evaluate significant interactions as appropriate.

Appendix Table 3.6.3: Fat & Lean mass

It is to be noted that this data (fat & lean mass) set failed for tests of normality (normal distribution) and equal variance, thus data was analyzed using a parametric Three-way ANOVA, details of the statistics are outlined below.

Three Way Analysis of Variance: Fat mass
Balanced Design
Dependent Variable: Fat mass
Normality Test (Shapiro-Wilk)   Failed   (P < 0.050)
Equal Variance Test: Failed   (P < 0.050)

Source of Variation	DF	SS	MS	F	P
Time	4	743.540	185.885	53.802	<0.001
GT	1	1213.183	1213.183	351.141	<0.001
Diet	1	601.978	601.978	174.235	<0.001
Time x GT	4	683.503	170.876	49.458	<0.001
Time x Diet	4	322.617	80.654	23.344	<0.001
GT x Diet	1	810.794	810.794	234.674	<0.001
Time x GT x Diet	4	496.912	124.228	35.956	<0.001
Residual	100	345.498	3.455		
Total	119	5218.024	43.849		

There is a statistically significant interaction between Time, GT and Diet (P = <0.001). This indicates that the effect of one factor is not consistent at all combinations of the two other factors; and, therefore, an unambiguous interpretation of the main effects is not possible, SigmaStat will evaluate significant interactions as appropriate.

Three Way Analysis of Variance: Lean mass
Balanced Design
Dependent Variable: Lean mass

Normality Test (Shapiro-Wilk)   Failed   (P < 0.050)
Equal Variance Test: Passed (P = 0.468)

Source of Variation	DF	SS	MS	F	P
Time	4	14226686.511	3556671.628	1.005	0.409
GT	1	3501145.180	3501145.180	0.989	0.322
Diet	1	3561719.477	3561719.477	1.007	0.318
Time x GT	4	14164531.070	3541132.767	1.001	0.411
Time x Diet	4	14165737.411	3541434.353	1.001	0.411
GT x Diet	1	3547340.225	3547340.225	1.002	0.319
Time x GT x Diet	4	14169133.304	3542283.326	1.001	0.411
Residual	100	353866498.563	3538664.986		
Total	119	421202791.741	3539519.258		

The difference in the mean values among the different levels of Time are not great enough to exclude the possibility that the difference is just due to random sampling variability after allowing for the effects of differences in GT and Diet. There is not a statistically significant difference (P = 0.409).

The difference in the mean values among the different levels of GT are not great enough to exclude the possibility that the difference is just due to random sampling variability after allowing for the effects of differences in Time and Diet. There is not a statistically significant difference (P = 0.322).

The difference in the mean values among the different levels of Diet are not great enough to exclude the possibility that the difference is just due to random sampling variability after allowing for the effects of differences in Time and GT. There is not a statistically significant difference (P = 0.318).

The effect of different levels of Time does not depend on what level of GT is present. There is not a statistically significant interaction between Time and GT. (P = 0.411)

The effect of different levels of Time does not depend on what level of Diet is present. There is not a statistically significant interaction between Time and Diet. (P = 0.411)

The effect of different levels of GT does not depend on what level of Diet is present. There is not a statistically significant interaction between GT and Diet. (P = 0.319)

Energy excreted

$p^{Genotype} = 0.013$
$p^{Diet} < 0.001$
$p^{Time} = 0.017$
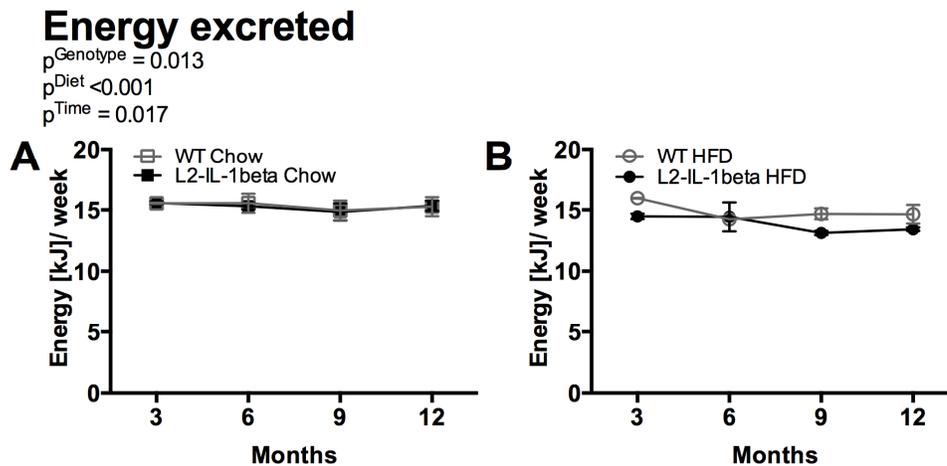
Appendix Figure 3.6.2: Energy balance in WT- and L2-mice on HFD.
Shown are the average values for weekly (A. B) excreted energy over the dietary intervention period (3 – 12-months of age). Group size (n=5). All data are means ± standard deviation. Statistical analysis was performed using Three-way ANOVA and Holm-Sidak's multiple comparisons test. Refer to Appendix Table 3.6.4 for detailed statistical analysis. Data is separated by diet for better visualization.

Appendix Table 3.6.4: Food intake, Energy intake, Excreted energy & Energy assimilated

Three Way Analysis of Variance: Food intake
Balanced Design
Dependent Variable: Food intake
Normality Test (Shapiro-Wilk)   Passed (P = 0.461)
Equal Variance Test: Passed (P = 0.441)

Source of Variation	DF	SS MS		F	P
Time	3	107.037	35.679	2.739	0.051
GT	1	17.478	17.478	1.342	0.251
Diet	1	28.434	28.434	2.183	0.144
Time x GT	3	37.382	12.461	0.957	0.419
Time x Diet	3	28.709	9.570	0.735	0.535
GT x Diet	1	8.439	8.439	0.648	0.424
Time x GT x Diet	3	21.846	7.282	0.559	0.644
Residual	64	833.646	13.026		
Total	79	1082.971	13.708		

The difference in the mean values among the different levels of Time are not great enough to exclude the possibility that the difference is just due to random sampling variability after allowing for the effects of differences in GT and Diet. There is not a statistically significant difference (P = 0.051).

The difference in the mean values among the different levels of GT are not great enough to exclude the possibility that the difference is just due to random sampling variability

after allowing for the effects of differences in Time and Diet. There is not a statistically significant difference (P = 0.251).

The difference in the mean values among the different levels of Diet are not great enough to exclude the possibility that the difference is just due to random sampling variability after allowing for the effects of differences in Time and GT. There is not a statistically significant difference (P = 0.144).

The effect of different levels of Time does not depend on what level of GT is present. There is not a statistically significant interaction between Time and GT. (P = 0.419)

The effect of different levels of Time does not depend on what level of Diet is present. There is not a statistically significant interaction between Time and Diet. (P = 0.535)

The effect of different levels of GT does not depend on what level of Diet is present. There is not a statistically significant interaction between GT and Diet. (P = 0.424)

Three Way Analysis of Variance: Energy intake

Balanced Design
Dependent Variable: **Energy intake**
Normality Test (Shapiro-Wilk)   Passed (P = 0.541)
Equal Variance Test: Passed (P = 0.324)

Source of Variation	DF	SS	MS	F	P
Time	3	38736.396	12912.132	2.556	0.063
GT	1	4086.071	4086.071	0.809	0.372
Diet	1	230756.830	230756.830	45.681	<0.001
Time x GT	3	10232.259	3410.753	0.675	0.570
Time x Diet	3	18830.018	6276.673	1.243	0.302
GT x Diet	1	15640.931	15640.931	3.096	0.083
Time x GT x Diet	3	26969.512	8989.837	1.780	0.160
Residual	64	323298.294	5051.536		
Total	79	668550.312	8462.662		

The difference in the mean values among the different levels of Time are not great enough to exclude the possibility that the difference is just due to random sampling variability after allowing for the effects of differences in GT and Diet. There is not a statistically significant difference (P = 0.063).

The difference in the mean values among the different levels of GT are not great enough to exclude the possibility that the difference is just due to random sampling variability after allowing for the effects of differences in Time and Diet. There is not a statistically significant difference (P = 0.372).

The difference in the mean values among the different levels of Diet are greater than would be expected by chance after allowing for the effects of differences in Time and GT. There is a statistically significant difference (P = <0.001). To isolate which group(s) differ from the others use a multiple comparison procedure.

The effect of different levels of Time does not depend on what level of GT is present. There is not a statistically significant interaction between Time and GT. (P = 0.570)

The effect of different levels of Time does not depend on what level of Diet is present. There is not a statistically significant interaction between Time and Diet. (P = 0.302)

The effect of different levels of GT does not depend on what level of Diet is present. There is not a statistically significant interaction between GT and Diet. (P = 0.083)

Three Way Analysis of Variance: Energy excreted
Balanced Design
Dependent Variable: **Energy excreted**
Normality Test (Shapiro-Wilk)   Passed (P = 0.607)
Equal Variance Test: Failed (P < 0.050)

Source of Variation	DF	SS	MS	F	P
Time	3	4.156	1.385	4.589	0.017
GT	1	2.339	2.339	7.746	0.013
Diet	1	6.862	6.862	22.729	<0.001
Time x GT	3	0.777	0.259	0.858	0.483
Time x Diet	3	0.977	0.326	1.078	0.386
GT x Diet	1	1.813	1.813	6.005	0.026
Time x GT x Diet	3	1.310	0.437	1.447	0.266
Residual	16	4.830	0.302		
Total	31	23.063	0.744		

The difference in the mean values among the different levels of Time are greater than would be expected by chance after allowing for the effects of differences in GT and Diet. There is a statistically significant difference (P = 0.017). To isolate which group(s) differ from the others use a multiple comparison procedure.

The main effects for GT cannot be properly interpreted since the size of the factor's effect depends upon the level of another factor.

The main effects for Diet cannot be properly interpreted since the size of the factor's effect depends upon the level of another factor.

The effect of different levels of Time does not depend on what level of GT is present. There is not a statistically significant interaction between Time and GT. (P = 0.483)

The effect of different levels of Time does not depend on what level of Diet is present. There is not a statistically significant interaction between Time and Diet. (P = 0.386)

The effect of different levels of GT depends on what level of Diet is present. There is a statistically significant interaction between GT and Diet. (P = 0.026)

Appendix Table 3.6.4 continued

Three Way Analysis of Variance: Energy assimilated
Balanced Design
Dependent Variable: **Energy assimilated**
Normality Test (Shapiro-Wilk)   Passed (P = 0.679)
Equal Variance Test: Failed (P < 0.050)

Source of Variation	DF	SS	MS	F	P
Time	3	12502.566	4167.522	210.425	<0.001
GT	1	2535.877	2535.877	128.041	<0.001
Diet	1	82760.288	82760.288	4178.702	<0.001

Time x GT	3	6155.885	2051.962	103.607	<0.001
Time x Diet	3	10121.382	3373.794	170.348	<0.001
GT x Diet	1	2901.990	2901.990	146.526	<0.001
Time x GT x Diet	3	6494.243	2164.748	109.302	<0.001
Residual	16	316.884	19.805		
Total	31	123789.114	3993.197		

There is a statistically significant interaction between Time, GT and Diet (P = <0.001). This indicates that the effect of one factor is not consistent at all combinations of the two other factors; and, therefore, an unambiguous interpretation of the main effects is not possible, SigmaStat will evaluate significant interactions as appropriate.

Energy consumption (Indirect calorimetry)
3 months
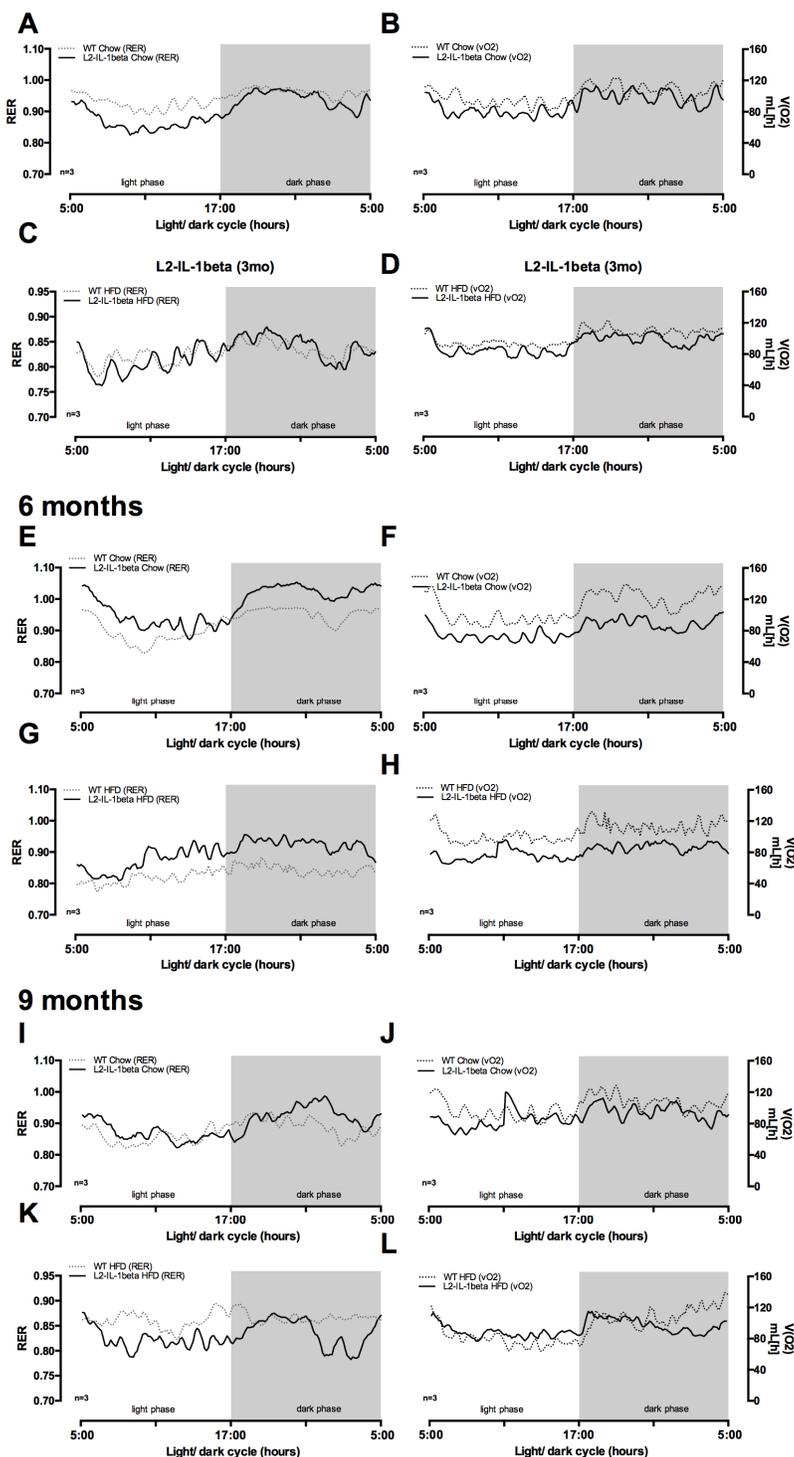
Appendix Figure 3.6.3: Energy consumption (indirect calorimetry) of WT-and L2-mice over the dietary intervention period (3- to 9- months).
Mice on Chow (A. B) and HFD (C. D) were analyzed for energy consumption including measures of respiratory exchange ratio (RER) and volume oxygen consumed (V(O$_2$)) over 24hours (n=3).

Appendix Table 3.6.5: Indirect calorimetry

It is to be noted that this data set failed for tests of normality (normal distribution) and equal variance, thus data was analyzed using a parametric Three-way ANOVA, details of the statistics are outlined below.

Three Way Analysis of Variance: RER
Balanced Design
Dependent Variable: **RER**
Normality Test (Shapiro-Wilk)   Failed (P < 0.050)
Equal Variance Test: Passed (P = 0.588)

Source of Variation	DF	SS	MS	F	P
Time	3	0.00178	0.000594	1.640	0.200
GT	1	0.00441	0.00441	12.161	0.001
Diet	1	0.0192	0.0192	52.966	<0.001
Time x GT	3	0.0161	0.00536	14.782	<0.001
Time x Diet	3	0.00608	0.00203	5.594	0.003
GT x Diet	1	0.00101	0.00101	2.782	0.105
Time x GT x Diet	3	0.00384	0.00128	3.533	0.026
Residual	32	0.0116	0.000363		
Total	47	0.0640	0.00136		

There is a statistically significant interaction between Time, GT and Diet (P = 0,026).This indicates that the effect of one factor is not consistent at all combinations of the two other factors; and, therefore, an unambiguous interpretation of the main effects is not possible. SigmaStat will evaluate significant interactions as appropriate.

Three Way Analysis of Variance: HP (mean daily)
Balanced Design
Dependent Variable: **HP (mean daily)**
Normality Test (Shapiro-Wilk)   Passed (P = 0.551)
Equal Variance Test: Passed (P = 0.930)

Source of Variation	DF	SS	MS	F	P
Time	3	4861.310	1620.437	0.876	0.464
GT	1	118380.501	118380.501	63.961	<0.001
Diet	1	2468.344	2468.344	1.334	0.257
Time x GT	3	27357.843	9119.281	4.927	0.006
Time x Diet	3	30645.705	10215.235	5.519	0.004
GT x Diet	1	4163.246	4163.246	2.249	0.143
Time x GT x Diet	3	47709.908	15903.303	8.593	<0.001
Residual	32	59226.037	1850.814		
Total	47	294812.895	6272.615		

There is a statistically significant interaction between Time, GT and Diet (P = <0.001). This indicates that the effect of one factor is not consistent at all combinations of the two other factors; and. Therefore, an unambiguous interpretation of the main effects is not possible, SigmaStat will evaluate significant interactions as appropriate.

Three Way Analysis of Variance: RMR
Balanced Design
Dependent Variable: **RMR**
Normality Test (Shapiro-Wilk)   Passed (P = 0.753)

Equal Variance Test: Passed (P = 0.499)

Source of Variation	DF	SS	MS	F	P
Time	3	48.169	16.056	1.412	0.257
GT	1	416.541	416.541	36.618	<0.001
Diet	1	73.013	73.013	6.419	0.016
Time x GT	3	55.129	18.376	1.615	0.205
Time x Diet	3	241.043	80.348	7.063	<0.001
GT x Diet	1	44.083	44.083	3.875	0.058
Time x GT x Diet	3	354.947	118.316	10.401	<0.001
Residual	32	364.007	11.375		
Total	47	1596.932	33.977		

There is a statistically significant interaction between Time, GT and Diet (P = <0.001). This indicates that the effect of one factor is not consistent at all combinations of the two other factors; and therefore, an unambiguous interpretation of the main effects is not possible, SigmaStat will evaluate significant interactions as appropriate.

Three Way Analysis of Variance: MMR
Balanced Design
Dependent Variable: **MMR**
Normality Test (Shapiro-Wilk)   Passed (P = 0.496)
Equal Variance Test: Passed (P = 0.372)

Source of Variation	DF	SS	MS	F	P
Time	3	42.527	14.176	0.366	0.778
GT	1	1229.175	1229.175	31.710	<0.001
Diet	1	23.660	23.660	0.610	0.440
Time x GT	3	335.337	111.779	2.884	0.051
Time x Diet	3	82.756	27.585	0.712	0.552
GT x Diet	1	78.797	78.797	2.033	0.164
Time x GT x Diet	3	263.416	87.805	2.265	0.100
Residual	32	1240.420	38.763		
Total	47	3296.088	70.130		

The difference in the mean values among the different levels of Time are not great enough to exclude the possibility that the difference is just due to random sampling variability after allowing for the effects of differences in GT and Diet. There is not a statistically significant difference (P = 0.778).

The difference in the mean values among the different levels of GT are greater than would be expected by chance after allowing for the effects of differences in Time and Diet. There is a statistically significant difference (P = <0.001). To isolate which group(s) differ from the others use a multiple comparison procedure.

The difference in the mean values among the different levels of Diet are not great enough to exclude the possibility that the difference is just due to random sampling variability after allowing for the effects of differences in Time and GT. There is not a statistically significant difference (P = 0.440).

The effect of different levels of Time does not depend on what level of GT is present. There is not a statistically significant interaction between Time and GT. (P = 0.051)

The effect of different levels of Time does not depend on what level of Diet is present. There is not a statistically significant interaction between Time and Diet. (P = 0.552)

The effect of different levels of GT does not depend on what level of Diet is present. There is not a statistically significant interaction between GT and Diet. (P = 0.164).

Resting Metabolic Rate (RMR) $p^{Genotype} < 0.001$
$p^{Diet} = 0.016$

Maximal Metabolic Rate (MMR) $p^{Genotype} < 0.001$
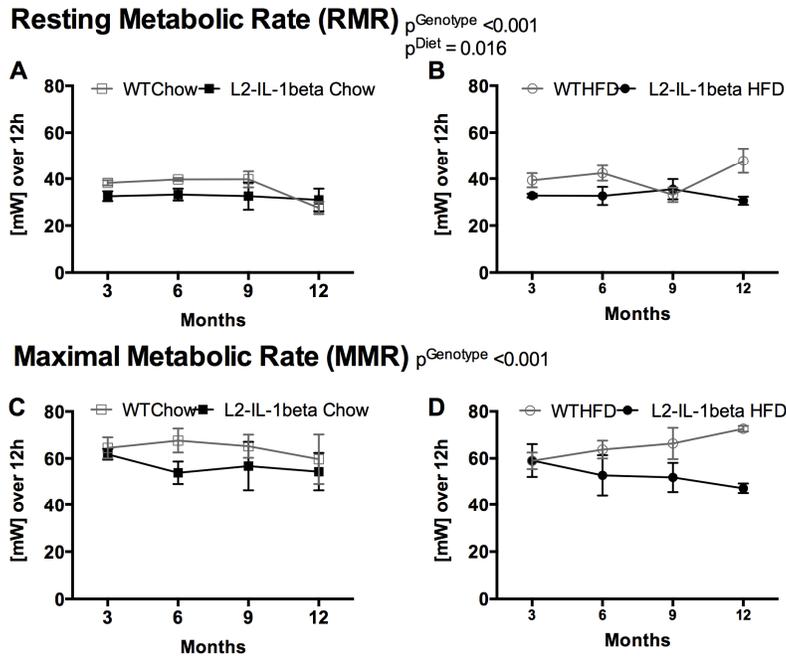
Appendix Figure 3.6.4: Energy consumption (indirect calorimetry) over the dietary intervention period (3- to 12-months) continued.
WT- and L2-mice on Chow and HFD were analyzed for energy consumption over 24hours (n=3). (A. B) Resting metabolic rate (RMR) and (C. D) maximal metabolic rate (MMR). Statistical analysis was performed using Three-way ANOVA and Holm-Sidak's multiple comparisons test. Refer to Appendix Table 3.6.5 for detailed statistical analysis. Data is separated by diet for better visualization.

Daily activity over 72 h
3months
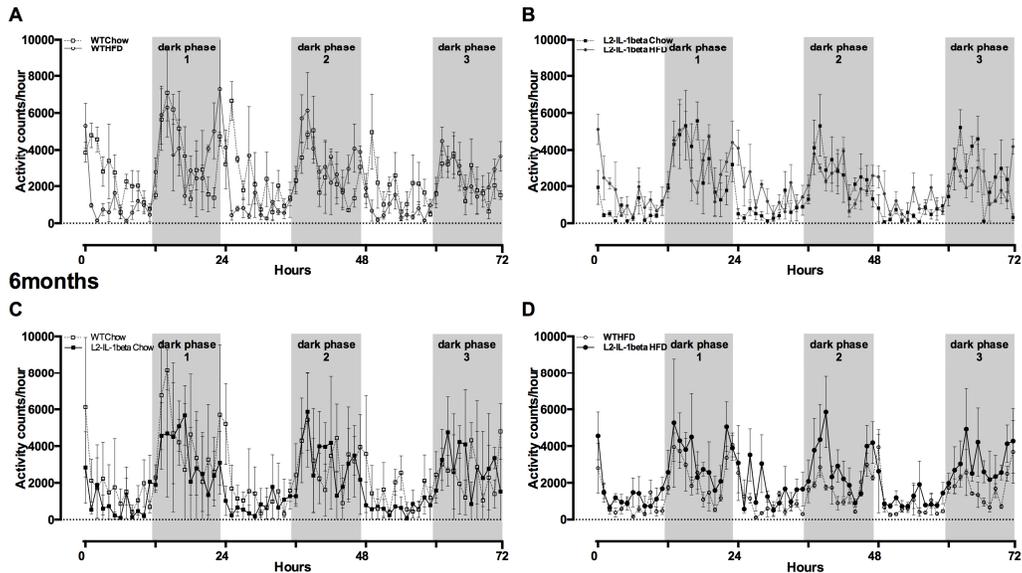
6months

Appendix Figure 3.6.5; Activity monitoring of WT- and L2-mice on Chow and HFD over a period of 72 hours.

At 3- and 6-months of age, the activity counts of WT- and L2-mice were assessed for changes in behavior. Graphs are separated based on diet for easier viewing. Grey regions represent the dark phase hours (17-5h).

Appendix Table 3.6.6: Activity monitoring

T**hree Way Analysis of Variance: Activity counts**
Balanced Design
Dependent Variable: Activity counts
Normality Test (Shapiro-Wilk)   Passed (P = 0.067)
Equal Variance Test: Passed (P = 0.731)

Source of Variation	DF	SS	MS	F	P
Time	2	21846042884.056	10923021442.028	6.138	0.007
GT	1	1067209113.361	1067209113.361	0.600	0.446
Diet	1	1350133784.028	1350133784.028	0.759	0.392
Time x GT	2	1656918155.389	828459077.695	0.466	0.633
Time x Diet	2	104853126.389	52426563.194	0.0295	0.971
GT x Diet	1	16723964148.028	16723964148.028	9.398	0.005
Time x GT x Diet	2	946097737.722	473048868.861	0.266	0.769
Residual	24	42707713649.333	1779488068.722		
Total	35	86402932598.306	2468655217.094		

The difference in the mean values among the different levels of Time are greater than would be expected by chance after allowing for the effects of differences in GT and Diet. There is a statistically significant difference (P = 0.007). To isolate which group(s) differ from the others use a multiple comparison procedure.

The main effects for GT cannot be properly interpreted since the size of the factor's effect depends upon the level of another factor.

The main effects for Diet cannot be properly interpreted since the size of the factor's effect depends upon the level of another factor.

The effect of different levels of Time does not depend on what level of GT is present. There is not a statistically significant interaction between Time and GT. (P = 0.633)

The effect of different levels of Time does not depend on what level of Diet is present. There is not a statistically significant interaction between Time and Diet. (P = 0.971)

The effect of different levels of GT depends on what level of Diet is present. There is a statistically significant interaction between GT and Diet. (P = 0.005)

It is to be noted that this data set failed for tests of normality (normal distribution) and equal variance, thus data was analyzed using a parametric Three-way ANOVA, details of the statistics are outlined below.

Three Way Analysis of Variance: Distance
Balanced Design
Dependent Variable: **Distance**
Normality Test (Shapiro-Wilk)   Failed   (P < 0.050)
Equal Variance Test: Passed (P = 0.980)

Source of Variation	DF	SS	MS	F	P
Time	2	16091027544.889	8045513772.444	4.107	0.029
GT	1	25303476993.778	25303476993.778	12.917	0.001
Diet	1	0.000	0.000	0.000	1.000
Time x GT	2	2810078160.889	1405039080.444	0.717	0.498
Time x Diet	2	0.000122	0.0000610	3.116E-014	1.000
GT x Diet	1	0.000122	0.000122	6.231E-014	1.000
Time x GT x Diet	2	0.000	0.000	0.000	1.000
Residual	24	47014926366.667	1958955265.278		
Total	35	91219509066.222	2606271687.606		

The difference in the mean values among the different levels of Time are greater than would be expected by chance after allowing for the effects of differences in GT and Diet. There is a statistically significant difference (P = 0.029). To isolate which group(s) differ from the others use a multiple comparison procedure.

The difference in the mean values among the different levels of GT are greater than would be expected by chance after allowing for the effects of differences in Time and Diet. There is a statistically significant difference (P = 0.001). To isolate which group(s) differ from the others use a multiple comparison procedure.

The difference in the mean values among the different levels of Diet are not great enough to exclude the possibility that the difference is just due to random sampling variability after allowing for the effects of differences in Time and GT. There is not a statistically significant difference (P = 1.000).

The effect of different levels of Time does not depend on what level of GT is present. There is not a statistically significant interaction between Time and GT. (P = 0.498)

The effect of different levels of Time does not depend on what level of Diet is present. There is not a statistically significant interaction between Time and Diet. (P = 1.000)

The effect of different levels of GT does not depend on what level of Diet is present. There is not a statistically significant interaction between GT and Diet. (P = 1.000)

Chapter 4

Following metabolic phenotyping of the L2-IL-1beta mouse model and detailing several behavioral aspects in terms of energy expenditure, food consumption, energy intake, excreted energy, and activity, the L2-IL1-beta mice on Chow and HFD were assessed in further detail to understand the progression of the BE/EAC disease state.

4.1 HFD Accelerates the Development Esophagitis, Barrett-Like Metaplasia and Dysplasia in the L2-model

In order to determine the level of progression of the disease state, macroscopic pictures of the stomach region were documented for all experimental animals sacrificed for assessment, Figure 4.1.1 A and Appendix Figure 4.12.1 serve as examples for each cohort. Furthermore a macroscopic scoring system was established based on percentage of inflammation in the regions of interest, taken in combination with the size of the macroscopic lesions and tumors as detailed in Chapter 2, Section 2.6. The esophagus and cardia regions of a total of 12 mice per cohort and diet were macroscopically scored at each time-point.

On a macroscopic level, the esophagus, squamous forestomach and cardia region of the L2-Chow mice appeared to be thickened and inflamed in comparison to age-matched WT-Chow mice that presented a smooth, un-inflamed overall normal appearance. Mice that were aged on HFD revealed a distinctly progressed phenotype. HFD appeared to accelerate the presence of visible tumors and lesions in number density and size in L2-mice These mice presented markedly thickened esophageal, squamous forestomach and cardia tissue at 9- and 12-months of age (Figure 4.1.1 A).

As can be seen in Figure 4.1.1 A, L2-HFD mice showed a visible increase in the appearance of lesions documented in the esophagus compared to mice on a Chow diet. Documented macroscopic observations show that starting at 3-months of age (Appendix Figure 4.12.1), L2-HFD mice began to present a thickened esophagus, with long regions of raised, inflamed tissue. As these HFD-mice aged to 6-, 9-, and 12-months of age, these tumors and lesions continued to
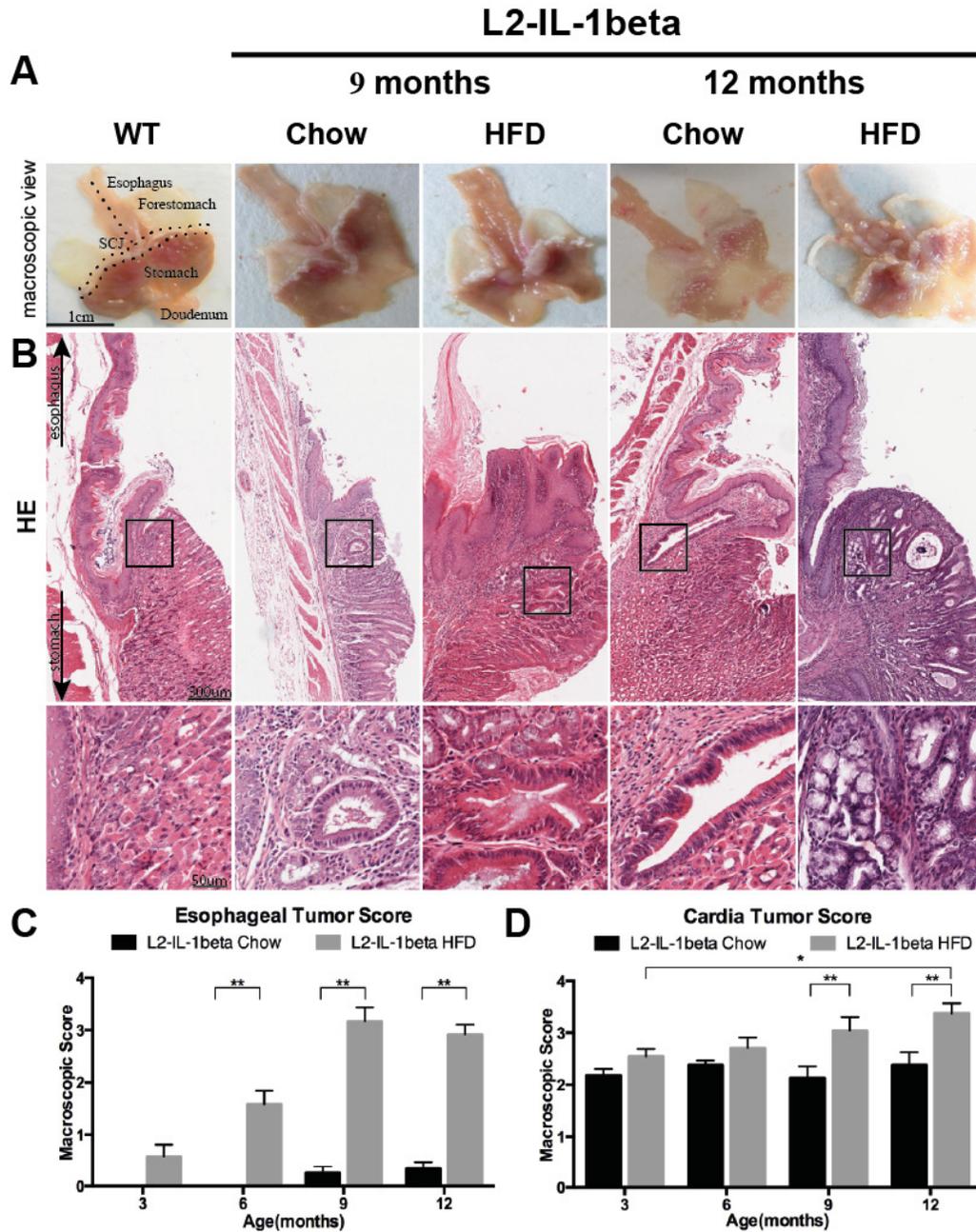
Figure 4.1.1: IL-1beta over-expression induced inflammation in the esophagus and cardia leading to the development of visible tumors and lesions in L2-mice on Chow and HFD.
Stomachs of WT and L2-IL-1beta mice showing the (A) macroscopic (scale bar 1cm) and (B) histological step-wise progression of BE to EAC through HE stainings, respectively (scale bar of larger panels, 500 µm, scale bar of smaller panels, 50 µm. (C, D) Quantification of visible lesions in the esophagus and cardia of L2-mice. All data are means ± standard deviation; group size remained constant (n=12). Statistical analysis was performed using two-way ANOVA and Sidak's multiple comparison's test. Asterisks indicate significant differences compared with control or between groups (****p≤0.0001, ***p≤0.001, **p≤0.01, *p≤0.05).

expand in size and number significantly as noted in Figure 4.1.1 C.

Beginning at 3-months of age, and continuing to 6-months of age, L2-Chow and – HFD mice presented with no significant differences in cardia lesions, however an increased trend was notable in the HFD cohort. At 9- and 12-months of age, the HFD cohort revealed significant acceleration of the disease, while the L2-mice on Chow appeared to show only a small, insignificant increase in their cardia tumor score. WT mice on both diets were also evaluated, however they revealed a completely normal phenotype, with 100% of WT animals attaining a macroscopic score of zero.
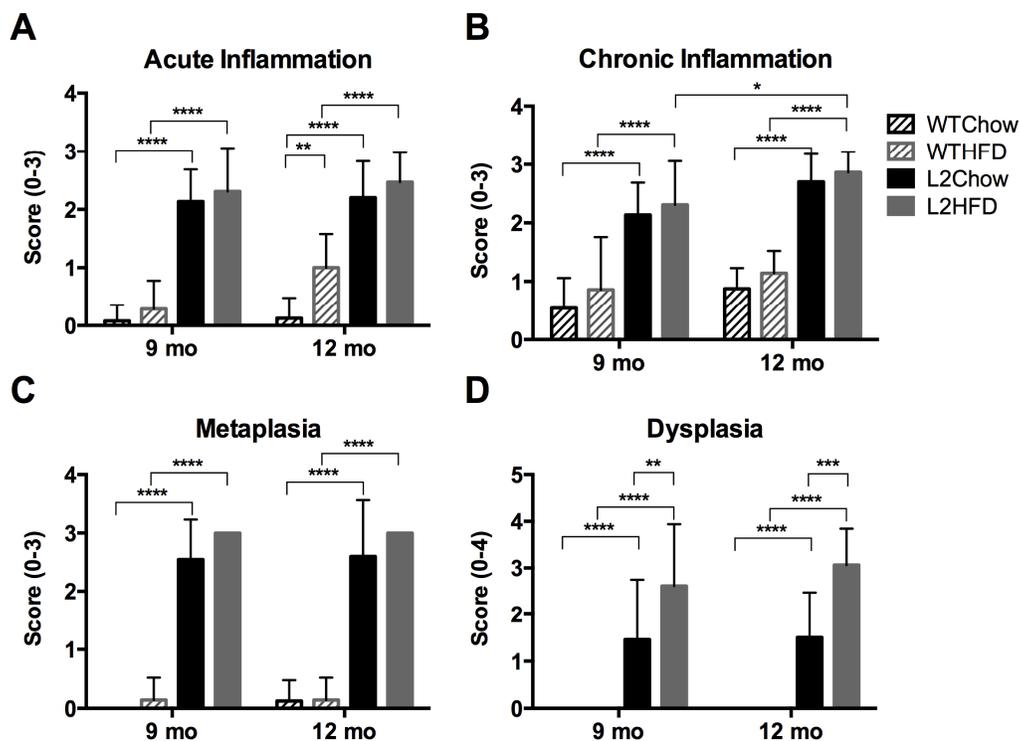
Figure 4.1.2: IL-1beta over-expression induced acute and chronic inflammation in the esophagus and cardia leading to the development of metaplasia and dysplasia in L2-mice on Chow an HFD.
Blinded histopathological scoring was conducted by a pathologist and medical doctor on sections of esophagus and cardia tissue from 9-and 12-month old WT and L2-IL-1beta mice on Chow and HFD. (A) Acute inflammation, (B) chronic inflammation, (C) metaplasia and (D) dysplasia in columnar and mucinous tissues were assessed using HE stained slides. All data are means ± standard deviation; group size varied (n=9-12 slides/ group (genotype and diet). Statistical analysis was performed using two-way ANOVA and Sidak's multiple comparison's test. Asterisks indicate significant differences compared with control or between groups (****$p \leq 0.0001$, ***$p \leq 0.001$, **$p \leq 0.01$, *$p \leq 0.05$).

To establish whether the L2-IL-1beta mouse model develops metaplasia and dysplasia as seen in the human disease state, histopathological evaluation was performed on sagittal sections through the esophagus and stomach. Based upon previously described criteria[146] a histopathological scoring system for the mouse SCJ was developed, detailed in Chapter 2, Section 2.8.7 and carried out in a blinded fashion by a pathologist and medical doctor.

This analysis revealed that major histopathological changes in the L2-IL-1beta mouse occurred in the esophagus and at the squamocolumnar junction, dually noted by the stepwise progression to BE and EAC observed in HE staining. Additionally, L2-HFD mice showed an accelerated histopathological progression, evident in mice aged 9- and 12-months, Figure 4.1.2.

In the 9- and 12-month cohorts, L2-mice on Chow and HFD presented no significant differences in acute inflammation in esophagus, SJC and stomach regions. Furthermore, while no significant differences were noted in L2-mice on Chow and HFD in terms of chronic inflammation, an increasing trend was noted in L2-HFD mice, with a significant increase between 9- and 12-month old L2-HFD mice going from average moderate inflammation scores to average severe inflammation scores, Figures 4.1.2 A, B. Metaplasia was observed in all L2-mice, with L2-HFD presenting with a high-score of "3" at both time-points, corresponding to multiple metaplastic glands, Figure 4.1.2 C. L2-Chow mice also presented with metaplasia but with lower average scores corresponding to single metaplastic glands interspersed along the SCJ. Importantly, analysis of dysplasia revealed a significant difference between L2-Chow and L2-HFD at both time-points, as noted in Figure 4.1.2 D. These higher score values corresponded with presentation of low- and high-grade dysplasia resulting from HFD, while L2-Chow mice mostly presented with superficial epithelial atypia or in some cases atypia in glanular complexity. It is to be noted that WT-Chow and –HFD mice were also scored simultaneously but presented only with mild inflammation and no metaplasia; rare-mucus cells were occasionally noted in some older WT-mice. Lastly, none of the WT-mice presented with any forms of dysplasia.

4.2 Increased Development of Metaplasia and Mucus Producing Cells in L2-IL-1beta Mice on HFD

Mucinous cells can be characterized using mucin histochemistry and columnar cells of the gastric and intestinal regions contain Periodic acid-Schiff-positive (PAS+) neutral mucins (Figure 4.2). It is important to note that Alcian-blue-positive acidic mucins are primarily found in goblet cells of the intestinal type of metaplasia. While classical goblet cells are not observed in the L2-IL-1beta model, the mucus producing columnar cell types observed in L2-mice in Figure 4.2 A were consistent with Barrett-like metaplasia [89, 147]. All of the L2-mice (regardless of diet) between 9- and 12-months of age presented with mucus producing (PAS+) cells at the SCJ, similar to human BE.

It appeared that both diet cohorts of L2-mice presented with more PAS+
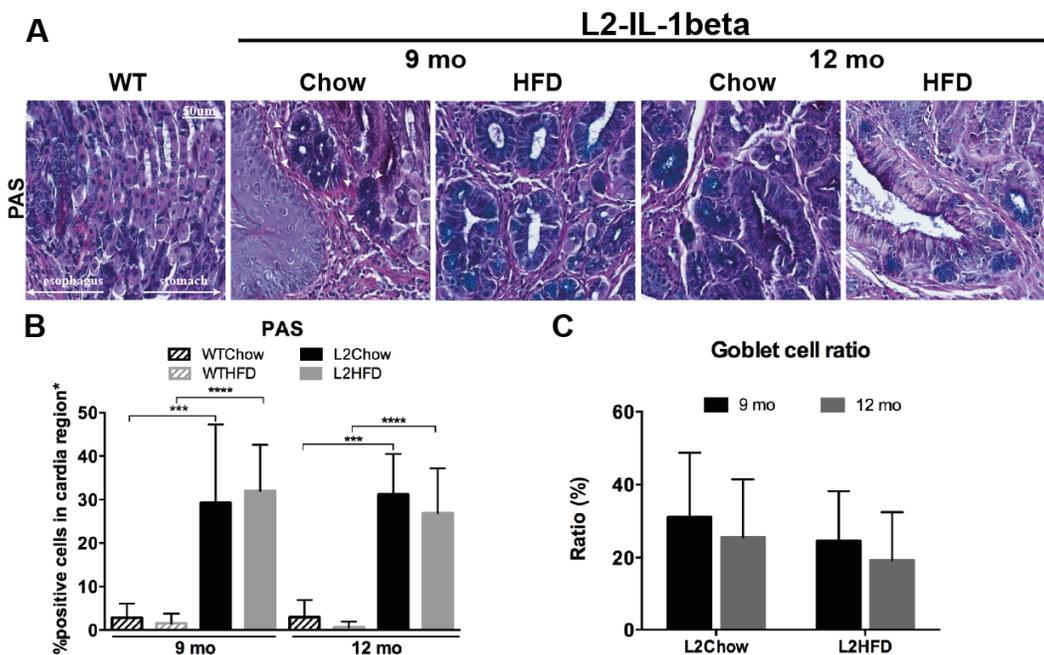
Figure 4.2: Mucus producing cells and goblet cell ratio appear to decrease over time in L2-HFD mice.
(A) PAS staining was carried out on 9- and 12-month old WT and L2-IL-1beta mice (scale bar, 50 μm). (B) Quantification of PAS+ cells in the cardia region of L2-IL-1beta mice on Chow and HFD were compared to WT mice on Chow and HFD. (C) Quantification of goblet cell ratios in the cardia region of L2-IL-1beta mice on Chow and HFD, group size (n=5-8). All data are means ± standard deviation. Statistical analysis was performed using one-way (B) and two-way ANOVA and Sidak's multiple comparisons test. Asterisks indicate significant differences compared with control or between groups (****$p \leq 0.0001$, ***$p \leq 0.001$, **$p \leq 0.01$, *$p \leq 0.05$).

mucinous cells in comparison to WT-mice. Quantification in terms of percentage (%) of the cardia region with PAS+ cells showed that in L2-Chow mice, there appeared to be no changes between 9- and 12-months of age. L2-HFD mice on the other hand, showed a trend towards decreasing % of PAS+ cells over time, Figure 4.2 B.

 Furthermore, quantification of goblet cells in the cardia region with Alcian blue+ cells showed no significant differences between L2-Chow and –HFD mice. However, observations revealed that L2-Chow mice presented with slightly higher goblet cell ratios compared to L2-HFD mice (Figure 4.2 C). Furthermore, goblet cell ratios appeared to decrease as the mice aged, and the disease phenotype increased in both diet groups. It is important to note that WT–mice occasionally presented with goblet cells, this was rare and insignificant.

These findings suggest that HFD and the acceleration of the phenotype result in a decrease in mucinous metaplasia and goblet ratio as the disease progresses in severity.

4.3 Inflammation Onset by HFD Leads to Increased Proliferation During the Development of Metaplasia in the L2-IL-1beta Model

Over all proliferation was assessed with Ki67 IHC staining. Ki67 is a nuclear protein that is expressed strictly in association with cell proliferation[132]. It is widely used as a pathological proliferation marker to measure the growth fractions in human and murine tumors[148].
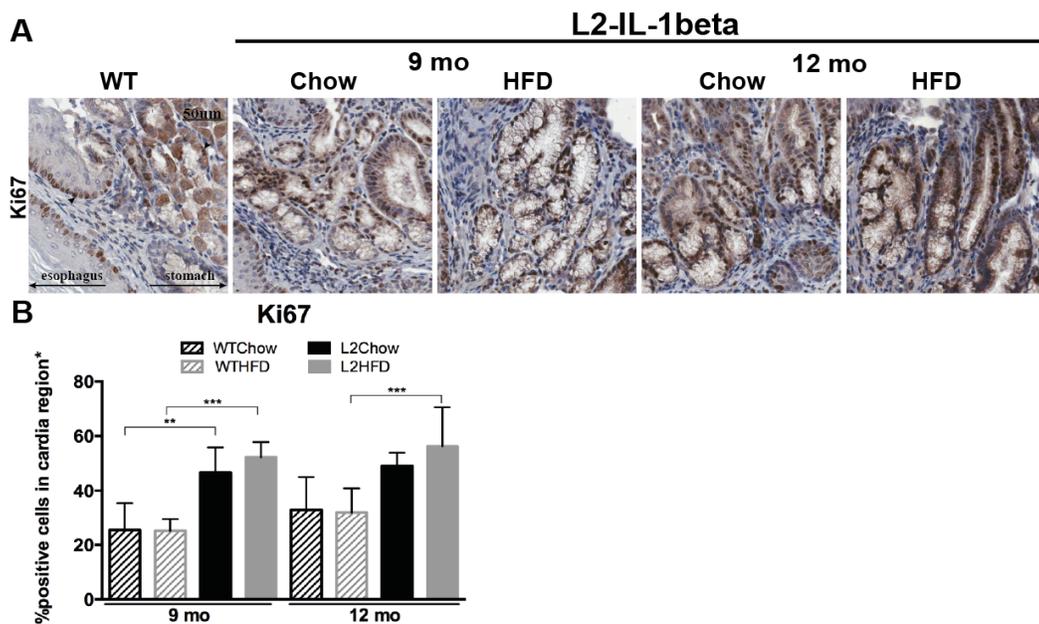
Figure 4.3: Proliferation in the cardia region of L2-mice on Chow and HFD.
(A) Ki-67staining was carried out on 9 - and 12-month old WT and L2-IL-1beta mice (scale bar, 50 μm). (B) Quantification of Ki67+ cells in the cardia region of L2-IL-1beta mice on Chow and HFD were compared to WT mice on Chow and HFD. All data are means ± standard deviation. Group size (n=5-8). Statistical analysis was performed using two-way ANOVA and Sidak's multiple comparisons test. Asterisks indicate significant differences compared with control or between groups (****$p \leq 0.0001$, ***$p \leq 0.001$, **$p \leq 0.01$, *$p \leq 0.05$).

It was expected that the accelerated phenotype observed with the introduction of a HFD would result in increased proliferation. As noted in Figure 4.3 B, quantification of proliferation in the cardia region based on percentage of Ki67+ staining did not show a significant difference between diets and ages directly, however L2-HFD showed an increasing trend in proliferation from 9- to 12-

months of age. WT-mice on both diets showed much lower proliferation at both time points.

4.4   HFD   Induces   Changes   in   the   Immune Microenvironment in BE in the L2-IL-1beta Model

It has been well reported that leukocytes play a major role in the development of a cancer promoting microenvironment[149]. Malignant cells recruit myeloid cells, including myeloid-derived suppressor cells (MDSCs), neutrophils, monocytes and macrophages into the tumor microenvironment where they begin to acquire a more pro-invasive and immunosuppressive phenotype[150]. Tu and colleagues previously suggested the importance of myeloid cell recruitment in the development of neoplasia in a similar model of IL-1beta induced carcinogenesis [151].

To understand the influence of HFD on IL-1beta mediated inflammation and carcinogenesis, in particular the role of inflammatory cells in the high fat setting, the distribution of leukocytes in the esophagus, forestomach and cardia (hence forth referred to as "cardia") at 12-months of age in the L2-IL-1beta model was examined.

In 12-month-old L2-IL-1beta mice presenting with low- and high-grade dysplasia resulting from HFD, a significantly increases recruitment of neutrophil (CD45+CD11B+F480-Ly6G+) (Figure 4.4.1 A, B) in esophageal tissue was observed by flow cytometry. Additionally, there was a significant accumulation of immature myeloid cells (IMC) (CD45+CD11b+Ly6G^{low}Ly6C+) in esophageal tissue (Figure 4.4.1 C, D). CD4+CD4+ T-helper cells revealed an increasing trend in L2-HFD-mice.

No   significant   changes   in   the   accumulation   of   macrophages (CD45+CD11B+F4/80+Ly6G-),   CD3+CD8+   cytotoxic   T-cells,   NKT   cells (CD3+CD4-CD8-NK1.1+)   and   gamma   delta   T-cells   (CD3+CD4-CD8-gdTCR+) (Appendix Figure 4.12.2 B-E, I-L) were noted. In the cardia region, neutrophils, macrophages and T-cell populations remained similar between diets (Appendix Figure 4.12.2 A, F-H).

To verify observations made from flow cytometry analysis, esophageal and cardia tissue from 12-month old mice on Chow and HFD were stained for immune cells of interest, including macrophages (F480), Ly6C (monocytes) and Ly6G (neutrophils) (Figure 4.4.2 A, C, E). Quantification of immune cells revealed

an increased presence of these immune cells predominantly in esophageal tissue, with low abundance in cardia. F480 and Ly6C positive cells appeared in higher abundance in L2-HFD mice in comparison to L2-Chow mice in esophageal tissue (Figure 4.4.2 B, D, F; cardia tissue staining: Appendix Figure 4.12.2 M). Ly6G staining for neutrophils appeared to be significantly increased in 12-month old L2-HFD mice compared to L2-Chow mice; this observation was only noticeable in the esophagus, in agreement with flow cytometry analysis (Figure 4.4.2 F). These findings are indicative of a key role for neutrophils in the development of the immune microenvironment seen in the accelerated phenotype of L2-HFD mice.
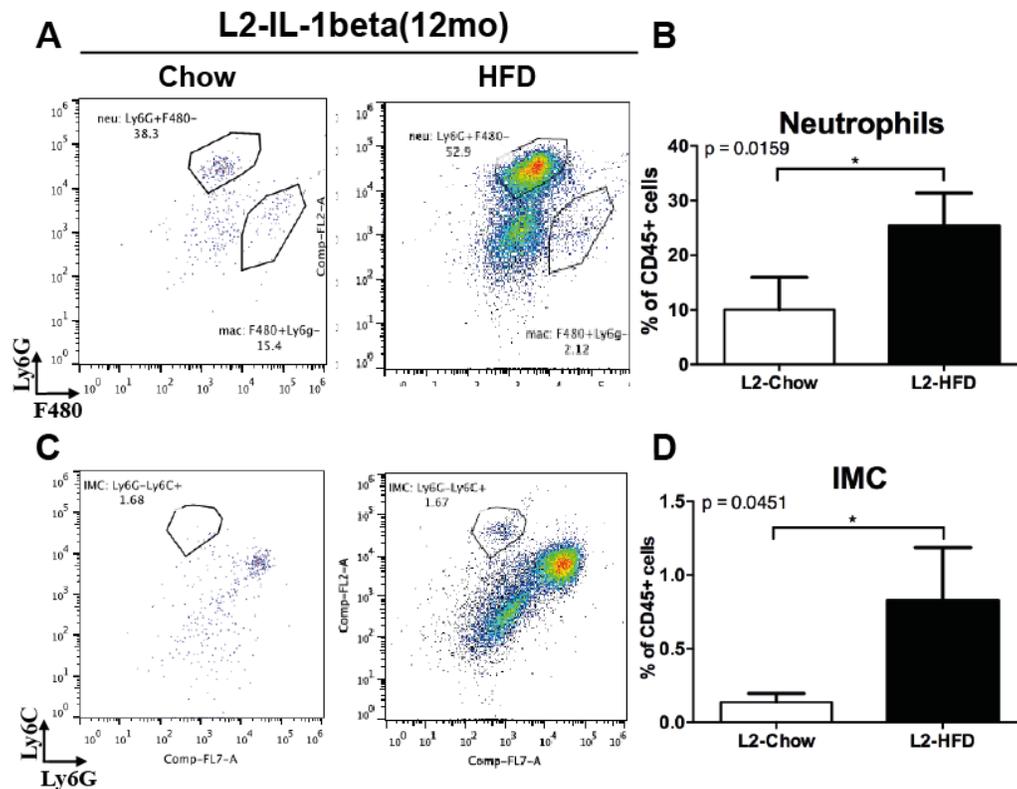
Figure 4.4.1: HFD accelerates immune cell accumulation, specifically neutrophil populations in the esophagus of L2- IL-1beta mice.
(A, B) Neutrophils and (C, D) immature myeloid cells (IMCs) from the esophagus and cardia regions of 12-month old L2-mice on Chow and HFD were analyzed by flow cytometry. All data are means ± standard deviation. Statistical analysis was performed using Student's t-test. Group size (n=3-4), p-value noted beside graphs.
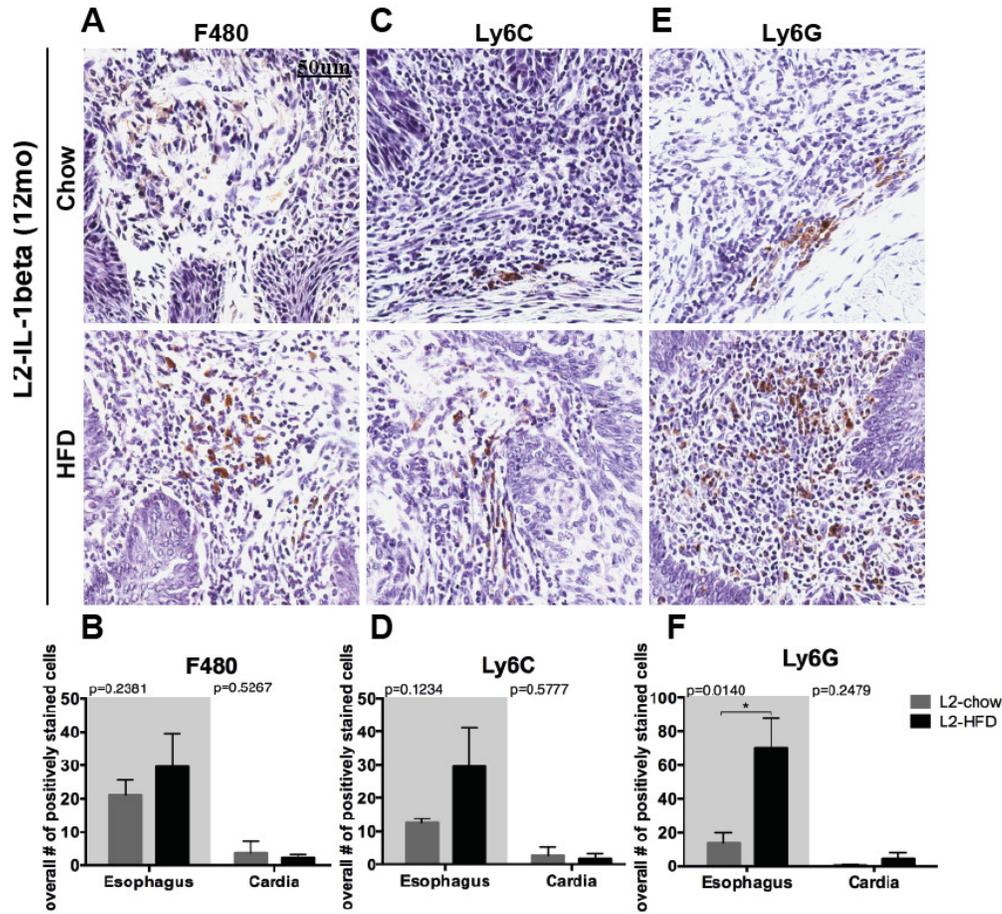
Figure 4.4.2: HFD accelerates immune cell accumulation, specifically neutrophil populations in the esophagus of L2-mice on Chow and HFD.
(A, B) Neutrophils and (C, D) immature myeloid cells (IMC) from the esophagus and cardia of 12-month old L2-IL-1beta mice on Chow and HFD diet were analyzed by flow cytometry. All data are means ± standard deviation. Statistical analysis was performed using Student's t-test. Group size (n=3-4), p-value noted beside graph.

4.5 HFD Increases Smooth Muscle Differentiation in L2-IL-1beta Mice

In order to assess whether HFD exerted an impact on differentiation of cells in the cardia region, alpha smooth muscle actin (aSMA) staining was conducted. aSMA is a universal marker of smooth muscle differentiation, and is useful in evaluating the switch from fibroblasts to myofibroblast[152].
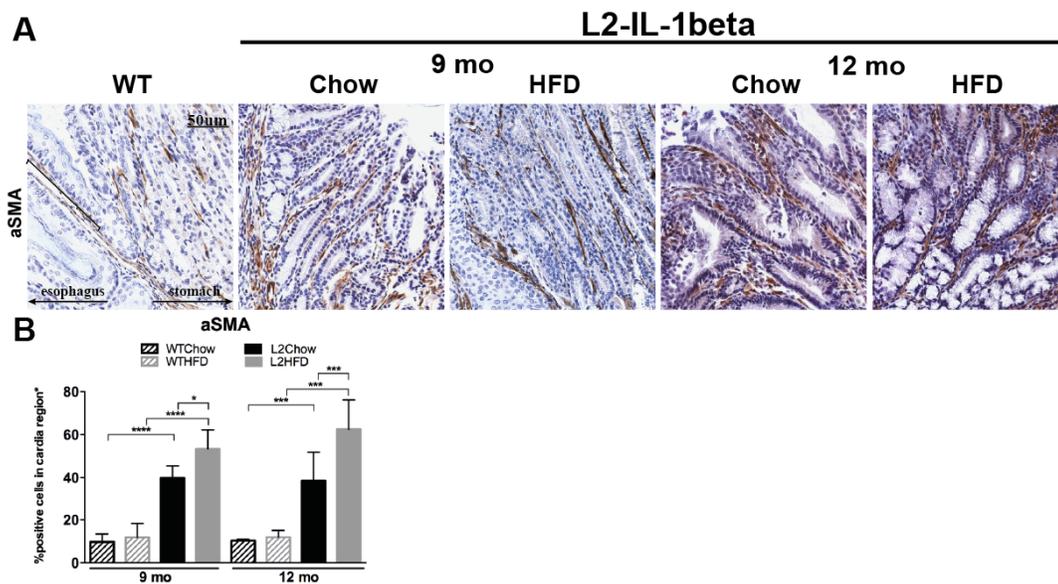
Figure 4.5: L2-mice on HFD showed increased smooth muscle differentiation in cardia tissue.
(A) aSMA staining was carried out on 9- and 12-month old WT and L2-IL-1beta mice (scale bar, 50 μm). (B) Quantification of aSMA-positive cells in the cardia region of WT- and L2-mice on Chow and HFD were compared. All data are means ± standard deviation. Statistical analysis was performed using two-way ANOVA and Sidak's multiple comparisons test. Group size remained constant (n=6). Asterisks indicate significant differences compared with control or between groups, ****$p \leq 0.0001$, ***$p \leq 0.001$, **$p \leq 0.01$, *$p \leq 0.05$.

Figure 4.5 illustrates the percentage (%) of positive aSMA cells in the cardia region of 9-and 12-month old L2-IL-1beta mice on Chow diet or HFD quantified from the assessment of 3-4 regions of esophagus/ stomach tissue per mouse; 5-8 mice were assessed per genotype and diet time-point. Furthermore, during this stepwise progression to cancer, a gradual increase in aSMA+ stromal myofibroblasts was observed in L2-Chow mice compared to WT-mice, the onset of a HFD further accelerated an increase in myofibroblasts in L2-mice (Figure 4.5

A), consistent with other models of inflammation-induced cancer [153]. Moreover, quantification of aSMA+ cells in the cardia region of the L2-mice on Chow and HFD diet showed an increasing trend with disease progression, (Figure 4.5 B).

The increase in aSMA localization in L2-HFD mice compared to L2-Chow mice might be a result of a more pro-tumorigenic microenvironment resulting from HFD.

4.6 Induces Changes in Esophagus and Cardia Tissue on an RNA Level

In the L2-model, it was observed that HFD accelerated esophageal tumor progression while resulting a unique phenotype (Chapter 4.1 - 4.5 and Chapter 3 respectively) characterized by low body weight, while influencing the immune microenvironment composition. To further investigate the mechanisms underlying this effect, it was pivotal to identify alterations induced by HFD in tissues of interest in L2-mice. While it is understood that adipose tissue can secrete a wide variety of growth factors and cytokines that are associated with tumor progression. It is also known that HFD can trigger the secretion of similar tumor associated growth factors[154, 155]. Given that L2-HFD mice had exceptionally low to negligible overall fat mass, the next step was to assess changes in gene expression in esophageal and cardia tissue.

4.6.1 Microarray Analysis

To further understand the molecular mechanisms underlying cell cycle control, tumor cell metabolism, apoptosis and tumor cell survival in the L2-model it was imperative to get a snapshot of the transcriptional activity in the cardia region of these L2-mice. Therefore, microarray technology was used to characterize gene expression in response to the HFD stimulus in the L2-model.

Transcriptional profile analysis was carried out as described in Section 2.7.2 using tissue with typical metaplastic and dysplastic lesions from the cardia region in 12-month old L2-Chow and –HFD mice and executed on an Affymetrix array.

A number of gastric and intestinal genes were significantly upregulated in the L2-IL-1beta model on Chow and –HFD, in addition to genes associated with HFD and carcinogenesis. Initial data processing was carried out by project collaborator and bioinformatician Dr. Richard Friedman, Columbia University, NY, USA. Data sets were further filtered by defining genes as being significantly differentially expressed as a result of genotype or diet if they exhibited >1.5 fold increase in gene expression or <0.65 fold decrease compared to genotype or diet controls; p-values were <0.05 in combination with the afore mentioned cutoffs.

Comparing the effect between the WT and L2-mice on Chow diet resulted in a total of 369 genes that were identified as differentially regulated. The gene set was further sorted based on genes associated with HFD and carcinogenesis that would be of primary interest given the observed phenotype. Resulting in 31 genes that were up-regulated and 26 genes that were down-regulated in the L2-model after adjusting for a p-value of <0.5 (Appendix Table 4.12.2).

When comparing the effect of the HFD on the L2-IL-1beta model, a total of 595 genes were identified as differentially regulated, based on the fold change cutoffs. Following filtering for genes associated with HFD and carcinogenesis, 32 were up regulated and 26 were down regulated in the L2-HFD model. Table 4.6.1 (detailed version in Appendix Table 4.12.2) highlights these genes of interest based on up- or down-regulation in addition to gene function. Up-regulation was primarily observed in genes encoding for cytokines (IL1b, IL17c, Wnt2b, Angpt2), chemokines (Cxcl13, Ccl2, CcL7, Ccl11, Ccl8, Ccl9), and their receptors (IL1ra, Csf1r, Cxcr4, Ccr5, Ccr2, Ccr7), extracellular enzymes/ molecules (Mmp7, Mmp10, Mmp25, Mmp12), translation, transcription and RNA processing (Hspa1a, Hspa1b), cell viability (Igf1, Igfbp4), receptor and cell adhesion and signaling (Tlr13, Tlr8, Ctsk, Mrc1, Vcam1), intracellular transport (Vim, Itga4, Ctsl). Functionality of genes observed to be down regulated was involved with cytokines and their receptors (IL20ra, Wnt7b), extracellular enzymes (Krt7, Muc2) and cell viability (Egf).

In pathway analysis using the BIOCARTA database, these transcripts were enriched for intracellular and vascular adhesion molecules, adherens junctions, tight junctions, chemokines and cytokines that stimulate proliferation and differentiation of various hematopoietic cell types. Appendix Table 4.12.4 features a list of the pathways of interest and a brief description.

These results were consistent with a role for HFD in promoting metaplasia and dysplasia by increased inflammation. Several key genes listed in Table 4.6.1 that are involved in promoting inflammation, tumor microenvironment and proliferation were selected and their gene expression in esophageal and/ or cardia tissue from L2-IL-1beta mice on Chow or HFD was quantified by RT-PCR to confirm the results of the Affymetrix array.

Table 4.6.1: Selected genes up- and down-regulated as a result of HFD in the L2-IL-1beta model.

(Based on cut-offs of fold changes >1.5 or <0.65 and p-values of <0.5. Gene function details in Appendix Table 4.11.2)

L2-HFD v. L2-Chow

Up-regulated	Symbol	Description	FC	P.Value
	Il1b	interleukin 1 beta	2.8931	0.0191
	Il17c	interleukin 17C	2.2093	0.0098
Cytokines & their receptors	Il2ra	interleukin 2 receptor, alpha chain	1.6505	0.0036
	Csf1r	colony stimulating factor 1 receptor	1.5206	0.075
	Wnt2b	wingless-type MMTV integration site family, member 2B	1.7256	0.0078
	Angpt2	angiopoietin 2	1.9333	0.0108
	Cxcl13	chemokine (C-X-C motif) ligand 13	3.613	0.0226
	Cxcr4	chemokine (C-X-C motif) receptor 4	1.8898	0.0073
	Ccl2	chemokine (C-C motif) ligand 2	2.6368	0.0366
	Ccl7	chemokine (C-C motif) ligand 7	2.4657	0.0148
Chemokines & their receptors	Ccl11	chemokine (C-C motif) ligand 11	2.2577	0.0024
	Ccr5	chemokine (C-C motif) receptor 5	1.8987	0.0325
	Ccr2	chemokine (C-C motif) receptor 2	1.8705	0.0208
	Ccl8	chemokine (C-C motif) ligand 8	1.8153	0.0184
	Ccr7	chemokine (C-C motif) receptor 7	1.7321	0.0289
	Ccl9	chemokine (C-C motif) ligand 9	1.5162	0.0537
Extracellular enzymes/ molecules	Mmp7	matrix metallopeptidase 7	3.5151	0.0132
	Mmp10	matrix metallopeptidase 10	1.8903	0.0464
	Mmp25	matrix metallopeptidase 25	1.5596	0.0411
	Mmp12	matrix metallopeptidase 12	1.5577	0.0238
Transcription, translation & RNA processing	Hspa1a	heat shock protein 1A	2.1531	0.0116
	Hspa1b	heat shock protein 1B	1.7076	0.0227
Cell viability	Igf1	insulin-like growth factor 1	1.5851	0.0283
	Igfbp4	insulin-like growth factor binding protein 4	1.696	0.006
	Tlr13	toll-like receptor 13	1.8489	0.0262
Receptors & cell adhesion/ signaling	Tlr8	toll-like receptor 8	1.691	0.0151
	Ctsk	cathepsin K	1.9414	0.0093
	Mrc1	mannose receptor, C type 1	2.4725	0.0097
	Vcam1	vascular cell adhesion molecule 1	1.5512	0.026
Intracellular transport	Vim	vimentin	1.655	0.0301
	Itga4	integrin alpha 4	1.5864	0.0315
	Ctsl	cathepsin L	1.4991	0.0553

L2-HFD v. L2Chow

Down-regulated	Symbol	Description	FC	P.Value
Cytokines & their receptors	Il20ra	interleukin 20 receptor, alpha	0.594	0.049
	Wnt7b	wingless-type MMTV integration site family, member 7B	0.6538	0.0209
Extracellular enzymes/ molecules	Krt7	keratin 7	0.6223	0.021
	Muc2	mucin 2	0.4981	0.0274
Cell viability	Egf	epidermal growth factor	0.5443	0.0076

4.6.2 Real-Time PCR

Real-time PCR (RT-PCR) was used to identify possible changes in transcriptional activity in esophageal and cardia tissue observed in L2-mice on Chow and HFD and to verify differentially regulated genes of interest from the micro array results. As detailed in Sections 2.2.3 and 2.7.1, RNA was isolated from tissue with typical metaplastic and dysplastic lesions areas from the cardia region. RT-PCR analysis of esophageal and cardia tissue of L2-Chow and -HFD mice harboring low and high-grade metaplasia at 9- and 12-month of age showed interesting changes in the expression of several inflammatory cytokines/ chemokines, chemotactic proteins and secreted signaling proteins, and genes associated with degradation of the extracellular matrix.

Starting with genes involving extracellular enzymes and molecules, several genes of the Mmp family were selected including Mmp7 and Mmp10, which appeared to be up regulated on the Affymetrix array in L2-HFD mice, in addition to Mmp3 (Figure 4.6.2.1 A-E). In the esophagus, RT-PCR quantification showed Mmp3 and Mmp7 to be significantly up regulated in L2-HFD mice. In the cardia however, Mmp3 and Mmp10 appeared to be significantly increased only in 9-month old L2-HFD mice, while Mmp7 appeared to be significantly up-regulated in L2-Chow mice at 9-months of age and remained unchanged in L2-HFD from 9- to 12-month time points. Mmp10 was significantly higher in L2-HFD mice at 9-months of age and showed an increasing trend in the L2-HFD mice at 12-months of age).

Genes from the Wnt family were selected due to their involvement in the development of carcinogenesis, including Wnt2, Wnt2b, Wnt3a, Wnt5a, Wnt5b and Wnt7b (Figure 4.6.2.2 A-C). Interestingly, in the esophagus, Wnt2 and Wnt5a expression appeared to be significantly higher in L2-Chow fed mice. Wnt3a however had a different expression profile, appearing to be expressed in significantly higher levels in L2-HFD mice than in L2-Chow mice (Figure 4.6.2.2 C). Expression of these genes of interest was rather varied in the cardia (Figure 4.6.2.3 A-E). Wnt2 showed significantly increased expression in the L2-HFD at 12-months of age, this was observed with a trend of increase over time in the L2-model independent of diet. Wnt5a showed overall higher expression in the L2-Chow mice compared to L2-HFD mice; an increasing trend over time was

observed in both groups. While not significantly different, Wnt2b showed overall high expression in L2-HFD mice, however this observation was accompanied by no change over time.

Mmp family

Esophagus

Cardia (9 &12mo)
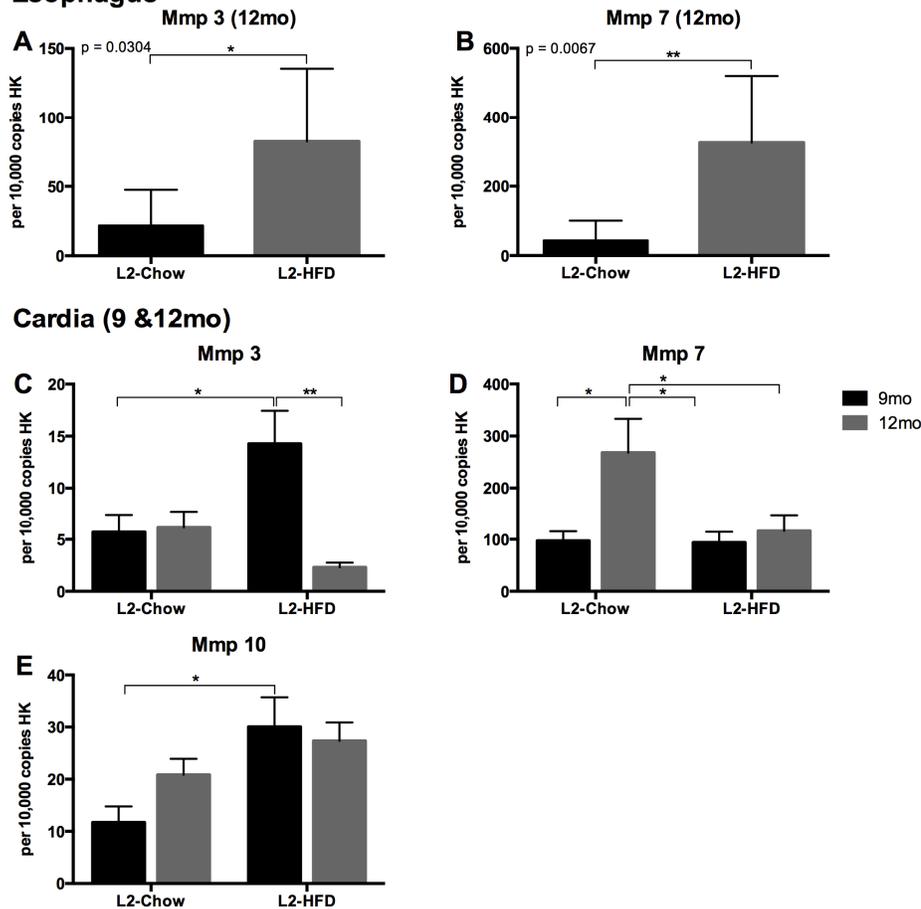
Figure 4.6.2.1: The influence of HFD on the Mmp-family in the L2-IL-1beta mouse model.

mRNA expression in the esophagus of L2-mice on Chow and HFD (A) Mmp3 and (B) Mmp7 in 12-month old L2-mice were quantified using RT-PCR. Group size (n=3-6). mRNA expression in the cardia of L2-mice on Chow and HFD(C) Mmp3 (D) Mmp7 and (E) Mmp10 were quantified using RT-PCR. Group size remained constant (n=6). All data are means ± standard deviation. Statistical analysis was performed using Student's t-tests where p-value is noted or two-way ANOVA and Sidak's post hoc-test, asterisks indicate significant differences compared with control or between groups, ****p≤0.0001, ***p≤0.001, **p≤0.01, *p≤0.05.

Wnt 5b also showed no significant differences between the groups while Wnt3a appeared to be expressed at higher levels at 9-months in both L2 groups; with L2-HFD Wnt3a expression being significantly higher at 9-months over 12-months.

Furthermore, assessment of other cytokines of interest including Ccr2, Csf1 AND Cxcr4 revealed no significant differences based on diet in the L2-model (Figure 4.6.2.4 A-C). Ccr2 in the cardia region appeared unchanged over time and by diet. Csf1 showed a slight decreasing trend over time in both L2 diet groups. Cxcr4 appeared to be increasing over time in both L2 diet groups; L2-HFD mice showed a higher trend in Cxcr4 levels compared to L2-Chow.

Wnt family
Esophagus
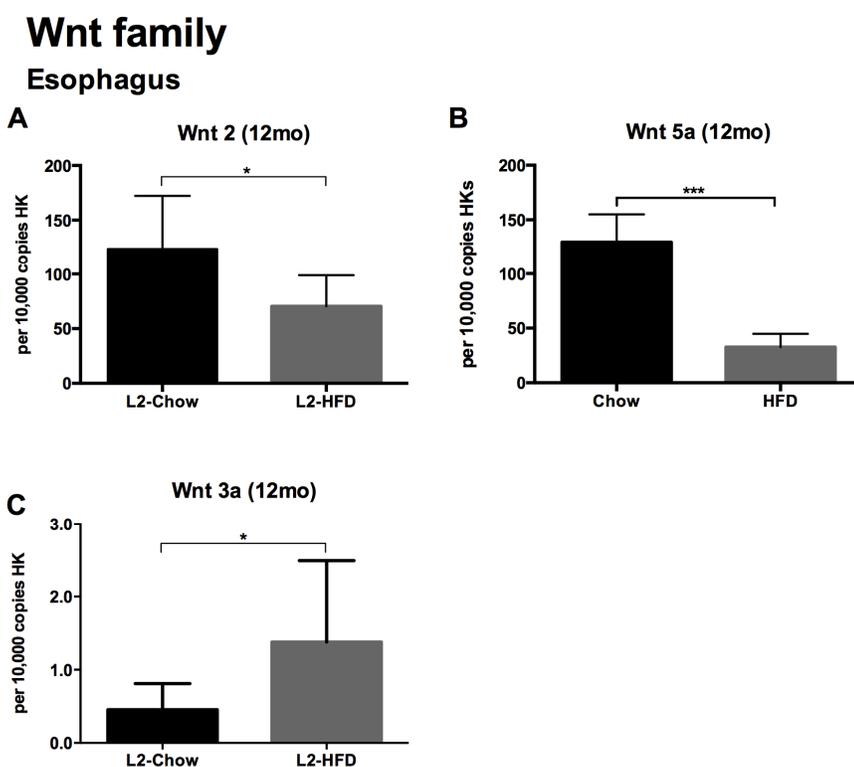
Figure 4.6.2.2: The influence of HFD on the Wnt-family in the esophagus of L2-mice.
mRNA expression in the esophagus of L2-mice on Chow and HFD (A) Wnt2 and (B) Wnt5a and (C) Wnt3a in 12-month old L2-mice were quantified using RT-PCR. Group size (n=3-6). All data are means ± standard deviation. Statistical analysis was performed using Student's t-tests where p-value is noted or two-way ANOVA and Sidak's test, asterisks indicate significant differences compared with control or between groups, ****p≤0.0001, ***p≤0.001, **p≤0.01, *p≤0.05

Wnt family

Cardia (9 &12mo)
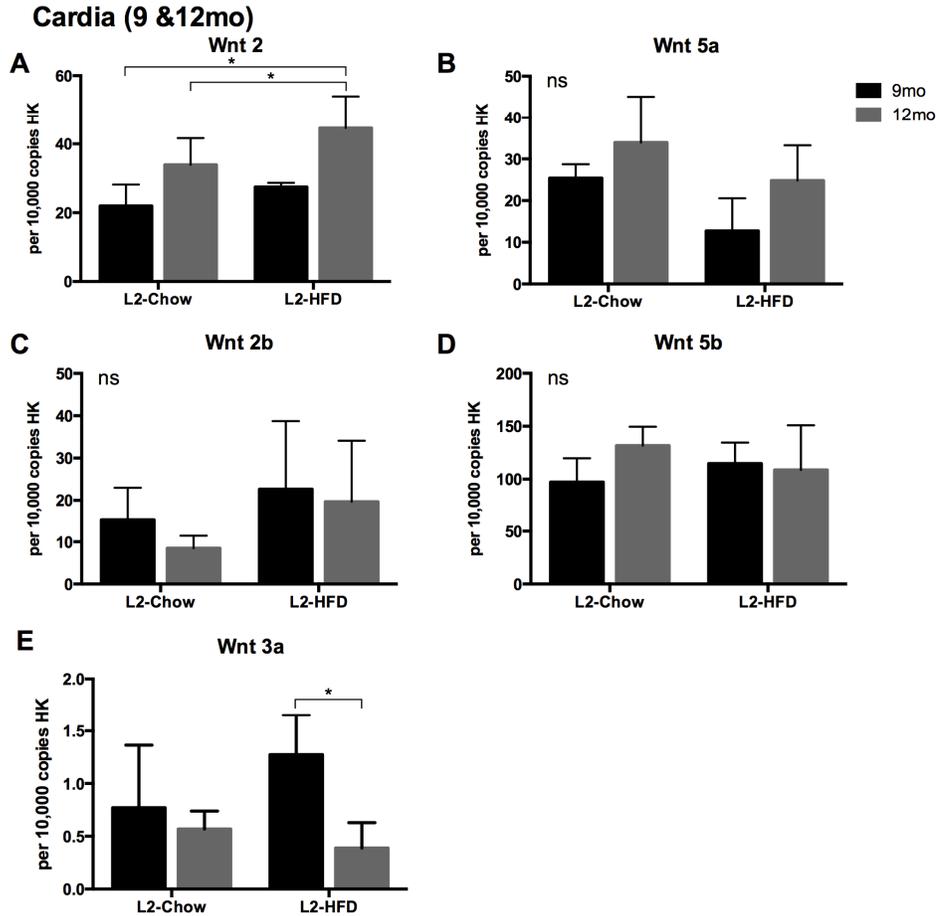
Figure 4.6.2.3: The influence of HFD on the Wnt-family in cardia region of L2-mice.

mRNA expression in the cardia of L2-mice on Chow and HFD (A) Wnt2, (B) Wnt5a, (C) Wnt2b, (D) Wnt5b, (E) Wnt3a in 9- and 12-month old L2-mice were quantified using RT-PCR. Group size remained constant (n=6). All data are means ± standard deviation. Statistical analysis was performed using Student's t-tests where p-value is noted or two-way ANOVA and Sidak's test, asterisks indicate significant differences compared with control or between groups, ****p≤0.0001, ***p≤0.001, **p≤0.01, *p≤0.05.

Cardia (9 &12mo)
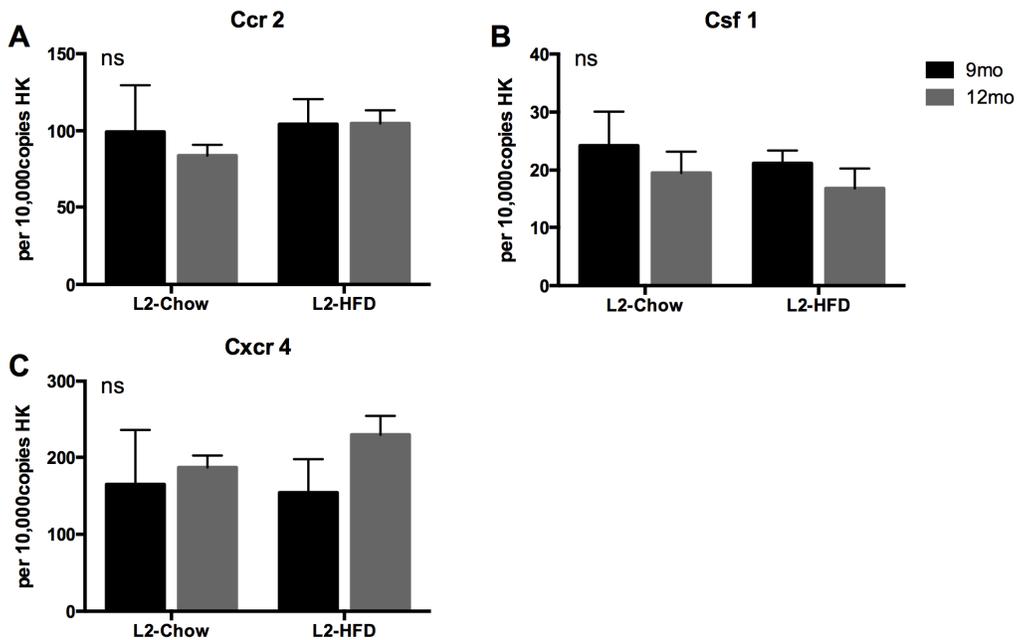
Figure 4.6.2.4: The influence of HFD on other cytokines the cardia of L2-mice.
mRNA expression in the cardia of L2-mice on Chow and HFD(A) Ccr2 (B) Csf1 and (C) Cxcr4 were quantified using RT-PCR. Group size remained constant (n=6). All data are means ± standard deviation. Statistical analysis was performed using Student's t-tests where p-value is noted or two-way ANOVA and Sidak's test, asterisks indicate significant differences compared with control or between groups, ****p≤0.0001, ***p≤0.001, **p≤0.01, *p≤0.05.

Using gene set enrichment analysis (GSEA) for pathways analysis revealed several hits for the chemokine IL-8, a myeloid chemoattractant (Appendix Table 4.12.3), this was of high interest since more neutrophils appeared to be recruited in the esophagus as a result of the HFD as noted from flow cytometry analysis (Section 4.4). Since mice do not express IL-8, KC, a functional murine homologue of IL-8, also known as Cxcl1, along with its receptors Cxcr1 and Cxcr2 were further analyzed by RT-PCR (Figure 4.6.2.5).

A significant up-regulation of KC was observed, upon chronic HFD, in the L2 model in comparison to WT-HFD mice at 9- and 12-months of age. Both groups of WT-mice showed very low expression of the chemokine. Additionally, the L2-Chow mice showed a significantly lower expression of KC in the esophagus and the cardia regions in comparison to L2-HFD mice.

Esophagus (12mo)

Cardia (9 & 12mo)

Cardia (12mo)
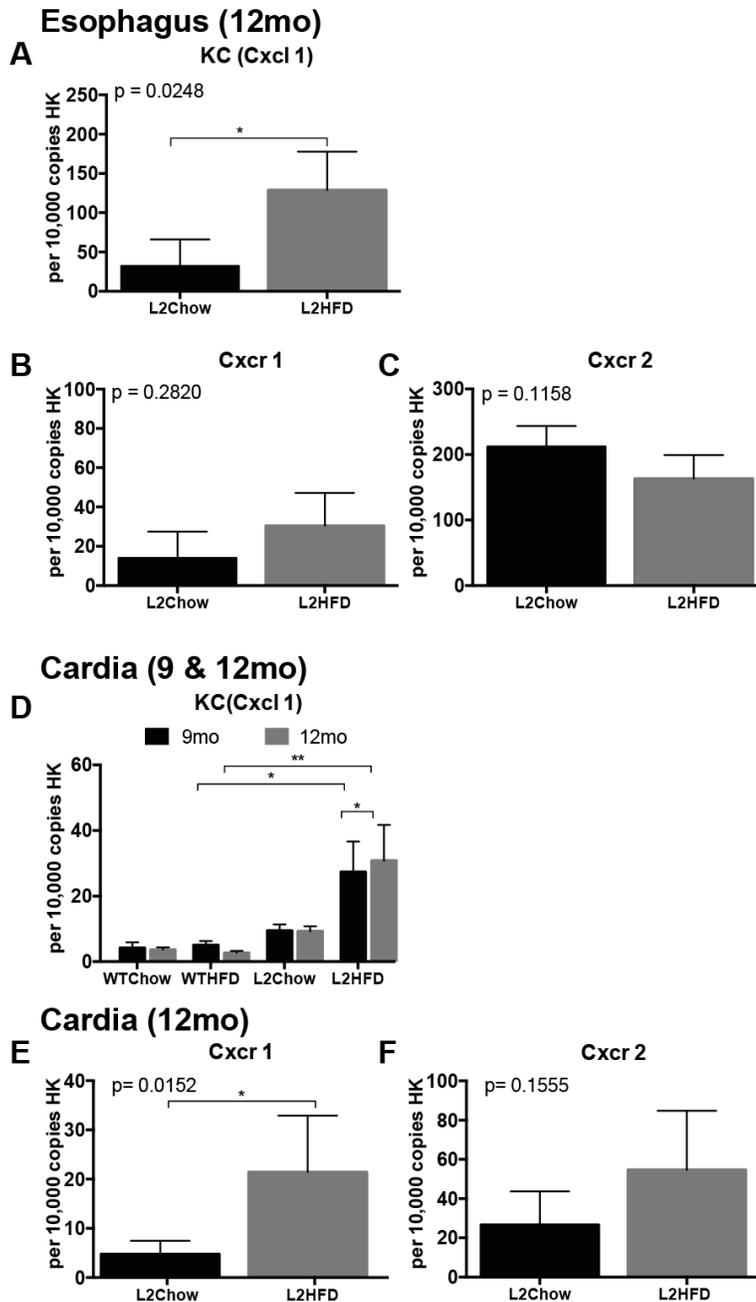
Figure 4.6.2.5: HFD stimulates increase expression of KC and its receptors Cxcr1 and Cxcr2 in the L2-mice.
mRNA Expression in the esophagus of L2-mice on Chow and HFD (A) KC (Cxcl1), and its receptors in 12-month old L2-mice (B) Cxcr1 and (C) Cxcr2 were quantified using RT-PCR. Group size (n=3-6). mRNA expression in the cardia of L2-mice on Chow and HFD(D) KC (Cxcl1), and its receptors in 12-month old L2-mice (E) Cxcr1 and (F) Cxcr2 were quantified using RT-PCR. Group size remained constant (n=6). All data are means ± standard deviation. Statistical analysis was performed using Student's t-tests where p-value is noted or two-way ANOVA and Sidak's test, asterisks indicate significant differences compared with control or between groups, ****p≤0.0001, ***p≤0.001, **p≤0.01, *p≤0.05

The observations associated with increased KC expression in esophagus and cardia tissue in L2-HFD mice were noted in parallel to changes in expression of the receptors Cxcr1 and Cxcr2. Notably, Cxcr1 appeared to be significantly up-regulated as a result of HFD in the L2-model in both the esophagus and cardia regions. Cxcr2 however, appeared insignificantly different in the esophagus (p = 0.1158), but significantly up-regulated in the cardia region.

The findings from RT-PCR analysis revealed interesting changes in chemoattractants of myeloid cells, KC levels and its receptors, as well as, in genes associated with the inflammatory process, tumor microenvironment, angiogenesis, cancer progression, invasion and metastasis such as Mmp and Wnt.

4.7 HFD Induces Chemokine and Cytokine Changes in Serum and Tissue on a Protein Level

Interestingly, chemokine, cytokine and molecular pathways involved in promoting tumor progression were predominant in the microarray (Table 4.6.1) and GSEA (Appendix Table 4.12.3). Therefore it was of interest to have a comprehensive analysis of chemokine and cytokine profiles on a protein level. Profiling was conducted to assess changes in circulating cytokine levels in the serum and at the tumor site using tissue lysates.

4.7.1 Cytokine Profiles of L2-IL-1beta Serum and Tissue Lysates

Secreted proteins present in the serum of Chow and HFD fed L2-IL-1beta mice were analyzed with the Proteome Profiler™ Mouse XL Cytokine Array, capable of recognizing 111 analytes. More than 50 proteins were identified, including several serum adipokine previously shown to be altered in experimental studies of HFD-fed and obese animals as well as obese humans.

Cytokine/Chemokine/Growth factor	Location	Up/Down in L2-HFD mice
ClqR1/CD93	A15 16	Up
Cxcl13/BLC/BCA-1	D7 D8	Up
Cxcl16	D9 10	Up
Egf	D17 18	Up
Fgf-acidic	E1 2	Up
Gas6	E7 E8	Up
Igfbp-6	F5 6	Up
IL5	F19 20	Up
Mmp-2	H11 12	Up
Ccl6/C10	B3 4	Down
Ccl20/ Mip-3alpha	B13 14	Down
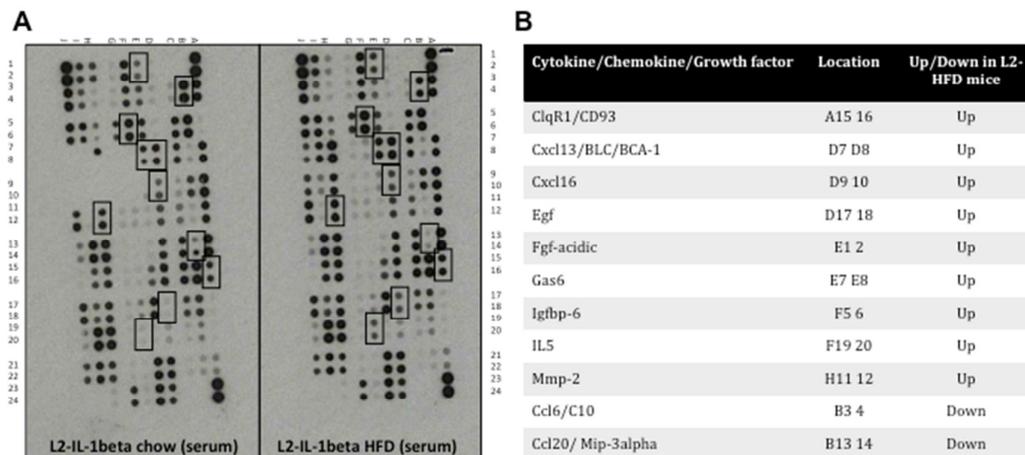
Figure 4.7.1.1: Levels of cytokines, chemokines and growth factors of interest analyzed in the serum of L2-mice on Chow and HFD.
Serum was isolated from the blood of 12-month old L2-mice on Chow and HFD was analyzed for changes in cytokine profiles. Freshly isolated serum was pooled from Chow (n=4) and HFD (n=6) mice.

Consistent with this, notably higher levels of Cxcl13, Cxcl16, Egf, Fgf-acidic, IL-5 and Mmp2 were observed in the sera L2-HFD mice compared to L2-Chow mice, while Ccl6 and Ccl20 were lower in the L2-HFD mice (Figure 4.7.1.1).

This overall increases in cytokine levels indicates that some other factors besides adipose tissues is responsible for the release of cytokines in L2-HFD mice, as these elevated cytokine levels do not correlate with the weights of fat mass measured in HFD-fed mice (Appendix Table Chapter 3.6.1).

To further understand the effects of HFD on the L2-model, tissue lysates from the esophagus, forestomach and cardia regions were isolated and quantified by BCA assay (Chapter 2, Section 2.11).

Cytokine/Chemokine/Growth factor	Location	Up/Down in L2-HFD mice
Ccl6/C10	B3 4	Up
Ccl11	B5 6	Up
Tnfrsf11b/Osteoprotegerin	H21 22	Up
Serpin F1/PEDF	J9 10	Up
Ccl21/6Ckine	B15 16	Down
C-Reactive Protein/ Crp	C15 16	Down
Complement Factor D	C13 14	Down
Fetuin A/ Ahsg	D23 24	Down
Igfbp-2	E23 24	Down
Osteopontin/Opn/Eta-1/Spp1	H19 20	Down
Mmp-3	H13 14	Down
Resistin/Adsf	I21 22	Down
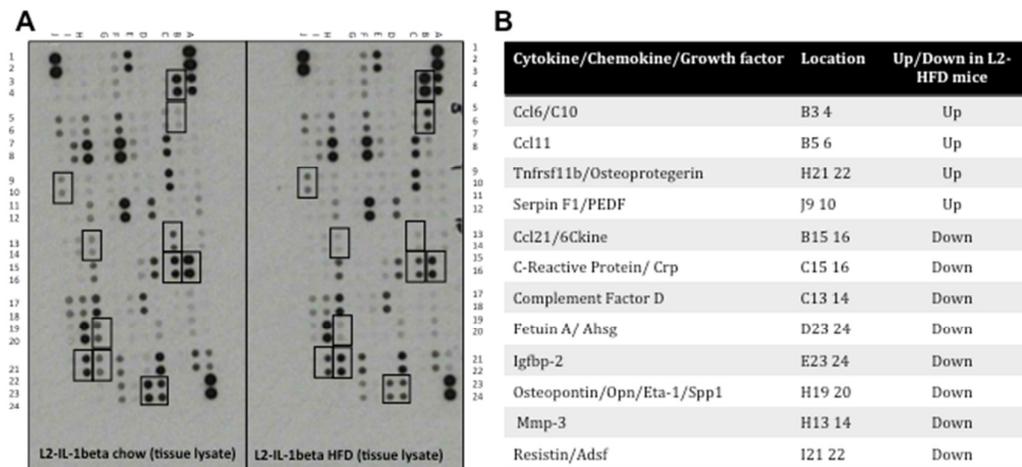
Figure 4.7.1.2: Levels of cytokines, chemokines and growth factors of interest analyzed in the tissue lysate from the esophagus, forestomach and cardia regions of L2-mice on Chow and HFD.
Tissue was isolated from 12-month old L2-mice on Chow (n=4) and HFD (n=6), and pooled for analysis of changes in cytokine profiles..

A different profile of up- and down-regulated cytokines was observed from tissue lysates obtained from L2-Chow and –HFD mice. Interestingly, fewer cytokines levels appeared to be elevated L2-HFD mice compared to L2-Chow mice. Up-regulation was noted in Ccl6, Ccl11, Osteoprotegerin and Serapin F1, while Ccl21, Crp, Complement D, Feutin A, IGFBP-2, Osteopontin, Mmp3 and Resistin were down-regulated in L2-HFD mice (Figure 4.7.1.2).

4.7.2 L2-IL-1beta Mice Develop Splenomegaly

Changes observed in the serum and tissue lysate also correlated with the observation of enlarged spleens in the L2-HFD model. Chronic HFD feeding resulted in the L2-IL-1beta mice developing splenomegaly. This observation was most noticeable when assessed as a ratio with body mass (Figure 4.7.2). The higher spleen to body mass ratios observed in L2-mice regardless of diet

resulted from enlarged and heavier spleens in combination with low overall body mass compared to the WT mice that presented with average spleen weights and higher body weights on Chow and HFD. While there appeared to be no significant difference between L2- Chow and –HFD mice at 9- and 12-months of age, a slight increasing trend was observed in spleen to body mass ratio (%) in the L2-HFD mice (9-months of age - WT-Chow, 0.35 ± 0.14%, WT-HFD, 0.25 ± 0.12%, L2-Chow, 0.40 ± 0.10%, L2-HFD, 0.44 ± 0.19%; 12-months of age WT-Chow, 0.30 ± 0.09%, WT-HFD, 0.23 ± 0.04%, L2-Chow, 0.43 ± 0.11%, L2-HFD, 0.46 ± 0.14%). Significant differences were observed in spleen to body mass ratio (%) between WT-HFD and L2-HFD mice at 9-months and between WT and L2 mice on Chow and HFD respectively, at 12-months of age.
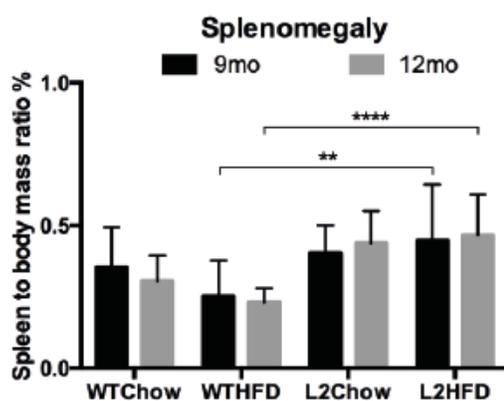
Figure 4.7.2: L2-mice develop splenomegaly.
At time of sacrifice, spleens were resected and weighed, (A) spleen to body mass ratio was calculated based on body weight at time of sacrifice in 9- and 12-month old WT and L2-IL-1beta mice. All data are means ± standard deviation. Statistical analysis was performed using one-way ANOVA and Tukeys post hoc-test. Group size remained constant (n=12). Asterisks indicate significant differences compared with control or between groups, ****p≤0.0001, ***p≤0.001, **p≤0.01, *p≤0.05.

The results gathered from the flow cytometry analysis, as well as the RT-PCR and gene microarray analysis, highlight IL-8 as a key player in the inflammation process associated with the L2-model on HFD. IL-8 appeared to be involved in recruiting neutrophils and shifting the inflammatory niche towards more a more acute response. The next step was to assess the direct role of the chemokine IL-8 in relationship to BE and EAC in the L2-IL-1beta model.

4.8 HFD Induces Increased Inflammation Which Leads to Expansion of Gastric Cardia Progenitor and Stem Cells in the L2-IL-1beta Model

To further address the role of HFD in the L2-model, the localization of known stem cell or progenitor cell markers were assessed.

4.8.1 Dclk-1

Doublecortin-like kinase (Dclk-1) is a gene associated with neurogenesis, mainly expressed in the fetal and adult brain, as well as in single cells of the human and murine adult gastrointestinal tract. Dclk-1 was found to have a high expression in the stem cell zone of mouse gastric glands and was proposed as a new gastrointestinal stem cell marker [156]. As previously noted with the L2-IL-1beta model, the Dclk-1 marker was absent from the normal squamous esophageal epithelium in WT mice, however an increased expression over time was observed, with expression first appearing in the gastric cardia and SCJ region[89].

Dclk-1 immunohistochemistry staining was performed as described in Chapter 2, Section 2.8.5. The percentage (%) of positive cells in the cardia region of 9-and 12-month old L2-IL-1beta mice on Chow diet or HFD quantified from assessment of 3-4 regions of esophagus/ stomach tissue per mouse; 5-8 mice were assessed per genotype and diet time-point.

Immunohistochemistry staining revealed an accumulation of Dclk-1+ cells adjacent to metaplastic mucus producing cells within the BE area. An abundance of Dclk-1+ cells were noted along the gastric cardia region. A gradual accumulation of Dclk-1+ cells along the SCJ in the L2-IL-1beta mice was positively correlated with the development of metaplasia along the SCJ.

Quantification of Dclk-1+ cells in the cardia region of the L2-IL-1beta mice on Chow diet showed an increasing trend with disease progression (Figure 4.8.1 B).
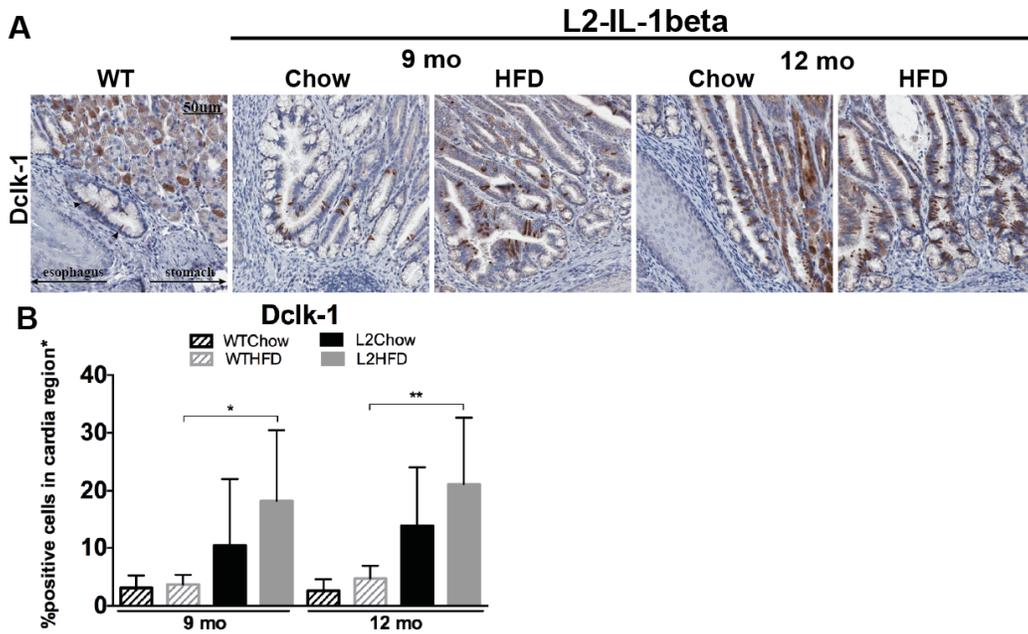
Figure 4.8.1: Expansion of Dclk-1+ cells in the cardia region of L2-mice on Chow and HFD.
(A) Dclk-1 staining was carried out on 9*- and 12-month old WT and L2-IL-1beta mice (scale bar, 50um). (B) Quantification of Dclk-1 positive cells in the cardia region of L2-IL-1beta mice on Chow and HFD were compared to WT mice on Chow and HFD, group size (n=5-8). All data are means ± standard deviation. Statistical analysis was performed using two-way ANOVA and Sidak's multiple comparisons test. Asterisks indicate significant differences compared with control or between groups (****p≤0.0001, ***p≤0.001, **p≤0.01, *p≤0.05 (9* month old WT mice Ki67 staining: data not shown).

It is important to note that in mice that displayed a very severe phenotype; with high-grade dysplasia, a lower number of Dclk-1+ cells were observed, as was reported in the original L2-IL-1beta model[89]. However since only a few mice progressed faster than the others therefore this observation was lost in quantification (data not shown).

4.8.2 Lgr5

Lgr5 is an established stem cell marker in the mouse gut, however in the stomach, it is only expressed in the gastric antrum and cardia regions [157].

Using *in-situ* hybridization, cardia regions from 12-month old L2-Chow and –HFD mice were stained for Lgr5+ cells. Lgr5+ cells were detected in L2-Chow mice, however in low number. L2-HFD mice on the other hand showed significantly more Lgr5+ localization in the cardia regions (Figure 4.8.2 B).
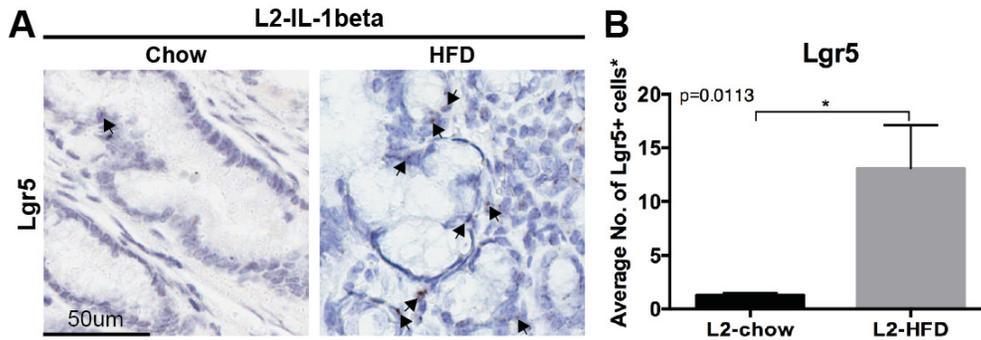
Figure 4.8.2: Expansion of Lgr5+ cells in the cardia region of L2-mice on Chow and HFD.
(A) Lgr5 staining was carried out on 12-month old L2-IL-1beta mice (scale bar, 50um). (B) Quantification of Lgr5-positive cells in the cardia region of L2-IL-1beta mice on Chow and HFD, group size (n=3-5). *Quantification was obtained by averaging positively stained cells counted from 8 separate, high power fields (40 X) per mouse. All data are means ± standard deviation. Statistical analysis was performed using Student's t-test, p-value noted in bar graph.

In summary, theses findings clearly indicate a convincing role for HFD in the acceleration of the BE/EAC phenotype observed in the L2-IL-1beta model. HFD drives the progression of BE to high-grade dysplasia, as noted through the increased histopathological scorings by 12-months of age. Furthermore, it appears to shift the immune microenvironment of L2-mice towards one where neutrophils maybe functioning as tumor initiators and promoters as observed in flow cytometry analysis of 12-month old L2-HFD mice. These results taken in combination with microarray data, RT-PCR and cytokine array analysis of esophagus and cardia tissue point towards a significant role for the neutrophil recruiting cytokine IL-8. Lastly, assessment of localization of progenitor and stem cell markers point towards an increase in inflammation, leading to an expansion of these markers in the gastric cardia of L2-mice as a result of HFD.

4.9 Impact of an Animal Fat Based High Fat Diet

The high fat diet used in the L2-HFD study was a plant-oil based diet, with the main fat component being palm oil (HFD^{palmoil}). While this is a well-established and tested diet for experimental obesity studies, it was also of interest to assess the impact on the disease progression utilizing an animal fat based diet. Using a micro- and macro nutrient matched diet to the HFD^{palmoil}, palm oil was replaced by pork lard (HFD^{porklard}) (Ssniff, Germany).

Dietary treatment was carried out in a small cohort of WT and L2-mice, as illustrated in Figure 4.9 A. Mice were aged to 12-months and were allowed access to the HFD^{porklard} *ad libitum.* Preliminary results highlighted similar trends as was observed in L2-mice on HFD^{palmoil}. As seen in the body mass curves in Figure 6.4B, WT mice appear to steadily increase in body mass as they age on HFD^{porklard}, L2- mice show a slow increase in body mass, however by age 24-weeks (6-months of age) they begin showing a significant decrease in body mass, which continues until the 52-week (12-months of age) end time-point. Furthermore, lean and fat mass showed similar trends as previously observed in the L2- HFD^{palmoil} mice, where WT mice showed progressive increases over time in lean and fat mass, while L2-mice on HFD^{porklard} showed the opposite trend of a decrease in lean and fat mass over time. Lastly, at the end of the dietary treatment, the macroscopic phenotype of WT- and L2-mice (Figure 4.9 D) was very similar to the phenotype observed on HFD^{palmoil} in Figure 4.2. Further analysis of the macroscopic lesions in the esophagus and cardia regions showed no phenotype in the WT-mice, however, the L2- HFD^{porklard} showed a strong acceleration of the BE/EAC phenotype, as was observed in L2- HFD^{palmoil}.

A complete analysis characterizing the histopathological changes, differentially regulated genes, and inclusion in the microbiome study remains to be carried out in order to make conclusive comparisons between the similarities and differences observed in the L2-model on HFD^{palmoil} and HFD^{porklard}.
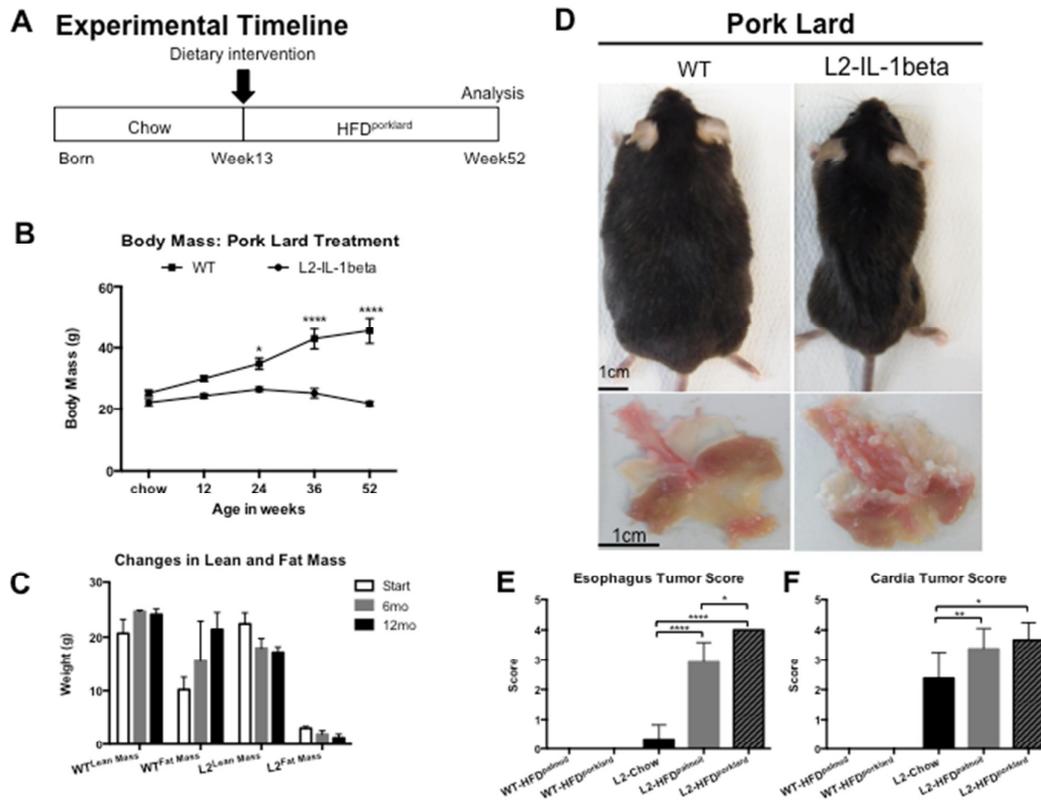
Figure 4.9: Preliminary results of the effects of a pork lard based HFD on the L2-IL-1beta model.
(A) WT and L2-IL-1beta mice were started on HFD^{porklard} at 13-weeks of age (3-months) and age to 52-weeks (12-months), prior to which they were fed a Chow diet; both diets were available ad libitum. (B) Over all body mass and (C) Lean and Fat Mass measurements as WT- and L2-mice aged on HFD^{porklard}. (D) Macroscopic views of the overall appearance and of the esophagus and stomach regions of WT- and L2-mice at the end of the HFDporklard dietary treatment. (E, F) Macroscopic score of lesions in the esophagus and cardia regions of WT- and L2-mice at the end of the HFD^{porklard} dietary treatment compared to L2-Chow and –HFD^{palmoil} mice. Statistical analysis was performed using two-way ANOVA and Sidak's post-hoc test for body mass over time and one-way ANOVA and Tukey's post-hoc test was used for Macroscopic score. Group size (n=3). Asterisks indicate significant differences compared with control or between groups. ****p≤0.0001, ***p≤0.001, **p≤0.01, *p≤0.05.

4.10 Effects of a Genetic Model of Obesity on the L2-IL-1beta Model

Given the lack of a DIO phenotype in the L2-model on HFD^{palmoil} and HFD^{porklard}, and the strong association between BE, EAC and obesity, the next step was to cross the L2-model with one of genetic obesity to see if an effect could be achieved.

This was carried out by crossing L2-mice with Mc4r^{X16}knock-in mice (Mc4r stands for melanocortin-4-receptor), an established model of genetic obesity generously that was generously shared in collaboration with Prof. Martin Klingenpor, Technische Universität München, Germany, as described in Chapter 1, Section 1.4.3.

Crossing this model proved challenging in acquiring the combination of L2-IL-1beta and Mc4r^{X16}knock-in (henceforth referred to as L2/Mc4r^{X16}knock-in). Of several breeding cohorts, and litters with Mendelian ratios, only three successful L2/ Mc4r^{X16}knock-in mice were acquired and aged. Preliminary data from crossing these two lines showed an abrogation of the obese phenotype and a similarity to the L2-HFD phenotype, as evident in Figure 4.10 A.

L2/ Mc4r^{X16}knock-in and L2/ Mc4r^{X16}heterozygous (het) mice showed a similar over all body masses as they aged to 12-months, while the Mc4r^{X16}knock-in retained its characteristic obese phenotype and the Mc4r^{X16}het mice showed a WT phenotype. Macroscopically, the cardia of L2/ Mc4r^{X16}knock-in and L2/ Mc4r^{X16}het scored similarly to L2-mice, Mc4r^{X16}knock-in and Mc4r^{X16}het controls had showed a WT phenotype in the esophagus and cardia regions.

This is remains an ongoing project and a complete analysis characterizing the histopathological changes, assessing differentially regulated genes, and inclusion in the microbiome study remains to be carried out to understand the mechanisms underlying the abrogation of genetic obesity in the L2/ Mc4r^{X16}knock-in cross.
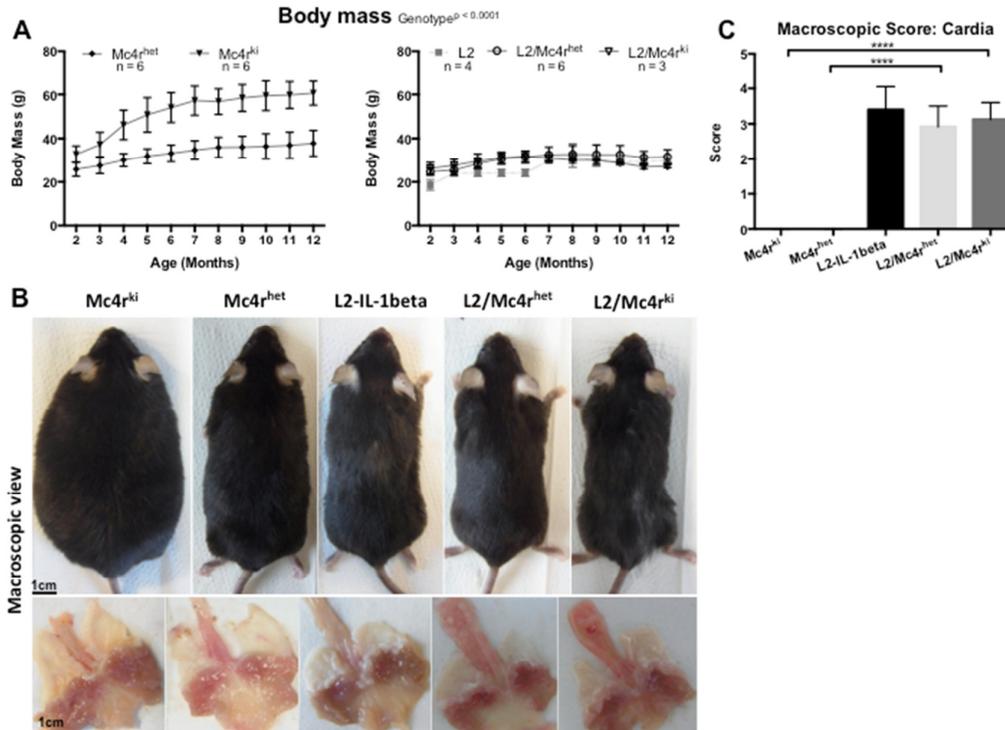
Figure 4.10: Preliminary results of crossing the L2-IL-1beta model with the Mc4r model; a model of genetic obesity.
(A) Body mass changes in L2/Mc4rhet and L2/Mc4rki mice and their controls until 12-months of age. (B) Macroscopic images of L2/Mc4rhet and L2/Mc4rki mice and their controls, in addition to macroscopic views of the esophagus and stomach regions of these mice. (C) Macroscopic scoring of cardia tissue. Group size note in body mass graphs, panel A. Statistical analysis was performed using two-way ANOVA and Sidak's post-hoc test for macroscopic scoring. Asterisks indicate significant differences compared with control or between groups. ****$p \leq 0.0001$, ***$p \leq 0.001$, **$p \leq 0.01$, *$p \leq 0.05$.

4.11 Impact of HFD on the Microbiome in the L2-IL-1beta Model

Given the lack of DIO in L2-HFD mice, assessing the microbiome of the L2- model was of importance in understanding how a pivotal factor like the intestinal microbiota might be affected by diet and inflammation or might be contributing to increased systemic inflammation through diet, thereby accelerating the disease.

Samples were collected as described in Chapter 2, Section 2.13.1. Preliminary data from the 12-month cohort revealed that the number of observed OTUs and the diversity of species was lower in the high fat diet fed mice (data not shown). Furthermore, analysis of the phylogenetic distances between the sequences showed that samples clustered by similarity based on species composition and number of sequences found per OTU.

The samples were clustered by similarity in the species composition and the number of sequences found per OTU by analyzing the phylogenetic distances between the sequences. Figure 4.11 A shows fairly nicely separated clusters of HFD and Chow samples; however, genotype does not appear to be relevant for species composition.

In order to identify relevant differences between L2-IL-1beta mice and Wildtype mice on HFD, LEfSe analysis was performed. Figure 4.11 B highlights several OTUs that are significantly different between L2-IL-1beta and Wildtype mice on HFD. Unfortunately, a majority of the identified OTUs remained to be described and cultivated.

Of the OTUs that were identifiable, OTU_7 *Bacteroides dorei* (DSM 17855) was highly associated with L2-IL-1beta mice on HFD. A comparison of the macroscopic lesion score (Figure 4.1.1 C, D) in the esophagus showed a potential trend of a high abundance of OUT_7 correlating with a higher lesion score as seen in Figure 4.11 C.

Ultimately, due to small sample sizes and the lack of Control Diet fecal samples, additional mice are currently being aged to ensure strong cohort numbers for future assessment. Additionally, germ-free L2-IL-1beta mice are currently being aged and studied for changes in phenotype in the lab of Dr. James Fox at the

Division of Comparative Medicine, Massachusetts Institute of Technology, USA, as part of a collaboration study.
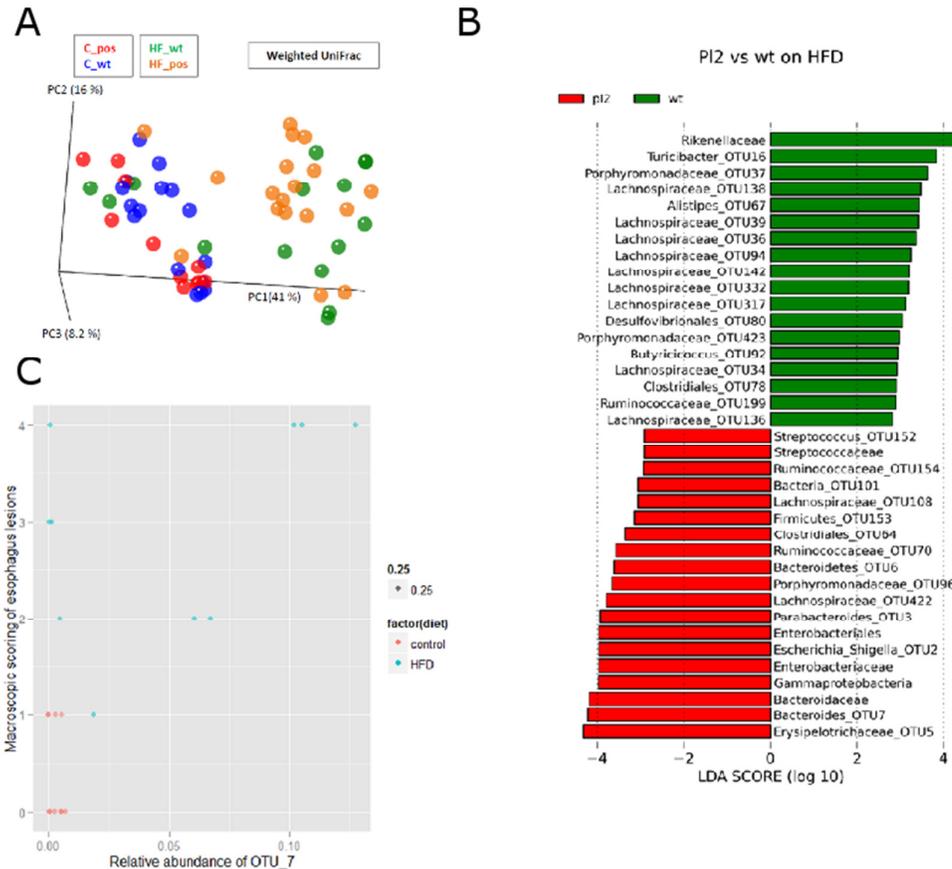
Figure 4.11: Preliminary results of 16s sequencing of fecal samples.
(A) Weighted UniFrac analysis of the phylogenetic distances and abundances of OTUs, where "C_wt" and "HF_wt" refer to WT-mice on Chow and HFD and "C_pos" and "HF_pos" refer to L2-IL-1beta-mice on Chow and HFD respectively (B) Plot of a Linear discriminant analysis Effect Size (LEfSe), (C) Relative abundance of OTU 7 in comparison to macroscopic esophageal lesion scores.

4.12 Appendix Figures & Tables
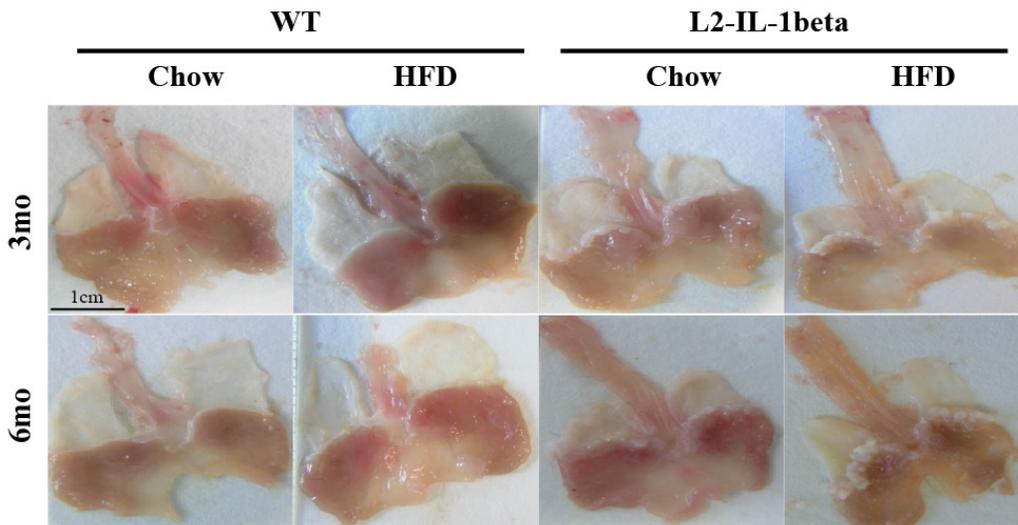
Figure 4.12.1: Macroscopic view of the esophagus and stomach in 3- and 6-month old WT and L2-IL-1beta mice on Chow and HFD.
Overview showing macroscopic development and progression of BE (scale bar 1cm).

Esophagus

Myeloid cell populations
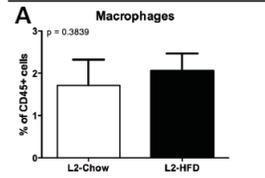
T-helper cell populations
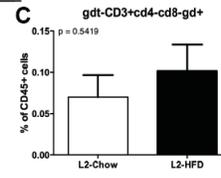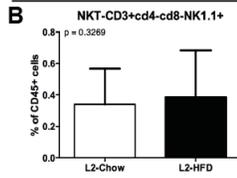
T-helper cell populations continued
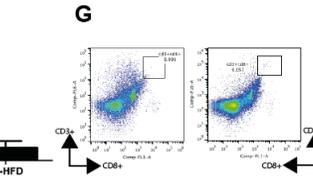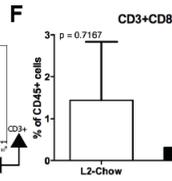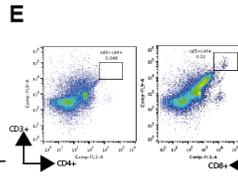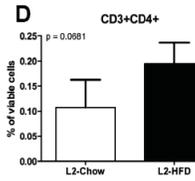
Cardia

Myeloid cell populations
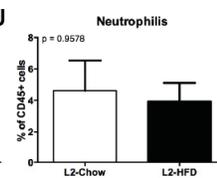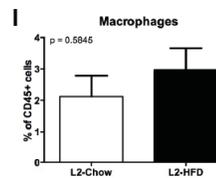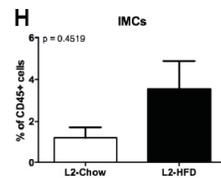
T-helper cell populations
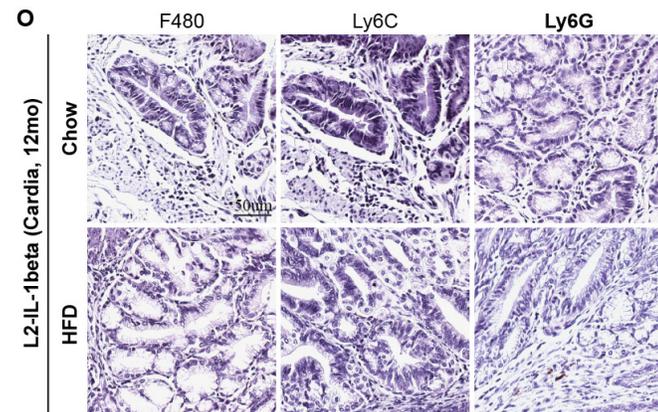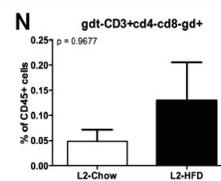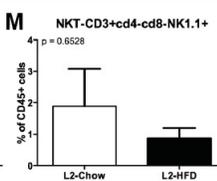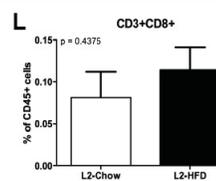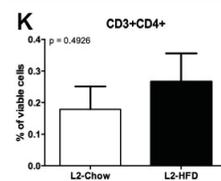
Appendix Figure 4.12.2: Quantification of flow cytometry analysis and immune stainings in 12-month old L2-mice on Chow and HFD.
Quantification of (A) Macrophages, and T-cell populations including (B) NKT and (C) gdT (D, E) CD4+, (F, G) CD8+ cells in esophageal tissue. Quantification of (H) IMCs, (I) Macrophages, (J) Neutrophils and T-cell populations including (K) CD4+, (L) CD8+, (M) NKT and (N) gdT cells in cardia tissue, group size remained constant (n=6). (O) F480, Ly6C and Ly6G were stained in cardia tissue (n=3). All data are means ± SEM. Statistical analysis was performed using Student's t-tests.

Appendix Table 4.12.1: Extended Table of selected genes up- and down-regulated as a result of HFD in the L2-IL-1beta model.
(Based on cut-offs of fold changes >1.5 or <0.65 and p-values of <0.5.)

L2-HFD v. L2-Chow

Symbol	Description	Gene function	FC	P.Value
Cxcl13	chemokine (C-X-C motif) ligand 13	B lymphocyte chemoattractant	3.6130	0.0226
Mmp7	matrix metallopeptidase 7	Enzyme with broad substrate specificity in ECM. Promotes wound healing, angiogenesis, tumor invasion and metastasis	3.5151	0.0132
Il1b	interleukin 1 beta	Multifunctional, pro-inflammatory, proangiogenic cytokine	2.8931	0.0191
Ccl2	chemokine (C-C motif) ligand 2	Chemotactic activity for monocytes and basophils	2.6368	0.0366
Mrc1	mannose receptor, C type 1	Type I membrane receptor that mediates the endocytosis of glycoproteins by macrophages	2.4725	0.0097
Ccl7	chemokine (C-C motif) ligand 7	Chemotactic activity for macrophages during inflammation and metastasis	2.4657	0.0148
Ccl11	chemokine (C-C motif) ligand 11	Chemotactic activity for eosinophils	2.2577	0.0024
Il17c	interleukin 17C	T cell-derived cytokine reported to stimulate the release of tumor necrosis factor alpha and interleukin 1 beta from a monocytic cell line	2.2093	0.0098
Hspa1a	heat shock protein 1A	Stabilizes existing proteins against aggregation and mediates the folding of newly translated proteins in the cytosol and in organelles	2.1531	0.0116
Ctsk	cathepsin K	Involved in bone remodeling and resorption, expressed in a significant fraction of human breast cancers, where it could contribute to tumor invasiveness	1.9414	0.0093
Angpt2	angiopoietin 2	Encoded protein disrupts the vascular remodeling ability of ANGPT1 and may induce endothelial cell apoptosis	1.9333	0.0108
Ccr5	chemokine (C-C motif) receptor 5	Expressed by T cells and macrophages, may play a role in granulocyte lineage proliferation and differentiation	1.8987	0.0325
Mmp10	matrix metallopeptidase 10	Involved in the breakdown of extracellular matrix in normal physiological processes, such as embryonic development, reproduction, and tissue remodeling, as well as in disease processes, such as arthritis and metastasis	1.8903	0.0464
Cxcr4	chemokine (C-X-C motif) receptor 4	Receptor for SDF-1 (CXCL12) – which regulates hematpoietic stemm and regulates hematpoietic stem and myeloid cell recruitment by tissues. Involved in proliferation and metatasis of tumor cells	1.8898	0.0073
Ccr2	chemokine (C-C motif) receptor 2	Isoform monocyte chemoattractant protein-1 is involved in monocyte infiltration in inflammatory diseases as well as in the inflammatory response against tumors	1.8705	0.0208
Tlr13	toll-like receptor 13	Member of the Toll-like receptor (TLR) family which plays a fundamental role in pathogen recognition and activation of innate immunity	1.8489	0.0262
Ccl8	chemokine (C-C motif) ligand 8	Chemotactic activity for monocytes, lymphocytes, basophils and eosinophils	1.8153	0.0184
Ccr7	chemokine (C-C motif) receptor 7	Controlsl the migration of memory T cells to inflamed tissues, as well as stimulate dendritic cell maturation	1.7321	0.0289
Wnt2b	wingless-type MMTV integration site family, member 2B	May play a role in human development as well as carcinogenesis	1.7256	0.0078
Hspa1b	heat shock protein 1B	Intracellular enzyme. Stabilizes existing proteins against aggregation & mediates folding of newly translated proteins	1.7076	0.0227

Igfbp4	insulin-like growth factor binding protein 4	Binds both insulin-like growth factors (IGFs) I and II and circulates in the plasma in both glycosylated and non-glycosylated form	**1.6960**	**0.0060**
Tlr8	toll-like receptor 8	Member of the Toll-like receptor (TLR) family which plays a fundamental role in pathogen recognition and activation of innate immunity	**1.6910**	**0.0151**
Vim	vimentin	Involved in the immune response, and controls the transport of low-density lipoprotein (LDL)-derived cholesterol from a lysosome to the site of esterification. It functions as an organizer of a number of critical proteins involved in attachment, migration, and cell signaling	**1.6550**	**0.0301**
Il2ra	interleukin 2 receptor, alpha chain	Interleukin 2 (IL2) receptor, resulting from extracellular proteolyisis	**1.6505**	**0.0036**
Itga4	integrin alpha 4	Forms an integrin that may play a role in cell motility and migration	**1.5864**	**0.0315**
Igf1	insulin-like growth factor 1	Involved in mediating growth and development	**1.5851**	**0.0283**
Mmp25	matrix metallopeptidase 25	May play a role in tumor invasion and metastasis through activation of MMP2.	**1.5596**	**0.0411**
Mmp12	matrix metallopeptidase 12	Involved in the breakdown of extracellular matrix in normal physiological processes, such as embryonic development, reproduction, and tissue remodeling, as well as in disease processes, such as arthritis and metastasis	**1.5577**	**0.0238**
Vcam1	vascular cell adhesion molecule 1	Mediates leukocyte-endothelial cell adhesion and signal transduction	**1.5512**	**0.0260**
Csf1r	colony stimulating factor 1 receptor	Receptor for colony stimulating factor 1, a cytokine which controls the production, differentiation, and function of macrophages	**1.5206**	**0.0750**
Ccl9	chemokine (C-C motif) ligand 9	Chemotactic activity for dendritic cells that possess the cell surface molecule CD11b and the chemokine receptor CCR1. It is constitutively expressed in macrophages and myeloid cells	**1.5162**	**0.0537**
Ctsl	cathepsin L	Encoded protein plays a major role in intracellular protein catabolism. Associated as amajor controlling element of neutrophil elastase activity.	**1.4991**	**0.0553**
Wnt7b	wingless-type MMTV integration site family, member 7B	Encodes secreted signaling proteins that have been implicated in oncogenesis and in several developmental processes, including regulation of cell fate and patterning during embryogenesis	**0.6538**	**0.0209**
Krt7	keratin 7	Specifically expressed in the simple epithelia lining the cavities of the internal organs and in the gland ducts and blood vessels	**0.6223**	**0.0210**
Il20ra	interleukin 20 receptor, alpha	Receptor for interleukin 20, a cytokine that may be involved in epidermal function.	**0.5940**	**0.0490**
Egf	epidermal growth factor	Dysregulation of this gene has been associated with the growth and progression of certain cancers	**0.5443**	**0.0076**
Muc2	mucin 2	The protein encoded by this gene is secreted and forms an insoluble mucus barrier that protects the gut lumen	**0.4981**	**0.0274**

Appendix Table 4.12.2: Selected genes up- and down-regulated as a result of HFD in the L2-IL-1beta model.

(Based on cut-offs of fold changes >1.5 or <0.65 and p-values of <0.5.)

L2-Chow v. WT-Chow

Symbol	Description	FC	P.Value
Cd177	CD177 antigen	16.4549	0.0000
Cxcl5	chemokine (C-X-C motif) ligand 5	7.4586	0.0000
Krt6b	keratin 6B	5.9908	0.0000
Muc5b	mucin 5, subtype B, tracheobronchial	3.7898	0.0019
Il22ra1	interleukin 22 receptor, alpha 1	3.1793	0.0000
Cxcr6	chemokine (C-X-C motif) receptor 6	3.0913	0.0000
Il1rn	interleukin 1 receptor antagonist	3.0040	0.0000
Ccl28	chemokine (C-C motif) ligand 28	2.9747	0.0000
Il34	interleukin 34	2.7261	0.0000
Cxcr2	chemokine (C-X-C motif) receptor 2	2.7260	0.0027
Arg1	arginase, liver	2.5905	0.0034
Casp1	caspase 1	2.5743	0.0000
Hif1a	hypoxia inducible factor 1, alpha subunit	2.3893	0.0002
Angptl4	angiopoietin-like 4	2.3428	0.0025
Casp4	caspase 4, apoptosis-related cysteine peptidase	2.2083	0.0002
Il20ra	interleukin 20 receptor, alpha	2.1646	0.0046
Il12rb2	interleukin 12 receptor, beta 2	2.0953	0.0052
Muc4	mucin 4	2.0812	0.0023
Notch3	notch 3	1.9745	0.0017
Krt5	keratin 5	1.8955	0.0006
Lep	leptin	1.8946	0.0022
Krt14	keratin 14	1.8843	0.0105
Ccl20	chemokine (C-C motif) ligand 20	1.8703	0.0239
Ctsj	cathepsin J	1.8403	0.0005
Cxcl15	chemokine (C-X-C motif) ligand 15	1.8193	0.0461
Hif3a	hypoxia inducible factor 3, alpha subunit	1.7791	0.0003
Cd44	CD44 antigen	1.7461	0.0018
Wnt4	wingless-type MMTV integration site family, member 4	1.5539	0.0125
Notch2	notch 2	1.5386	0.0060
Wnt5a	wingless-type MMTV integration site family, member 5A	1.5017	0.0169
Mif	macrophage migration inhibitory factor	1.4961	0.0027
Igf1	insulin-like growth factor 1	0.6718	0.0433
Ccl9	chemokine (C-C motif) ligand 9	0.6666	0.0487
Fgf1	fibroblast growth factor 1	0.6311	0.0035
Angpt2	angiopoietin 2	0.6261	0.0456
Casp3	caspase 3	0.6126	0.0051
Mmp17	matrix metallopeptidase 17	0.5983	0.0523
Ctsb	cathepsin B	0.5881	0.0000
Tlr3	toll-like receptor 3	0.5852	0.0041
Krt4	keratin 4	0.5795	0.0120

Ccl11	chemokine (C-C motif) ligand 11	**0.5660**	**0.0165**
Ctsl	cathepsin L	**0.5645**	**0.0077**
Lgr5	leucine rich repeat containing G protein coupled receptor 5	**0.5547**	**0.0235**
Mc4r	melanocortin 4 receptor	**0.5411**	**0.0005**
Wnt2b	wingless-type MMTV integration site family, member 2B	**0.5391**	**0.0024**
Lgals1	lectin, galactose binding, soluble 1	**0.5372**	**0.0144**
Cxcl12	chemokine (C-X-C motif) ligand 12	**0.5368**	**0.0155**
Cd34	CD34 antigen	**0.5052**	**0.0115**
Ccl7	chemokine (C-C motif) ligand 7	**0.5009**	**0.0420**
Tgfb3	transforming growth factor, beta 3	**0.4979**	**0.0028**
Fn1	fibronectin 1	**0.4944**	**0.0492**
Casp6	caspase 6	**0.4936**	**0.0012**
Fgf18	fibroblast growth factor 18	**0.4694**	**0.0025**
Ero1lb	ERO1-like beta (S. cerevisiae)	**0.4383**	**0.0291**
Egf	epidermal growth factor	**0.3559**	**0.0001**
Ccl2	chemokine (C-C motif) ligand 2	**0.3547**	**0.0210**
Cxcl13	chemokine (C-X-C motif) ligand 13	**0.2791**	**0.0180**

Appendix Table 4.12.3: GSEA pathway analysis.

NAME	SIZE	ES	NES	NOM p-val	FDR q-val	LEADING EDGE	
	16	0.81458104	2.291377	0	0	tags=88%, signal=102%	list=14%,

BIOCARTA_LAIR_PATHWAY

GENE SYMBOL	GENE_TITLE
SELP	selectin P (granule membrane protein 140kDa, antigen CD62)
TNF	tumor necrosis factor (TNF superfamily, member 2)
C7	complement component 7
VCAM1	vascular cell adhesion molecule 1
ICAM1	intercellular adhesion molecule 1 (CD54), human rhinovirus receptor
ITGA4	integrin, alpha 4 (antigen CD49D, alpha 4 subunit of VLA-4 receptor)
IL1A	interleukin 1, alpha
ITGB2	integrin, beta 2 (complement component 3 receptor 3 and 4 subunit)
ITGAL	integrin, alpha L (antigen CD11A (p180), lymphocyte function-associated antigen 1; alpha polypeptide)
SELPLG	selectin P ligand
IL8	interleukin 8
C6	complement component 6
IL6	interleukin 6 (interferon, beta 2)
ITGB1	integrin, beta 1 (fibronectin receptor, beta polypeptide, antigen CD29 includes MDF2, MSK12)

NAME	SIZE	ES	NES	NOM p-val	FDR q-val	LEADING EDGE	
	29	0.68509066	2.2847722	0	0	tags=59%, signal=69%	list=15%,

BIOCARTA_NKT_PATHWAY

GENE SYMBOL	GENE_TITLE
CD4	CD4 molecule
CXCR4	chemokine (C-X-C motif) receptor 4
CCR5	chemokine (C-C motif) receptor 5
IL18R1	interleukin 18 receptor 1
CCR2	chemokine (C-C motif) receptor 2
CCR7	chemokine (C-C motif) receptor 7
CCR1	chemokine (C-C motif) receptor 1
TGFB1	transforming growth factor, beta 1 (Camurati-Engelmann disease)
TGFB2	transforming growth factor, beta 2
TGFB3	transforming growth factor, beta 3
CD40LG	CD40 ligand (TNF superfamily, member 5, hyper-IgM syndrome)
IFNGR1	interferon gamma receptor 1
CXCR3	chemokine (C-X-C motif) receptor 3
CCR4	chemokine (C-C motif) receptor 4
IL12RB1	interleukin 12 receptor, beta 1
IL4R	interleukin 4 receptor
CSF2	colony stimulating factor 2 (granulocyte-macrophage)

NAME	SIZE	ES	NES	NOM p-val	FDR q-val	LEADING EDGE	
	17	0.7451112	2.125659	0	4.75E-04	tags=59%, signal=66%	list=11%,

BIOCARTA_COMP_PATHWAY

GENE SYMBOL	GENE_TITLE	RANK IN GENE LIST	RANK METRIC SCORE	RUNNING ES

C4B	complement component 4B (Childo blood group)
C1QB	complement component 1, q subcomponent, B chain
CFB	complement factor B
MASP1	mannan-binding lectin serine peptidase 1 (C4/C2 activating component of Ra-reactive factor)
C1QC	complement component 1, q subcomponent, C chain
C1QA	complement component 1, q subcomponent, A chain
C7	complement component 7
C2	complement component 2
C1R	complement component 1, r subcomponent
C6	complement component 6

NAME	SIZE	ES	NES	NOM p-val	FDR q-val	LEADING EDGE	
	22	0.65924215	2.0116708	0	0.00483408	tags=59%, signal=73%	list=19%,

	GENE SYMBOL	GENE_TITLE	RANK IN GENE LIST	RANK METRIC SCORE	RUNNING ES
BIOCARTA_DC_PATHWAY	CD40	CD40 molecule, TNF receptor superfamily member 5			
	CD33	CD33 molecule			
	TLR9	toll-like receptor 9			
	CD7	CD7 molecule			
	ITGAX	integrin, alpha X (complement component 3 receptor 4 subunit)			
	TLR2	toll-like receptor 2			
	IFNA1	interferon, alpha 1			
	CD2	CD2 molecule			
	CSF2	colony stimulating factor 2 (granulocyte-macrophage)			
	ANPEP	alanyl (membrane) aminopeptidase (aminopeptidase N, aminopeptidase M, microsomal aminopeptidase, CD13, p150)			
	TLR7	toll-like receptor 7			
	IL13	interleukin 13			
	IFNG	interferon, gamma			

NAME	SIZE	ES	NES	NOM p-val	FDR q-val	LEADING EDGE	
	29	0.5976681	1.9369745	0.001694915	0.01429560	tags=55%, signal=68%	list=19%,

	GENE SYMBOL	GENE_TITLE
BIOCARTA_INFLAM_PATHWAY	CD4	CD4 molecule
	TNF	tumor necrosis factor (TNF superfamily, member 2)
	CSF1	colony stimulating factor 1 (macrophage)
	TGFB1	transforming growth factor, beta 1 (Camurati-Engelmann disease)
	IL1A	interleukin 1, alpha
	HLA-DRB1	major histocompatibility complex, class II, DR beta 1
	TGFB2	transforming growth factor, beta 2
	TGFB3	transforming growth factor, beta 3
	CSF3	colony stimulating factor 3 (granulocyte)
	IL8	interleukin 8
	IL6	interleukin 6 (interferon, beta 2)
	IFNA1	interferon, alpha 1
	CSF2	colony stimulating factor 2 (granulocyte-macrophage)

146

IL15	interleukin 15	
IL13	interleukin 13	
IFNG	interferon, gamma	

NAME	SIZE	ES	NES	NOM p-val	FDR q-val	LEADING EDGE	
						tags=67%, signal=83%	list=19%,
	15	0.6728527	1.9028649	0.003478261	0.02038801		
	GENE SYMBOL	GENE_TITLE	RANK IN GENE LIST	RANK METRIC SCORE	RUNNING ES		
BIOCARTA_ERYTH_PATHWAY	IGF1	insulin-like growth factor 1 (somatomedin C)					
	FLT3	fms-related tyrosine kinase 3					
	TGFB1	transforming growth factor, beta 1 (Camurati-Engelmann disease)					
	IL1A	interleukin 1, alpha					
	TGFB2	transforming growth factor, beta 2					
	TGFB3	transforming growth factor, beta 3					
	CSF3	colony stimulating factor 3 (granulocyte)					
	IL6	interleukin 6 (interferon, beta 2)					
	CSF2	colony stimulating factor 2 (granulocyte-macrophage)					
	CCL3	chemokine (C-C motif) ligand 3					

NAME	SIZE	ES	NES	NOM p-val	FDR q-val	LEADING EDGE	
						tags=73%, signal=100%	list=27%,
	15	0.6672669	1.8451097	0	0.03616629		
	GENE SYMBOL	GENE_TITLE	RANK IN GENE LIST	RANK METRIC SCORE	RUNNING ES		
BIOCARTA_IL22BP_PATHWAY	SOCS3	suppressor of cytokine signaling 3					
	STAT4	signal transducer and activator of transcription 4					
	IL10RA	interleukin 10 receptor, alpha					
	STAT3	signal transducer and activator of transcription 3 (acute-phase response factor)					
	STAT1	signal transducer and activator of transcription 1, 91kDa					
	JAK2	Janus kinase 2 (a protein tyrosine kinase)					
	IL22	interleukin 22					
	JAK1	Janus kinase 1 (a protein tyrosine kinase)					
	STAT5B	signal transducer and activator of transcription 5B					
	STAT2	signal transducer and activator of transcription 2, 113kDa					
	IL22RA2	interleukin 22 receptor, alpha 2					

NAME	SIZE	ES	NES	NOM p-val	FDR q-val	LEADING EDGE	
						tags=63%, signal=74%	list=15%,
	16	0.6562302	1.8096406	0.005272408	0.04436662		
	GENE SYMBOL	GENE_TITLE	RANK IN GENE LIST	RANK METRIC SCORE	RUNNING ES		
BIOCARTA_NO2IL12_PATHWAY	CD4	CD4 molecule					
	CD3G	CD3g molecule, gamma (CD3-TCR complex)					
	CCR5	chemokine (C-C motif) receptor 5					
	STAT4	signal transducer and activator of transcription 4					
	null	null					
	CD3E	CD3e molecule, epsilon (CD3-TCR complex)					
	CXCR3	chemokine (C-X-C motif) receptor 3					
	IL12RB1	interleukin 12 receptor, beta 1					

CD2	CD2 molecule
JAK2	Janus kinase 2 (a protein tyrosine kinase)

NAME	SIZE	ES	NES	NOM p-val	FDR q-val	LEADING EDGE	
						tags=47%, signal=55%	list=15%,
	15	0.6391734	1.8070811	0.007326007	0.04075229		
	GENE SYMBOL	**GENE_TITLE**	**RANK IN GENE LIST**	**RANK METRIC SCORE**	**RUNNING ES**		
	CD4	CD4 molecule					
	CSF1	colony stimulating factor 1 (macrophage)					
	CSF3	colony stimulating factor 3 (granulocyte)					
BIOCARTA_STEM_PATHWAY	IL8	interleukin 8					
	CD8A	CD8a molecule					
	IL6	interleukin 6 (interferon, beta 2)					
	CSF2	colony stimulating factor 2 (granulocyte-macrophage)					

NAME	SIZE	ES	NES	NOM p-val	FDR q-val	LEADING EDGE	
						tags=44%, signal=58%	list=24%,
	36	0.51840615	1.7849919	0.001715266	0.04629288		
	GENE SYMBOL	**GENE_TITLE**	**RANK IN GENE LIST**	**RANK METRIC SCORE**	**RUNNING ES**		
	IL2RA	interleukin 2 receptor, alpha					
	NMI	N-myc (and STAT) interactor					
	IL2RG	interleukin 2 receptor, gamma (severe combined immunodeficiency)					
	SOCS3	suppressor of cytokine signaling 3					
	FASLG	Fas ligand (TNF superfamily, member 6)					
	GRB2	growth factor receptor-bound protein 2					
	SYK	spleen tyrosine kinase					
BIOCARTA_IL2RB_PATHWAY	CFLAR	CASP8 and FADD-like apoptosis regulator					
	PTPN6	protein tyrosine phosphatase, non-receptor type 6					
	SOCS1	suppressor of cytokine signaling 1					
	E2F1	E2F transcription factor 1					
	IL2RB	interleukin 2 receptor, beta					
	JAK1	Janus kinase 1 (a protein tyrosine kinase)					
	IKZF3	IKAROS family zinc finger 3 (Aiolos)					
	BCL2	B-cell CLL/lymphoma 2					
	STAT5B	signal transducer and activator of transcription 5B					

NAME	SIZE	ES	NES	NOM p-val	FDR q-val	LEADING EDGE	
						tags=50%, signal=63%	list=20%,
	18	0.6069005	1.7726668	0.009041592	0.046646424		
	GENE SYMBOL	**GENE_TITLE**	**RANK IN GENE LIST**	**RANK METRIC SCORE**	**RUNNING ES**		
	IL2RA	interleukin 2 receptor, alpha					
	CD3G	CD3g molecule, gamma (CD3-TCR complex)					
BIOCARTA_TOB1_PATHWAY	TGFB1	transforming growth factor, beta 1 (Camurati-Engelmann disease)					
	TGFB2	transforming growth factor, beta 2					
	TGFB3	transforming growth factor, beta 3					
	CD3E	CD3e molecule, epsilon (CD3-TCR complex)					
	TGFBR2	transforming growth factor, beta receptor II (70/80kDa)					

IFNG	interferon, gamma	
TGFBR1	transforming growth factor, beta receptor I (activin A receptor type II-like kinase, 53kDa)	

NAME	SIZE	ES	NES	NOM p-val	FDR q-val	LEADING EDGE	
						tags=39%, signal=48%	list=19%,
	23	0.56030774	1.706622	0	0.08098701		

BIOCARTA_CCR3_PATHWAY

GENE SYMBOL	GENE_TITLE	RANK IN GENE LIST	RANK METRIC SCORE	RUNNING ES
CCL11	chemokine (C-C motif) ligand 11			
NOX1	NADPH oxidase 1			
null	null			
PLCB1	phospholipase C, beta 1 (phosphoinositide-specific)			
LIMK1	LIM domain kinase 1			
MYL2	myosin, light chain 2, regulatory, cardiac, slow			
RHOA	ras homolog gene family, member A			
CFL1	cofilin 1 (non-muscle)			
GNB1	guanine nucleotide binding protein (G protein), beta polypeptide 1			

NAME	SIZE	ES	NES	NOM p-val	FDR q-val	LEADING EDGE	
						tags=56%, signal=76%	list=26%,
	16	0.5968773	1.6776568	0.014260249	0.09837541		

BIOCARTA_IL7_PATHWAY

GENE SYMBOL	GENE_TITLE	RANK IN GENE LIST	RANK METRIC SCORE	RUNNING ES
NMI	N-myc (and STAT) interactor			
IL2RG	interleukin 2 receptor, gamma (severe combined immunodeficiency)			
FYN	FYN oncogene related to SRC, FGR, YES			
JAK1	Janus kinase 1 (a protein tyrosine kinase)			
BCL2	B-cell CLL/lymphoma 2			
LCK	lymphocyte-specific protein tyrosine kinase			
STAT5B	signal transducer and activator of transcription 5B			
IL7R	interleukin 7 receptor			
EP300	E1A binding protein p300			

NAME	SIZE	ES	NES	NOM p-val	FDR q-val	LEADING EDGE	
						tags=53%, signal=65%	list=19%,
	17	0.5901258	1.6672796	0.014109347	0.09977724		

BIOCARTA_IL10_PATHWAY

GENE SYMBOL	GENE_TITLE	RANK IN GENE LIST	RANK METRIC SCORE	RUNNING ES
TNF	tumor necrosis factor (TNF superfamily, member 2)			
IL1A	interleukin 1, alpha			
STAT4	signal transducer and activator of transcription 4			
IL10RA	interleukin 10 receptor, alpha			
STAT3	signal transducer and activator of transcription 3 (acute-phase response factor)			
IL10RB	interleukin 10 receptor, beta			
IL6	interleukin 6 (interferon, beta 2)			
STAT1	signal transducer and activator of transcription 1, 91kDa			
JAK1	Janus kinase 1 (a protein tyrosine kinase)			

NAME	SIZE	ES	NES	NOM p-val	FDR q-val	LEADING EDGE	
	18	0.56710243	1.6400455	0.017636685	0.1182908	tags=44%,	list=13%,

ART A_CT LA4_ PAT HW

signal=51%

GENE SYMBOL	GENE_TITLE	RANK IN GENE LIST	RANK METRIC SCORE	RUNNING ES
CD3G	CD3g molecule, gamma (CD3-TCR complex)			
CTLA4	cytotoxic T-lymphocyte-associated protein 4			
CD80	CD80 molecule			
GRB2	growth factor receptor-bound protein 2			
HLA-DRB1	major histocompatibility complex, class II, DR beta 1			
CD86	CD86 molecule			
CD3E	CD3e molecule, epsilon (CD3-TCR complex)			
ICOS	inducible T-cell co-stimulator			

NAME	SIZE	ES	NES	NOM p-val	FDR q-val	LEADING EDGE	
						tags=47%, signal=56%	list=15%,
	19	0.55310553	1.6192266	0.019264448	0.13256052		

GENE SYMBOL	GENE_TITLE	RANK IN GENE LIST	RANK METRIC SCORE	RUNNING ES
CD40	CD40 molecule, TNF receptor superfamily member 5			
IL2RA	interleukin 2 receptor, alpha			
IL18R1	interleukin 18 receptor 1			
HLA-DRB1	major histocompatibility complex, class II, DR beta 1			
CD86	CD86 molecule			
CD40LG	CD40 ligand (TNF superfamily, member 5, hyper-IgM syndrome)			
IFNGR1	interferon gamma receptor 1			
IL12RB1	interleukin 12 receptor, beta 1			
IL4R	interleukin 4 receptor			

BIOCARTA_TH1TH2_PATHWAY

NAME	SIZE	ES	NES	NOM p-val	FDR q-val	LEADING EDGE	
						tags=39%, signal=49%	list=20%,
	23	0.51610255	1.6166061	0.011705685	0.12796181		

GENE SYMBOL	GENE_TITLE	RANK IN GENE LIST	RANK METRIC SCORE	RUNNING ES
CD79B	CD79b molecule, immunoglobulin-associated beta			
TGFB1	transforming growth factor, beta 1 (Camurati-Engelmann disease)			
TGFB2	transforming growth factor, beta 2			
MDM2	Mdm2, transformed 3T3 cell double minute 2, p53 binding protein (mouse)			
TGFB3	transforming growth factor, beta 3			
CD79A	CD79a molecule, immunoglobulin-associated alpha			
TGFBR2	transforming growth factor, beta receptor II (70/80kDa)			
SMAD5	SMAD, mothers against DPP homolog 5 (Drosophila)			
TGFBR1	transforming growth factor, beta receptor I (activin A receptor type II-like kinase, 53kDa)			

BIOCARTA_CTCF_PATHWAY

NAME	SIZE	ES	NES	NOM p-val	FDR q-val	LEADING EDGE	
						tags=43%, signal=56%	list=24%,
	21	0.53111434	1.6125036	0.019748654	0.12476949		

GENE SYMBOL	GENE_TITLE	RANK IN GENE LIST	RANK METRIC SCORE	RUNNING ES
IL2RA	interleukin 2 receptor, alpha			
IL2RG	interleukin 2 receptor, gamma (severe combined immunodeficiency)			
GRB2	growth factor receptor-bound protein 2			

BIOCARTA_IL2_PATHWAY

SYK	spleen tyrosine kinase
IL2RB	interleukin 2 receptor, beta
JAK1	Janus kinase 1 (a protein tyrosine kinase)
JUN	jun oncogene
LCK	lymphocyte-specific protein tyrosine kinase
STAT5B	signal transducer and activator of transcription 5B

NAME	SIZE	ES	NES	NOM p-val	FDR q-val	LEADING EDGE	
	32	0.48099118	1.6103619	0.013651877	0.12046393	tags=41%, signal=47%	list=14%,
	GENE SYMBOL	**GENE_TITLE**	**RANK IN GENE LIST**	**RANK METRIC SCORE**	**RUNNING ES**		
	TNF	tumor necrosis factor (TNF superfamily, member 2)					
	IL1B	interleukin 1, beta					
	TGFB1	transforming growth factor, beta 1 (Camurati-Engelmann disease)					
	IRAK3	interleukin-1 receptor-associated kinase 3					
	IL1A	interleukin 1, alpha					
	IL1RN	interleukin 1 receptor antagonist					
	MYD88	myeloid differentiation primary response gene (88)					
	TGFB2	transforming growth factor, beta 2					
	TGFB3	transforming growth factor, beta 3					
	IL1RAP	interleukin 1 receptor accessory protein					
	MAPK14	mitogen-activated protein kinase 14					
	IL6	interleukin 6 (interferon, beta 2)					
	IFNA1	interferon, alpha 1					

(BIOCARTA_IL1R_PATHWAY)

NAME	SIZE	ES	NES	NOM p-val	FDR q-val	LEADING EDGE	
	17	0.5490539	1.5755872	0.038732395	0.14988309	tags=65%, signal=88%	list=26%,
	GENE SYMBOL	**GENE_TITLE**	**RANK IN GENE LIST**	**RANK METRIC SCORE**	**RUNNING ES**		
	TNFAIP3	tumor necrosis factor, alpha-induced protein 3					
	TANK	TRAF family member-associated NFKB activator					
	TRAF1	TNF receptor-associated factor 1					
	DUSP1	dual specificity phosphatase 1					
	TNFRSF1B	tumor necrosis factor receptor superfamily, member 1B					
	TRAF3	TNF receptor-associated factor 3					
	RIPK1	receptor (TNFRSF)-interacting serine-threonine kinase 1					
	NFKB1	nuclear factor of kappa light polypeptide gene enhancer in B-cells 1 (p105)					
	TRAF2	TNF receptor-associated factor 2					
	RELA	v-rel reticuloendotheliosis viral oncogene homolog A, nuclear factor of kappa light polypeptide gene enhancer in B-cells 3, p65 (avian)					
	IKBKAP	inhibitor of kappa light polypeptide gene enhancer in B-cells, kinase complex-associated protein					

(BIOCARTA_TNFR2_PATHWAY)

Table 4.12.4 Brief description of BIOCARTA pathways.

Standard name	Systematic name	Brief description
LAIR	M3952	Cells and Molecules involved in local acute inflammatory response
NKT	M4047	Selective expression of chemokine receptors during T-cell polarization
COMP	M917	Complementary pathway
DC	M9177	Dendritic cells in regulating TH1 and TH2 Development
ERYTH	M9367	Erythrocyte Differentiation Pathway
IL22BP	M8066	IL22 Soluble Receptor Signaling Pathway
NO2IL12	M6231	NO2-dependent IL 12 Pathway in NK cells
STEM	M5298	Regulation of hematopoiesis by cytokines
TOB1	M18215	Role of Tob in T-cell activation
CCR3	M9152	CCR3 signaling in Eosinophils
IL10	M6778	IL-10 Anti-inflammatory Signaling Pathway
CTLAA	M1467	The Co-Stimulatory Signal During T-cell Activation
CTCF	M11420	CTCF: First Multivalent Nuclear Factor
IL1R	M12095	Signal transduction through IL1R

Chapter 5

5.1 IL-8 levels in human patients with BE and EAC

Human patient data kindly shared by collaborators from Trinity College, Dublin, Ireland showed interesting findings on levels of IL-8 in circulation, within a human-study cohort including BE and EAC patients. Remarkably no correlation was found between human BMI and IL-8 circulating levels (Figure 5.1A). Patients were assessed solely on BMI measurement and IL-8 concentration measured in serum. Interestingly enough, when compared to BE patients, patients who progressed to EAC revealed significantly elevated IL-8 levels in serum (Figure 5.1 B).
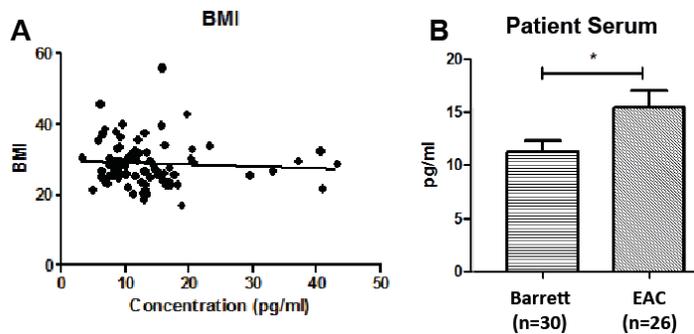
Figure 5.1: Human data highlighting levels of IL-8 in disease progression of BE and EAC.
(A) Correlation between IL-8 serum levels (pg/mL) and BMI measurements from patients in a Clinical study at Trinity College, Dublin. (B) Measured concentrations of IL-8 (pg/mL) in patient serum. (Data kindly shared by the Lysaght and O'Sullivan labs, Trinity College, Dublin, Ireland; p-value not provided by collaborators).

These findings, taken together with the low-body mass phenotype (Section 3.3), a strong increase in neutrophil recruitment in the esophagus and cardia tissue (Section 4.4), along with an increase in inflammatory cytokines, including KC and its receptors (Section 4.6.2), made a strong case for examining of the role of IL-8 in the L2-IL-1beta model.

5.2 IL-8 Over-Expression Accelerates BE and EAC Phenotype in the L2-IL-1beta Mouse Model

To assess the influence of IL-8, the L2-model was crossed with a transgenic model of human-IL-8 over-expression to create the L2-IL-1beta/IL-8Tg (here onwards referred to as L2/IL-8Tg) mouse line.

L2/IL-8Tg offspring were born at a normal Mendelian ratio, and were aged alongside L2-controls, up to 9- and 12-month time-points and then sacrificed and organs collected for further analysis.
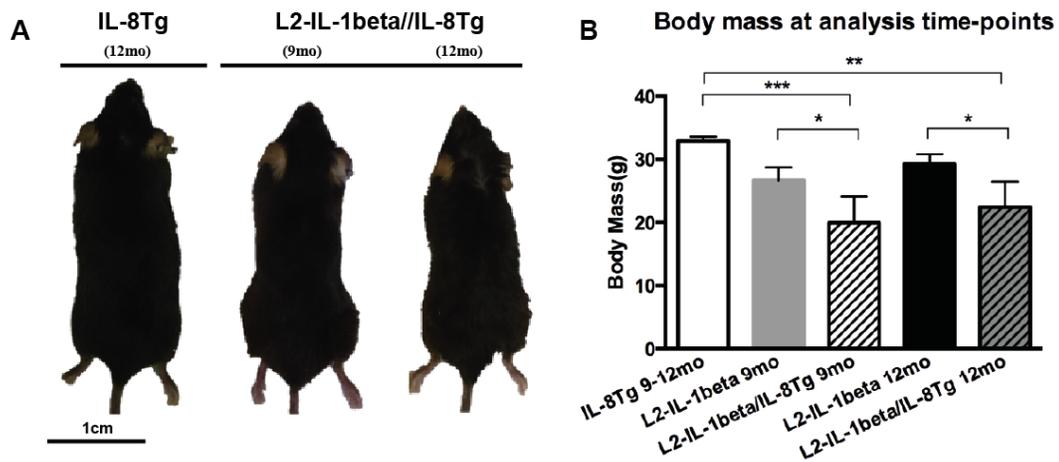
Figure 5.2.1: Phenotype of the L2/IL-8Tg mouse model.
L2-IL-1beta mice were crossed with IL-8Tg mice, resulting in the L2-IL-1beta/IL-8Tg (L2/IL-8Tg) line. L2/IL-8Tg mice were aged to 9- and 12-months of age. (A) Phenotypically, the L2/IL-8Tg mice appeared smaller than their IL-8Tg controls, similarly, (B) lower body mass was observed in the L2/IL-8Tg mice. Scale bar set to 1cm, group size (n=3-6). All data are means ± standard deviation. Statistical analysis was performed using one-way ANOVA and Tukey's post-hoc test. Group size (n=3-5). Asterisks indicate significant differences, ****p≤0.0001, ***p≤0.001, **p≤0.01, *p≤0.05.

As with L2-HFD mice, the L2/ IL-8Tg mice did not increase significantly in body mass as they aged (Figure 5.2.1). In fact, morphologically they appeared smaller in size when compared to IL-8Tg mice, and similar in stature to the L2-HFD mice (Figure 4.1.1). The L2/IL-8Tg mice displayed a leaner physique, accompanied by a pronounced curved spine and raised fur at 9- and 12-months of age. This correlated with a significantly lower overall body mass in comparison with IL-8Tg mice and L2-mice (9-12 months of age, IL-8Tg, 32.87 ± 0.75g. 9-months of

age L2-control, 26.68 ± 2.03g, L2/IL-8Tg, 19.96 ± 4.18g, 12-months of age L2-control, 29.25 ± 1.56g, L2/IL-8Tg, 22.44 ± 4.02g). Body mass values were similar to those noted in the HFD study in Chapter 3, Appendix table 3.6.1. Upon organ resection, little to no fat mass was observed visually.
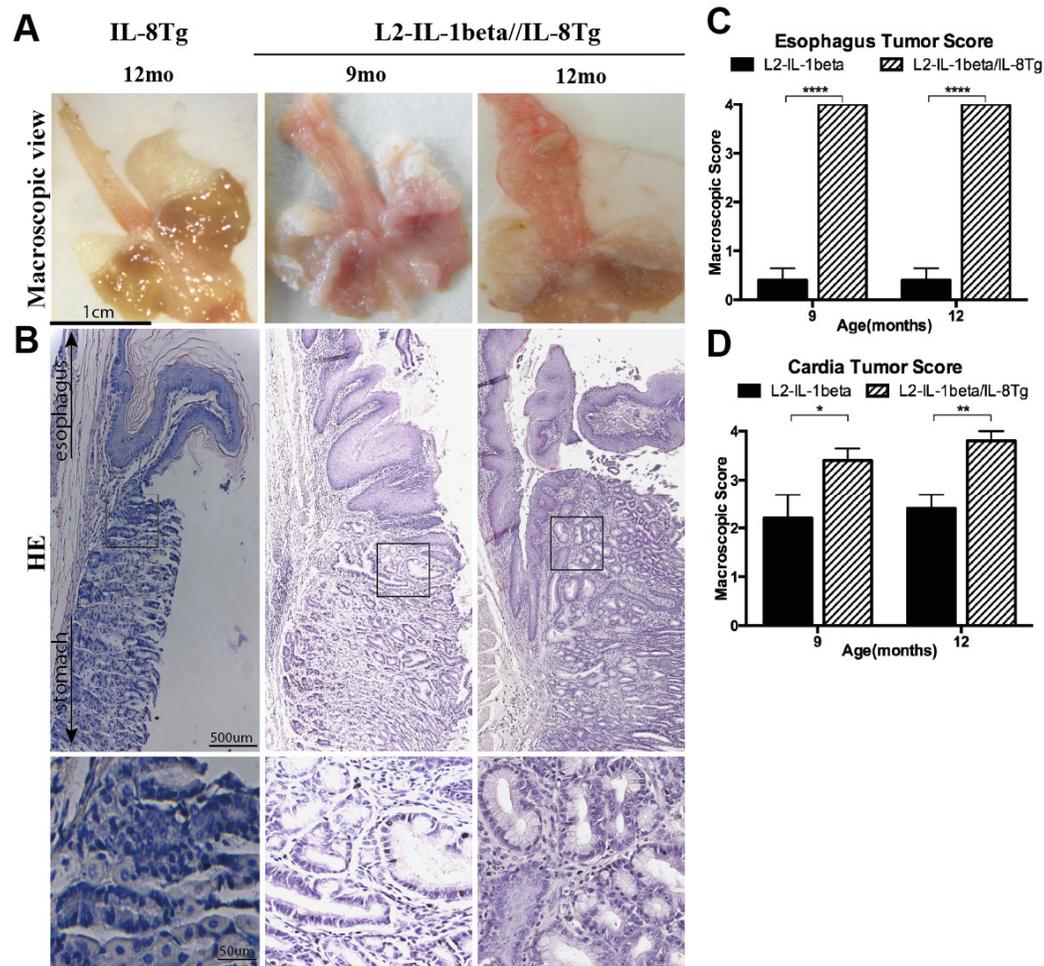
Figure 5.2.2: The macroscopic phenotype of the L2/IL-8Tg model shows an accelerated phenotype.
L2/IL-8Tg mice were aged to 9- and 12-months of age and the esophagus and stomachs were resected and observed for (A) macroscopic and (B) histological step-wise progression of BE to EAC through pictures and HE stainings, respectively (scale bar in large panels, 500 μm, scale bar in small panels, 50 μm). (C, D) Quantification of visible lesions/ tumors in the esophagus and cardia of L2/IL-8Tg mice compared to L2-IL-1beta mice. All data are means ± standard deviation. Statistical analysis was performed using two-way ANOVA and Tukey's post-hoc test. Group size (n=3-5). Asterisks indicate significant differences, Figure 5.2.2: The macroscopic phenotype of the L2/IL-8Tg model shows an accelerated phenotype. ****$p \leq 0.0001$, ***$p \leq 0.001$, **$p \leq 0.01$, *$p \leq 0.05$.

Assessment of the resected esophagus and stomach revealed a very similar macroscopic phenotype to the one observed in L2-HFD mice (Figure 4.1.1 A) at both analysis time points in the L2/IL-8Tg model (Figure 5.2.1 A). Large, visible lesions (up to 4mm in length) were noted in the esophagus of the mice, in addition to visible lesions in the cardia region. L2/IL-8Tg mice also revealed significant acceleration of the disease based on macroscopic scoring of the esophagus (IL-8Tg (9-12mo), 0.00 ± 0.00, L2 (9mo) 0.40 ± 0.54, L2/IL-8Tg (9mo), 4.00 ± 0.00, L2 (12mo) 0.40 ± 0.57, L2/IL-8Tg (12mo), 4.00 ± 0.00) and of the cardia region (IL-8Tg (9-12mo), 0.00 ± 0.00, L2 (9mo) 2.10 ± 0.89, L2/IL-8Tg (9mo), 3.40 ± 0.54, L2 (12mo) 2.40 ± 0.65, L2/IL-8Tg (12mo), 3.8 ± 0.44). Additionally, IL-8Tg displayed an identical phenotype as was previously seen in WT-mice in the HFD study described in Chapter 4 (Macroscopic images: Figure 5.2.1 A, showing IL-8Tg mice and Figure 4.1.1 A, showing WT mice). Evaluation of IL-8Tg mice resulted in macroscopic scores of zero in the esophagus and cardia regions for all mice (therefore, data not shown in graphs in Figure 5.2.2 C, D).

Based upon previously described criteria[146] a histopathological scoring system for the mouse SCJ was developed to establish whether the L2/IL-8Tg mouse model develops metaplasia as seen in the human disease state and previously observed in the L2-IL-1beta model. Histopathological evaluation conducted by a pathologist and medical doctor was performed on sagittal sections through the esophagus and stomach in a blinded fashion.

L2/IL-8Tg mice at 9- and 12-month time-points presented with acute and chronic inflammation throughout the esophagus, SJC and stomach regions. The degree of acute and chronic inflammation appeared to increase from moderate inflammation towards severe inflammation with age. Regardless of time-points, L2-IL-8Tg mice presented with high scores for metaplasia, showing multiple metaplastic glands throughout the SCJ area. Interestingly, as L2/IL-8Tg mice aged, they presented with increased dysplasia. 9-month old mice presented with atypia in glanular complexity and low-grade dysplasia, and by 12-months of age this increased in severity scores to low-grade and in some mice high-grade dysplasia.

This analysis revealed a stepwise progression to BE, to metaplasia and dysplasia observed in HE stainings with the major histopathological changes occurring at the squamocolumnar junction (SCJ) as was previously observed in the HFD study.
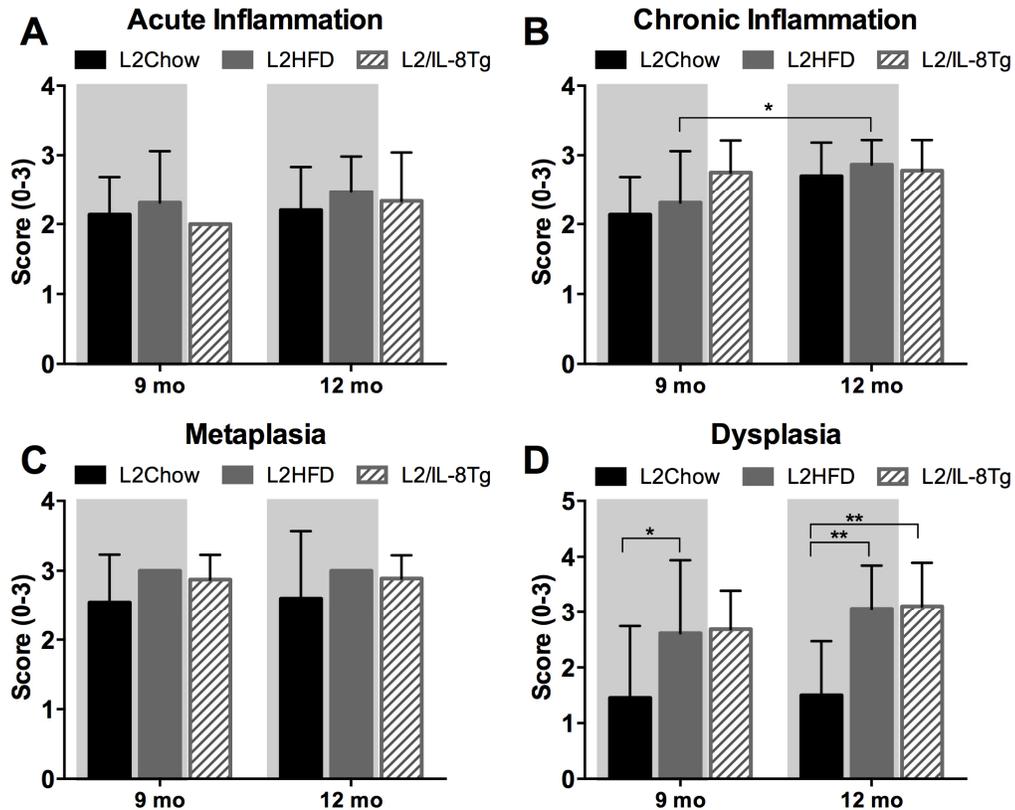
Figure 5.2.3: Pathological scoring of esophageal and cardia tissue in L2/IL-8Tg mice.
IL-8 over-expression induced acute and chronic inflammation in the esophagus and cardia leading to the development of metaplasia and dysplasia in the L2/IL-8Tg mouse model at 9- and 12-months of age. Blinded histopathological scoring was conducted by a pathologist and medical doctor on sections of esophagus and cardia tissue from L2/IL-8Tg mice. (A) Acute inflammation, (B) chronic inflammation, (C) metaplasia and (D) dysplasia in columnar and mucinous tissues were assessed using HE stained slides. All data are means ± standard deviation; group size varied (n=9-12 slides/ group (genotype and diet). Statistical analysis was performed using two-way ANOVA and Sidak's multiple comparisons test. Asterisks indicate significant differences compared with control or between groups (****$p \leq 0.0001$, ***$p \leq 0.001$, **$p \leq 0.01$, *$p \leq 0.05$).

Furthermore, in order to verify that the IL-8 transgene was successfully crossed into the L2/IL-8Tg model, several genes were quantified as proof of principle. These included the IL-8 transgene (human), and IL-1beta (human and murine

forms). As was expected, IL-8 transgene expression was detected in the esophagus, forestomach and cardia regions of the L2/IL-8Tg model (Figure 5.2.3 A). While not significantly different, there appeared to be a higher level of expression in the esophagus of L2/IL-8Tg mice in comparison with the L2-model. IL-8 expression was significantly higher in the forestomach and cardia of the L2/IL-8Tg model compared to the L2-model. Very insignificant levels of IL-8 were detected in the stomach tissue from the L2- and L2/IL-8Tg model. The expression of h-IL-1beta was also detected, as a direct result of the h-IL-1beta cDNA insert that targets expression in the oral cavity, esophagus, forestomach and cardia regions in the L2-IL-1beta model (Figure 5.2.3 B). As expected, the L2-model had the highest expression of h-IL-1beta; L2/IL-8Tg mice also expressed this cytokine, however at slightly lower levels in the cardia region. Murine IL-1beta levels were also expressed at similar levels between the L2- and L2/IL-8Tg (9- and 12-months) models compared to IL-8Tg expression (Figure 5.2.3 C).
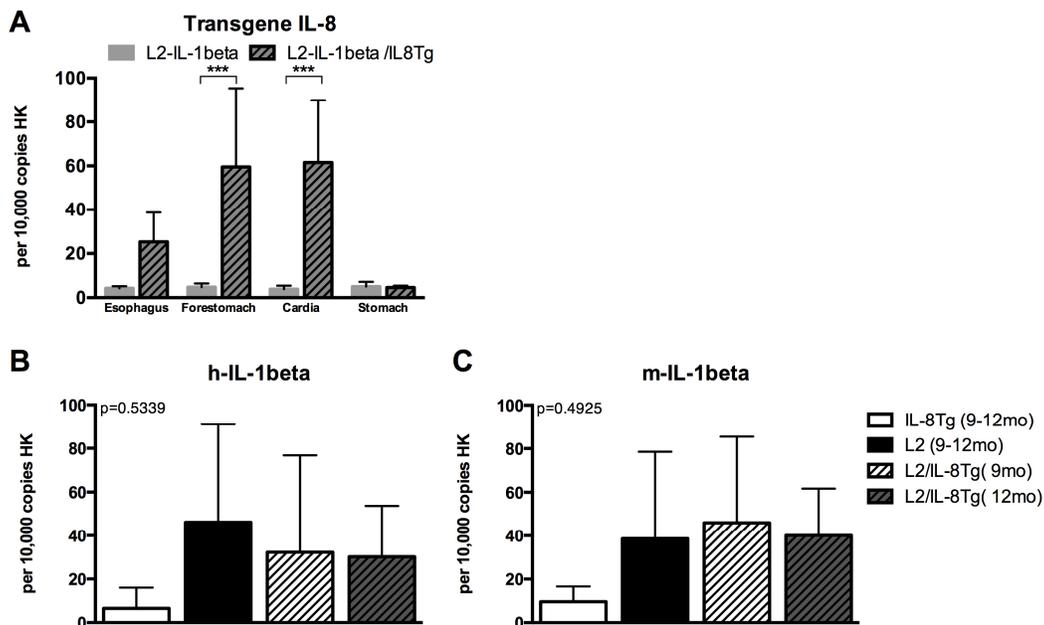
Figure 5.2.3: Proof of principle gene expression profiles in the L2/IL-8Tg model.
(A) Expression levels of the transgene IL-8 (human) in esophageal, forestomach, cardia and stomach tissue of 12-month of L2-IL-1beta and L2/IL-8Tg mice. Expression of IL-beta (B) human and (C) murine in IL-8Tg, L2-IL-1beta and 9- and 12- month old L2/IL-8Tg mice. All data are means ± standard deviation. Statistical analysis was performed using two-way ANOVA and Sidak's post hoc-test for transgene IL-8, and one-way ANOVA for h- and m-IL-1beta. Group size (n=4-8). Asterisks indicate significant differences, ****$p \leq 0.0001$, ***$p \leq 0.001$, **$p \leq 0.01$, *$p \leq 0.05$

5.3 IL-8 Over-Expression Leads to Increased Metaplasia and Dysplasia, Proliferation, Expansion of Gastric Cardia Progenitor cells and Smooth Muscle Differentiation in the L2/IL-8Tg model

Alcian-blue-positive acidic mucins (PAS+) are primarily found in goblet cells of the intestinal type of metaplasia[147]. While classical goblet cells are not observed in the L2-IL-1beta model, nor the L2/IL-8Tg model, the mucus producing columnar cell types observed in Figure 5.3.1 A, in the L2-IL-8Tg mouse model were consistent with Barrett-like metaplasia[89].

All of the L2/IL-8Tg mice between 9- and 12-months of age in the study, presented with mucus producing (PAS+) cells at the SCJ, similar to human BE. Figure 5.3.1, illustrates the % of positive cells in the cardia region of 9-and 12-month old L2/IL-8Tg mice, quantified from assessment of 3-4 regions of esophagus/ stomach tissue per mouse; 5-8 mice were assessed per time-point.

A clear statistical difference was observed in a direct comparison of 9- and 12-month old L2/IL-8Tg mice in terms of % of the cardia region with PAS+ cells (Figure 5.3.1 B). Furthermore, when compared to the L2-Chow and –HFD mice, the L2/IL-8Tg mice revealed no significant difference in the percentage of PAS+ cells between 9- and 12-month time points. Both L2-HFD and L2/IL-8Tg groups showed a higher trend in PAS+ cells compared to the L2-Chow mice.

It appeared that both age cohorts of the L2/IL-8Tg model develop severe columnar metaplasia. Aging also highlighted an increase in the occurrence of low- and high-grade dysplasia in this model.

As was carried out with the L2-IL-1beta mice, overall proliferation in esophagus and cardia tissues of L2/IL-8Tg was assessed with Ki67 stainings. An increasing trend in overall proliferation was noted as the L2/IL-8Tg mice aged (Figure 5.3.1 C), this was in agreement with the results observed in the L2-HFD model (Figure 4.3). While not significantly higher, L2-HFD and L2/IL-8Tg esophageal and cardia regions were more proliferative than those of L2-Chow mice (Figure 5.3.1 D).

As was carried out with the L2-IL-1beta model on chow and HFD, progenitor cells in the gastric cardia of the L2/IL-8Tg model were also assessed for alterations. In the L2/IL-8Tg model, IHC staining revealed an accumulation of Dclk-1+ cells adjacent to metaplastic mucous producing cells within the BE area (Figure 5.3.2 C), as was previously observed in the L2-HFD mice (Figure 4.8.1 A). An abundance of Dclk-1+ cells were noted along the gastric cardia region and this gradual accumulation of Dclk-1+ cells along the SCJ in the L2/IL-8Tg mice was positively correlated with the development of metaplasia along the SCJ. Quantification of Dclk-1+ cells in the cardia region of the L2/IL-8Tg mice showed unchanged amounts of Dclk-1+ cells with disease progression (Figure 5.3.2 D).
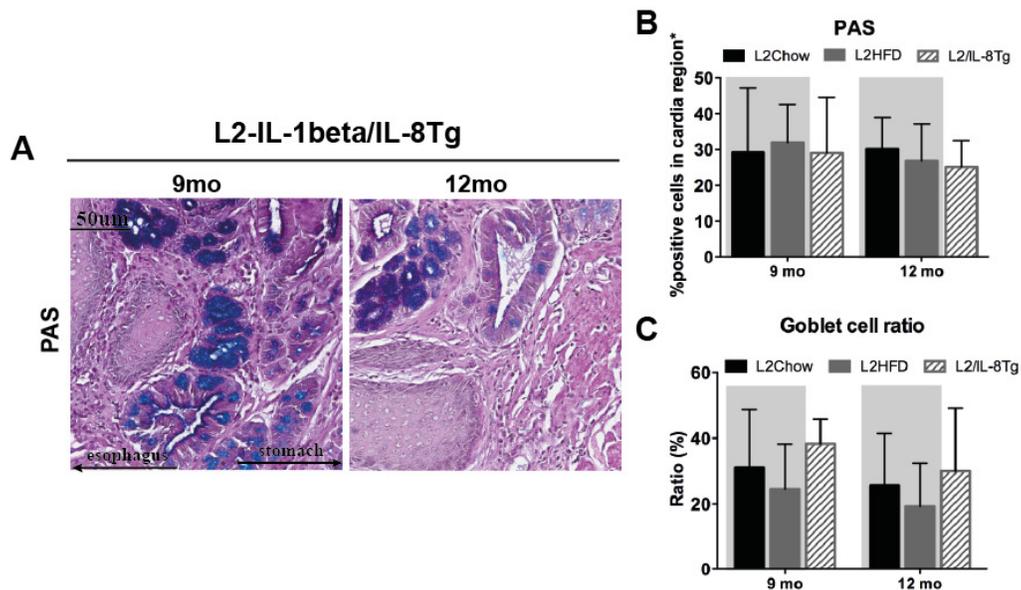
Figure 5.3.1: IL-8 over-expression triggers metaplasia in L2-IL-1beta mice at 9- and 12-months of age.
(A) PAS staining and (B) quantification of % of PAS+ cells in the cardia region of L2/IL-8Tg mice and (C) goblet cell ratio (scored by pathologist and medical doctor) in L2/IL-8Tg mice in comparison with L2-Chow and –HFD mice. Scale bar, 50 μm. All data are means ± standard deviation. Statistical analysis was performed using two-way ANOVA and Sidak's multiple comparisons test (Group size (n=5-8), assessment of 3-4 regions of esophagus/ stomach tissue per mouse per time point used for quantification. Asterisks indicate significant differences, ****$p \leq 0.0001$, ***$p \leq 0.001$, **$p \leq 0.01$, *$p \leq 0.05$. Grey region in bar graphs represents L2-HFD study data already shown in Chapter 4, shown here for comparison of the models.

However, L2-IL-1beta mice on HFD presented a significant increase in Dclk-1 cells as they aged and progressed from stages of metaplasia to dysplasia compared to L2-Chow mice. While a statistical significance was not determined between L2-HFD and L2/IL-8Tg mice, a visible trend was noticed;IL-8 over-expression result in an expansion of gastric cardia progenitor cells in the L2model, but not as dramatically as with HFD.

As noted in the Chapter 4, it is important to keep in mind that in mice with a very severe phenotype and high-grade dysplasia, a lower number of Dclk-1+ cells were observed as was reported in the original publication[89] on the L2-IL-1beta model. However since only a few mice progressed much faster than the others, this observation was lost in quantification.

Lastly, smooth muscle differentiation was also observed in L2/IL-8Tg mice. During the stepwise progression to high-grade dysplasia, a gradual increase in aSMA+ stromal myofibroblasts (Figure 5.3.2 E, F) was observed in L2-Chow mice, while the onset of a HFD revealed a significant increase at 12-months of age. In comparison to the two L2-groups, the L2/IL-8Tg model showed a further significant increase in aSMA+ cells by 9-months, which appeared to remain constant at 12-months.

The findings from these IHC stainings reveal that IL-8 over-expression in the L2/IL-8Tg model can lead to increased metaplasia and dysplasia, in addition to increased proliferation; expansion of the gastric cardia progenitor cells Dclk-1 and increased smooth muscle differentiation.

Lastly, it is to be noted that IL-8Tg mice were not further assessed with IHC due to the WT-phenotype that was observed in 100% of mice.
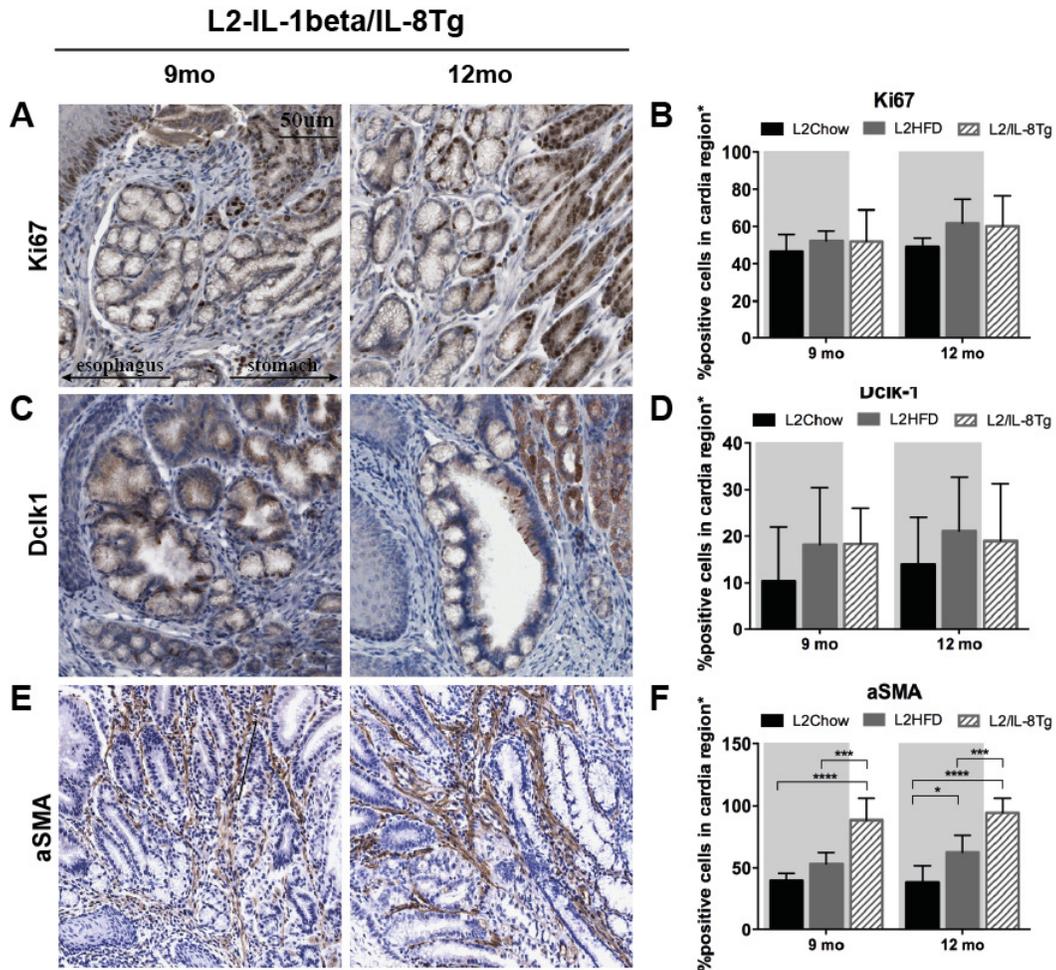
Figure 5.3.2: IL-8 over-expression triggers increased proliferation, overall expansion of the gastric cardia progenitor cells and aSMA differentiation in L2-IL-1beta mice at 9- and 12-months of age.
% Positive cells in the cardia region of L2/IL-8Tg mice were evaluated for (A) Ki67 staining and (B) quantification of % of Ki67+ cells (C) Dclk-1 staining and (D) quantification of % of Dclk-1+ cells (E) aSMA+ staining and (F) quantification of % aSMA+ cells. Scale bar, 50 μm. All data are means ± standard deviation. Statistical analysis was performed using two-way ANOVA and Sidak's multiple comparisons test (Group size (n=5-8), assessment of 3-4 regions of esophagus/ stomach tissue per mouse per time point used for quantification. Asterisks indicate significant differences, ****$p \leq 0.0001$, ***$p \leq 0.001$, **$p \leq 0.01$, *$p \leq 0.05$. Grey region in bar graphs represents L2-HFD study data already shown in Chapter 4, shown here for comparison of the models

5.4 IL-8 Induces a Similar Immune Cell Microenvironment Composition in the L2/IL-8Tg model as was Observed with HFD in the L2-IL-1beta Model

To understand the influence of IL-8 on IL-1beta mediated inflammation and carcinogenesis, in particular the role of inflammatory cells in the L2/IL-8Tg model, the distribution of leukocytes in the esophagus, forestomach and cardia (hence forth referred to as "cardia") at 9 and 12-months of age in the L2/IL-8Tg model were examined.

In 9-month-old L2/IL-8Tg mice with low- to high-grade dysplasia, showed an increased trend in neutrophil (CD45+CD11B+F480-Ly6G+) accumulation in esophageal tissue was observed by flow cytometry (Figure 5.4.1 A-C). Additionally, while there did not appear to be a significant accumulation of immature myeloid cells (IMC) (CD45+CD11b+Ly6G^{low}Ly6C+) in esophageal tissue there did appear to be an increasing trend in the L2/IL-8Tg mice at both time points (Figure 5.4.1 D-F). Of the other myeloid cell type that was assessed, macrophages (CD45+CD11b+F4/80+Ly6G-) revealed an increasing trend from 9- to 12-months of age in the L2/IL-8Tg model, however this observation was not significant (Figure 5.4.1 G).

No significant changes in the accumulation of CD3+CD4+ and CD3+CD8+ cytotoxic T-cells were observed (Figure 5.4.1 H-M). CD3+CD4+ cells showed a trend towards increased expression in the L2/IL-8Tg model compared to the L2-model, however, over time no changes were observed. CD3+CD4+ cells were significantly higher in 9-month of L2/IL-8Tg mice compared to L2-mice, however this trend was reversed at 12-months of age, where L2-mice showed higher levels. NKT cells (CD3+CD4-CD8-NK1.1+) showed a trend towards increased levels in the L2/IL-8Tg model compared to L2-mice at 9- and 12-month time-points (Figure 5.4.1 N). Lastly, gamma delta T-cells (CD3+CD4-CD8-gdTCR+) appeared at higher levels in L2-mice at 9-months, however at 12-months there appeared to be no difference between the two model (Figure 5.4.1 O).

Esophagus
Myeloid cell populations
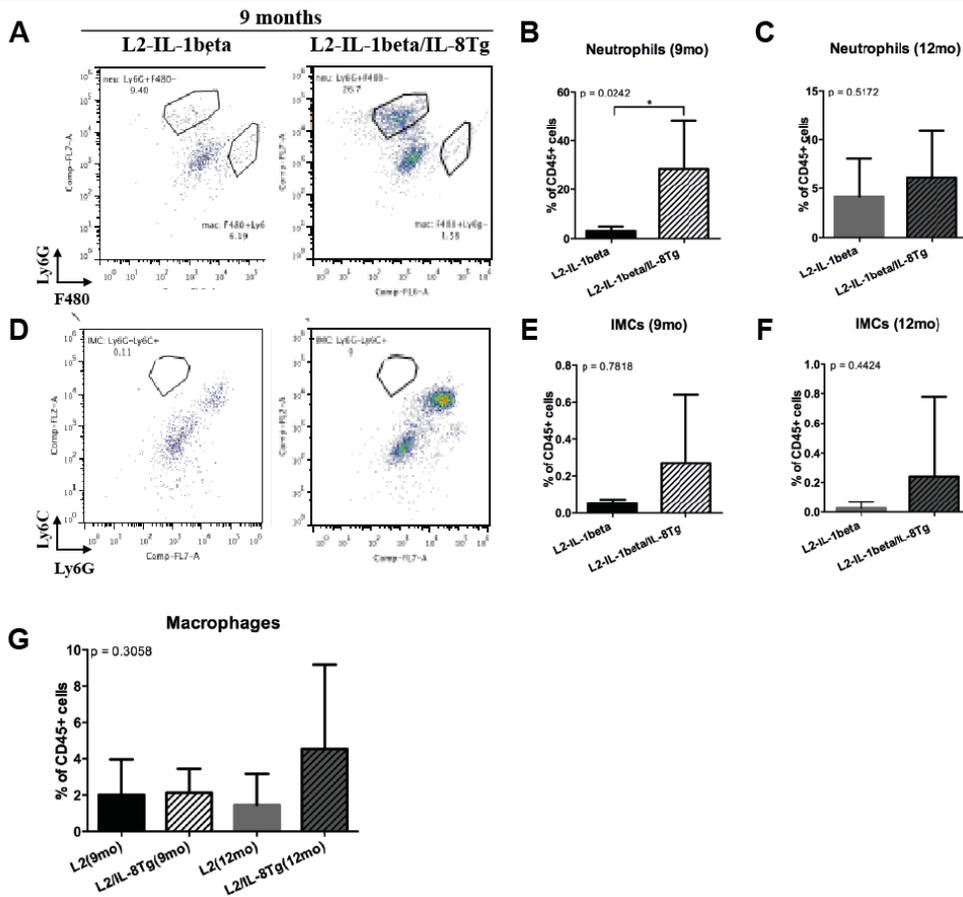
Figure 5.4.6: IL-8 over-expression accelerates immune cell accumulation, specifically neutrophil populations in the esophagus of L2/IL-8Tg mice.
(A-C) Neutrophils and (D-F) immature myeloid cells (IMC) from the esophagus of 9- and 12-month old L2/IL-8Tg mice were analyzed by flow cytometry and quantified. All data are means ± standard deviation. Statistical analysis was performed using one-way ANOVA or Student's t-tests. Asterisks indicate significant differences compared with control or between groups. ****$p \leq 0.0001$, ***$p \leq 0.001$, **$p \leq 0.01$, *$p \leq 0.05$.

In the cardia region, myeloid cell populations showed no significant differences between L2- and L2/IL-8Tg-mice, however higher cell populations were observed in the L2/IL-8Tg mice at 9- and 12-months of age (Appendix Figure 5.8.1 A-C). Interestingly, the population of CD3+CD4+ cells was much lower in the L2/IL-8Tg mice at both time points, in cardia tissue. On the other hand, CD3+CD8+ cells appeared in higher levels the L2/IL-8Tg mice at both time points, as well as in the 12-month old L2-mice (Appendix Figure 5.8.1 D, E). NKT cell populations (CD3+CD4-CD8-NK1.1+) remained relatively low across the

groups, except for a higher amount of cells noted in 12-month old L2-mice (Appendix Figure 5.8.1 F).

T-cell populations
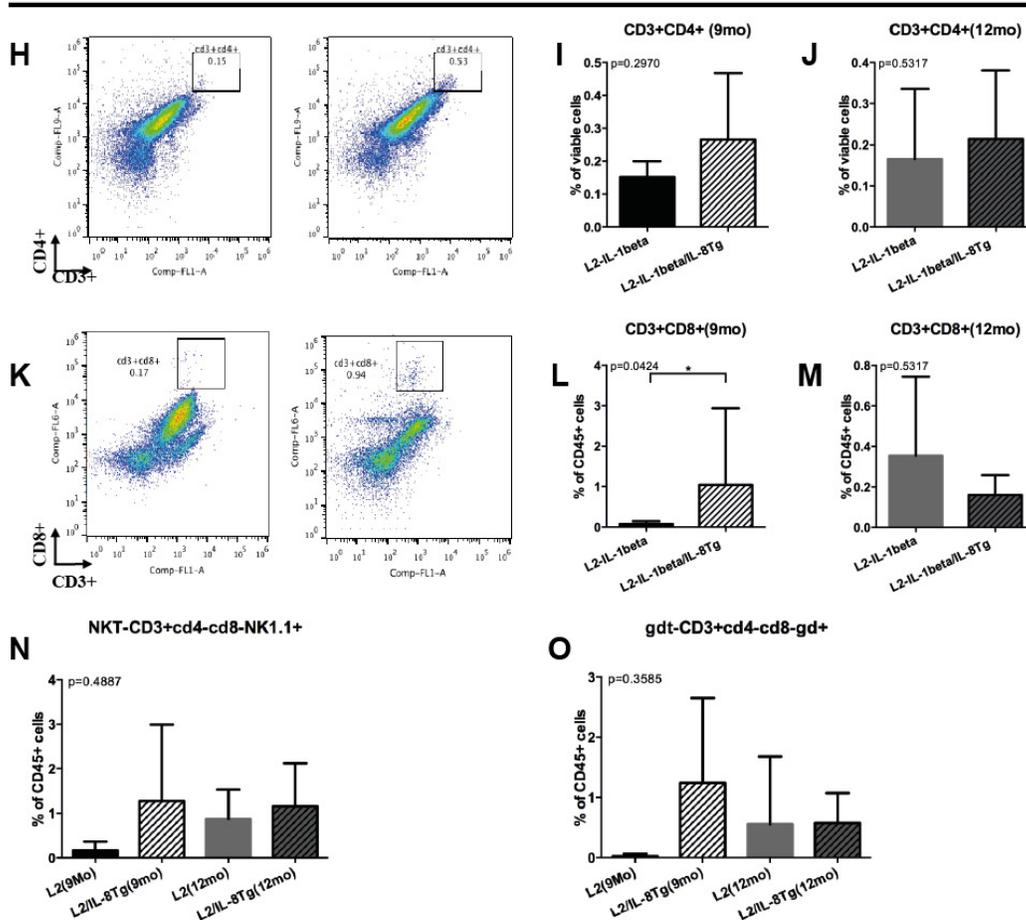
Figure 5.4.2: Changes in T-cell populations in the esophagus resulting from IL-8 over-expression in the L/IL-8Tg model.
T-helper cells (H-CD3+CD4+, (K-M) CD4+CD8+, NKT (N)(CD3+CD4-CD8-NK1.1+) and gamma delta T-cells (O)(D3+CD4-CD8-gdTCR+) cells from the esophagus of 9- and 12-month old L2/IL-8Tg mice were analyzed by flow cytometry and quantified. All data are means ± standard deviation. Statistical analysis was performed using one-way ANOVA or Student's t-tests. Asterisks indicate significant differences compared with control or between groups. ****p≤0.0001, ***p≤0.001, **p≤0.01, *p≤0.05.

Lastly, gamma delta T-cells (CD3+CD4-CD8-gdTCR+) appeared higher in both L2 and L2/IL-8Tg mice at the 9-months time-point. This trend decreased to lower cell counts at 12-months in both models (Appendix Figure 5.8.1 G).

Furthermore to verify observations made from flow cytometry analysis, esophageal and cardia tissue from 9- and 12-month old L2/IL-8Tg mice were

stained for immune cells of interest, including macrophages (F480), Ly6C (monocytes) and Ly6G (neutrophils) (Figure 5.4.3 A, C, E and Appendix Figure 5.8.2). Quantification revealed increased presence of these immune cells predominantly in esophageal tissue, with low abundance in cardia.

Similar to the trend that as was observed with flow cytometry, F480 positively stained cells appeared to be significantly higher in 9-month old L2/IL-8Tg mice compared to L2/IL-8Tg mice at 12-months of age and L2-mice in the esophagus (Figure 5.4.3 A, B). No significant differences of trends were noted in the cardia region (Appendix Figure 5.8.2).
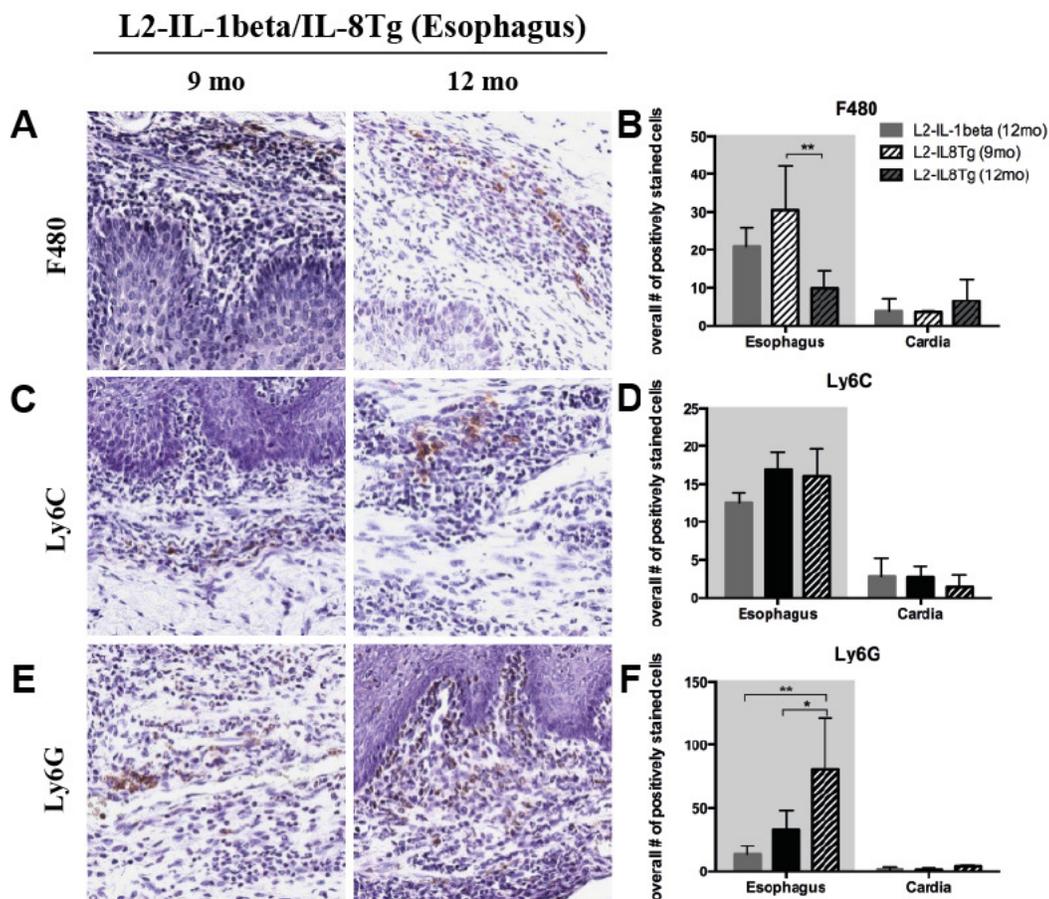
Figure 5.4.3: Immune cells stainings in L2/IL-8Tg esophageal tissue.
(A) F480, (C) Ly6C and (E) Ly6G were stained and quantified (B, D, and F) in the esophagus and cardia of L2/IL-8Tg mice (staining for cardia tissue shown in Appendix Figure 5.8.2). Scale bar, 50 μm. All data are means ± standard deviation. Statistical analysis was performed using two-way ANOVA and Tukey's post-hoc test. Group size (n=3). Asterisks indicate significant differences compared with control or between groups. ****p≤0.0001, ***p≤0.001, **p≤0.01, *p≤0.05. Grey region in bar graphs represents L2-HFD study data already shown in Chapter 3, shown here for comparison of the models.

In the esophagus, Ly6C positive cells appeared to show a trend in slightly higher abundance in L2/IL-8Tg mice at 9- and 12-months when compared to L2-mice at 12-months of age (Figure 5.4.3 C, D); cardia tissue showed no significant differences or trends (Appendix Figure 5.8.2).

Lastly, Ly6G staining for neutrophils appeared to be significantly increased in 12-month old L2/IL-8Tg mice compared to 9-month old L2/IL-8Tg and L2-mice mice; this observation was only noticeable in the esophagus in agreement with the flow cytometry analysis (Figures 5.4.3 B and 5.4.1 E, F). As with the F480 and LY6C staining, no significant differences or trends where observed in the cardia for the LY6G staining (Appendix Figure 5.8.2).

A detailed summary of the flow cytometry values obtained from L2-HFD mice and L2/IL-8Tg mice (9- and 12-months) is listed in Chapter 7, for esophagus and cardia tissue respectively. Overall, similarities were observed primarily in esophageal tissue, especially in IMCs and neutrophils. Significantly higher IMC cell numbers were observed in L2-HFD, and higher cell number trends were observed in L2/IL-8Tg 9- and 12-month old mice. Further more, significantly higher neutrophil cell numbers were observed in L2-HFD and L2/IL-8Tg 9-month old mice, and higher cell number trends were observed in L2/IL-8Tg 12-month old mice.

These results point towards a neutrophil driven niche for the development and progression of BE to metaplasia and low/ high grade dysplasia in the L2/IL-8Tg model.

5.5 IL-8 Over-Expression Leads to the Development of Splenomegaly in the L2/IL-8Tg Model

Since the L2-mice on HFD presented enlarged spleens, it was of interest to characterize the effects of chronic IL-8 over-expression in the spleens of the L2/IL-8Tg model. Documentation of spleen length revealed that 9- and 12-month old L2/IL-8Tg mice presented with macroscopically enlarged spleens. This was visibly notable when compared to WT and L2-IL-1beta spleen lengths, as seen in Figure 5.5 (spleen length: L2/IL-8Tg 9mo, 15.37 ± 1.50mm, 12mo, 15.70 ± 2.35mm).

Chronic IL-8 over-expression in the L2/IL-8Tg model led to development of enlarged spleens, also known as splenomegaly at 9- and 12-months of age, as was previously documented in the L2-HFD model in terms of a higher spleen to body mass ratio (Section 4.6, Figure 3.6 A)

This observation was assumed to be occurring in combination with an increase in inflammatory cytokines, which were further analyzed on an RNA level.
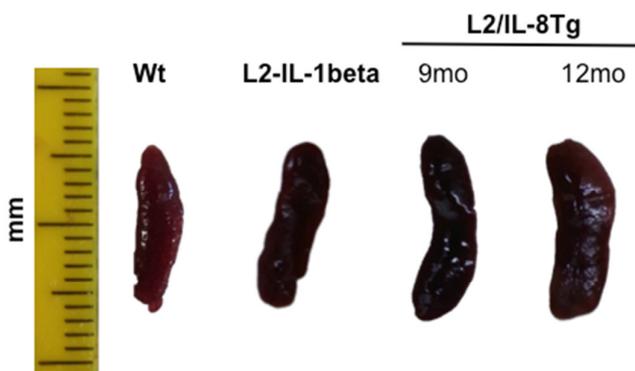
Figure 5.5: Spleen enlargement resulting from IL-1beta over-expression in combination with IL-8 over-expression.
Spleens resected from L2/IL-8Tg mice at 9- and 12-months of age arranged beside spleens from 12-month old WT and L2-IL-1beta mice to assess spleen enlargement. Group size (9mo: n=8, 12mo: n=11), measurements were documented from macroscopic pictures, spleen length noted in millimeters (mm) ± standard deviation.

5.6 HFD Induces Changes in Esophagus and Cardia Tissue on an RNA Level

IL-8 over-expression in the L2/IL-8Tg model accelerated esophageal tumor progression that resulted in a phenotype similar to the one observed in the L2-HFD model (Chapter 4 and Chapter 3, respectively).

To further investigate the mechanisms underlying this effect, it was pivotal to identify alterations induced by IL-8 at the RNA level in tissues of interest including esophageal and cardia tissue from L2/IL-8Tg mice.

5.6.1 Real-Time PCR

Real-time PCR (RT-PCR) was utilized to identify possible changes in transcriptional activity in cardia tissue observed in L2/IL-8Tg mice. As detailed in Section 2.2.3, RNA was isolated from tissue with typical metaplastic and dysplastic lesions areas from the cardia region. RT-PCR analysis of cardia tissue from L2/IL-8Tg mice harboring low and high-grade metaplasia at 9- and 12-month of age showed interesting changes in the expression of several inflammatory cytokines/ chemokines, chemotactic proteins and secreted signaling proteins, and genes associated with degradation of the extracellular matrix.

KC, the murine homologue of IL-8 was quantified using RT-PCR, in addition to its receptors Cxcr1 and Cxcr2. As expected, comparable levels of KC, and its receptors were expressed in 9- and 12-month L2/IL-8Tg mice. KC appeared to be expressed at slightly higher levels in 9-month old L2/IL-8Tg mice (Figure 5.6.1.1 A). Both receptors also appeared slightly higher in the L2/IL-8Tg model at 9- and 12-months than the L2-model, however after taking into consideration the variation between samples, this appeared comparable (Figure 5.6.1.1 B, C).

A

B

C
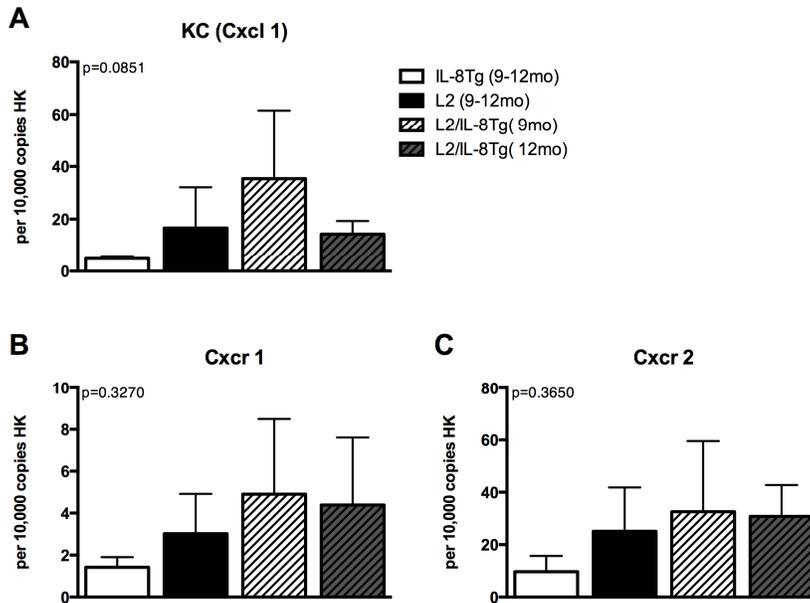
Figure 5.6.1.1: IL-8 over-expression stimulates increase expression of KC and its receptors Cxcr1 and Cxcr2 in the L2/IL-8Tg mouse model.
mRNA expression in the cardia of L2/IL-8Tg mice (A) KC (Cxcl1), and its receptors in 9- and 12-month old L2/IL-8Tg mice (B) Cxcr1 and (C) Cxcr2 were quantified using RT-PCR. Group size (n=4-6). All data are means ± standard deviation. Statistical analysis was performed using one-way ANOVA, asterisks indicate significant differences compared with control or between groups, ****$p \leq 0.0001$, ***$p \leq 0.001$, **$p \leq 0.01$, *$p \leq 0.05$.

Additionally, several members of the Wnt family, such as Wnt5a, Wnt5b, Wnt7a and Wnt7b were also analyzed.

Interestingly, Wnt5a appeared to be highly expressed primarily in the L2-model, while the L2/IL-8Tg model expressed this gene, it was comparable to expression levels in the IL-8Tg model (Figure 5.6.1.2 A). No statistical differences were noted in the cardia for Wnt5b expression amongst IL-8Tg, L2-mice and L2/IL-8Tg mice at 9- and 12-months of age (Figure 5.6.1.2 B).

Wnt7a, similarly to Wnt5a also appeared to be highly expressed in the L2-model only; this was significantly different to the expression levels in IL-8Tg, and the 9- and 12-month old L2/IL-8Tg mice (Figure 5.6.1.2 C). Lastly, Wnt7b expression appeared to be highly increased only in 9-month old L2/IL-8Tg mice compared to the IL-8Tg, L2-mice and L2/IL-8Tg mice at 12-months of age (Figure 5.6.1.2 D).

These expression results were not identical to those observed in the L2-HFD model, however similar trends were observed in the expression of KC, the neutrophil chemoattractant. Furthermore, changes in Wnt family expression may contribute towards understanding the mechanisms at play resulting from IL-8 over-expression in the L2/IL-8Tg model.
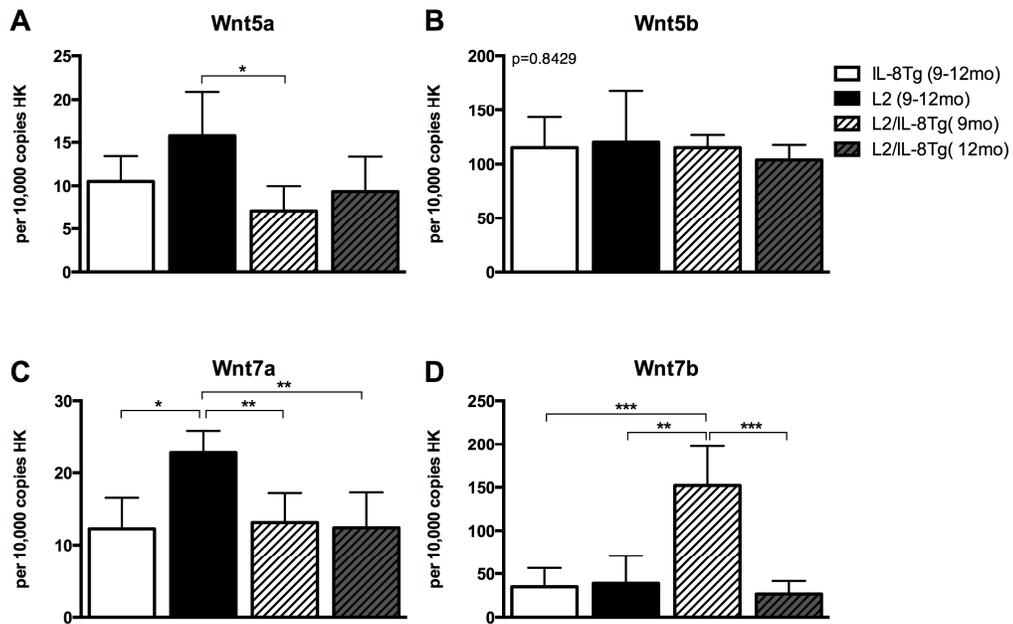
Figure 5.6.1.2: Expression of Wnt family genes in the L2/IL-8Tg mouse model.
mRNA expression in the cardia of L2/IL-8Tg mice (A) Wnt5a, (B) Wnt5b, (C) Wnt7a, (D) Wnt7b in 9- and 12-month old L2/IL-8Tg mice was quantified using RT-PCR. Group size (n=4-6). All data are means ± standard deviation. Statistical analysis was performed using one-way ANOVA, asterisks indicate significant differences compared with control or between groups, ****p≤0.0001, ***p≤0.001, **p≤0.01, *p≤0.05.

5.6.2 Microarray Analysis

As with the L2-HFD mice a snapshot of the transcriptional activity in the cardia region was attained using microarray technology in order to characterize gene expression in response to the IL-8 stimulus and to further understand the molecular mechanisms underlying cell cycle control, tumor cell metabolism, apoptosis and tumor cell survival in the L2/IL-8Tgmodel.

Transcriptional profile analysis was carried out as described in Section 2.7.2 using tissue with typical metaplastic lesions areas from the cardia region in 9- and 12-month old L2/IL-8Tg mice and 12-month old L2-IL-1beta mice and was executed on an Affymetrix array.

A number of gastric and intestinal genes were significantly up-regulated in the L2/IL-8Tg model. Genes were defined as being significantly differentially expressed as a result of genotype or diet if they exhibited >1.5 fold increase in gene expression or <0.65 fold decrease compared to genotype or diet controls; p-values were <0.05 in combination with the afore mentioned cutoffs.

A total of 2,982 genes were identified as differentially regulated when comparing the effect between the 9-month old L2/IL-8Tg mice with 12-month old L2-IL-1beta mice resulted in The gene set was further sorted based on the fold change cutoffs noted above and filtered for genes associated with carcinogenesis. Resulting in 17 genes that were up-regulated and 21 genes that were down-regulated in the L2/IL-8Tg model after adjusting for a p-value of <0.5 (Appendix Table 5.8.4).

Furthermore, a total of 1,155 genes that identified as differentially regulated when comparing the effect between the 12-month old L2/IL-8Tg mice with 12-month old L2-IL-1beta mice. The gene set was further sorted based on the fold change cutoffs noted above and filtered for genes associated with carcinogenesis. This resulted in 14 genes that were up-regulated and 51 genes that were down-regulated in the L2/IL-8Tg after adjusting for a p-value of <0.5(Appendix Table 5.8.4).

When assessing the effect of IL-8 on the L2-IL-1beta model through flow cytometry, the 9-month old time-point revealed a much stronger immune phenotype. Table 5.6.2 highlights genes of interest that appeared to be

differently regulated at the 9-months time-point (A more detailed version, including gene function is presented in Appendix Table 5.8.4. Up-regulation was primarily observed in genes encoding for cytokines (IL1b, Wnt11), chemokines (Cxcl5, Cxcl3), extracellular enzymes/ molecules (Mmp28, Mmp15, Muc4, Krt20), cell viability (Tnfrsf11b, Tnfrsf10b, Egfr, Casp2), and receptor and cell adhesion and signaling (Nos2). Down-regulated genes were involved with cytokines and their receptors (Wnt2b, IL7r, Lepr, Angptl2), chemokines and their receptors (Ccl7, Cxcl14, Ccr7, Ccl5, Cxcl15, Ccl11, Cxcl12), extracellular enzymes/ molecules (Mmp3, Mmp19, Mmp7, Mmp2, Timp3), cell viability (Tnfrsf26, Igf1), receptors and cell adhesion/ signaling (Mrc2, Epas1, Nos3, Ctsk), transcription, translation and processing (Hspb8), cell adhesion and cell junction molecules (Cd34) and intracellular transport (Ctsf).

Therefore, these results show that IL-8 over-expression may mediate the acceleration of carcinogenesis in the L2/IL-8Tg model through differential regulations of cytokines and chemokines, in addition to extracellular enzymes and regulators of transcription and translation.

Table 5.6.2: Selected genes up- and down-regulated as a result of IL-8 over-expression in the L2/IL-8Tg model at 9-months of age.
(Based on cut-offs of fold changes >1.5 and <0.65 and p-values of <0.5. Gene function details in Appendix Table 5.8.4).

		L2/IL-8Tg v. L2-IL-1beta		
Up-regulated	**Symbol**	**Description**	**FC**	**P.Value**
Cytokines & their receptors	IL1b	interleukin 1 beta	**1.6146**	**0.3051**
	Wnt11	wingless-type MMTV integration site family, member 11	**2.3790**	**0.0003**
Chemokines & their receptor	Cxcl5	chemokine (C-X-C motif) ligand 5	**3.3857**	**0.0021**
	Cxcl3	chemokine (C-X-C motif) ligand 3	**3.1129**	**0.0768**
Extracellular enzymes/ molecules	Mmp28	matrix metallopeptidase 28 (epilysin)	**2.1528**	**0.0002**
	Mmp15	matrix metallopeptidase 15	**1.9322**	**0.0085**
	Muc4	mucin 4	**2.5188**	**0.0023**
	Krt20	keratin 20	**2.4024**	**0.0424**
Cell viability	Tnfrsf11b	tumor necrosis factor receptor superfamily, member 11b (osteoprotegerin)	**2.6103**	**0.0027**
	Tnfrsf10b	tumor necrosis factor receptor superfamily, member 10b	**1.5474**	**0.0278**
	Egfr	epidermal growth factor receptor	**1.5399**	**0.0017**
	Casp2	caspase 2	**1.5293**	**0.0089**
Receptors & cell adhesion/signaling	Nos2	nitric oxide synthase 2, inducible	**1.7583**	**0.0226**

		L2/IL-8Tg v. L2-IL-1beta		
Down-regulated	**Symbol**	**Description**	**FC**	**P.Value**
Cytokines & their receptors	Wnt2b	wingless-type MMTV integration site family, member 2B	**0.5816**	**0.0267**
	Il7r	interleukin 7 receptor	**0.4332**	**0.0085**
	Lepr	leptin receptor	**0.4049**	**0.0002**
	Angptl2	angiopoietin-like 2	**0.4841**	**0.0131**
Chemokines & their receptors	Ccl7	chemokine (C-C motif) ligand 7	**0.6550**	**0.0994**
	Cxcl14	chemokine (C-X-C motif) ligand 14	**0.6015**	**0.0031**
	Ccr7	chemokine (C-C motif) receptor 7	**0.5950**	**0.0091**
	Ccl5	chemokine (C-C motif) ligand 5	**0.5125**	**0.0028**
	Cxcl15	chemokine (C-X-C motif) ligand 15	**0.4266**	**0.0164**
	Ccl11	chemokine (C-C motif) ligand 11	**0.3255**	**0.0001**
	Cxcl12/SDF-1	chemokine (C-X-C motif) ligand 12	**0.3175**	**0.0006**
Extracellular enzymes/ molecules	Mmp3	matrix metallopeptidase 3	**0.5491**	**0.0464**
	Mmp19	matrix metallopeptidase 19	**0.5104**	**0.0036**
	Mmp7	matrix metallopeptidase 7	**0.4843**	**0.0375**
	Mmp2	matrix metallopeptidase 2	**0.3847**	**0.0000**

	Timp3	tissue inhibitor of metalloproteinase 3	**0.2020**	**0.0003**
Cell viability	Tnfrsf26	tumor necrosis factor receptor superfamily, member 26	**0.6366**	**0.0289**
	Igf1	insulin-like growth factor 1	**0.3971**	**0.0008**
Receptors & cell adhesion/signaling	Mrc2	mannose receptor, C type 2	**0.5838**	**0.0126**
	Epas1	endothelial PAS domain protein 1	**0.6520**	**0.0031**
	Nos3	nitric oxide synthase 3, endothelial cell	**0.4895**	**0.0017**
	Ctsk	cathepsin K	**0.3568**	**0.0004**
Transcription, translation & RNA processing	Hspb8	heat shock protein 8	**0.4935**	**0.0239**
Cell adhesion & cell junction molecules	Cd34	CD34 antigen	**0.2799**	**0.0001**
Intracellular transport	Ctsf	cathepsin F	**0.5693**	**0.0019**

5.6.3 GSEA Analysis

Taking into consideration the phenotype observed in the L2-model on HFD, a comparison was carried against the L2/IL-8Tg model; in order to assess similarities in pathways that were activated or halted, gene set enrichment analysis (GSEA) was executed using data sets obtained from the Affymetrix microarray.

GSEA was conducted to compare key genes up-regulated by diet or genotype. Genes up-regulated as a direct result of the HFD was calculated as a result of fold changed of WT-mice on HFD compared to WT-mice on Chow. Genes up-regulated as a result of the IL-1beta transgene was calculated as the fold changed WT-mice on Chow to L2-mice on Chow. Lastly, The up-regulated L2/IL-8Tg gene set was calculated utilizing the fold change of L2/IL-8Tg mice compared to L2-mice.

GSEA showed that the L2-HFD gene set was significantly enriched in the L2-L2/IL-8Tg gene set.
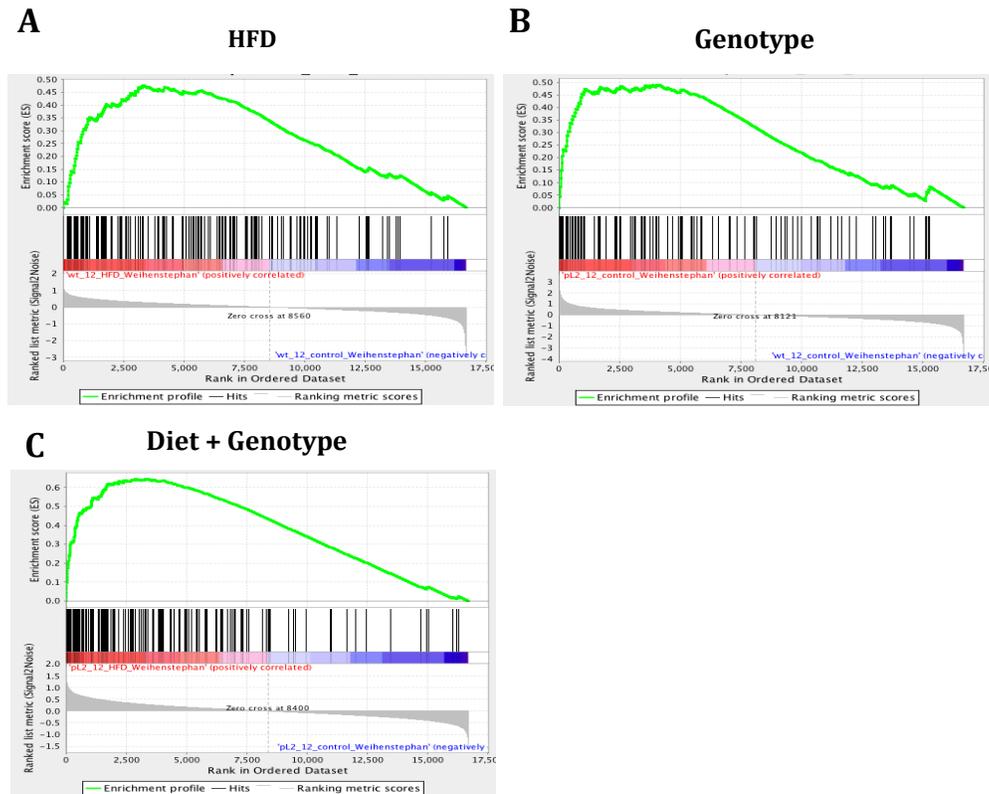
Figure 5.6.3: Microarray results assessed using gene set enrichment analysis to verify possible mechanistic pathways.
Plots show comparisons of (A) Diet (HFD), (B) genotype (IL-1beta Transgene) (C) Diet and genotype in comparison to the IL-8 gene set.

176

These results were consistent with a role for IL-8 accelerating metaplasia and dysplasia by increased inflammation that thereby induced oncogenic pathways. Several key genes listed Table 5.6.2 that are involved in promoting inflammation, tumor microenvironment and proliferation were selected and their gene expression in cardia tissue from L2/IL-8Tg mice on at 9- and 12-months was quantified by RT-PCT to confirm the results of the Affymetrix array.

5.7 *in vitro* Studies of Cardia Organoid Cultures

In addition to the human IL-8 data described at the beginning of Section 5.1, collaboration partners at the Lysaght lab was also kind enough to share data on IL-8 levels measured in cell lines and from tumor conditioned medium. Cell lines derived from benign human BE (QH) and human esophageal adenocarcinoma cell line OE33 showed significantly higher IL-8 levels when compared to a normal human esophageal squamous cell line (Het). Additionally, the EAC cell line expressed significantly higher IL-8 concentrations that the BE (QH) cell line (Figure 5.7.1 A). Lastly, medium conditioned with human patient samples revealed a strong trend of increasing IL-8 concentration with increased disease progression. As noted in Figure 5.7.1 B tissue-conditioned medium from tumor samples showed significantly higher IL-8 levels compared to normal and BE.
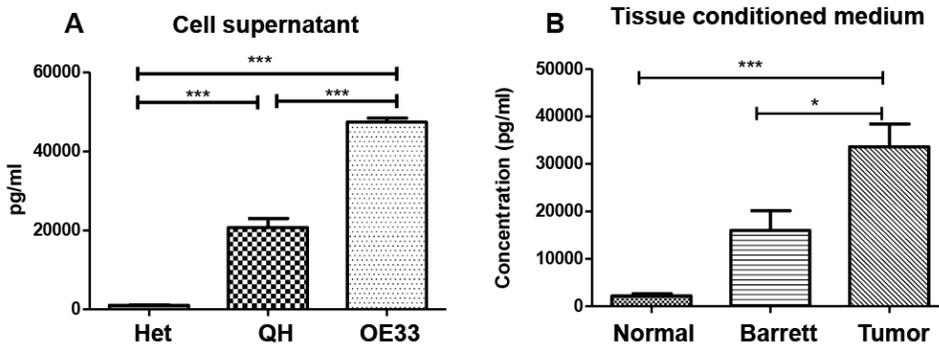
Figure 5.7.1: *In-vitro* **studies showing the levels of IL-8 in cell lines and tissue in the disease progression of BE and EAC.**
(A) IL-8 concentrations measured in a normal esophageal squamous cell line (Het), a benign BE cell line (QH) and esophageal adenocarcinoma cell line OE33 and (B) measured IL-8 concentrations in tissue conditioned medium from normal, BE and tumor tissue from human patients. All data are means ± SEM. Statistical analysis was performed using one-way, asterisks indicate significant differences compared with control or between groups, ****$p \leq 0.0001$, ***$p \leq 0.001$, **$p \leq 0.01$, *$p \leq 0.05$ (Data and statistics kindly shared by the Lysaght and O'Sullivan labs, Trinity College, Dublin, Ireland).

In addition, collaborators from the Wang Lab at Columbia University, NY, USA, also made interesting observations with regards to IL-8 and organoid proliferation. Data kindly shared by them, showed that organoids from IL-8Tg mice treated with lean and obese human serum for 48 hours resulted in a significant increase in organoid numbers (Figure 5.7.2 A). Furthermore,

supernatant collected following the treatment period, analyzed using ELISA, revealed a significantly higher production of IL-8 when treated with obese human serum (Figure 5.7.2 B).
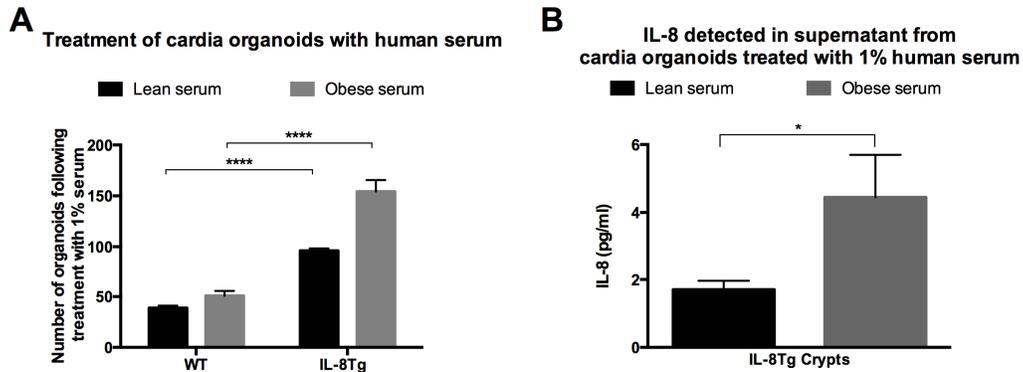
Figure 5.7.2: Treatment of IL-8Tg cardia organoids with lean and obese human serum.
(A) Cardia crypts isolated from WT and IL-8Tg mice were treated with serum from obese and lean patients for 48 hours. (B) IL-8 levels detected in the supernatant from the treatment of WT and IL-8Tg cardia organoids with human serum. All data are means ± SEM. Statistical analysis was performed using one-way ANOVA or Student's t-tests, asterisks indicate significant differences compared with control or between groups, ****$p \leq 0.0001$, ***$p \leq 0.001$, **$p \leq 0.01$, *$p \leq 0.05$ (Data kindly shared by the Wang Lab, Columbia University, NY, USA and the Lysaght Lab, Trinity College, Dublin, Ireland).

Using the same *in-vitro* approach used in the Wang lab, isolated cardia crypts were grown using 3-D culture techniques to form organoid bodies (Chapter 2.12). These organoids recapitulate the epithelial architecture and cellular diversity of the mammalian stomach cardia tissue and serve as a proxy for cardia stem cell activity, since only stem cells can initiate and maintain these structures long-term, however it is crucial to note that the organoid culture system has limitations as they cannot recreate the gradient present along the crypt-villus axis as seen *in vivo* [158].

Organoids were cultured in a Matrigel® drop in combination with culture medium containing essential growth factors such as R-Spondin, EGF, and Noggin. Following the first passage, organoids were treated to assess the effects of several factors such as recombinant human IL-8, serum from L2-IL-1beta HFD mice, as well as serum from obese and lean human patients.

5.7.1 *in-vitro* treatment of L2-IL1-beta Cardia Organoids with Human Interleukin-8

KC and receptors Cxcr1 and 2 were shown to have significantly higher expression in L2-HFD mice, and a trend towards increased expression in L2/IL-8Tg mice, these observation were accompanied by the acceleration of the BE/EAC phenotype both models. Therefore, the impact of h-IL-8 on cardia organoids from L2-IL-1beta mice on a Chow diet was of interest.

Organoids were cultured from cardia tissue resected from L2-IL-1 beta mice between the ages of 9 and 12months that were only fed a Chow diet through out their lifetimes. Following passage 1, the organoids were treated with normal growth medium as a control, and with 100ng/mL of recombinant human IL-8 (noted as IL-8 henceforth) for 48 hours. Medium was replaced every 24 hours. Interestingly, organoids in both groups appeared to grow well for the first 24 hours but by 48 hours the organoid numbers dropped dramatically (average number of organoids with SEM, data from 4 separate experiments. At start: control, 47.25 ± 12.35, IL-8, 56.75 ± 15.23. 24h: control, 59.00 ± 18.13, IL-8, 69.50 ± 21.60. At 48h: control, 56 ± 18.80, IL-8, 57.25 ± 20.25). Of the organoids that survived the initial 24h, those treated with IL-8 appeared to grow drastically in size by 48 hours (average values of the change in the size of organoids (μm) with SEM, data from 4 separate experiments (Figure 5.7.1). Size of organoids at start: control, 101.12 ± 11.75, IL-8, 95.59 ± 11.00. 24h: control, 113.04 ± 18.94, IL-8, 106.19 ± 20.00. At 48h: control, 144.11 ± 24.77, IL-8, 138.38 ± 28.25).

While not definitive, these results suggest that IL-8 alone is insufficient in accelerating the unique phenotype observed in the L2/IL-8Tg model. Rather, a combination of factors triggered by IL-8 over-expression may be mediating the accelerated disease progression in this model.
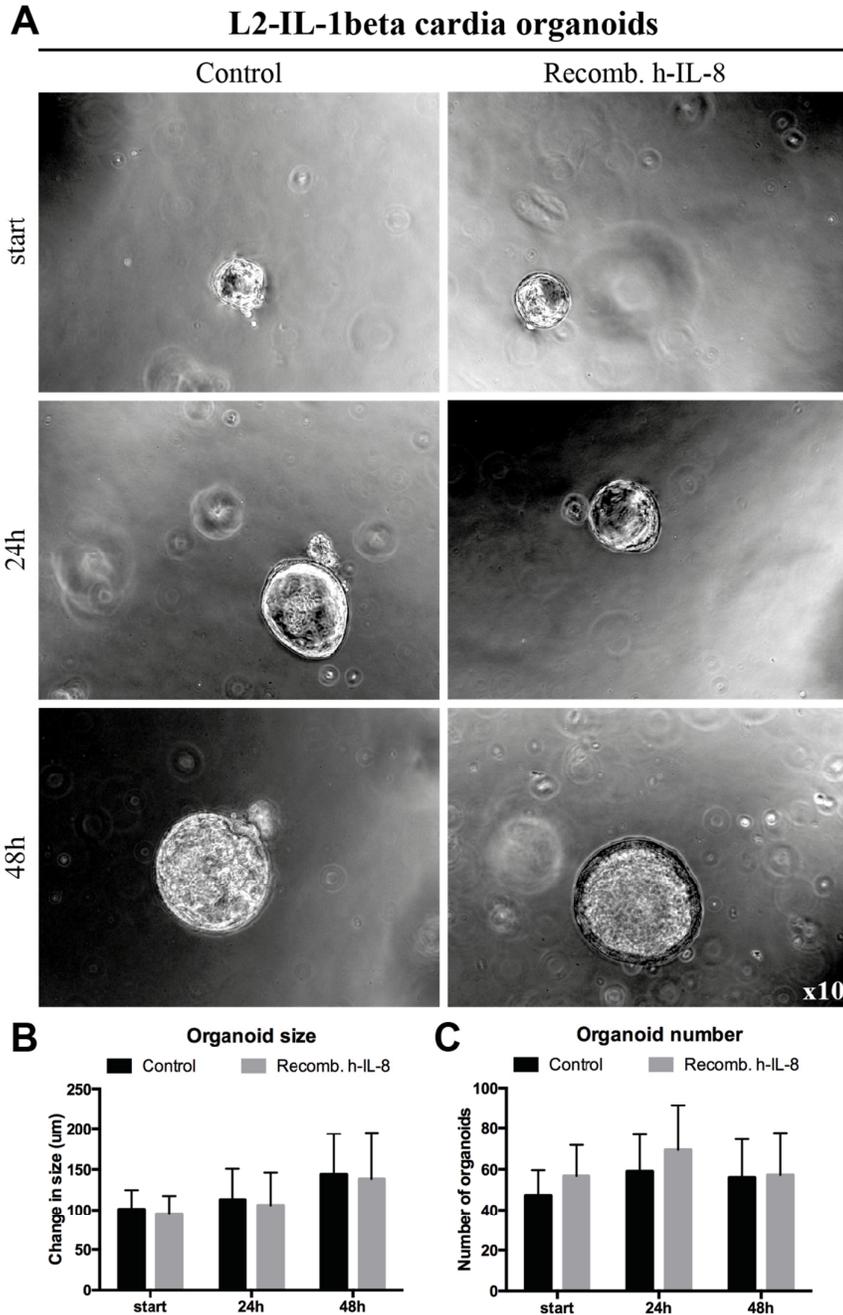
Figure 5.7.1: Treatment of L2-IL-1beta organoids with recombinant human IL-8 over a 48-hour period.

Organoids from the cardia region of 9-12-month old L2-IL-1beta mice were cultured and treated with growth medium containing 100ng/mL Recombinant human IL-8 once a day and observed for 48 hours. (A) Appearance of treated and untreated crypts at the start of treatment, 24 and 48 hours. (B) Changes in organoid size and (C) changes in organoid number. Experiment was carried out in duplicate and repeated four times. Statistical analysis was performed using one-way ANOVA and Tukey's post-hoc test. Asterisks indicate significant differences compared with control or between groups. ****p≤0.0001, ***p≤0.001, **p≤0.01, *p≤0.05.

5.7.2 *in-vitro* treatment of L2-IL1-beta Cardia Organoids with Serum from HFD

The observation that the L2-IL-1beta model on HFD did not succumb to an obesity phenotype, but still showed a drastic acceleration of the BE/EAC phenotype was suggested to be in part due to the influence of the HFD. To assess the effect of the HFD on the L2-model, cardia organoids were treated with serum from L2- HFD mice.

Organoids were cultured from cardia tissue resected from L2-IL-1 beta mice between the ages of 9 and 12months that were only fed Chow through out their lifetimes. Following passage 1, the organoids were treated with normal growth medium with 10% serum from Chow mice as a control, and with 10% serum from HFD mice. Medium was replaced every 24 hours for a 48-hour period.

Over the 48-hour treatment period, no significant differences were observed in organoid sizes; however, HFD-treated organoids appeared to be slightly larger over all. Interestingly, after the initial 24 hours of treatment, organoids treated with Chow-serum appeared to decrease in number, furthermore at 48 hours, of the organoids that survived, a slight increase in size was observed over time (Figure 5.7.2) (average values of the change in the size of organoids (μm) with SEM, data from 4 separate experiments. Size of organoids at start: Chow-serum, 110.81 ± 26.28, HFD-serum, 93.18 ± 10.82. 24h: Chow-serum, 116.37 ± 22.23, HFD-serum, 117.07 ± 17.59. At 48h: Chow-serum, 155.62 ± 40.10, HFD-serum 160.89 ± 42.10).

While not statistically significant, HFD-treated organoids appeared to increase in number at the 24-hour measurement, however this decreased slightly at the 48-hour measurement, but not to the extent observed with the Chow-treated organoids (average number of organoids with SEM, data from 4 separate experiments. At start: Chow-serum, 95.00 ± 57.00, HFD-serum, 100.00 ± 67.00. 24h: Chow-serum, 79.00 ± 41.00, HFD-serum, 135.00 ± 98.00. At 48h: Chow-serum, 67.00 ± 35.00, HFD-serum 107.50 ± 76.50).

These results suggest that the HFD resulted in a unique serum profile in the L2-model that caused a trend towards and increase in the number of organoids

budding from cardia organoids harvested from L2-Chow mice over a 48-hour treatment period.

A

L2-IL-1beta cardia organoids
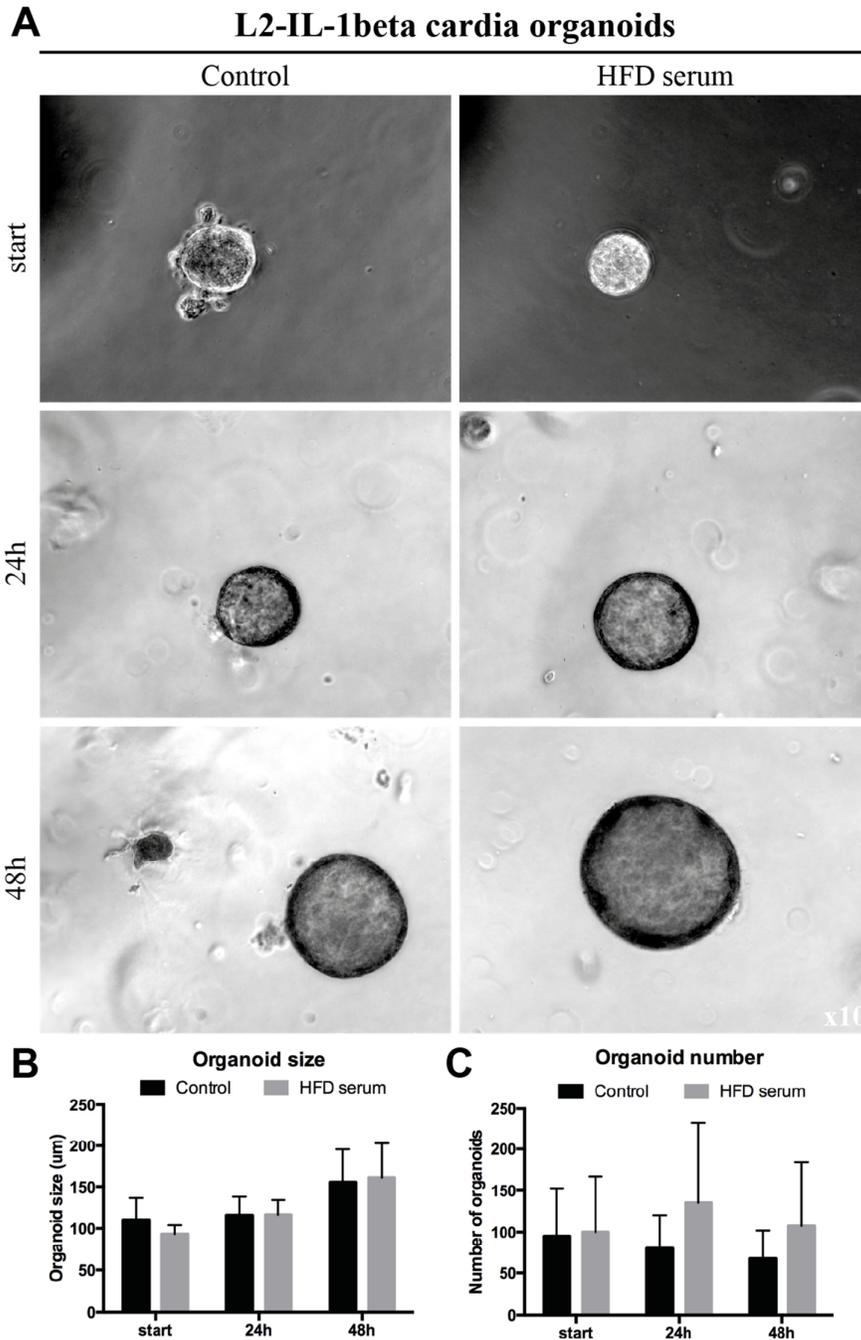
Figure 5.7.2: Treatment of L2-IL-1beta organoids with 10% serum from HFD mice over a 48-hour period.
Organoids from the cardia region of 9-12-month old L2-IL-1beta mice were cultured and treated with growth medium containing 10% serum from Chow fed mice as a control or 10% serum from HFD mice. (A) Appearance of treated and untreated crypts and (B) changes in organoid size and (C) changes in organoid number as observed at start, 24 and 48 hours. Experiment was carried out in duplicate and repeated four times. Statistical analysis was performed using one-way ANOVA and Tukey's post-hoc test. Asterisks indicate significant differences compared with control or between groups. ****$p \leq 0.0001$, ***$p \leq 0.001$, **$p \leq 0.01$, *$p \leq 0.05$.

5.7.3 *in-vitro* treatment of L2-IL1-beta Cardia Organoids with Serum from Lean and Obese Humans

Given the observations noted from the treatment of L2-IL-1beta mice with IL-8 and HFD-murine serum, it was of interest to observe the effects human serum might impose on organoids cultured from L2/IL-8Tg mice.

Cardia organoids were cultured from cardia tissue resected from L2/IL-8Tg mice between the ages of 9 and 12months. The organoids were treated with normal growth medium with 10% serum from lean patients as a control, and with 10% serum from obese patients. Medium was replaced every 24 hours for a 48-hour period. Organoids were seeded after passage 1 and treatment began immediately. Observations were noted after 24 hours and 48 hours of treatment. While the treatment of L2/IL-8Tg organoids with lean and obese human serum revealed no significant changes in size over a 48-hour treatment period (average values of the change in the size of organoids (μm) with SEM, data from n=2 mice. Size of organoids at 24h: lean serum, 76.85 ± 3.42, obese serum, 82.32 ± 5.06. At 48h: lean serum, 81.07 ± 5.43, obese serum, 79.07 ± 7.47), a slight increasing trend was noted in the number of newly formed organoids resulting from treatment with obese serum following 48 hours of treatment (Figure 5.7.3) (average number of organoids with SEM, data from n=2 mice. 24h: lean serum, 102.50 ± 12.50, obese serum, 105.00 ± 12.00. At 48h: lean serum, 118.50 ± 7.500, obese serum, 163.00 ± 19.00).

A   **L2-IL-1beta/IL-8Tg cardia organoids**
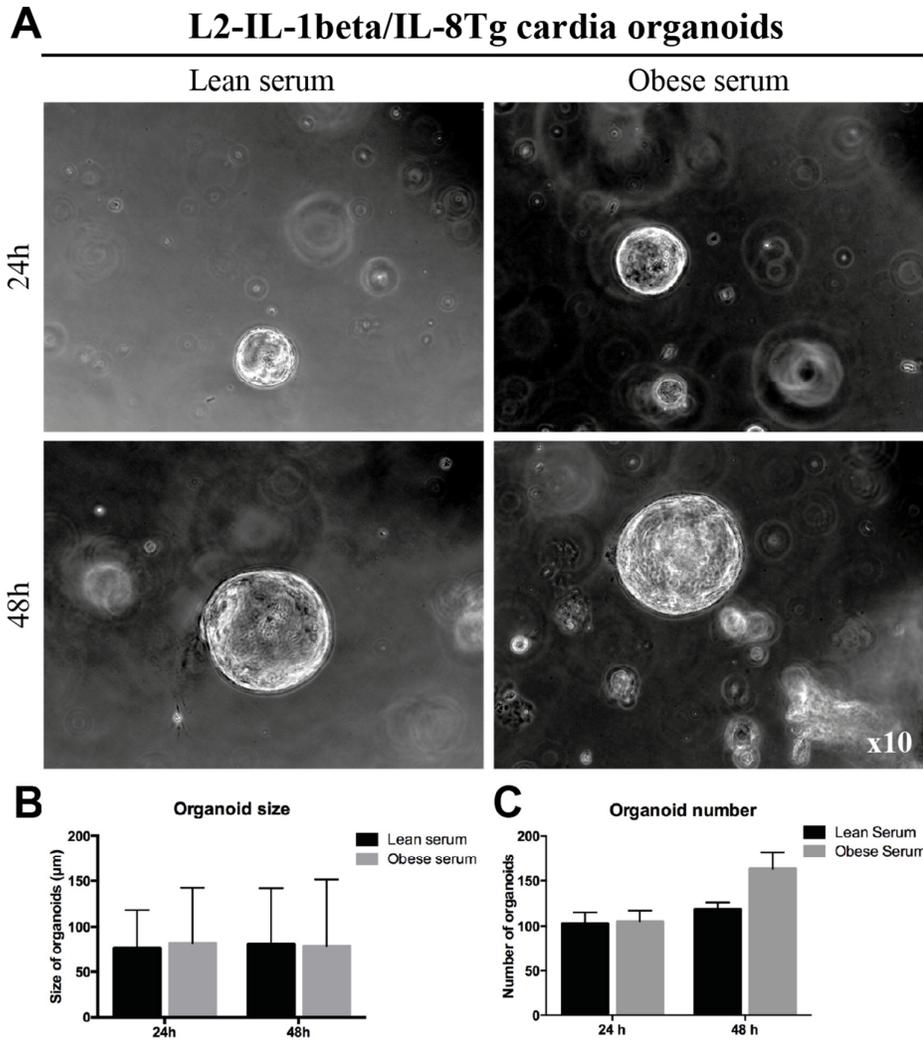
Figure 5.7.3: Treatment of L2-IL-1beta/IL8Tg organoids with 10% serum from lean and obese human patients over a 48-hour period.
Organoids from the cardia region of 9-12-month old L2-IL-1beta/IL8Tg mice were cultured and treated with growth medium containing 10% serum from lean patients as a control or 10% serum from obese patients. (A) Appearance of treated and untreated crypts at 24 and 48 hours. (B) Changes in organoid size and C, changes in organoid number as observed at 24 and 48 hours, (n=2). Statistical analysis was performed using a Student's t-test.

In summary, the various treatment conditions of cardia organoids did not reveal a significant difference in organoid number or size. While several trends were observed, it can be concluded that further studies are required to grasp a better understanding of the mechanisms at play in this *in-vitro* setting.

5.8 Appendix Figures and Tables

Cardia
Myeloid cell populations

T-helper cell populations
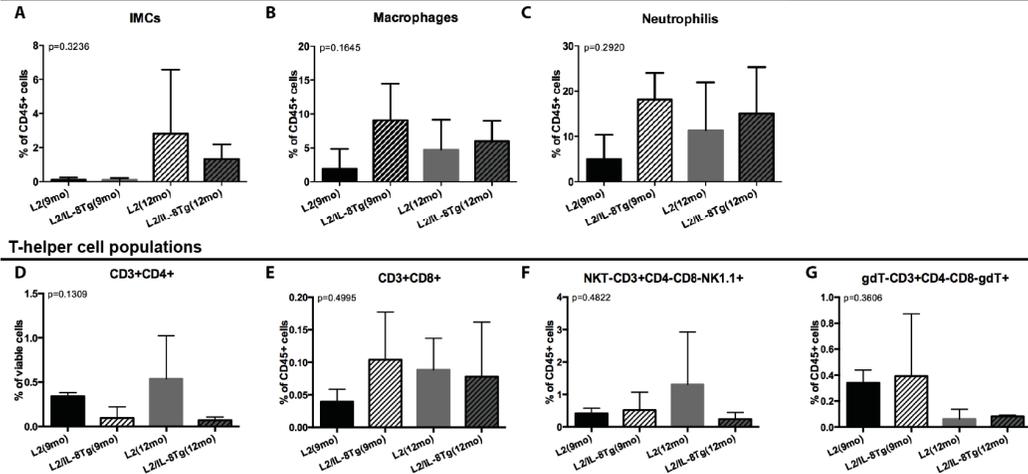
Appendix Figure 5.8.1: Changes in immune cell populations resulting from IL-8 over-expression in the cardia region of IL-8Tg mice using flow cytometry.

Myeloid cells that were quantified included (A) immature myeloid cells (IMCs), (B) macrophages and (C) neutrophils from the cardia of 9- and 12-month old L2/IL-8Tg mice. T-helper cells included (D) CD3+CD4+, (E) CD4+CD8+, NKT (F)(CD3+CD4-CD8-NK1.1+) and gamma delta T-cells (G)(D3+CD4-CD8-gdTCR+) cells from the cardia of 9- and 12-month old L2/IL-8Tg mice were analyzed by flow cytometry and quantified. All data are means ± standard deviation. Statistical analysis was performed using one-way ANOVA. Asterisks indicate significant differences compared with control or between groups. ****$p \leq 0.0001$, ***$p \leq 0.001$, **$p \leq 0.01$, *$p \leq 0.05$.
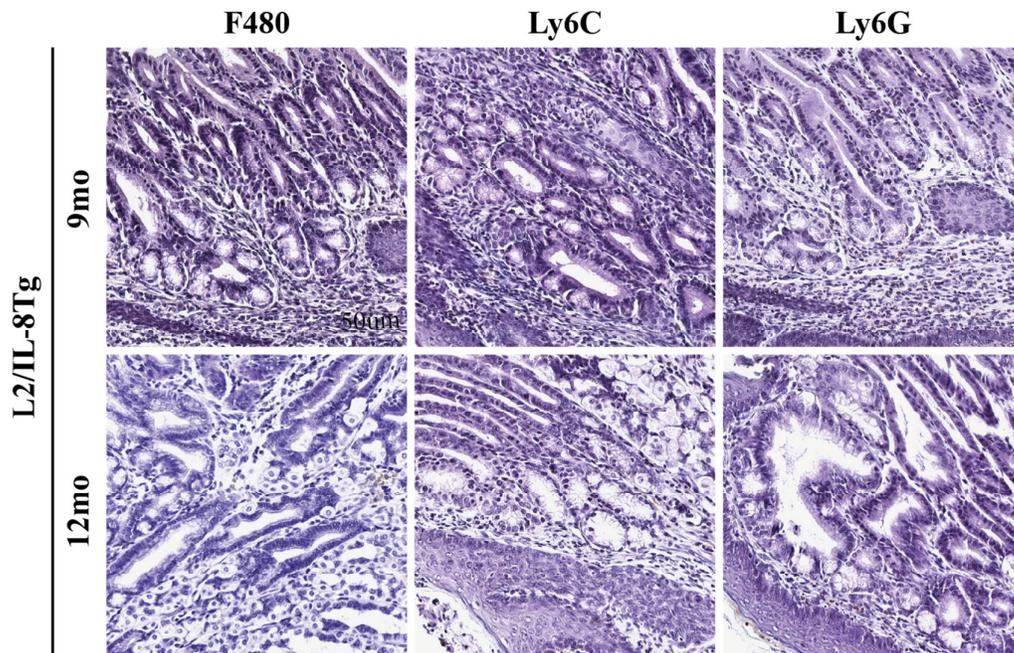
Appendix Figure 5.8.2 Immune cells stained in the cardia region of L2/IL-8Tg mice at 9- and 12-months of age.
F480, Ly6C and Ly6G were stained in cardia tissue. Quantification shown in Figure 5.4.3, Scale bar, 50um.

Appendix Table 5.8.4: Extended Table of selected genes up- and down-regulated as a result of HFD in the L2-model..
(Based on cut-offs of fold changes >1.5 or <0.65 and p-values of <0.5)

L2/IL-8Tg v. L2-IL-1beta

Up-regulated	Symbol	Description	Gene Function	FC	P.Value
Cytokines & their receptors	IL1b	interleukin 1 beta	Multifunctional, pro-inflammatory, proangiogenic cytokine	**1.6146**	**0.3051**
	Wnt11	wingless-type MMTV integration site family, member 11	This gene may play roles in the development of skeleton, kidney and lung, and is considered to be a plausible candidate gene for High Bone Mass Syndrome.	**2.3790**	**0.0003**
Chemokines & their receptor	Cxcl5	chemokine (C-X-C motif) ligand 5	Bind chemokine (C-X-C motif) receptor 2 to recruit neutrophils, to promote angiogenesis and to remodel connective tissues. This protein is thought to play a role in cancer cell proliferation, migration, and invasion.	**3.3857**	**0.0021**
	Cxcl3	chemokine (C-X-C motif) ligand 3	This protein plays a role in inflammation and as a chemoattractant for neutrophils.	**3.1129**	**0.0768**
Extracellular enzymes/ molecules	Mmp28	matrix metallopeptidase 28 (epilysin)	This gene encodes a secreted enzyme that degrades casein. Its expression pattern suggests that it plays a role in tissue homeostasis and in wound repair.	**2.1528**	**0.0002**
	Mmp15	matrix metallopeptidase 15	The encoded preproprotein is proteolytically processed to generate the mature protease. This protein may play a role in cancer progression.	**1.9322**	**0.0085**
	Muc4	mucin 4	Plays an important	**2.5188**	**0.0023**

		role in the protection of the epithelial cells and have been implicated in epithelial renewal and differentiation.		
	Krt20	keratin 20	This cytokeratin is a major cellular protein of mature enterocytes and goblet cells and is specifically expressed in the gastric and intestinal mucosa.	**2.4024**	**0.0424**
Cell viability	Tnfrsf11b	tumor necrosis factor receptor superfamily, member 11b (osteoprotegerin)	This protein and its ligand play a role in lymph-node organogenesis and vascular calcification.	**2.6103**	**0.0027**
	Tnfrsf10b	tumor necrosis factor receptor superfamily, member 10b	This receptor can be activated by tumor necrosis factor-related apoptosis inducing ligand (TNFSF10/TRAIL/APO-2L), and transduces an apoptosis signal.	**1.5474**	**0.0278**
	Egfr	epidermal growth factor receptor	EGFR is a cell surface protein that binds to epidermal growth factor. Binding of the protein to a ligand induces receptor dimerization and tyrosine autophosphorylation and leads to cell proliferation.	**1.5399**	**0.0017**
	Casp2	caspase 2	The encoded protein may function in stress-induced cell death pathways, cell cycle maintenance, and the suppression of tumorigenesis.	**1.5293**	**0.0089**
Receptors & cell adhesion/signaling	Nos2	nitric oxide synthase 2, inducible	This gene encodes a nitric oxide synthase that is inducible by a combination of lipopolysaccharide and certain cytokines.	**1.7583**	**0.0226**

L2/IL-8Tg v. L2-IL-1beta

Down-regulated	Symbol	Description	Gene Function	FC	P.Value
	Wnt2b	wingless-type MMTV integration site family, member 2B	May play a role in human development as well as carcinogenesis	**0.5816**	**0.0267**
	Il7r	interleukin 7 receptor	The protein encoded by this gene is a receptor for interleukin 7 (IL7). This protein has been shown to play a critical role in V(D)J recombination during lymphocyte development.	**0.4332**	**0.0085**
Cytokines & their receptors	Lepr	leptin receptor	This protein is a receptor for leptin (an adipocyte-specific hormone that regulates body weight), and is involved in the regulation of fat metabolism, as well as in a novel hematopoietic pathway that is required for normal lymphopoiesis.	**0.4049**	**0.0002**
	Angptl2	angiopoietin-like 2	ANGPTL2 protein is a secreted glycoprotein with homology to the angiopoietins and may exert a function on endothelial cells through autocrine or paracrine action.	**0.4841**	**0.0131**
Chemokines & their receptors	Ccl7	chemokine (C-C motif) ligand 7	The protein is an in vivo substrate of matrix metalloproteinase 2, an enzyme which degrades components of the extracellular matrix.	**0.6550**	**0.0994**
	Cxcl14	chemokine (C-X-C motif) ligand 14	This cytokine displays chemotactic activity for monocytes but not for lymphocytes, dendritic cells, neutrophils or macrophages. It has been implicated that	**0.6015**	**0.0031**

		this cytokine is involved in the homeostasis of monocyte-derived macrophages rather than in inflammation.		
Ccr7	chemokine (C-C motif) receptor 7	This receptor is expressed in various lymphoid tissues and activates B and T lymphocytes. It has been shown to control the migration of memory T cells to inflamed tissues, as well as stimulate dendritic cell maturation. Signals mediated by this receptor regulate T cell homeostasis in lymph nodes, and may also function in the activation and polarization of T cells, and in chronic inflammation pathogenesis.	**0.5950**	**0.0091**
Ccl5	chemokine (C-C motif) ligand 5	This chemokine, a member of the CC subfamily, functions as a chemoattractant for blood monocytes, memory T helper cells and eosinophils. It causes the release of histamine from basophils and activates eosinophils.	**0.5125**	**0.0028**
Cxcl15	chemokine (C-X-C motif) ligand 15	It is a highly abundant, small cytokine in mice, in epithelial cells of the lung,and can also be found in other mucosal organs such as the urogenital and gastrointestinal tracts, and in endocrine organs like the adrenal gland.[	**0.4266**	**0.0164**
Ccl11	chemokine (C-C motif) ligand 11	Chemotactic activity for eosinophils	**0.3255**	**0.0001**
Cxcl12/SDF-1	chemokine (C-X-C motif) ligand 12	This chemokine, a member of the CC subfamily, displays chemotactic activity for eosinophils, but	**0.3175**	**0.0006**

			not mononuclear cells or neutrophils.		
Extracellular enzymes/ molecules	Mmp3	matrix metallopeptidase 3	The enzyme is thought to be involved in wound repair, progression of atherosclerosis, and tumor initiation.	**0.5491**	**0.0464**
	Mmp19	matrix metallopeptidase 19	The encoded protein is secreted as an inactive proprotein, which is activated upon cleavage by extracellular proteases.	**0.5104**	**0.0036**
	Mmp7	matrix metallopeptidase 7	Enzyme with broad substrate specificity in ECM. Promotes wound healing, angiogenesis, tumor invasion and metastasis	**0.4843**	**0.0375**
	Mmp2	matrix metallopeptidase 2	This protein is thought to be involved in multiple pathways including roles in the nervous system, endometrial menstrual breakdown, regulation of vascularization, and metastasis.	**0.3847**	**0.0000**
	Timp3	tissue inhibitor of metalloproteinase 3	The proteins encoded by this gene family are inhibitors of the matrix metalloproteinases, a group of peptidases involved in degradation of the extracellular matrix (ECM). Expression of this gene is induced in response to mitogenic stimulation and this netrin domain-containing protein is localized to the ECM.	**0.2020**	**0.0003**
Cell viability	Tnfrsf26	tumor necrosis factor receptor superfamily, member 26	This receptor can be activated by tumor necrosis factor-related apoptosis and is know to be an inflammatory mediator	**0.6366**	**0.0289**
	Igf1	insulin-like growth factor	The protein encoded by this gene is similar	**0.3971**	**0.0008**

		1	to insulin in function and structure and is a member of a family of proteins involved in mediating growth and development.		
Receptors & cell adhesion/sig naling	Mrc2	mannose receptor, C type 2	Expression of this gene may play a role in the tumorigenesis and metastasis of several malignancies including breast cancer, gliomas and metastatic bone disease.	**0.5838**	**0.0126**
	Epas1	endothelial PAS domain protein 1	This gene encodes a transcription factor involved in the induction of genes regulated by oxygen, which is induced as oxygen levels fall.	**0.6520**	**0.0031**
	Nos3	nitric oxide synthase 3, endothelial cell	Variations in this gene are associated with susceptibility to coronary spasm.	**0.4895**	**0.0017**
	Ctsk	cathepsin K	This protein, which is a member of the peptidase C1 protein family, is predominantly expressed in osteoclasts. However, the encoded protein is also expressed in a significant fraction of human breast cancers, where it could contribute to tumor invasiveness.	**0.3568**	**0.0004**
Transcriptio n, translation & RNA processing	Hspb8	heat shock protein 8	This gene appears to be involved in regulation of cell proliferation, apoptosis, and carcinogenesis, and mutations in this gene have been associated with different neuromuscular diseases	**0.4935**	**0.0239**
Cell adhesion & cell junction molecules	Cd34	CD34 antigen	The protein encoded by this gene may play a role in the attachment of stem cells to the bone marrow extracellular matrix or to stromal	**0.2799**	**0.0001**

			cells.		
Intracellular transport	Ctsf	cathepsin F	Cathepsins are papain family cysteine proteinases that represent a major component of the lysosomal proteolytic system. Cathepsin F contains five potential N-glycosylation sites, and it may be targeted to the endosomal/lysosomal compartment via the mannose 6-phosphate receptor pathway.	**0.5693**	**0.0019**

Chapter 6: Discussion

Esophageal adenocarcinoma is a serious malignancy because of its aggressive nature and poor prognosis[119]. EAC ranks as the eighth most common cancer globally and is currently the sixth leading cause of cancer-related mortality in recent years[159]. Over approximately the same period the prevalence of obesity has increased substantially. It has been established that obesity results in a chronic low-grade inflammatory environment which is also an associated risk factor for BE and EAC. This drastic and disturbing rise in BE and EAC prevalence and the parallel rise in BMI and/or obesity is challenging to explain due to the multifaceted nature of both diseases. Nonetheless, insightful hypotheses and valuable findings have been uncovered in assessing the pathogenic links between obesity and the susceptibility to EAC.

For this study, using an established transgenic mouse model of esophageal inflammation, we were able to reconfirm that specific IL-1beta expression in the mouse squamous esophagus induced Barrett-like metaplasia and dysplasia at the SCJ[89], highlighting a fundamental role of IL-1beta in carcinogenesis, which is also know to be highly upregulated in human BE and EAC[160, 161]. The L2-IL-1beta model closely resembles human disease as evident from gene expression analysis, IHC, EM and endoscopy as previously outlined by Quante and colleagues, and was therefore used to analyze the role of obesity (i.e. HFD) during esophageal carcinogenesis. Our data showed that L2-mice had a drastic acceleration of the BE/EAC phenotype and we believe that the HFD influenced this rapid progression. In the results described in Chapter 3-5, we showed that while HFD did not result in DIO in the L2-model, it was capable of causing a shift in the immune microenvironment, stromal cells, cytokine expression levels and progenitor cell migration, in addition to impacting the microbiome.

6.1 Effects of High Fat Diet and Obesity in a Mouse Model of Esophageal Inflammation

Diet is one of many lifestyle factors that directly influences health and disease through cancer incidence and progression. What is consumed on a daily basis directly affects the availability of nutrients and can indirectly modulate growth factors and hormone levels, deregulation of tissue homeostasis and tumor initiation[162]. Given that obesity is an established risk factor for BE and EAC, the first aim of this thesis was to utilize HFD to understand its role during carcinogenesis in a mouse model of EAC. Specifically, the question addressed was whether life-long HFD feeding would result in weight gain and/ or obesity, which in turn would result in earlier phenotype development and tumor initiation in a setting of IL-1beta overexpression.

6.1.1 Possible Mechanisms of Obesity Driven BE and EAC

There have been parallels between the increases in obesity and EAC in the last few decades, as discussed in Chapter 1, highlighting obesity as a clear risk factor for BE and EAC[3, 162] and human subjects with EAC were shown to have significantly higher amounts of visceral adipose tissue than healthy controls[2]. Additionally, meta-analysis of patient data reaffirms that central obesity as a key factor in the pathogenesis of BE and EAC; with consistent results in numerous studies using multiple measures of central adiposity such as computed tomography (CT) assessment of visceral fat (but not subcutaneous fat), measured WHR and WC, after adjusting for multiple confounders[144, 163]. In addition to increasing abdominal obesity, BMI has also been associated with cancer risk[101]. A systematic review and meta-analyses showed that a BMI ≥ 25 was associated with an increased risk of EAC in males (OR: 2.2; 95% CI: 1.8e2.7) and females (OR: 1.9; 95% CI:1.5e2.5); this risk was even higher in obese males and females as BMI increased (OR: 2.4; 95% CI: 1.9e3.2 and OR: 1.9; 95% CI: 1.5e2.5, respectively) in comparison to overweight individuals[164].

These data lead us to two potential mechanisms by which obesity may be increasing the risk of EAC. One being the hypothesis that obesity increases the prevalence of gastroesophageal reflux and exposure of the LES to bile acids[4, 5,

34, 73], size of hiatus hernia[49], and increased transient lower esophageal relaxations[165] by increasing intra-abdominal pressure. While the other hypothesis suggests that acceleration of EAC occurs through increased inflammation mediated by an abundance of adipokines, cytokines and chemokines[124, 166, 167].

Regarding the intra-abdominal pressure hypothesis, some experimental data has shown that increased exposure to acid and/or bile reflux, as a result of mechanistic force, can promote cancer; including stimulation of proliferation, inhibition of apoptosis, and generation of free radicals[50, 51, 168]. Bile acids are a component of GERD and have been strongly linked to the development of BE and junctional cancer by multiple studies [89, 109, 169-171]. Bile acids are capable of changing the inflammatory microenvironment and possibly altering the microbiome[89, 109] and it is possible that in obese patients there is a greater proximal extension of bile acid within the LES thereby inducing damage and altering the tumorigenic microenvironment[169]. However, it is most likely that visceral obesity exerts direct and indirect effects on the promotion of EAC as discussed by Alexandre and colleagues, since the majority of literature show an association with BE and/or EAC independently of measures of reflux[2, 115, 145, 172, 173].

Our data shows that chronic HFD feeding of L2-mice did not lead to DIO; rather a lean phenotype was observed in association with an accelerated disease phenotype. As observed in this study, the L2-IL-1beta model progressed through the pathological stages of BE, to develop metaplasia, low-grade and high-grade dysplasia and occasionally esophageal adenocarcinoma, between 9- and 12-months of age, previously observed by Quante et al. between to occur at 15- to 20-months of age[89].

Long-term observations of the L2-model revealed that L2-HFD mice had a lean phenotype (Figure 3.2), accompanied by low body weight (Figure 3.3.1), which decreased as the mice aged, along side a reduction in fat mass (Figure 3.3.2 A & B). The lack of an obese phenotype in combination with acceleration of the BE/ EAC phenotype from HF feeding made it impossible to study this model under the hypothesis that inter-abdominal pressure resulting from obesity results in increased acid and bile reflux that accelerate development of BE and EAC.

6.1.2 Lack of an Obesity Phenotype in L2-IL-1beta mice

To further substantiate these findings, L2-mice were also fed a dietary-component-matched HFD^{porklard} diet as described in Chapter 3, Section 3.6, to assess if DIO and disease acceleration could be achieved with an animal fat based diet. Murine studies utilizing HFD^{porklard} diets (45%-65%) have shown increased levels of cytokine expression in blood and adipose tissue, which were associated with the stimulation of tumor progression[154, 174-176]. In our study, WT mice reproduced the expected DIO phenotype, while L2-HFD^{porklard} mice presented an accelerated BE/EAC phenotype with very low body weight and negligible FM, as seen with L2-HFD^{palmoil} mice. HFD^{porklard} diet was able to induce significantly more esophageal tumors as noted in Figure 4.9 D, E, and while not significantly different there appeared to be an increased trend in the cardia tumor score Figure 4.9 F, highlighting the influence of animal fats, which more closely mimics Western diets. Further analysis with a larger cohort may reveal a more advanced acceleration of the phenotype, increased inflammatory levels and increased immune cell recruitment to the tumor microenvironment. The L2-HFD phenotype led us to speculate that the L2-model was resistant to DIO and that another approach was necessary to achieve an obese phenotype in combination with the L2-model.

We sought to achieve this by crossing L2-mice with a genetic model of obesity, the Mc4r^{X16}knock-in as described in Chapter 4, Section 4.10. The observations made of littermates without the L2-gene, i.e. Mc4r^{X16}knock-in and Mc4r^{X16}heterozygous showed the development of obesity as they aged. However, L2/ Mc4r^{X16}knock-in and L2/ Mc4r^{X16}heterozygous mice showed a complete abrogation of the genetic obesity phenotype.

The lean L2-HFD phenotype, in addition to phenotypic observations of HFD^{porklard} feeding and the Mc4r^{X16}knock-in-cross further discredit the mechanism of inter-abdominal pressure; rather they point in the direction of an overwhelming inflammatory effect heightened by certain components of HFD in combination with the local and systemic inflammation typical to the L2-IL-1beta model. While the exact dietary components triggering this acceleration remain to be identified, they appear to be imparting a strong effect on the tumor microenviroment (TME) of the SCJ. We speculate that in addition to direct contact during the

process of digestion, circulation of these HFD components appear to be stimulating an increased production of inflammatory cytokines and influencing bile acid (BA) production while recruiting a unique immune cell profile to the site of tumor development.

6.1.3 Metabolic Phenotyping

Further metabolic measurements made regarding food / energy intake showed L2-Chow mice consumed comparable amount of food over the course of the dietary intervention, as the WT-controls (Figure 3.4.1 A). L2-HFD mice however showed a decrease in food intake starting around 6-months of age, around the onset of metaplasia/ low-grade dysplasia and subsequently had lowered energy excretion and assimilated energy measurements (Figures 3.4.1 C, D & 3.4.2). These observations could be the direct result of the development of tumors and lesions obstructing the intake of food. Indeed, macroscopic tumors were observed as early as 6-months of age in L2-HFD mice (Appendix Figure 4.13.1). In agreement with our data of decreasing body weight, accompanied by low fat and lean mass in L2-HFD mice (Figure 3.3.2), loss of fat and skeletal mass and systematic inflammation arising from complex host-tumor interactions can contribute to malnutrition in human patients with EAC; weight-loss and cachexia is further influenced by eating difficulties related to the stage and location of the tumor(s)[177].

Interestingly, while no significant differences were noted from activity monitoring, analysis of activity over 72 hours showed some separation between the WT- and L2-genotypes on each diet (Figures 3.5.3). Activity measurements took into account movements in the X, Y and Z directions (rearing onto hind legs). It appeared that WT-Chow mice are more active than L2-mice, which might be the result of the progression of the disease. WT-HFD mice appeared to be the least active of the groups, with a decreasing trend in activity as the mice aged and grew more obese. Interestingly, L2-HFD mice showed an increase in activity followed by a step decrease until the 12-month time point (Figure 3.5.3 B). While it was expected that these mice be the least active of the groups due to the accelerated disease phenotype, it could also be reasoned that the increased activity is a result of discomfort and uneasiness during the earlier stages of the

disease, followed by a steep decline that appeared in parallel with body mass reduction and disease progression. As with observations made for the measurement of activity, L2-HFD appeared to cover a greater distance over the course of the dietary treatment period compared to their WT-controls (Figure 3.5.3 C, D). Published data on mouse behavior as a result of distress from esophageal tumors does not exist, we can only speculate a causative effect of the macroscopic tumors on animal activity since we were unable to quantify chronic or visceral pain conditions such as tumor pain, abnormal positioning, hunching, flinching or shaking[178] due to lack of measuring resources and hindsight to assess pain and discomfort as a potential driving factor of increased late-stage physical activity. Existing literature assessing pain in cancer mouse models use tests such as mechanical allodynia, cold allodynia, and hyperalgesia using a von Frey filament, acetone, and radiant heat, respectively[179] in short-term or fast progressing cancer models of bone cancer primarily[180, 181]. However, since ours is a long-term model, a novel suggestion would be to rely on recorded footage of individual animals during the activity-monitoring period, to evaluate abnormal behavior and quantify postures associated with discomfort.

 In comparison to their WT-controls, L2-mice on both diets had slightly lower heat production, which could be attributed to the over all lower body mass observed in the model (Figure 3.5.2 C, D). Analysis of weekly energy consumption revealed lower RER values in WT-HFD as was expected, and interestingly, L2-HFD showed a similar trend, despite their resistance to DIO (Figure 3.5.2 A, B). This could be due to the metabolism of the tumors themselves, an important aspect that will be followed up and further studied in the future. Theoretically, *in-vivo* analysis of tumor metabolism in the L2-HFD can be achieved using ^{13}C isotopic studies as done in other cancer models such as Glioblastoma (GBM) studies[182]. ^{13}C-labeled nutrients can be infused into tumors in L2-HFD mice and metabolites extracted from tumors can be analyzed to detect the metabolic fates of glucose and glutamine; metabolic marker candidates of EAC[183], in tumors compared to normal tissue using ^{13}C NMR spectroscopy[182, 183]. While literature and experimental studies are limited in this field in regards to EAC tumors, an alternative possibility would be to conduct a similar analysis as Zhang and colleagues using LC-MS and ^{1}H NMR, [183].

Utilizing a combination of both methods, the authors were able to derive metabolic profiles from patient serum that readily distinguished EAC patients; we could take it a step further with our mouse model, and analyze tumor lysates as the disease progressed to attain a better understating of tumor metabolism in relation to the over all metabolism of the L2-model. Or as is planned for the future, starting out by simply analyzing tumor tissue using RT-PCR to examined expression of two markers associated with energy metabolism, ATP5B a marker of oxidative phosphorylation and PKM2 a marker of glycolysis as previously carried out with patient tumors by our collaborating partners from Trinity College, Dublin, Ireland[184]. Based on their previous results, we speculate that L2-HFD tumors could also have a distinct metabolic profile with mitochondrial dysfunction and an altered energy metabolism with expression of oxidative phosphorylation or glycolytic enzymes that are associated with obesity or HFD.

The implications that our findings have on obese patients with BE suggests that dietary choices more so than increased adiposity, WHR or WC might be influencing the levels of inflammation and thereby facilitating a proinflammatory microenvironment suitable for the progression of the disease state rather than mechanistic forces. Or the altering of circulating adipokines abundant in obese BE patients because of high fat dietary choices maybe resulting in a more aggressive pro-inflammatory tumor niche[185], or perhaps some combination of the two.

In regards to the L2-IL-1beta mouse model, previous and current results point towards the acceleration of the disease phenotype via the inflammation hypothesis. Given that the L2-model was resistant to DIO, the combination of IL-1beta over-expression and chronic HFD proved sufficient in accelerating the previously observed phenotype by several months.

6.1.4 The Role of Inflammation in the L2-IL-1beta model

Il-1beta is a multifunctional cytokine with potent inflammatory potential[161] associated with the inflammatory gradient within BE[160]. The consumption of foods rich in fat by humans and rodents alike results in an influx of free fatty acids (FFAs) or saturated fatty acids from the diet. This can lead to the expansion of adipose tissue and/or obesity or a state of low-grade inflammation, due to

factors released from the enlarged adipose tissue or by a component of the diet itself[186]. In this study, the implementation of chronic HFD feeding accelerated the previously observed phenotype sans obesity, with signs of metaplasia appearing as early as 3-months of age (data not shown), visible tumors by 6-months of age and high-grade dysplasia presenting as early as 9- to 12-months of age. It has been suggested that inflammation itself maybe a key activator, in combination with an altered immune and tumor microenvironments providing a driving force for disease progression[187-189]. The TME, which is made up of different cell populations, signaling factors and structural molecules interacts with tumor cells to assist with the development and progression of all stages of tumorigenesis[190]. In BE and EAC, environmental factors, such as diet, can activate acute and chronic inflammation in susceptible tissues and in circulation, leading to constitutive activation of pro-inflammatory signaling pathways which in turn promote survival and proliferation[127, 191]

The association between inflammation and cancer has been well established [122, 123]; in particular elevated IL-1beta has been identified as a mediator of tumorigenesis in the L2-mouse model of esophageal cancer[89, 109]. Chronic HFD feeding is known to induce adipose tissue inflammation characterized by increased adipose tissue macrophage (ATM)[91, 158, 192]. The L2-IL-1beta model on HFD appeared to be resistant to DIO, instead a lean, cachexic-like phenotype was observed accompanied by low fat mass values and comparable lean mass, which decreased over time and disease progression. Although weight gain was not observed in the L2-model (Chow and HFD treatments), a similar observation in relationship to severe inflammation and high fat was made in lipoprotein lipase inhibitor Angptl4 KO mice. Lichenstein and colleagues found that feeding a diet rich in saturated fat to mice lacking Angptl4 induced a severe cachexic phenotype[193] and this was also due to an accelerated inflammatory phenotype with an expansion of the lymphatic organs (lymph nodes) similar to our observation of splenomegaly (Figure 4.7.2) and increased inflammation in the esophagus. Additionally, they observed that part of the inflammatory reaction was caused by saturated fatty acids, which originated from macrophages in the lymph nodes.

An increased intake of saturate fatty acids (SFAs) has been associated with an increased risk of type 2 diabetes, obesity and CVD. Abundant SFAs such as palmitate (Pal) and stearate (Ste) are commonly linked to endothelial dysfunction, pro-inflammatory signaling and apoptosis[155]. It was elegantly shown by Snodgrass and colleagues that Palmitic acid activated TLR2, up-regulate NALP3 expression and induced inflammasome mediated IL-1beta production in human monocytes. This in turn can result in enhanced inflammation in peripheral tissues, suggesting that these pathways are strongly modulated by dietary fat[154]. While we did not actively evaluate the influence of individual components of the HFD, Palmitic acid is present in the HFD[palmoil] and HFD[porklard] diets and could serendipitously be the dietary component responsible in part for the disease acceleration. Proposed future studies could involve feeding L2-mice with higher amounts of this saturated fat to assess whether the phenotype is in fact accelerated while another cohort could be fed a diet lacking Palmitic acid to see if the phenotype is abrogated or at least reduced. Another interesting aspect to investigate in the future would be the influence of HFD on the fatty acid composition of immune cells in the L2-model. Studies on rodents have shown that diet influences and alters the fatty acid (FA) composition of immune cells, typically increasing in composition of the FA(s) of the enriched diet[194-196]. Moreover, the FA composition of human immune cells including different mononuclear cells (MNCs), as well as neutrophils have also been modified by oral intake of FAs of interest[197-200]. The suggested mechanism by which an altered supply of fatty acids could affect the immune response starts off with altering the composition of immune cell phospholipids, which in turn can cause membrane alterations and trigger signal transduction pathways and/ or lipid mediators which leads to an alteration of immune cell function (phenotype) and incites an altered immune response[201]. While we have yet to identify the composition of the immune cells of interest in our study, in relation to our existing data, these findings support our hypothesis that diet, rather than obesity maybe a greater contributor to the inflammatory TME niche of the L2-model.

In summary, in addition to body mass observations, the L2-model on HFD was subject to metabolic phenotyping including food consumption and activity monitoring, direct and indirect calorimetry, all of which did not reveal a distinct metabolic phenotype compared to L2-Chow mice, however a distinction from the WT controls was clearly noted.

With regards to obesity models, the inflammatory state predominantly resides in adipose tissue and the liver, however, with the resistance to DIO, the lean phenotype and scarcity of adipose tissue in the L2-HFD model, it was assumed that diet in combination with the innate inflammation of the model rather than adipose mediated inflammation or mechanistic pressure triggered the accelerated phenotype.

6.2 The effects of HFD on the Local and Immune Microenvironment in L2-IL-1beta Mice

The local microenvironment of the esophagus and SCJ in humans, and the cardia region in the mouse model are complex. In addition to tumor cells, there is strong evidence suggesting that normal cells within the tumor stroma including fibroblasts and immune cells contribute to tumor development and progression as part of the TME[202, 203].

Fibroblasts may be the most abundant stromal cells in most cancers[204], cancer associated fibroblasts, commonly referred to as CAFs, have a myofibroblastic phenotype; with secretory and contractile cells which express aSMA[205, 206]. CAFs isolated from EAC patients have been recently implicated as promoters of tumor cell invasion *in vitro* and growth *in vivo* by signaling to EAC cells through the secretion of extracellular matrix proteins[202]. During the stepwise progression of metaplasia to high-grade dysplasia, we observed a gradual increase in aSMA+ stromal myofibroblasts in the cardia region of L2-HFD mice compared to L2-Chow and WT-mice (Figure 4.5). This is of significance because fibroblasts not only play a crucial role in immune responses through the production of pro-inflammatory cytokines and chemokines[207], but they are instrumental in mediating the quality and quantity of immune response and creating a microenviroment of chronic inflammation and immune intolerance [208]. Mechanistically, CAFs can recruit macrophages, neutrophils and lymphocytes through secretory factors, resulting in the release endothelial cell stimulants such as VEGF, HGF, MMP2, and IL-8[208, 209].

In addition to the stromal influence on inflammation in the TME, immune cells also contribute significantly to the inflammatory niche implicated in disease development and progression. Expression of proinflammatory cytokines in response to bile and acid reflux[188] and HFD[187] from epithelial cells in the esophagus, SCJ and gut include IFN-γ, IL-1beta, IL-6, and IL-8, which in turn stimulate several proinflammatory cell types such as neutrophils, eosinophils, mast cells, macrophages as well T- and B- cells[141]. Esophagitis, resulting from acid reflux activates a T_H1 pro-inflammatory response, with increased IFN-gamma production[210], and the progression to BE has been indicated with a

shift to a T$_H$2 response accompanied by changes in cytokine patterns with increased expression of cytokine including IL-4, IL-5, IL-10 and IL-13 [186], this transition could be responsible for inducing an immunosuppressive and tumor-promoting environment[211].

It was previously shown that IL-1beta overexpression induced metaplasia and dysplasia in the SCJ region through recruitment of immature myeloid cells (IMCs) in the L2-model; IMCs also increased in early disease progression in the distal esophagus of the L2-model[89]. The phenotype observed from flow cytometry profiles of esophageal tissue from L2-HFD model led us to believe that the immune cell microenviroment in this model is one where IMCs, neutrophils and CD3+CD4+ T-helper cell levels are significantly increased or show a tendency to be elevated in the esophagus (Table 6.2.1).

On HFD the L2-mice developed an enhanced pro-tumorigenic esophageal microenvironment, characterized by a significant increase in IMC infiltration compared to L2-Chow mice (Table 6.2.1). IMCs (CD11b+Gr-1+) are involved in inducing inflammatory cytokine by activating innate immune pathways and contribute greatly to tumor progression and promote tumor evasion from immune attack[211]. A previous study assessing the effects of HFD on B Lymphopoiesis also saw an increase in IMCs resulting from HFD in C57BL/6J mice following a 3 week feeding period[212]. Furthermore, collaborative partners showed that DIO C57BL/6 male mice were infected with *H. felis (at 8 weeks of age)* and placed on a high-fat diet between 10-15 months had increased bone marrow-derived immature myeloid cells in blood and gastric tissue [213]. Gastric IMCs increase early in disease progression and have been linked to cancer initiation[135]. Neither of these studies were able to directly associate a mechanism connecting obesity with the increased IMC populations, rather they speculated like we do, that some component(s) of the HFD could also be responsible for triggering this increase.

These findings further support the notion that dietary component(s) of the HFD, in addition to IL-1beta overexpression in the L2-model may be causing a shift in the inflammatory profile that leads to an abundant accumulation of IMCs in the esophagus of L2-mice through chemotactic cytokines rather than mechanistic obesity. Suggesting that HFD influences esophageal carcinogenesis in

combination with IL-1beta overexpression through a proinflammatory positive feedback-signaling loop between abundant circulating cytokines/ chemokines and esophageal tissue. These circulating cytokines and/ or chemokines modulate esophageal IMC mobilization, possibly via KC (CXCL1) and a T_H17 response via IL-6 (a downstream target of IL-1beta) and leptin (shown to be up regulated in the L2-model in the microarray) resulting in a pro-tumorigenic SCJ microenviroment as described in the *H felis model[213].*

Table 6.2.1: Summary of flow cytometry analysis for myeloid and T-helper cells in the esophagus of L2-Chow, -HFD and L2/IL-8Tg mice.

Esophagus	L2Chow v. L2-HFD	L2 v. L2/IL-8Tg
Myeloid cells		
IMCs	↑*	↑
Macrophages	no difference	no difference
Neutrophils	↑*	↑*
T-helper cells		
CD3+CD4+	↑	↑
CD3+CD8+	↓	↑*
NKT-cells	no difference	↑
gdT-cells	↑	↑

Table 6.2.2: Summary of flow cytometry analysis for myeloid and T-helper cells in the cardia of L2-Chow, -HFD and L2/IL-8Tg mice.

Cardia	L2Chow v. L2--HFD	L2 v. L2/IL-8Tg
Myeloid cells		
IMCs	↑	no difference
Macrophages	↑	↑
Neutrophils	no difference	↑
T-helper cells		
CD3+CD4+	↑	↓
CD3+CD8+	↓	↑
NKT-cells	no difference	no difference
gdT-cells	↑	no difference

*Indicates significant differences.

We speculate that the observed increase in the IMC population in L2-HFD mice might be because these cells are differentiating into neutrophils further down the line. A recent study by Casbon and colleagues demonstrated that tumor production of granulocyte-colony stimulating factor (*G-CSF)* induced chronic activation of myeloid differentiation in bone marrow (BM), which led to inefficient erythropoiesis, anemia, and splenomegaly to meet the demands of

neutrophil and red blood cell (RBC) production during tumor growth, thereby regulating BM to generate T cell-suppressive neutrophils in cancer[214]. This goes along with our observations that with HFD treatment in the L2-model, the acceleration of dysplasia parallels a shift in the myeloid phenotype towards a more granulocytic type of differentiation. The increase in neutrophils observed in the distal esophagus likely contributed to esophageal inflammation and carcinogenesis through secretion of pro-inflammatory cytokines and chemokines including IL-8 and NFkB, shifting towards a more acute/ chronic inflammatory response in the carcinogenic state as noted through flow cytometry analysis, Figure 6.2.1. The significant difference in neutrophil cell populations between L2-Chow and –HFD mice was further confirmed by IHC stainings of neutrophils in the esophagus and cardia of 12-month old L2-mice on the respective diets (Figures 4.4.2 E & F and Figure 4.13.2 O). Additionally, the postprandial phase following a high fat meal, in humans subjects, is characterized by increased levels of glucose and triglycerides, which are accompanied by a recruitment of neutrophils[141] which fits our theory that a dietary component(s) of the HFD might play a significant role in stimulating neutrophil recruitment.

Gene set enrichment analysis of L2-HFD mice in comparison to L2-Chow and WT-mice showed the activation of several pathways associated with inflammation. Of particular interest were genes that were differentially regulated in the LAIR, COMP, INFLAM and STEM BIOCARTA pathways, including TNF, IL-1alpha, IL-8, CXCR4, CSF1 & 2 and TGFB 1 & 2 (Appendix Table 4.13.2). These pathways and cytokines illustrate the existing state of inflammation in the L2-model brought on by HFD. Other noteworthy signaling pathways included the DC, ERYTH and TNFR2 BIOCARTA pathways, which highlight the activation of immune cells and the differentiation of granulocytes and monocytes, in addition to activation of endothelial cells that lead to the increased expression of adhesion molecules.

While cytokine arrays carried out on esophageal and cardia tissue were not able to verify all of these differentially regulated genes of interest, they did further validate the ongoing inflammatory state. Cytokines that appeared to be up-regulated in the esophagus have been implicated as chemoattractants and recruiters of different immune cell types including monocytes and lymphocytes,

stimulating inflammatory responses, and further inducing inflammatory cytokines down-stream and involved in cell growth, proliferation and differentiation (Mmp2, Cxcl13 & 16, Ccl6 & 20 and Egf). While in the cardia region, cytokines involved as chemoattractants of immune cells, in addition to recruiters of eosinophils and factors secreted by macrophages appeared to be up-regulated (Ccl6 & 11, Ccl21 and Crp). Interestingly, Resistin, an adipose tissue-specific secretory factor associated with the inflammatory immune response appeared to be down-regulated in the cardia tissue of L2-HFD mice. Taken together these results confirm the unique inflammatory state in the esophagus and cardia of the L2-HFD model, emphasizing that the esophagus appears to be promoting the differentiation of IMCs to neutrophils in addition to the recruitment of neutrophils thereby creating an inflammatory driven niche that stimulates the production of factors such as Mmps and Wnt molecules to promote a tumor driven microenvironment ideal for the development and progression from metaplasia to high-grade dysplasia.

Members of the MMP[215, 216] (Figure 4.6.2.1) and WNT[217, 218] families (Figures 4.6.2.2 and 4.6.2.3) are known to recruit immune cells and appeared to be differentially regulated in the esophagus and cardia of 12-month old L2-HFD mice showing typical pathology of low- and high-grade dysplasia. MMPs are a family of extracellular enzymes that control several diverse proteins associated with normal repair and inflammation[219], in addition to pathological cellular processes including embryogenesis, angiogenesis, wound healing and cancer[220, 221]. MMP3 has been pathologically associated in squamous cell carcinoma (SCC) and the literature points to evidence for pro-tumorigenic capabilities[220, 222, 223]. MMP7 expressed almost exclusively by mucosal epithelia have functions in various processes of innate immunity[224], as well as regulating neutrophil recruitment in wound healing and angiogenesis[225]. MMP10 is known for moderating the proinflammatory response of resident and infiltrating macrophages[226] and has been shown to play a significant role in tumor growth and progression through regulation of angiogenic and apoptotic pathways in cervical cancers[227].

WNT signaling has been elegantly shown to contribute to human tumor progression[217]. Of the Wnt genes verified through RT-PCR in esophageal and

cardia tissue from L2-HFD mice, differential regulation of Wnt2, 5a, and 3a have been implicated in signaling pathways crucial to cell regulation, differentiation, proliferation, and death[122, 218](Wnt genes of interest are discussed in greater detail in relation to stem and progenitor cells in Section 6.3).

While both the esophagus and cardia were processed and analyzed at the same time, there were no significant changes observed in cardia tissue. It appeared that this unique immune phenotype was predominantly occurring in the esophagus of L2-HFD and L2/IL-8Tg mice.

Taken together, we hypothesis that the esophagus is recruiting these immune cell types and further stimulating the local inflammatory process that is promoting carcinogenesis in the cardia region which is in close proximity through gastric cardia cell expansion.

6.2.1 The Role of IL-8

In addition to the influence of the aforementioned signaling factors, RT-PCR showed KC levels, the murine homologue of IL-8, were elevated in the esophageal and cardia tissue of the L2-model, suggesting a crucial role for this cytokine in the acceleration of the observed HFD phenotype.

KC is a known chemoattractant neutrophil recruiter. It is involved in recruiting and activating neutrophils by binding with the receptors Cxcr1 and Cxcr2 that are expressed on the neutrophil surface. When these CXC-family of chemokines become deregulated they begin to be chronically expressed and can cause tissue damage resulting in angiogenesis with tumorigenesis [228]. Additionally, CXCL1 was shown to be significantly overexpressed during esophageal carcinogenesis with significant IL-8 levels detected in serum of patients with EAC, suggesting a potential biomarker and implicating a role for this chemokine in EAC[229]. This fits well with our Irish collaborator's data (Figure 5.1), which shows IL-8 levels to be increasing in human BE to EAC, while having no association with BMI levels, and the increasing levels of IL-8 measured in a normal esophageal squamous cell line (Het), a benign BE cell line (QH) and an esophageal adenocarcinoma cell line OE33 as well as in tissue conditioned medium from

normal, BE and tumor tissue from human patients (Figure 5.8.1). Further supporting the inflammatory hypothesis over the mechanistic hypothesis in this model. Likewise, GSEA data confirmed a role for the cytokine IL-8 evident in several pathways including the LAIR, INFLAM and STEM BIOCARTA pathways that were up-regulated in L2-HFD mice, highlighted in Appendix Table 4.12.3

Thus far we have shown that the L2-model has a distinct profile of immune cell populations as a result of HFD; one that is driven by increased neutrophil recruitment and infiltration in the esophagus that in turn accelerates the pathological progression of metaplasia and dysplasia in the cardia tissue. Local cell types from innate and adaptive immune cells are likely major contributors to the pro- and anti-inflammatory cytokines present within the esophageal and cardia tissue[187]. Given that proinflammatory cytokines IL-8 (KC in mice) and IL-1beta were shown to be elevated in esophagitis and Barrett's epithelium, and markedly elevated in adenocarcinoma[211], as was similarly observed in our L2-HFD model, the next step was to assess the role of IL-8 over-expression in the L2-IL-1beta mouse model.

The successful crossing of L2-IL-1beta mice with transgenic mice that over-express human IL-8 led to the creation of the L2/IL-8Tg model. This IL-8BAC transgene is only induced following inflammatory stimulation and show significant increased levels of IL-8 in diseased tissue and circulation[135]. The L2-IL-8Tg model showed an almost identical phenotype to the L2-HFD phenotype (Figures 5.2.1 & 5.2.2) in terms of low-body weight and macroscopic lesions present in the esophagus and cardia. Furthermore, they also progressed in a similar fashion from metaplasia to low- and high-grade dysplasia as they aged.

Further assessment of esophageal and cardia tissue form mice presenting typical metaplasia and dysplasia by flow cytometry showed an increased accumulation of IMCs and neutrophils in the esophagus at 9- and 12-months of age, as expected given the role of IL-8 as a neutrophil recruiter (Figure 6.2.1). Neutrophils are typically recruited in the early stages of tumor development[230], evident in the comparison of esophageal and cardia tissue of L2/IL-8Tg mice at 9-months of age (Table 6.2.1 and 6.2.2). Macrophages

recruitment occurs later on[231], as evident in the increased cell populations noted in esophageal and cardia tissue of L2/IL-8Tg mice at 12-months of age.

Also in-line with the inflammation-immune response, our microarray data showed that nitric oxide synthase (Nos2) was significantly upregulated in L2/IL-8Tg mice. Neutrophils express Nos2 in order to suppress CD8+ T cell-mediated antitumor immune response, thereby promoting tumor progression[159]. While we did not see significant changes in either group, both 12-month old L2-HFD mice and 9-month old L2/IL-8Tg mice showed a trend towards an increase in T-cell populations in the esophagus. 12-month old L2-HFD mice also showed this trend in the cardia.

Furthermore, during the stepwise progression of metaplasia to high-grade dysplasia in the L2/IL-8Tg model, we observed a gradual increase in aSMA+ stromal myofibroblasts in the cardia region (Figure 5.3.2), as was noted in L2-HFD mice. This observation falls in favor with the notion that pro-inflammatory factors such as IL-8, which can also be produced by CAFs, sustains a chronic inflammatory state in the tumor microenvironment[208, 232].

Our collaborators from the Wang lab were able to show that upon treatment with human obese serum, cardia organoids from IL-8Tg mice proliferated significantly faster than WT-organoids (Figure 5.7.2). Furthermore, collaborators from the Lysaght lab showed that the supernatant from these organoid cultures treated with obese serum expressed IL-8 at significantly higher concentrations than those treated with lean serum. Suggesting that the obese serum was able to provoke a stronger inflammatory response and trigger the organoids to express higher levels of IL-8, given that the IL-8 transgene is activated following inflammatory stimulus. We suggest that this higher expression of IL-8 is partly responsible for increased recruitment of immune cells to the tumor microenvironment, in particular neutrophils.

These collective findings led us to examine the individual impact of IL-8 *in-vitro.*

Cardia organoid cultured from L2-IL-1beta mice on Chow diet treated with recombinant human IL-8 did not show any significant changes in organoid size or number. While IL-8 had no direct effect on epithelial cells, it is possible that it stimulates stem cells and tumor cells to increase recruitment of immune cells.

Similarly, treatment with serum from L2-HFD mice did not result in any significant differences. Both treatments however, showed a slight trend towards an increase in size or number.

Lastly, we treated L2/IL-8Tg cardia organoids with lean and obese human serum and saw a potential increase (not significant) in organoid number, perhaps further future trails will reveal a stronger effect. What we can conclude from these *in-vitro* trials is that neither diet, nor IL-8, nor circulating cytokines and adipokines alone leads to the acceleration of the local BE/EAC phenotype observed in the L2-model. Rather an inflammatory microenvironment recruits immune cells and with such a niche, stem cells might be accelerating carcinogenesis. This is, nevertheless, a phenotype that cannot be fully recreated, but only partially mimicked in a 3D organoid cultures. Of note, serum from HF fed L2-mice and obesity patients was able to induce IL-8 expression in epithelial cells suggesting that HFD is accelerating the phenotype through the expression of other well known cytokines in the esophageal tissue and therefore induces the recruitment of IMC that differentiate to neutrophils in the esophagus.

With the over-expression of one chemokine, IL-8 we were able to mimic the macroscopic phenotype observed in L2-IL-1beta on a chronic HFD. Furthermore, both models, the L2-HFD and L2/IL-8Tg, show a similar immune microenviroment profile. We were able to show that they appear to have unique total microenviroment based on the results of the microarray analysis, cytokine array findings and organoid cultures, leading us to believe that inflammation in combination with a unique tumor immune cell niche plays a crucial role in the disease progression observed here. Based on this, we suggest that the murine esophagus appears to be building a niche to recruit intestinal stem cells which then form BE and EAC.

6.3 Regulation of the L2-IL-1beta tissue stem and progenitor cell function by HFD and IL-8 over-expression

The effect of HFD on the functions of tissue stem cells and progenitor cells are not fully understood, however it has been observed that diet profoundly influences tissues regeneration and cancer incidence[233]. Adult stem cells respond to the physiologic consequences of diet and tend to accumulate mutations that lead to transformation, it can be hypothesized that early oncogenic events can occur in stem cells and differentiated cells, resulting in a larger pool of cells that are capable of undergoing early transformation, which along with surplus growth factors, nutrients and hormones can then drive tumor progression and growth[162].

A hypothesis fundamental to our research group, originally proposed by Hamilton and Yardley [153], suggests that BE and EAC arises from a gastric cardia lineage. This novel theory, based on data previously published by Quante and colleagues, advocates a crucial role for gastric progenitors through a tumor-promoting IL-1b-IL-6 signaling cascade and Dll1-dependent Notch signaling[89].

The expansion of progenitor cells in the gastric cardia, followed by migration towards the esophagus, was shown through temporal analysis of the L2-model at different stages of the disease. Lineage-tracing studies implicated Lgr5 cells as the likely origin of some of the metaplastic BE tissue from Lgr5+ cells within the gastric cardia. Moreover, progenitor markers that were absent in normal esophageal squamous epithelium were present in normal gastric cardia and significantly increase in BE, including LGR5 and DCLK-1[89].

To address the acceleration of the BE/EAC phenotype in the L2-model as a result of HFD, the localization of two stem/ progenitor cells, Lgr5+ and Dclk-1, in the cardia regions of mice on Chow and HFD were assessed.

Lgr5 is a validated stem or progenitor cell marker for the murine gut that has been recognized in the pathogenesis of different human cancers including hepatocellular carcinoma, basal cell carcinoma, endometrial, and colon and ovarian cancer[234-237]. Previous studies have demonstrated expression of

LGR5+ cells in human BE and EAC[238], and it was found to being significantly elevated in BE tissue in the L2-IL-1beta model with the high likelihood of it being the cell-of-origin for the metaplasia observed in the model[89]. Furthermore, *in-situ* hybridization has identified localization of LGR5+ cells in the middle of BE glands[239], as well as in areas between gastric and metaplastic glands in BE[44]. This suggests a strong role for LGR5+ cells as stem cells, since they demonstrated both gastric and intestinal differentiation. *In-situ* hybridization showed that L2-mice on HFD had significantly increased localization of Lgr5+ cells in cardia tissue of 12-month old mice compared to L2-Chow mice, suggesting that Lgr5+ cells act as stem cells in BE, maintaining the intestinal phenotype of BE and intestinal metaplasia. We speculate that activation of Lgr5 expressed by BE in cancer-initiating cells may sustain existing inflammatory responses, mediate a resistance to apoptosis and promote progression of the metaplasia - to - carcinoma sequence[240].

Additionally, the localization of Dclk-1, a microtubule-associated kinase neuron, said to be expressed in gut epithelial progenitors[241] and a possible marker of cancer stem cells (CSCs) since it is detected in potential cancer stem cells and not in normal stem cells[125, 242] also appeared to have increased localization in L2-mice as a result of HFD and L2/IL-8Tg mice. Localization of Dclk-1+ cells accumulated adjacent to metaplastic mucus producing cells in BE tissue in the gastric cardia region. It was elegantly shown by Westphalen and colleagues that DCLK-1 expression is important for the progression of early neoplastic lesions[191], supporting the increase in Dclk-1+ cells observed in L2-HFD and L2/IL-8Tg mice presenting low- and high-grades of dysplasia. This observation is supported by a previous study that also elegantly showed that intestinal inflammation induced NF-kB signaling and subsequent Wnt signaling, was sufficient to convert non-stem cells into potential cancer initiating cells[243], which could have emerged from mutated Dclk-1 C cells[191].

In our study, we observed a significant up-regulation of Wnt3a and a down-regulation of Wnt5a expression in the esophagus, while Wnt5a showed a trend of higher expression in the cardia of L2-HFD mice over L2-Chow mice, however expression levels decreased in both L2-groups as the mice aged (Figures 4.6.2.2 & 4.6.2.3 for esophagus and cardia tissue respectively). WNT3a has been shown

to be highly expressed in the intestine, while WNT5a was focally expressed in the gastric corpus[170]. This falls in line with the findings that BE is a form of intestinal metaplasia and is confirmed by increased Wnt3a expression noted in esophageal tissue. Furthermore, a recent publication by collaborators from the Wang lab proposes gastric innate lymphoid cells (ILCs) as a major source of Wnt5a, at least in the stomach of a mouse model of gastric carcinogenesis, highlighting their role in stem cell niche or cancer development in states of inflammation or infection[170]. Moreover, while we did not observe a loss of Wnt5a expression the decreased expression observed with disease progression in L2-mice is supported by another recent publication that proposes that loss of WNT5A with concurrent activation of WNT5A-independent ROR2 signaling may serves as a marker of EAC progression[244].

This upregulation of gastric columnar progenitor cells within the cardia region of L2-HFD and L2/IL-8Tg mice suggests that the metaplastic lineage of BE lesions are possibly derived from a gastric cardia lineage and that Lgr5 cells from the gastric cardia migrate into the distal esophagus and give rise BE tissue with increased Lgr5 expression. Increased inflammation in combination with a distinct immune cell phenotype, cytokine profile and the expression of MMPs or specific WNTs may form a niche that is ensued by this expansion of cardia stem cells in the esophagus where they find a microenvironment that induces proliferation and therefore drives eventual malignant transformation. These findings in the mouse model are similar to the increase in identical progenitor markers previously observed in gastric cardia and BE tissue from a cohort of human BE patients[89].

6.4 HFD Affects Luminal Components that Further Modulate Esophageal Mucosal and Systemic Inflammation

The esophagus is in continuous contact with luminal components including acid, pepsin, bile acids, food particulate matter and bacteria, which interact with epithelial, and underlying stromal and immune cells and affects the permeability of the epithelial barrier[166, 167].

As was briefly described in Section 6.1.1, frequent exposure of the esophagus to gastroesophageal reflux can elicit an inflammatory response through the stimulus of inflammatory cytokines leading to activation of innate immune responses of attraction and activation of neutrophils, dendritic cell, and monocytes. This reflux carrying bile, hydrochloric acid, and proteases abuses the esophageal epithelium, leading to the formation of premalignant BE and EAC, [235] which arise from intestinal metaplasia. Recent murine studies have shown that alternations of the gut microbiota can cause changes in host bile acid composition[245-247]. As we have previously demonstrate the effect of bile acid treatment in the mouse model[89], which might have changed the microbiome as well, we sought out to assess the influence of the microbiome in combination with HFD in the L2-model.

Bile acids and the intestinal microbiome appear to have a strong influence on each other. Intestinal microbiota are involved in the biotransformation of bile acids through deconjugation, dehydroxylation and reconjucation of bile acids[240] and there is evidence of BAs influencing and regulating intestinal epithelial functions[248].

While we did not examine the role of bile acids directly in the L2-HFD model, it has been previously described by Quante and colleagues in great detail in the original publication of the L2-IL-1beta model[89]. HFD, we hypothesize, maybe causing changes in BA production that maybe regulating the microbiome and intestinal epithelial functions which in turn could be further influencing BA production and conversion[249]. Based on this knowledge and the absence of DIO in the L2-HFD model, the luminal effects of an altered microbiome through

HFD and BAs, on the inflammatory state in the L2-IL-1beta model, primarily in the intestine were of interest to us.

It is well established that the microbiome can heavily influence the development and progression of several disease states, including obesity[250, 251] and certain cancers[250, 252, 253]. However, literature regarding the role of the microbiome, either at the tumor site or in the intestine, in relationship to disease progression of BE and EAC remains sparse. Of the few existing studies on human patients, data suggest that the esophageal microbiome could be transitory; classified into either a type I microbiome dominated by *Steptococcus* bacteria and representing the phenotypically normal esophagus, and a type II microbiome dominated by Gram negative anaerobes/ microaeriphiles that correlated with esophagitis (Odds Ratio: 15.4) and BE (Odds Ratio: 16.5) resulting from gastric reflux[254, 255].

While this proves interesting and might contribute in part to disease progression, it is difficult to verify in a mouse model due to their animalistic behavior of feces consumption. Alternatively, the "pathogenic microbial community" theory suggests that the entire community contributes to pathogenicity although no individual community members can be categorized as classic pathogens[256]. And it has been shown in mouse models of inflammatory bowel diseases that the development of mucosal inflammation and adenocarcinoma requires both a trigger (chemical or genetic), and presence of commensal bacteria [254, 257].

Aside from changes observed in metabolism, inflammatory cytokine profiles and TME, assessment of the microbiome of L2-HFD mice showed a profile shift towards lower species diversity. As described in Chapter 4, Section 4.9, LEfSe analysis of the microbiome revealed a significantly different OTU profile between L2- and WT-HFD mice. While many of these OTUs remain to be described or cultivated, one OTU of interest was *Bacteroides dorei* (DSM 17855), which was highly associated with L2-HFD mice. An increase in *Bacteroides* species, including *B. dorei* has been connected to several inflammatory gut diseases and potentially linked to causing T1D autoimmunity in children[258]. Furthermore, diets high in fat have been correlated with high *Bacteroides* populations [259]. If *B. dorei* is involved in the acceleration of the L2-phenotype through HFD, likely

routes include disruption of the epithelial layer or manipulation of immune system development. While this association alone is not sufficient to explain the accelerated HFD phenotype, a combination of several OTUs could be responsible for the disease acceleration observed under HFD in the L2-model.

Additionally, while the microbiome of L2-HFD^{porklard} mice remains to be analyzed, it can be assumed that the accelerated phenotype observed in L2-HFD^{porklard} resulting from a replacement in the dietary fat component by animal fat such as pork lard also alters the microbiome.

These results remain very preliminary, however they highlight a shift in the L2-microbiome influenced by HFD, which with further and more detailed analysis can lead to identifying specific OTUs unique to the model that may help in understanding possible combinations of mechanisms propelling this phenotype. Future findings from this microbiome study will provide us with deeper insight into the relationship of the luminal and host microenviroment that appear to be contributing towards a niche that accelerates BE carcinogenesis.

6.5 Conclusion

We demonstrate here that chronic HFD can increase the Barrett-like metaplasia phenotype observed in the L2-IL-1beta mouse model, and that this can accelerate the progression to dysplasia.

In summary, apart from the very low body weight phenotype, we were unable to distinguish a metabolic profile unique to the L2-model. We found that food intake decreased in L2-HFD as they aged and this was accompanied by a subsequent reduction in energy intake and assimilated energy. Additionally, we showed that L2-HFD compared to –Chow and WT-mice, appear to be more active and cover a greater distance traveled as they age; we speculate this restlessness maybe due to the level of discomfort experienced from the disease progression, however, this remains to be verified. It is possible that a unique metabolic phenotype might reveal itself with larger cohort sizes and longer measurement periods.

Furthermore, our data disproves the hypothesis of DIO propelling the progression of BE and EAC in the L2-model; we were able to show that the disease phenotype was infact accelerated with chronic high fat feeding in the absence of obesity, dispelling the theory of abdominal pressure resulting from obesity driven disease progression, particularly in our L2-model. Rather, our findings suggest a crucial role of inflammation, prolonged through diet and increased cytokine expression that causes a shift towards stromal and immune cells establishing a pro-tumorigenic microenviroment in the esophagus that maybe contributing to the disease progression of the L2-model.

Using flow cytometry, IHC and micro- and cytokine arrays, we verified a unique microenvironment shifted towards neutrophil infiltration through the increased presences of CAFs in the cardia region, increases in cytokine production, and more localization of stem and progenitor cells, all resulting from chronic high fat feeding in the L2-model. These observations also suggested an influential role of IL-8, as a contributor of disease acceleration in this model.

To analyze the role of IL-8 we crossed the L2-model with IL-8 over-expressing mice and established the L2/IL-8Tg model. With the L2/IL-8Tg model we were able to mimic the macroscopic phenotype of the L2-HFD model, and also documented a similar neutrophil rich microenviroment in the esophagus. Flow

cytometry analysis and staining of immune cells, in addition to IHC showing increased aSMA+ staining in the cardia region suggesting the influence of CAFs, point towards a tumorigenic microenvironment in the L2/IL-8Tg model.
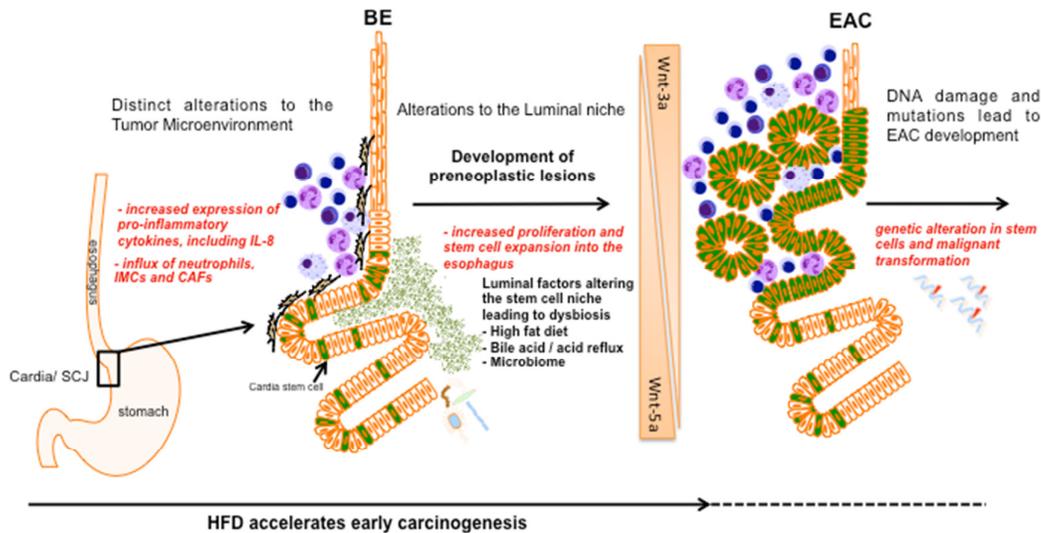
Figure 6.5: Suggested mechanisms that may be accelerating BE and EAC.
Based on findings from the studies conducted for this thesis, we propose that luminal factors such as bile acids, HFD and the microbiome can lead to a dysbiosis that in combination with on-going inflammation, contribute to an alteration of the immune microenvironment and stem cell niche through increased expression of pro-inflammatory cytokines which accelerate proliferation and stem cell expansion into the esophagus. Over time and continued exposure, these factors lead to genetic alterations within stem cells and malignant transformations that result in EAC. Figure adapted and used with permission from M. Quante[89, 125].

Additionally, these findings validate the hypothesis that alterations influenced by inflammation causes a shift towards a pro-tumorigenic niche. We were able to show through *in vitro* cultures of cardia organoids, that a complex series of factors are necessary for triggering proliferation and cell growth in L2-model, and that neither IL-8, diet nor obese serum alone were capable of reproducing this phenotype, rather we speculate it to be a combination of dietary components and other circulating inflammatory cytokines are necessary to stimulate this pro-tumorigenic niche. Moreover, a shift towards increased localization and expression of stem and progenitor cells including Lgr5 and Dclk-1 and differential expression of Wnt molecules 3a and 5a in the esophagus confirms the hypothesis that BE arises from a gastric cardia lineage and that the

microenvironment is responsible for the expansion of cardia stem cells into the esophagus, as a novel model for the development of BE and EAC.

Lastly, based on our preliminary microbiome data we suggest that HFD maybe altering the production and composition of BAs and the microbiome and/or vice-versa. The hypothesis that the intestinal microbiota influenced by HFD may be contributing to an accelerated phenotype in the L2-IL-1beta mouse model warrants further study.

Taken together, these findings also strongly suggest that BE and EAC disease progression in the L2-IL-1beta model is significantly accelerated by HFD through a shift in the immune microenvironment towards one of increased IMC and neutrophil recruitment, which is further augmented by an increased expression of inflammatory cytokines, including IL-8, as illustrated in Figure 6.5. This has direct implications for development of clinical routines and surveillance strategy. To date, intestinal metaplasia was used as a main risk factor for the development of dysplasia in the esophagus. Our data demonstrates that the inflammatory phenotype and potential alterations through different cytokines, immune cells or external factors (bile, HFD) is much more important than previously assumed. Therefore, we more attention be paid to the composition of the microenvironment including the immune cell niche and CAFs, and cytokine profile of the esophagus with its impact on stem cell recruitment and division. The uncontrolled expansion of stem cells in such a microenvironment seems to be a crucial factor for esophageal carcinogenesis. A deeper understanding of the molecular pathways of inflammation associated with BE and EAC tumorigenesis can lead to the development of targeted therapies and improved treatments for esophageal cancer.

Chapter 7: Future Perspectives

The results highlighted in Chapters 3-5 revealed a very interesting phenotype in the L2-IL-1beta mouse resulting from chronic HFD treatment and IL-8 over-expression. These findings suggest a significant role for inflammatory cytokines, impacted by diet, in accelerating the BE phenotype in this model. While the mechanism of what might be causing this acceleration has yet to be fully understood, ongoing and future experiments suggested below might provide more insight into what is at play in the L2-IL-1beta model.

Unfinished and ongoing projects will be completed by PhD candidate and GRK fellow Jonas Ingermann of the Quante Lab, Munich, Germany.

7.1 Micro- and macro-nutrient matched diets

A metabolic phenotype unique to the L2-model, one that distinguished it apart from WT-controls was not established from the results illustrated in Chapter 3. While certain metabolic measurements yielded significant differences like body mass, lean and fat mass over time, others failed to highlight a distinction between the genotypes despite the onset and acceleration of BE and EAC. One possible reason for this shortcoming could be the lack of a strict Control diet. Standard lab chow (Chow) was used for comparison with the original L2-IL-1beta experimental mice housed in Columbia University, USA.

To confirm a unique metabolic phenotype it would be of interest to assess the model on a Control diet that matches all nutritive dietary components of the HFD (palm oil) with the exception of the high fat content to isolate the effects of the dietary fat itself.

This dietary intervention is currently underway; L2-mice are being fed a matched-Control diet (Ssniff, Germany) *ad libitum,* under the same conditions as the L2-HFD study. Furthermore, as the mice age, detailed metabolic phenotyping will be carried to assess changes in body mass, fat and lean mass, energy in-take and assimilated energy, and glucose tolerance, along with indirect calorimetry and activity monitoring. Data collected from these studies will be compared with

the results from the L2-HFD study, in order re-evaluate the direct impact of the high fat dietary component on the accelerated L2-phenotype.

7.2 Blocking IL-8 receptor signaling in the L2-IL-1beta model

Studies have shown that blocking Cxcr2 signaling decreased tumor growth and microvessel density in a spontaneous tumor mouse-model of lung cancer[159, 161, 260]. To further assess and understand the role of KC (the murine homologue of IL-8) in the pathogenesis of BE/ EAC in the L2-IL-1beta model, it was of interest to address whether blocking Cxcr2 would result in a decrease or abrogation in the phenotype observed in L2-IL-1beta mice.

We seek to accomplish this by crossing the L2-model with a commercially available Cxcr2 knock out (KO) model. This KO mouse, the *Cxcr2^{tm1Mwm}* mouse, has been generously lent to us from the lab of Dr. Hana Algül (originally purchased from Jackson labs) for breeding purposes. Breeding is currently underway and upon the successful crossing of the two lines, the new L2/ *Cxcr2^{tm1Mwm}* mice will be aged for assessment of phenotype and the disease progression of BE/ EAC in comparison to the other experimental L2-models.

7.3 Summary of future perspectives

The observations and conclusions illustrated in Chapters 3-6 suggest a complex interplay between environmental triggers, genetic drivers and immune response in the L2-model. While much remains to be understood with this model, the unfinished and ongoing studies detailed in the previous results chapters as well as in this chapter will lead us closer to detailing the precise mechanisms that cause disease acceleration the L2-IL-1beta model.

References

1. *World Health Organization.* Health Topics, Obesity 2015 [cited 2015 August 1]; Available from: http://www.who.int/topics/obesity/en/.
2. Alexandre, L., E. Long, and I.L. Beales, *Pathophysiological mechanisms linking obesity and esophageal adenocarcinoma.* World J Gastrointest Pathophysiol, 2014. **5**(4): p. 534-49.
3. Long, E., Beales, I.L.P., *The role of obesity in oesophageal cancer development.* Therapeutic Advances in Gastroenterology, 2014. **7**(6): p. 247-268.
4. Jacobson, B.C., et al., *Body-Mass Index and Symptoms of Gastroesophageal Reflux in Women.* N Engl J Med, 2006. **354**(22): p. 2340-2348.
5. El-Serag, H.B., et al., *Obesity increases oesophageal acid exposure.* Gut, 2007. **56**(6): p. 749-55.
6. Campion, J., F.I. Milagro, and J.A. Martinez, *Individuality and epigenetics in obesity.* Obes Rev, 2009. **10**(4): p. 383-92.
7. Herrera, B.M., S. Keildson, and C.M. Lindgren, *Genetics and epigenetics of obesity.* Maturitas, 2011. **69**(1): p. 41-9.
8. Nguyen, T. and D.C.W. Lau, *The Obesity Epidemic and Its Impact on Hypertension.* 2012. **28**(3): p. 326-333.
9. Popkin, B.M., L.S. Adair, and S.W. Ng, *Global nutrition transition and the pandemic of obesity in developing countries.* Nutr Rev, 2012. **70**(1): p. 3-21.
10. Kelly, T., et al., *Global burden of obesity in 2005 and projections to 2030.* Int J Obes (Lond), 2008. **32**(9): p. 1431-7.
11. Ogden, C.L., et al., *The epidemiology of obesity.* Gastroenterology, 2007. **132**(6): p. 2087-102.
12. Ringseis, R., Eder, K., Mooren, F., Krüger, K., *Metabolic signals and innate immune activation in obesity and exercise.* Exercise and Innate Immune Activation, 2015. **21**: p. 58-68.
13. Kalupahana, N.S., N. Moustaid-Moussa, and K.J. Claycombe, *Immunity as a link between obesity and insulin resistance.* 2012. **33**(1): p. 26-34.
14. Galic, S., J.S. Oakhill, and G.R. Steinberg, *Adipose tissue as an endocrine organ.* 2010. **316**(2): p. 129-139.
15. Frayn, K.N., et al., *Integrative physiology of human adipose tissue.* 2003. **27**(8): p. 875-888.
16. Hoevenaars, F.P., et al., *Adipose tissue metabolism and inflammation are differently affected by weight loss in obese mice due to either a high-fat diet restriction or change to a low-fat diet.* Genes Nutr, 2014. **9**(3): p. 391.
17. Laugerette, F., Furet, J-P., et. al., *Oil composition of high-fat diet affects metabolic inflammation differently in connection with endotoxin receptors in mice.* Am J Physiol Endocrinol Metab., 2012. **302**: p. E374-386.
18. Trayhurn, P. and J.H. Beattie, *Physiological role of adipose tissue: white adipose tissue as an endocrine and secretory organ.* 2007. **60**(03): p. 329-339.

19. Fantuzzi, G., *Adipose tissue, adipokines, and inflammation.* 2005. **115**(5): p. 911-919.
20. Mraz, M. and M. Haluzik, *The role of adipose tissue immune cells in obesity and low-grade inflammation.* J Endocrinol, 2014. **222**(3): p. R113-27.
21. Maury, E., Brichard, S.M., *Adipokine dysregulation, adipose tissue inflammation and metabolic syndrome.* Molecular and Cellular Endocrinology, 2010. **314**(15): p. 1-16.
22. J. Jo, G., O., Pack, S., Jou, W., Mullen, S., Sumner, A.E., Cushman, S.W., Periwal, V., *Hypertrophy and/or Hyperplasia: Dynamics of Adipose Tissue Growth.* PLoS Computational Biology, 2009. **5**(3).
23. Teng, K., Chang, CY., Chang, LF., Nesaretnam, K., *Modulation of obesity-induced inflammation by dietary fats- mechanisms and clinical evidence.* Nutrition Journal, 2014. **13**(12).
24. Zhang, H.H., et al., *Lipase-selective functional domains of perilipin A differentially regulate constitutive and protein kinase A-stimulated lipolysis.* J Biol Chem, 2003. **278**(51): p. 51535-42.
25. Wang Y, S.S., Trujillo M, Lee MJ, Schneider SH, Brolin RE, Kang YH, Weber Y, Greenberg AS, Fried SK, *Perilipin expression in human adipose tissue: effects of severe obesity, gender, and depot.* Obes Res, 2003. **11**(8): p. 930-936.
26. Greenberg, A.S. and M.S. Obin, *Obesity and the role of adipose tissue in inflammation and metabolism.* 2006. **83**(2): p. 461S-465S.
27. Cinti, S., et al., *Adipocyte death defines macrophage localization and function in adipose tissue of obese mice and humans.* J Lipid Res, 2005. **46**(11): p. 2347-55.
28. Olefsky, J.M. and C.K. Glass, *Macrophages, inflammation, and insulin resistance.* Annu Rev Physiol, 2010. **72**: p. 219-46.
29. Laugerette, F., Furet, J-P., et. al., *Oil composition of high-dat diet affects smetabolic inflammation differntly in connection with endotoxin receptors in mice.* Am J Physiol Endocrinol Metab., 2011. **302**.
30. Weisberg, S.P., et al., *Obesity is associated with macrophage accumulation in adipose tissue.* Journal of Clinical Investigation, 2003. **112**(12): p. 1796-1808.
31. Osborn, O. and J.M. Olefsky, *The cellular and signaling networks linking the immune system and metabolism in disease.* 2012. **18**(3): p. 363-374.
32. Lumeng, C.N., et al., *Increased inflammatory properties of adipose tissue macrophages recruited during diet-induced obesity.* Diabetes, 2007. **56**(1): p. 16-23.
33. Lumeng, C.N., J.L. Bodzin, and A.R. Saltiel, *Obesity induces a phenotypic switch in adipose tissue macrophage polarization.* J Clin Invest, 2007. **117**(1): p. 175-84.
34. Nocon, M., et al., *Association of body mass index with heartburn, regurgitation and esophagitis: results of the Progression of Gastroesophageal Reflux Disease study.* J Gastroenterol Hepatol, 2007. **22**(11): p. 1728-31.
35. Hirosumi J, T.G., Chang L, Gorgun CZ, Uysal KT, Maeda K, Karin M, Hotamisligil GS, *A central role for JNK in obesity and insulin resistance.* Nature, 2002. **420**: p. 333-336.

36.   Solinas, G., et al., *JNK1 in hematopoietically derived cells contributes to diet-induced inflammation and insulin resistance without affecting obesity.* Cell Metab, 2007. **6**(5): p. 386-97.

37.   Hotamisligil, G.S., Shargil NS, Spiegelman BM, *Adipose expression of tumor necrosis factor-alpha: direct role in obesity-linked insulin resistance.* Science, 1993. **259**: p. 87-91.

38.   Fried SK, B.D., Greenberg AS, *Omental and subcutaneous adipose tissues of obese subjects release interleukin-6: depot difference and regulation by glucocorticoid.* Journal of Clinical Endocrinology and Metabolism, 1998. **83**(3): p. 847-850.

39.   Stezler I, Z.S., Raggam R, Prueller F, Trusching-Wilders M, Meinitzer A, Schnedl WI, Horejsi R, Moeller R, Weghuber D, Reeves G, Postolache TT, Mangge H, *Link between leptin and interleukin-6 levels in the intial phase of obesity related inflammation.* Journal of Laboratory and Clinical Medicine, 2011. **159**(2): p. 118-124.

40.   van Hall, G., et al., *Interleukin-6 stimulates lipolysis and fat oxidation in humans.* J Clin Endocrinol Metab, 2003. **88**(7): p. 3005-10.

41.   Wieser V, M.A., Tilg H, *Inflammation, Cytokines and Insulin Resistance: A Clinical Perspective.* Archivum Immunologiae et Therapiae Experimentalis, 2013. **61**(2): p. 119-125.

42.   El-Kadre L, T., A, *Interleukin-6 and obesity: the crosstalk between intestine, pancreas and liver.* Current Opinion in Clinical Nutrition & Metabolic Care, 2013. **16**(5): p. 564-568.

43.   Shen, W., H.R. Gaskins, and M.K. McIntosh, *Influence of dietary fat on intestinal microbes, inflammation, barrier function and metabolic outcomes.* J Nutr Biochem, 2014. **25**(3): p. 270-80.

44.   Jang, B.G., B.L. Lee, and W.H. Kim, *Intestinal Stem Cell Markers in the Intestinal Metaplasia of Stomach and Barrett's Esophagus.* PLoS One, 2015. **10**(5): p. e0127300.

45.   Huang, C.-J., Zourdos, M.C., Jo, E., Ormsbee, M.J., *Influence of Physical Activity and Nutrition on Obesity-Related Immune Function.* The Scientific World Journal, 2013. **2013**: p. 12.

46.   Wensveen, F.M., Valentić, S., Šestan, M., Wensveen, T.T., Polić, B., *The "Big Bang" in obese fat: events initiating obesity-induced adipose tissue inflammation.* Eur J Immunol., 2015.

47.   Santos, S., A. Oliveira, and C. Lopes, *Systematic review of saturated fatty acids on inflammation and circulating levels of adipokines.* Nutr Res, 2013. **33**(9): p. 687-95.

48.   Fontana, L., *Calorie restriction and cardiometabolic health.* Eur J Cardiovasc Prev Rehabil., 2008. **15**(1): p. 3-9.

49.   Pandolfino, J.E., et al., *Obesity: a challenge to esophagogastric junction integrity.* Gastroenterology, 2006. **130**(3): p. 639-49.

50.   Dvorak, K., et al., *Bile acids in combination with low pH induce oxidative stress and oxidative DNA damage: relevance to the pathogenesis of Barrett's oesophagus.* Gut, 2007. **56**(6): p. 763-71.

51.   Huo, X., et al., *Deoxycholic acid causes DNA damage while inducing apoptotic resistance through NF-kB activation in benign Barrett's epithelial cells.* Am J Physiol Gastrointest Liver Physiol, 2011. **301**(2): p. G278-G286.

52. Santos, S., Oliveira, A., Lopes, C., *Sytematic review of saturated fatty acids on inflammation and circulating levels of adipokines.* Nutr Res, 2013. **33**: p. 687-695.

53. Wong, S.W., et al., *Fatty acids modulate Toll-like receptor 4 activation through regulation of receptor dimerization and recruitment into lipid rafts in a reactive oxygen species-dependent manner.* J Biol Chem, 2009. **284**(40): p. 27384-92.

54. Mu, L., K.J. Mukamal, and A.Z. Naqvi, *Erythrocyte saturated fatty acids and systemic inflammation in adults.* Nutrition, 2014. **30**(11-12): p. 1404-8.

55. Jager, J., et al., *Interleukin-1beta-induced insulin resistance in adipocytes through down-regulation of insulin receptor substrate-1 expression.* Endocrinology, 2007. **148**(1): p. 241-51.

56. De Pergola, G. and F. Silvestris, *Obesity as a major risk factor for cancer.* J Obes, 2013. **2013**: p. 291546.

57. Vucenik, I. and J.P. Stains, *Obesity and cancer risk: evidence, mechanisms, and recommendations.* Obesity and cancer, 2012. **1271**(1): p. 37-43.

58. Calle, E.E. and M.J. Thun, *Obesity and cancer.* 2004. **23**(38): p. 6365-6378.

59. Maccio, A. and C. Madeddu, *Obesity, inflammation, and postmenopausal breast cancer: therapeutic implications.* ScientificWorldJournal, 2011. **11**: p. 2020-36.

60. Sjostrom, L., Narbro,K., Sjostrom, D., Karason, K., Larsson, B., Wede, H., Lystig., Sullivan, M., Bouchard, C., Carlsson, B., Bengtsson, C., Dahlgren, S., Gummesson, A., Jacobson, P., Karlsson, J., Lindross, AK., Lonroth, H., Naslund, I., Olbers, T., Stenlof, K., Torgerson, J., Agren, G., Carlsson, L., *Effects of Bariatric Surgery on Motality in Swedish Obese Subjects.* N Engl J Med, 2007. **357**: p. 741-752.

61. Sjostrom, L., *Review of the key results from the Swedish Obese Subjects (SOS) trial - a prospective controlled intervention study of bariatric surgery.* J Intern Med, 2013. **273**(3): p. 219-34.

62. Aleman, J.O., et al., *Mechanisms of obesity-induced gastrointestinal neoplasia.* Gastroenterology, 2014. **146**(2): p. 357-73.

63. Mantovani, A., et al., *Cancer-related inflammation.* 2008. **454**(7203): p. 436-444.

64. Park, J. and P.E. Scherer, *Leptin and cancer: from cancer stem cells to metastasis.* 2011. **18**(4): p. C25-C29.

65. Braun, S., K. Bitton-Worms, and D. LeRoith, *The link between the metabolic syndrome and cancer.* 2011. **7**(7): p. 1003-1015.

66. Berger, N.A., *Obesity and cancer pathogenesis.* Ann N Y Acad Sci, 2014. **1311**: p. 57-76.

67. Lashinger LM, F.N., Hursting SD, *Interacting Inflammatory and Growth Factor Signals Underlie the Obesity-Cancer Link.* The Journal of Nutrition, 2013. **144**: p. 109-113.

68. Faulds, M.H. and K. Dahlman-Wright, *Metabolic diseases and cancer risk.* 2012. **24**(1): p. 58-61.

69. Allavena, P., et al., *Chemokines in cancer related inflammation.* 2011. **317**(5): p. 664-673.

70. Abreu, M.T. and R.M. Peek, Jr., *Gastrointestinal Malignancy and the Microbiome.* Gastroenterology (146): p. 1534-1546.

71. Zhu, Y., et al., *Gut microbiota and probiotics in colon tumorigenesis.* 2011. **309**(2): p. 119-127.
72. Clemente, J.C., et al., *The Impact of the Gut Microbiota on Human Health: An Integrative View.* 2012. **148**(6): p. 1258-1270.
73. Quante, M., J.A. Abrams, and T.C. Wang, *The rapid rise in gastroesophageal junction tumors: is inflammation of the gastric cardia the underwater iceberg?* Gastroenterology, 2013. **145**(4): p. 708-11.
74. Braden, K. and D. Urma, *Esophagus - anatomy and development.* GI Motility online, 2006.
75. Madanick R., O.R., *Anatomy Histology, Embryology, and Developmental Anomalies of the Esophagus*, in *Gastrointestinal and Liver Disease*. 2016, Elsevier Saunders.
76. Mashimo, H. and R.K. Goyal, *Physiology of esophageal motility.* GI Motility online, 2006.
77. Pandolfino, J., Kahrila PJ., *Esophageal Neuromuscular Function and Motility Disorders*, in *Gastrointestinal and Liver Disease*. 2016, Elsevier Saunders.
78. Miller, L., et al., *The esophagogastric junction.* Ann N Y Acad Sci, 2011(1232): p. 323-330.
79. El-Serag, H.B., et al., *Update on the epidemiology of gastro-oesophageal reflux disease: a systematic review.* Gut, 2014. **63**(6): p. 871-80.
80. DeValt, K. and D. O Castell, *Updated Guidlines for the Diagnosis and Treatment of Gastroesophageal Reflux Disease* Am J Gastroenterol 2005(100): p. 190-200.
81. Badillo, R. and D. Francis, *Diagnosis and treatment of gastroesophageal reflux disease.* World J Gastrointest Pharmacol Ther, 2014. **5**(3): p. 105-12.
82. Barak, N., et al., *Gastro-oesophageal reflux disease in obesity-pathophysiological and therapeutic considerations.* Obesity Reviews, 2002(3): p. 9-15.
83. Hajar, N., et al., *Impedance pH confirms the relationship between GERD and BMI.* Dig Dis Sci, 2012. **57**(7): p. 1875-9.
84. Abdallah, J., et al., *The relationship between length of Barrett's oesophagus mucosa and body mass index.* Aliment Pharmacol Ther, 2015. **41**(1): p. 137-44.
85. di Pietro, M., D. Alzoubaidi, and R.C. Fitzgerald, *Barrett's esophagus and cancer risk: how research advances can impact clinical practice.* Gut Liver, 2014. **8**(4): p. 356-70.
86. Richter, J., Friedenberg, FK., *Gastroesophageal Reflux Disease*, in *Gastrointestinal and Liver Disease*. 2016, Elsevier Saunders.
87. Spechler, S.J., et al., *History, molecular mechanisms, and endoscopic treatment of Barrett's esophagus.* Gastroenterology, 2010. **138**(3): p. 854-69.
88. R, B.N., *Chronic peptic ulcer of the oesophagus and "oesophagitis".* Br J Surg, 1950. **38**: p. 175-182.
89. Quante, M., et al., *Bile Acid and Inflammation Activate Gastric Cardia Stem Cells in a Mouse Model of Barrett-Like Metaplasia.* Cancer Cell, 2012. **21**(1): p. 36-51.
90. Spechler, S.J., *Barrett esophagus and risk of esophageal cancer: a clinical review.* JAMA, 2013. **310**(6): p. 627-36.

91. Quante, M. and T.C. Wang, *Stem cells in gastroenterology and hepatology.* Nat Rev Gastroenterol Hepatol, 2009. **6**(12): p. 724-37.
92. Rustgi, A.K. and H.B. El-Serag, *Esophageal carcinoma.* N Engl J Med, 2014. **371**(26): p. 2499-509.
93. Wild, C.P. and L.J. Hardie, *Reflux, Barrett's oesophagus and adenocarcinoma: burning questions.* Nat Rev Cancer, 2003. **3**(9): p. 676-84.
94. Bresalier, R.S., *Barrett's Esophagus and Esophageal Adenocarcinoma.* 2009. **60**(1): p. 221-231.
95. Spechler, S.J. and R.F. Souza, *Barrett's esophagus.* N Engl J Med, 2014. **371**(9): p. 836-45.
96. El-Serag HB, G.M., Shub MD, Richarson P, Bancroft J, *The prevalence of suspected Barrett's esophagus in children and adolescents: a multicenter endoscopic study.* Gastrointestinal Endoscopy, 2006. **64**(5): p. 671-675.
97. Wang, A., et al., *Prevalence of complicated gastroesophageal reflux disease and Barrett's esophagus among racial groups in a multi-center consortium.* Dig Dis Sci, 2009. **54**(5): p. 964-71.
98. Winberg, H., et al., *Risk factors and chemoprevention in Barrett's esophagus--an update.* Scand J Gastroenterol, 2012. **47**(4): p. 397-406.
99. Akiyama, T., et al., *Visceral Obesity and the Risk of Barrett's Esophagus.* 2011. **83**(3): p. 142-145.
100. Orloff, M., et al., *Germline mutations in MSR1, ASCC1, and CTHRC1 in patients with Barrett esophagus and esophageal adenocarcinoma.* JAMA, 2011. **306**(4): p. 410-9.
101. Corley, D.A., et al., *Abdominal obesity and body mass index as risk factors for Barrett's esophagus.* Gastroenterology, 2007. **133**(1): p. 34-41; quiz 311.
102. Kamat, P., et al., *Exploring the association between elevated body mass index and Barrett's esophagus: a systematic review and meta-analysis.* Ann Thorac Surg, 2009. **87**(2): p. 655-62.
103. Edelstein, Z.R., et al., *Central adiposity and risk of Barrett's esophagus.* Gastroenterology, 2007. **133**(2): p. 403-11.
104. Aaron P. Thrift, N.J.S., Marilie D. Gammon, Leslie Bernstein, Brian J. Reid, Lynn Onstad, Harvey A. Risch, Geoffrey Liu, Nigel C. Bird, Anna H. Wu, Douglas A. Corley, Yvonne Romero, Stephen J. Chanock, Wong-Ho Chow, Alan G. Casson, David M. Levine, Rui Zhang, Weronica E. Ek, Stuart MacGregor, Weimin Ye, Laura J. Hardie, Thomas L. Vaughan, David C. Whiteman, *Obesity and Risk of Esophageal Adenocarcinoma and Barrett's Esophagus: A Mendelian Randomization Study.* JNCI, 2013. **106**(11).
105. Seidel, D., et al., *The association between body mass index and Barrett's esophagus: a systematic review.* Dis Esophagus, 2009. **22**(7): p. 564-70.
106. Bird-Lieberman EL, F.R., *Early diagnosis of oesophageal cancer.* Br J Cancer, 2009(101): p. 1-6.
107. Kubo, A., Corley, DA., *Body mass index and adenocarcinomas of the esophagus or gastric cardia: a systematic review and meta-analysis.* Cancer Epidemiol Biomarkers Prev, 2006(15): p. 872-878.
108. Everhart, J.E. and C.E. Ruhl, *Burden of Digestive Diseases in the United States Part I: Overall and Upper Gastrointestinal Diseases.* 2009. **136**(2): p. 376-386.

109. Quante, M., et al., *Barrett esophagus: What a mouse model can teach us about human disease.* Cell Cycle, 2012. **11**(23): p. -.

110. Rubenstein, J.H. and N.J. Shaheen, *Epidemiology, Diagnosis, and Management of Esophageal Adenocarcinoma.* Gastroenterology, 2015. **149**(2): p. 302-317 e1.

111. Eusebi, L.H., L. Fuccio, and F. Bazzoli, *The Role of Obesity in Gastroesophageal Reflux Disease and Barrett′s Esophagus.* 2012. **30**(2): p. 154-157.

112. Thrift, A.P., et al., *A Clinical Risk Prediction Model for Barrett Esophagus.* 2012. **5**(9): p. 1115-1123.

113. Reid, B.J., et al., *Barrett's oesophagus and oesophageal adenocarcinoma: time for a new synthesis.* 2010: p. 1-15.

114. Kavanagh, M.E., et al., *The esophagitis to adenocarcinoma sequence; the role of inflammation.* Cancer Lett, 2014. **345**(2): p. 182-9.

115. Lagergren, J., F. Mattsson, and O. Nyren, *Gastroesophageal reflux does not alter effects of body mass index on risk of esophageal adenocarcinoma.* Clin Gastroenterol Hepatol, 2014. **12**(1): p. 45-51.

116. Splechler SJ., S.R., *Barrett's Esophagus*, in *Gastrointestinal and Liver Disease*. 2016, Elsevier Saunders.

117. Spechler, S.J., et al., *American Gastroenterological Association Technical Review on the Management of Barrett's Esophagus.* Gastroenterology, 2011. **140**(3).

118. Falk GW, J.B., Riddell RH, Rubenstein JH, El-Zimaity H, Drewes AM, Roark KS, Sontag SJ, Schnell TG, Leya J, Chejfec G, Richter JE, Jenkins G, Goldman A, Dvorak K, Nardone G, *Barrett's esophagus: prevalence-incidence and etiology-origins.* Ann N Y Acad Sci, 2011. **1232**: p. 1-17.

119. Napier, K.J., M. Scheerer, and S. Misra, *Esophageal cancer: A Review of epidemiology, pathogenesis, staging workup and treatment modalities.* World J Gastrointest Oncol, 2014. **6**(5): p. 112-20.

120. Leodolter A, N.M., Vieth M, Lind T, Jaspersen D, Ritcher K, Willich S, Stolte M, Malfertheiner P, Labenz J, *Progresion of specialized intestinal metaplasia at the cardia to macroscopically evident Barrett's esophagus: an entity of concern in the ProGERD study.* Scand J Gastroenterol, 2012. **47**(12): p. 1429-1435.

121. Gales, D., et al., *The Chemokine CXCL8 in Carcinogenesis and Drug Response.* ISRN Oncol, 2013. **2013**: p. 859154.

122. Hanahan, D. and R.A. Weinberg, *Hallmarks of cancer: the next generation.* Cell, 2011. **144**(5): p. 646-74.

123. Colotta, F., et al., *Cancer-related inflammation, the seventh hallmark of cancer: links to genetic instability.* Carcinogenesis, 2009. **30**(7): p. 1073-81.

124. Hardikar, S., et al., *Inflammation and oxidative stress markers and esophageal adenocarcinoma incidence in a Barrett's esophagus cohort.* Cancer Epidemiol Biomarkers Prev, 2014.

125. Quante, M., et al., *The Gastrointestinal Tumor Microenvironment.* Gastroenterology, 2013. **145**(1): p. 63-78.

126. Borish, L.C. and J.W. Steinke, *2. Cytokines and chemokines.* Journal of Allergy and Clinical Immunology, 2003. **111**(2): p. S460-S475.

127. Grivennikov, S.I., F.R. Greten, and M. Karin, *Immunity, inflammation, and cancer.* Cell, 2010. **140**(6): p. 883-99.
128. Martynowicz, H., Janus, A., Nowacki, D., Mazur, G., *The Role of Chemokines in Hypertension.* Adv Clin Exp Med, 2014. **23**(3): p. 319-325.
129. Lin, W.W. and M. Karin, *A cytokine-mediated link between innate immunity, inflammation, and cancer.* J Clin Invest, 2007. **117**(5): p. 1175-83.
130. Dinarello, C., *Biology of interleukin 1.* FASEB J., 1988. **2**(2): p. 108-115.
131. Idris, A., Ghazali, NB., Koh, D., *Interleukin-1B- A potential Salivary Biomarker for Cancer Progression?* Biomark Cancer, 2015. **7**: p. 25-29.
132. Schlüter, C., et al., *The Cell Proliferation-associated Antigen of Antibody Ki-67: A Very Large, Ubiquitos Nuclear Protein wtih Numerous Repeated Elements, Representing a New Kind of Cell Cycle- maintaing Proteins.* The Journal of Cell Biology, 1993. **123**(3): p. 513-522.
133. Waugh, D.J., Wilson, C., *The Interleukin-8 Pathway in Cancer.* Clin Cancer Res, 2008. **14**(21): p. 6735-6741.
134. Hwang, Y.S., et al., *Interleukin-1beta stimulates IL-8 expression through MAP kinase and ROS signaling in human gastric carcinoma cells.* Oncogene, 2004. **23**(39): p. 6603-11.
135. Asfaha, S., et al., *Mice that express human interleukin-8 have increased mobilization of immature myeloid cells, which exacerbates inflammation and accelerates colon carcinogenesis.* Gastroenterology, 2013. **144**(1): p. 155-66.
136. Li, A., et al., *IL-8 Directly Enhanced Endothelial Cell Survival, Proliferation, and Matrix Metalloproteinases Production and Regulated Angiogenesis.* The Journal of Immunology, 2003. **170**(6): p. 3369-3376.
137. Fang, Y., et al., *Cellular origins and molecular mechanisms of Barrett's esophagus and esophageal adenocarcinoma.* Ann N Y Acad Sci, 2013. **1300**: p. 187-99.
138. Björkdahl, O., Åkerbald, P., Gjörloff-Wingren, A., Leanderson, T., Dohlsten, M., *Lymphoid hyperplasia in transgenic mice over-expressing a secreted form of the human interleukin-1B gene product.* Immunonology, 1999. **96**: p. 128-137.
139. Tu, S., et al., *Overexpression of Interleukin-1β Induces Gastric Inflammation and Cancer and Mobilizes Myeloid-Derived Suppressor Cells in Mice.* 2008. **14**(5): p. 408-419.
140. Nakagawa, H., Wang, T.C., Zukerberg, L., Odze, R., Togawa, K., May, GHW., Wilson, J., Rustigi, AK., *The targeting of the cyclin D1 oncogene by an Epstein-Barr virus promoter in transgenic mice causes dysplasia in the tongue, esophagus and forestomach.* Oncogene, 1997. **14**(10): p. 1185-1190.
141. Kong, J., et al., *Immature myeloid progenitors promote disease progression in a mouse model of Barrett's-like metaplasia.* Oncotarget, 2015. **6**(32): p. 32980-33005.
142. Bolze, F., et al., *Characterization of the melanocortin-4-receptor nonsense mutation W16X in vitro and in vivo.* Pharmacogenomics, 2013. **13**(1): p. 80-93.
143. Rozman, J., M. Klingenspor, and M. Hrabe de Angelis, *A review of standardized metabolic phenotyping of animal models.* Mamm Genome, 2014. **25**(9-10): p. 497-507.

144. Singh, S., et al., *Central adiposity is associated with increased risk of esophageal inflammation, metaplasia, and adenocarcinoma: a systematic review and meta-analysis.* Clin Gastroenterol Hepatol, 2013. **11**(11): p. 1399-1412 e7.

145. El-Serag, H.B., et al., *Visceral abdominal obesity measured by CT scan is associated with an increased risk of Barrett's oesophagus: a case-control study.* Gut, 2014. **63**(2): p. 220-9.

146. Fox, J.G., Beck, P., Dangler, C.A., Whary, M.T., Wang, T.C., Shi, H.N., Nagler-Anderson, C., *Concurrent enteric helminth infectionmodulates inflammation and gastric immune responses and reduces helicobacter-induced gastric atrophy.* Nature Medicine, 2000. **6**: p. 536-542.

147. Flejou, J.F., *Barrett's oesophagus: from metaplasia to dysplasia and cancer.* Gut, 2005. **54 Suppl 1**: p. i6-12.

148. Scholzen, T. and J. Gerdes, *The Ki-67 protein: From the know to the unknown.* Journal of Cellular Physiology, 2000. **182**(3): p. 311-322.

149. Whiteside, T.L., *The tumor microenvironment and its role in promoting tumor growth.* Oncogene, 2008. **27**(45): p. 5904-12.

150. Carmi, Y., et al., *The role of IL-1beta in the early tumor cell-induced angiogenic response.* J Immunol, 2013. **190**(7): p. 3500-9.

151. Tu, S., et al., *Overexpression of interleukin-1beta induces gastric inflammation and cancer and mobilizes myeloid-derived suppressor cells in mice.* Cancer Cell, 2008. **14**(5): p. 408-19.

152. Nakayama, H., et al., *aSmooth muscle actin positive stromal cells in gastric carcinoma.* j Clin Pathol, 2002. **55**: p. 741-744.

153. Hamilton, S.R. and J.H. Yardley, *Regenerative of cardiac type mucosa and acquisition of Barrett mucosa after esophagogastrostomy.* Gastroenterology, 1977. **72**(4 Pt 1): p. 669-675.

154. Cho, H.J., et al., *A high-fat diet containing lard accelerates prostate cancer progression and reduces survival rate in mice: possible contribution of adipose tissue-derived cytokines.* Nutrients, 2015. **7**(4): p. 2539-61.

155. Cowen, S., et al., *High-Fat, High-Calorie Diet Enhances Mammary Carcinogenesis and Local Inflammation in MMTV-PyMT Mouse Model of Breast Cancer.* Cancers (Basel), 2015. **7**(3): p. 1125-42.

156. Eliashar, R., et al., *DCLK1 expression in gastrointestinal stem cells and neoplasia.* journal of Cancer Therapeutics and Research, 2012. **1**(1): p. 12.

157. Hoyo, C., et al., *Body mass index in relation to oesophageal and oesophagogastric junction adenocarcinomas: a pooled analysis from the International BEACON Consortium.* Int J Epidemiol, 2012. **41**(6): p. 1706-18.

158. Sato, T., et al., *Single Lgr5 stem cells build crypt–villus structures in vitro without a mesenchymal niche.* Nature, 2009. **459**: p. 262-265.

159. Coffelt, S.B., M.D. Wellenstein, and K.E. de Visser, *Neutrophils in cancer: neutral no more.* Nat Rev Cancer, 2016.

160. Fitzgerald, R.C., et al., *Inflammatory gradiet in Barrett's oesophagus: implications for disease complications.* Gut, 2002. **51**(316-322).

161. Acharyya, S., et al., *A CXCL1 paracrine network links cancer chemoresistance and metastasis.* Cell, 2012. **150**(1): p. 165-78.

162. Duggan, C., et al., *Association between markers of obesity and progression from Barrett's esophagus to esophageal adenocarcinoma.* Clin Gastroenterol Hepatol, 2013. **11**(8): p. 934-43.

163. R., M., et al., *Visceral adipose tissue: the link with esophageal adenocarcinoma.* Scand J Gastroenterol, 2014. **49**(4).

164. Kubo, A. and D.A. Corley, *Body mass index and adenocarcinomas of the esophagus or gastric cardia: a systematic review and meta-analysis.* Cancer Epidemiol Biomarkers Prev, 2006. **15**(5): p. 872-8.

165. Wu, J.C., et al., *Obesity is associated with increased transient lower esophageal sphincter relaxation.* Gastroenterology, 2007. **132**(3): p. 883-9.

166. Mullin, J.M., et al., *Transepithelial Leak in Barrett's Esophagus.* Digestive Diseases and Sciences, 2006. **51**(12): p. 2326-2336.

167. Orlando, R.C., *Mechanisms of epithelial injury and inflammation in gastrointestinal diseases.* Rev Gastroenterol Disord., 2002. **2**(Suppl 2): p. S2-8.

168. Beales, I.L.P. and O.O. Ogunwobi, *Leptin synergistically enhances the anti-apoptotic and growth-promoting effects of acid in OE33 oesophageal adenocarcinoma cells in culture.* 2007. **274**(1-2): p. 60-68.

169. Quante, M., J.A. Abrams, and T.C. Wang, *The Rapid Rise in Gastroesphageal Junction Tumors: Is Inflammation of the Gastric Cardia the Underwater Iceberg?* Gastroenterology, 2013. **145**: p. 708-722.

170. Hayakawa, Y., et al., *Mist1 Expressing Gastric Stem Cells Maintain the Normal and Neoplastic Gastric Epithelium and Are Supported by a Perivascular Stem Cell Niche.* Cancer Cell, 2015. **28**(6): p. 800-14.

171. M., O., et al., *Immunosuppression in patients with Barrett's esophagus.* Surgery, 1992. **112**(1).

172. Lagergren, J., R. Bergström, and O. Nyrén, *Association between Body Mass and Adenocarcinoma of the Esophagus and Gastric Cardia.* Ann Intern Med, 1999. **130**(11): p. 883-890.

173. Garcia, J.M., et al., *Circulating inflammatory cytokines and adipokines are associated with increased risk of Barrett's esophagus: a case-control study.* Clin Gastroenterol Hepatol, 2014. **12**(2): p. 229-238 e3.

174. Teng, K.-T., et al., *Modulation of obesity-induced inflammation by dietary fats: mechanisms and clinical evidence.* Nutrition Journal, 2014. **13**(12).

175. van Dijk, S.J., et al., *A saturated fatty acid-rich diet induces an obesity-linked proinflammatory gene expression profile in adipose tissue of subjects at risk of metabolic syndrome.* Am J Clin Nutr, 2009. **90**(6): p. 1656-64.

176. Di Sebastiano, K.M. and M. Mourtzakis, *The role of dietary fat throughout the prostate cancer trajectory.* Nutrients, 2014. **6**(12): p. 6095-109.

177. Anandavadivelan, P. and P. Lagergren, *Cachexia in patients with oesophageal cancer.* Nature Reviews Clinical Oncology, 2016. **13**: p. 185-198.

178. Pacharinsak, C. and A. Beitz, *Animal Models of Cancer Pain.* Comparative Medicine, 2008. **58**(3): p. 220-233.

179. Lee, B.H., et al., *Behavioral Characteristics of a Mouse Model of Cancer Pain.* Yonsei Med J, 2005. **46**(2): p. 252-259.

180. Medhurst, S.J., et al., *A rat model of bone cancer pain.* PAIN, 2002. **96**(1-2): p. 129-140.

181. Schwei, M., et al., *Neurochemical and Cellular Reorganization of the Spinal Cord ina Murine Model of Bone Cancer Pain.* The Journal of Neuroscience, 1999. **19**(24): p. 10886-10897.

182. Marin-Valencia, I., et al., *Analysis of tumor metabolism reveals mitochondrial glucose oxidation in genetically diverse human glioblastomas in the mouse brain in vivo.* Cell Metab, 2012. **15**(6): p. 827-37.

183. Zhang, J., et al., *Esophageal cancer metabolite biomarkers detected by LC-MS and NMR methods.* PLoS One, 2012. **7**(1): p. e30181.

184. Lynam-Lennon, N., et al., *Excess visceral adiposity induces alterations in mitochondrial function and energy metabolism in esophageal adenocarcinoma.* BMC Cancer, 2014. **14**.

185. Fowler, A.J., et al., *A high-fat diet is associated with altered adipokine production and a more aggressive esophageal adenocarcinoma phenotype in vivo.* J Thorac Cardiovasc Surg, 2015. **149**(4): p. 1185-91.

186. Kohata, Y., et al., *Role of Th-2 cytokines in the development of Barrett's esophagus in rats.* J Gastroenterol, 2011. **46**(7): p. 883-93.

187. C, Y.L., *The Effect of High-Fat Diet-Induced Pathophysiological Changes in the Gut on Obesity: What Should be the Ideal Treatment?* Clin Transl Gastroenterol, 2013. **4**: p. e39.

188. Rieder, F., et al., *Inflammatory mediators in gastroesophageal reflux disease: impact on esophageal motility, fibrosis, and carcinogenesis.* American Physiological Society, 2010. **298**(5): p. G571-G581.

189. Lao-Sirieix, P. and R.C. Fitzgerald, *Role of the micro-environment in Barrett's carcinogenesis.* Biochem Soc Trans, 2010. **38**(2): p. 327-30.

190. Lin, E.W., et al., *The tumor microenvironment in esophageal cancer.* Oncogene, 2016.

191. Westphalen, C.B., M. Quante, and T.C. Wang, *Functional implication of Dclk1 and Dclk1 expressing cells in cancer.* Small GTPases, 2016.

192. Mountjoy, K.G., et al., *Localization of the melanocortin-4 receptor (MC4-R) in neuroendocrine and autonomic control circuits in the brain.* Mol Endocrinol, 1994. **8**(10): p. 1298-1308.

193. Lichtenstein, L., et al., *Angptl4 protects against severe proinflammatory effects of saturated fat by inhibiting fatty acid uptake into mesenteric lymph node macrophages.* Cell Metab, 2010. **12**(6): p. 580-92.

194. Wallace, F.A., et al., *Dietary fats affect macrophage-mediated cytotoxicity towards tumor cells.* Immunol. Cell Biol., 2000. **78**: p. 40-48.

195. Wallace, F.A., et al., *Dietary fatty acids influence the production of Th1- but not Th2-type cytokines.* J. Leuk. Biol., 2001. **69**: p. 449-457.

196. Kew, s., et al., *The effect of eicosapentaenoic acid on rat lymphocyte proliferation depends upon its position in dietary triaclyglycerols.* J. Nutr., 2003. **133**: p. 4230-4238.

197. Healy, D.A., et al., *Effect of low-to-moderate amounts of dietary fish oil on neutrophil lipid composition and function.* Lipids, 2000. **35**(7): p. 763-768.

198. Mantzioris, E., et al., *Dietary substitution with an alpha-linolenic acid-rich vegetable oil increases eicosapentaenoic acid concentrations in tissues.* Am J Clin Nutr, 1994. **59**(6): p. 1304-1309.

199. Caughey, G.E., et al., *The effect on human tumor necrosis factor alpha and interleukin 1 beta production of diets enriched in n-3 fatty acids from vegetable oil or fish oil. .* Am J Clin Nutr, 1996. **63**(1): p. 116-122.

200. Thies, F., et al., *Dietary supplementation with g-linolenic acid or fish oil decreases T lymphocyte proliferation in healthy older humans.* J. Nutr., 2001. **131**(7): p. 1918-1927.

201. Calder, P.C., *The relationship between the fatty acid composition of immune cells and their function.* Prostaglandins Leukot Essent Fatty Acids, 2008. **79**(3-5): p. 101-8.

202. Underwood, T.J., et al., *Cancer-associated fibroblasts predict poor outcome and promote periostin-dependent invasion in oesophageal adenocarcinoma.* J Pathol, 2015. **235**(3): p. 466-77.

203. Hu, M. and K. Polyak, *Microenvironmental regulation of cancer development.* Curr Opin Genet Dev., 2008. **18**(1): p. 27-34.

204. Shimoda, M., K.T. Mellody, and A. Orimo, *Carcinoma-associated fibroblasts are a rate-limiting determinant for tumour progression.*

. Semin Cell Dev Biol., 2010. **21**(1): p. 19-25.

205. Massarelli, G., et al., *Myofibroblasts in the epithelial-stromal junction of basal cell carcinoma.* Appl Pathol., 1983. **1**(1): p. 25-30.

206. Ohtani, H. and N. Sasano, *Stromal cell changes in human colorectal adenomas and carcinomas. An ultrastructural study of fibroblasts, myofibroblasts, and smooth muscle cells.* Virchows Arch A Pathol Anat Histopathol., 1983. **401**(2): p. 209-222.

207. Bucala, R., et al., *Constitutive Production of Inflammatory and Mitogenic Cytokines by Rheumatoid Synovial Fibroblasts.* J. Exp. Med, 1991. **173**: p. 569-574.

208. Xing, F., J. Saidou, and K. Watade, *Cancer associated fibroblasts (CAFs) in tumor microenvironment.* Front Biosci., 2011. **15**: p. 166-179.

209. Swann, J.B. and M.J. Smyth, *Immune surveillance of tumors.* J Clin Invest, 2007. **117**(5): p. 1137-46.

210. Fitzgerald, R.C., et al., *Diversity in the oesophageal phenotypic response to gastro-oesophageal reflux: immunological determinants.* Gut, 2002. **50**: p. 451-459.

211. Derks, S., et al., *Epithelial PD-L2 Expression Marks Barrett's Esophagus and Esophageal Adenocarcinoma.* Cancer Immunol Res, 2015. **3**(10): p. 1123-9.

212. Adler, B.J., et al., *High fat diet rapidly suppresses B lymphopoiesis by disrupting the supportive capacity of the bone marrow niche.* PLoS One, 2014. **9**(3): p. e90639.

213. Ericksen, R.E., et al., *Obesity accelerates Helicobacter felis-induced gastric carcinogenesis by enhancing immature myeloid cell trafficking and TH17 response.* Gut, 2014. **63**(3): p. 385-94.

214. Casbon, A.-J., et al., *Invasive breast cancer reprograms early myeloid differentiation in the bone marrow to generate immunosuppressive neutrophils.* Proc Natl Acad Sci U S A, 2015. **112**(6): p. E566-575.

215. Kessenbrock, K., V. Plaks, and Z. Werb, *Matrix metalloproteinases: regulators of the tumor microenvironment.* Cell, 2010. **141**(1): p. 52-67.

216. Burkholder, B., et al., *Tumor-induced perturbations of cytokines and immune cell networks.* Biochim Biophys Acta, 2014. **1845**(2): p. 182-201.

217. Polakis, P., *Wnt signaling in cancer.* Cold Spring Harb Perspect Biol, 2012. **4**(5).

218. Zhang, S., et al., *Functions of the Wnt/β-catenin pathway in esophageal cancer.* Int J Exp Med, 2016. **9**(2): p. 4348-4355.

219. Parks, W.C., C.L. Wilson, and Y.S. López-Boado, *Matrix metalloproteinases as modulators of inflammation and innate immunity.* Nature Reviews Immunology, 2004. **4**: p. 617-629.

220. Brinckerhoff, C.E. and L.M. Martisian, *Matrix metalloproteinases: a tail of a grof that became a prince.* Nat Rev Mol Cell Biol., 2002. **3**(3): p. 207-214.

221. Hanahan, D. and R.A. Weinberg, *The Hallmarks of Cancer.* Cell. **100**(1): p. 57-70.

222. McCawley, L.J., et al., *Keratinocyte expression of MMP3 enhances differentiation and prevents tumor establishment.* Am J Pathol, 2008. **173**(5): p. 1528-39.

223. Egeblad, M. and Z. Werb, *New functions for the matrix metalloproteinases in cancer progression.* Nature Reviews Cancer, 2002. **2**: p. 161-174.

224. Swee, M., et al., *Matrix metalloproteinase-7 (matrilysin) controls neutrophil egress by generating chemokine gradients.* J Leukoc Biol, 2008. **83**(6): p. 1404-12.

225. Löffek, S., O. Schilling, and C.-W. Franzke, *Biological role of matrix metalloproteinases: a critical balance.* European Respiratory Journal, 2011. **38**(1): p. 191-208.

226. McMahan, R.S., et al., *Stromelysin-2 (MMP10) Moderates Inflammation by Controlling Macrophage Activation.* The Journal of Immunology, 2016.

227. Zhang, G., et al., *Matrix metalloproteinase-10 promotes tumor progression through regulation of angiogenic and apoptotic pathways in cervical tumors.* BMC Cancer, 2014. **14**(310).

228. Dhawan, P. and A. Richmond, *Role of CXCL1 in tumorigenesis of melanoma.* Journal of Leukocyte Biology, 2002. **72**(1): p. 9-18.

229. Shrivastava, M.S., et al., *Targeting chemokine pathways in esophageal adenocarcinoma.* Cell Cycle, 2014. **13**(21): p. 3320-7.

230. Uribe-Querol, E. and C. Rosales, *Neutrophils in Cancer: Two Sides of the Same Coin.* J Immunol Res, 2015. **2015**: p. 983698.

231. Quail, D.F. and J.A. Joyce, *Microenvironmental regulation of tumor progression and metastasis.* Nat Med, 2013. **19**(11): p. 1423-37.

232. Jobe, N.P., et al., *Simultaneous blocking of IL-6 and IL-8 is sufficient to fully inhibit CAF-induced human melanoma cell invasiveness.* Histochem Cell Biol, 2016. **146**(2): p. 205-17.

233. Ray, K., *High-fat diet influences intestinal stem cell biology.* Nature Reviews Gastroenterology & Hepatology, 2016. **13**: p. 250-251.

234. Inagaki, T., et al., *Regulation of antibacterial defense in the small intestine by the nuclear bile acid receptor.* Proc Natl Acad Sci U S A, 2006. **103**(10): p. 3920-5.

235. Guan, B., et al., *Inhibition of farnesoid X receptor controls esophageal cancer cell growth in vitro and in nude mouse xenografts.* Cancer, 2013. **119**(7): p. 1321-9.

236. Makishima, M., et al., *Identification of a Nuclear Receptor for Bile Acids.* Science, 1999. **284**(5418): p. 1362-1365.

237. Capello, A., et al., *Bile acid-stimulated expression of the farnesoid X receptor enhances the immune response in Barrett esophagus.* Am J Gastroenterol, 2008. **103**(6): p. 1510-6.

238. Becker, L., Q. Huang, and H. Mashimo, *Lgr5, an intestinal stem cell marker, is abnormally expressed in Barrett's esophagus and esophageal adenocarcinoma.* Dis Esophagus, 2010. **23**(2): p. 168-74.

239. Lavery, D.L., et al., *The stem cell organisation, and the proliferative and gene expression profile of Barrett's epithelium, replicates pyloric-type gastric glands.* Gut, 2014. **63**(12): p. 1854-63.

240. Ridlon, J.M., D.J. Kang, and P.B. Hylemon, *Bile salt biotransformations by human intestinal bacteria.* J Lipid Res, 2006. **47**(2): p. 241-59.

241. Giannakis, M., et al., *Molecular properties of adult mouse gastric and intestinal epithelial progenitors in their niches.* J Biol Chem, 2006. **281**(16): p. 11292-300.

242. Nakanishi, Y., et al., *Dclk1 distinguishes between tumor and normal stem cells in the intestine.* Nature Genetics, 2013. **45**: p. 93-103.

243. Schwitalla, S., et al., *Intestinal Tumorigenesis Initiated by Dedifferentiation and Acquisition of Stem-Cell-like Properties.* Cell, 2013. **152**(1): p. 25-38.

244. Lyros, O., et al., *Dysregulation of WNT5A/ROR2 Signaling Characterizes the Progression of Barrett-Associated Esophageal Adenocarcinoma.* Mol Cancer Res, 2016. **14**(7): p. 647-59.

245. Sayin, S.I., et al., *Gut microbiota regulates bile acid metabolism by reducing the levels of tauro-beta-muricholic acid, a naturally occurring FXR antagonist.* Cell Metab, 2013. **17**(2): p. 225-35.

246. Swann, J.R., et al., *Systemic gut microbial modulation of bile acid metabolism in host tissue compartments.* Proc Natl Acad Sci U S A, 2011. **108 Suppl 1**: p. 4523-30.

247. Li, F., et al., *Microbiome remodelling leads to inhibition of intestinal farnesoid X receptor signalling and decreased obesity.* Nat Commun, 2013. **4**: p. 2384.

248. Keating, N. and S.J. Keely, *Bile acids in regulation of intestinal physiology.* Current Gastroenterology Reports, 2009. **11**(5): p. 375-382.

249. Ridlon, J.M., et al., *Cirrhosis, bile acids and gut microbiota.* Gut Microbes, 2013. **4**(5): p. 382-387.

250. Parekh, P.J., L.A. Balart, and D.A. Johnson, *The Influence of the Gut Microbiome on Obesity, Metabolic Syndrome and Gastrointestinal Disease.* Clin Transl Gastroenterol, 2015. **6**: p. e91.

251. Kobyliak, N., O. Virchenko, and T. Falalyeyeva, *Pathophysiological role of host microbiota in the development of obesity.* Nutr J, 2016. **15**: p. 43.

252. Kau, A.L., et al., *Human nutrition, the gut microbiome and the immune system.* 2011. **474**(7351): p. 327-336.

253. Thomas, R.M. and C. Jobin, *The Microbiome and Cancer: Is the 'Oncobiome' Mirage Real?* Trends in Cancer, 2015. **1**(1): p. 24-35.

254. Yang, L., et al., *Inflammation and intestinal metaplasia of the distal esophagus are associated with alterations in the microbiome.* Gastroenterology, 2009. **137**(2): p. 588-97.

255. Yang, L., F. Francois, and Z. Pei, *Molecular Pathways: Pathogenesis and Clinical Implications of Microbiome Alteration in Esophagitis and Barrett Esophagus.* 2012. **18**(8): p. 2138-2144.

256. Ley, R.E., et al., *Microbial ecology: Human gut microbes associated with obesity.* Nature, 2006. **444**: p. 1022-1023.

257. Yang, L. and Z. Pei, *Bacteria, inflammation, and colon cancer.* World J Gastroentero, 2006. **12**(42): p. 6741-6746.

258. Davis-Richardson, A.G., et al., *Bacteroides dorei dominates gut microbiome prior to autoimmunity in Finnish children at high risk for type 1 diabetes.* Front Microbiol, 2014. **5**: p. 678.

259. Wu, G.D., et al., *Linking long-term dietary patterns with gut microbial enterotypes.* Science, 2011. **334**(6052): p. 105-8.

260. Keane, M.P., et al., *Depletion of CXCR2 Inhibits Tumor Growth and Angiogenesis in a Murine Model of Lung Cancer.* The Journal of Immunology, 2004. **172**(5): p. 2853-2860.

Abbreviations

ANOVA	Analysis of Variance
AP1	Activator Protein 1
APC	Anaphase-promoting complex
APCs	Antigen Presenting Cells
aSMA	alpha Smooth Muscle Actin
ATMs	Adipose Tissue Macrophages
BA	Bile Acids
BAC	Bacterial Artificial Chromosome
BCA	Bicinchoninic Acid
BE	Barrett Esophagus
BLAST	Basic Local Alignment Search Tool
BM	Bone Marrow
BMI	Body Mass Index
CAFs	Cancer Associated Fibroblasts
CCM	Conditioned Complete Medium
CCR2	Chemokine Receptor type 2
CD11B	Cluster of Differentation 11B, MAC-1alpha
CD3	Cluster of Differentiation 3, T-cell co-receptor
CD45	Cluster of Differentiation 45, Leukocyte common antigen
CD8	Cluster of Differentation 8, T-cell co-receptor
CDC	Center for Disease Control
cDNA	complementary DNA
CM	Complete Medium
CO_2	Carbon Dioxide
CRP	C-reactive Protein
CT	Computed Tomography
CVD	Cardiovascular Disease
CXCL8	Chemokine (C-X-C motif) Ligand-8
Dclk-1	Doublecortin like kinase 1
DEPC	Diethylpyrocarbonate
DES	Distal Esophageal Spasm
dH20	De-ionized water
DIO	Dietary Induced Obesity
DMEM	Dulbecco's Modified Eagle Medium
DNA	Deoxyribonucleic Acid
EAC	Esophageal Adenocarcinoma
EAT	Epididymal Adipose Tissue
ED-L2	Epstein-Barr virus promoter location-2
EGD	Esophagogastroduodenoscopy
EGFR	Epidermal Growth Factor Receptor
EGJ	Esophageal Gastric Junction
en%	% Energy
ENR	Medium containing EGF, Noggin and R-spondin
ESCC	Esophageal Squamous Cell Carcinoma

EUT	Euthanize (time-point)
Fas/FFA	Fatty Acids/ Free Fatty Acids
FcR	Fc Receptor
FCS	Fetal Calf Serum
FFPE	Formalin-Fixed Paraffin-Embedded
FM	Fat Mass
GAPDH	Glyceraldehydephosphate dehydrogenase
G-CSF	Granulocyte-colony stimulating factor
gDNA	genomic DNA
GE	Gross Energy
GERD	Gastroesophageal Reflux Disease
GF	Growth Factors
GSEA	Gene Set Enrichment Analysis
H&E	Hematoxylin and Eosin
hBAC	human Bacterial Artificial Chromosome
HFD	High Fat Diet
HGF	Hepatocyte Growth Factor
hGH	human growth hormone
IFNg	Interferon gamma
IGF-1	Insulin-like Growth Factor-1
IL-10	Interleukine-10
IL-12	Interleukine-12
IL-17	Interleukine-17
IL-17	Interleukine-17
IL-1b	Interleukine-1beta
IL-1Ra	Interleukine-1Receptor antagonist
IL-22	Interleukine-22
IL-23	Interleukine-23
IL-6	Interleukine-6
IL-8	Interleukine-8
IL-8	Interleukine-8
IL-8Tg	Interleukine-8 Transgenetic
ILCs	Innate Lymphoid Cells
IMCs	Immature Myeloid Cells
IVC	Individually Ventilated Cages
JNK	c-Jun N-terminal protein kinases
KC	Murine homolog of IL-8
kDa	kilo Dalton
KFB	Kompetenzzentrum Floureszente Bioanalytik der Universität Regensburg, Germany
LES	Lower Esophageal Sphincter
Lgr5	Leucine-rich repeat-containing G-protein coupled receptor 5
LM	Lean Mass
LPS	Lipopolysaccharide
MC	Mast Cells
MCP-1	Monocyte Chemotactic Protein-1
MDSCs	Myeloid Derived Suppressor Cells

MNCs	Mononuclear Cells
ME	Metabolizable Energy
mm	millimeter
MRI	Magnetic Resonance Imaging
N_2	Nitrogen gas
NAP-2	Neutrophil Activating Protein-2
NCBI	National Center for Biotechnology Information
NFkB	Nuclear Factor kappa-light-chain enhancer of activated B-cells
ng	nanogram
NK	Natural Killer cells
NMR	Nuclear Magnetic Resonance
PAS	Periodic Acid-Schiffs
PBS	Phosphate Buffered Saline
PCR	Polymerase Chain Reaction
PPIs	Proton Pump Inhibitors
PUFA	Polyunsaturated Fatty Acids
RNA	Ribonucleic Acid
ROS	Reactive Oxygen Species
RT	Reverse Transcription/ Room Temperature depending on context
SCJ	Squamo-Columnar Junction
SEER	Surveillance Epidemiology and End Results
SFA	Saturated Fatty Acids
SOS	Swedish Obese Subjects
SPF	Specific-Pathogen-Free facilities
STAT	Signal Transducer and Activator of Transcription
TAMs	Tumor Associated Macrophages
TBS-T	Tris-Buffered Saline and Tween 20
TD1	Type 1 diabetes
TGFb	Transforming Growth Factor beta
Th	T-helper cells
TLR	Toll-like Receptor
TME	Tumor Microenvironment
TNF-a	Tumor Necrosis Factor-alpha
TRAIL	TNF-related Apoptosis-Inducing Ligand
UES	Upper Esophageal Sphincter
VEGF	Vascular Endothelial Growth Factor
WAT	White Adipose Tissue
WC	Waist Circumference
WHO	World Health Organization
WT	Wild Type

Genes of interest from the Results Chapters have been described in Section 2.15: Tables and Appendices.

Curriculum Vitae

Münch, Natasha Stephens

Geburtsdatum/-ort: 13.12.1985/ Honolulu, Hawaii, USA
Elsässerstrasse 24,
81667 München, DE
(0176) – 84743468
natashasmuench@gmail.com

Ausbildung

University of California Davis	Bachelor of Science, Juni 2008
Davis, Kalifornien, USA	*Food Science & Technology*
University of California Davis	Master of Science, September 2011
Davis, Kalifornien, USA	*Food Science & Technology, Nutrition*
Technische Universität München	Dr. rer. nat., Oktober 2016
München, Deutschland	*Ernährung und Immunologie*

Wissenschaftliche Erfahrungen

09/2011-Heute   Doktorandin, Wissenschaftszentrum Weihenstephan für Ernährung, Landnutzung und Umwelt, Technische Universität München (Arbeitsgruppe PD Dr. med. M. Quante)
- Hochfettdiät beschleunigt ösophageale Dysplasie in einem Mausmodell für Barrett-Ösophagus durch IL-8 gesteuerte Bildung einer inflammatorischen Nische

Sommer 2012/2013 Junior Mentor, DAAD Rise Programs
- Anleitung und Mentoring von 4 internationalen Studenten während deren 12 wöchigem Praktika in Onkologie und Ernährungsbiologie.

03-04/2012   Gastwissenschaftlerin, Beth Israel Deaconess Medical Center, Harvard Medical School Teaching Hospital (Arbeitsgruppe Dr. C. Mantzoros)
- Durchführung eines Kollaborationsprojekt als Gastwissenschaftlerin. Dabei wurden neue Analysemethoden erlernt.

09/2009- 09/2011 Master Studentin, Lehrstuhl Lebensmittelwissenschaft und Technik, UC Davis (Arbeitsgruppe Dr. C. Slupsky)
- Einfluss von Stresshormonen auf intestinale Epithelzellen und das Mikrobiom.

05/2009- 12/2010 Lehrassistentin, Lehrstuhl Lebensmittelwissenschaft und Technik, UC Davis
- Assistentin in zwei Laborkursen. Inhalte / Aufgaben: Durchführung von Experimenten, Bewertungen von Arbeiten und wöchentlichen Testaten.

01/2007-04/2007 Wissenschaftlicher Mitarbeiter, Lehrstuhl Lebensmittelwissenschaft und Technik, UC Davis
- Probenverarbeitung von Granatapfel- und Gerstenextrakten, Analyse von Inhaltsstoffen als auch deren sensorischen Beschaffenheit.

Konferenzen und Präsentationen
1. Interact München, 2015, München, Deutschland – Poster Präsentation (April, 2015)
2. II.Med Molecular Medicine Retreat, Tegernsee, Deutschland - Vortrag (Oktober, 2014)
3. Keystone Symposium, Inflammation, Infection and Cancer, Whistler, Kanada - Poster Präsentation (März, 2014)
4. Mildred Scheel Cancer Conference, Deutsche Krebshilfe, Königswinter/Bonn, Deutschland – Poster Präsentation (Juni, 2013 & 2015)
5. Molecular Medicine Seminar Series, Klinikum rechts der Isar, Munich, Deutschland – Vortrag (Januar, 2013)

Preise und Ehrungen
1. TUM Graduate School International Travel Award (2014)
2. California Walnut Commission Travel Award (2013)
3. President, UC Davis Food Science Graduate Student Association *(2010-2011)*
4. UC Davis Unternehmertum Akademie für Ernährung und Gesundheit, Produktentwicklung & Marketing (2011)
5. UC Davis Dean's Honor List (Winter 2007, Winter 2008, Winter 2011)
6. Ehrungen und Stipendien von Lehrstuhl für Lebensmittelwissenschaft und Technik (2007-2011)
7. Teammitglied, UC Davis Produktentwicklung Team: Developing Solutions for Developing Countries and IFTSA Product Development Competition (2007-2011)

Referenzen
PD Dr. med. Michael Quante, Klinikum rechts der Isar
Tel: +49 89 4140 7870. Michael.Quante@tum.de

Dr. Carolyn Slupsky, Assistant Professor
Lehrstuhl für Lebensmittelwissenschaft und Technik, UC Davis, Kalifornien, USA
Tel: +1 530 219 5757. cslupsky@ucdavis.edu

Dr. Charles Bamforth, Professor
Lehrstuhl für Lebensmittelwissenschaft und Technik, UC Davis, Kalifornien, USA
Tel: +1 530 752 9476. cwbamforth@ucdavis.edu

Acknowledgement

This journey I embarked upon five years ago is not one that was travelled alone.

First and foremost, to my supervisor Dr. Michael Quante, thank you for taking me on as one of your first Ph.D. students, for supporting me financially through the GRK and independently, and for advising me scientifically. When you offered me the position five years ago, you changed my life forever, thank you for giving me this opportunity!

Dr. Hsin-Yu Fang, thank you for all you have done; for painstakingly re-analyzing data to be certain of our results, reading through my revisions and helping with my lab work once I found out I was pregnant, I am truly grateful. Jonas Ingermann, my other half in this project, for your laughter and friendship on the countless rides to and from Freising and for never hesitating to help with my lab work especially after I found out I was pregnant, I am beyond grateful! Vincenz Sahm, thank you for being my German translator for this thesis. Marina Grether and Steffi Neupert, thank you for cutting, cutting, cutting! Victoria Kellner, thank you for your hard work and for being a great Master's student. Carlo Maurer, thanks for leaving me your project, good thing it turned out well! To the rest of the "Quante lablings" and colleagues from the II. Med, thank you for all your help along the way and for making it a memorable journey!

Ana Hidalgo-Sastre, thank you for your revisions, but especially for your friendship and encouragement to push through!

Dr. Florian Bolze, Nadine Rink, and members of the Klingenspor lab, who introduced me to methods and techniques for metabolic phenotyping, thank you for your patience! Thank you Florian, for all your help and advice with my data.

To my GRK buddies and the friends I have made along this journey, thank you for making it a great ride! Thank you Dorothea, for all you have done for me.

To Jutta and Andreas, thank you for making feel like part of the family since I moved here almost 5 years ago and for your encouragement along the way.

To my parents, thank you for sharing your passion for science with me and supporting my decision to move far, far away from home to follow my dreams. Tami, thank you for being my sister and friend, I hope you too will follow your dreams and I promise to be just as supportive of them as you have been of mine.

To my sweet baby girl, thank you for choosing me to be your mother, and motivating me from within to finish this work before your arrival!

Lastly, I would like to thank the "cherry on top" of this incredible sundae! Steffen, from the moment we met our life together has been the greatest adventure. Thank you for encouraging me, challenging me, loving me and marrying me. I could not have done this without you by my side.